Experimental investigation of damage evolution during strain burst in brittle rocks for deep mines

By

Selahattin Akdag

The School of Civil, Environmental and Mining Engineering

This thesis is submitted in fulfilment of the requirements for the degree of

Doctor of Philosophy

in the Faculty of Engineering, Computer and Mathematical Sciences

Adelaide 2019

I dedicate this work to my dearest mum Serpil Akdag

STATEMENT OF ORIGINALITY

I certify that this work contains no material which has been accepted for the award of any other degree or diploma in my name, in any university or other tertiary institution and, to the best of my knowledge and belief, contains no material previously published or written by another person, except where due reference has been made in the text. In addition, I certify that no part of this work will, in the future, be used in a submission in my name, for any other degree or diploma in any university or other tertiary institution without the prior approval of the University of Adelaide and where applicable, any partner institution responsible for the joint-award of this degree.

I give consent to this copy of my thesis when deposited in the University Library, being made available for loan and photocopying, subject to the provisions of the Copyright Act 1968.

The author acknowledges that copyright of published works contained within this thesis resides with the copyright holder(s) of those works.

I also give permission for the digital version of my thesis to be made available on the web, via the University's digital research repository, the Library Search and also through web search engines, unless permission has been granted by the University to restrict access for a period of time.

Selahattin Akdag Date: 2nd May 2019

Abstract

Experimental investigation of damage evolution during strain burst in brittle rocks for deep mines

A Thesis submitted for the degree of Doctor of Philosophy

Selahattin Akdag

The School of Civil, Environmental and Mining Engineering

The University of Adelaide

Adelaide, 2019

The increasing demand for resources and depletion of near ground mineral resources caused deeper mining operations under high-stress and high-temperature rock mass conditions. As a results of this, strain burst, which is the sudden and violent release of stored strain energy during dynamic brittle failure of rocks, has become more prevalent and created considerable safety risks damaging underground infrastructures. This research focuses on the development of experimental methodologies to better understand the fundamental knowledge concerning the failure mechanism of strain burst and the influence of thermal damage, high confining pressure and various loading rate on the overall mechanical behaviour of highly brittle granitic rocks leading to strain burst.

Strain burst is related to the elastic stored strain energy and how this stored energy is released during the unstable spontaneous failure. Therefore, it is significant to investigate the energy state during strain burst from the viewpoint of energy theory. In this sense, circumferential strain controlled quasi-static tests on Class II rocks over a wide range of confining pressures at different heat-treatment temperatures were conducted to capture the snap-back behaviour and calculate excess strain energy that is responsible for the spontaneous instability. A new energy calculation method associated with acoustic emission (AE) was developed to express the propensity of strain burst and investigate the post-peak energy distribution characteristics for brittle rocks under the coupling influence of confinement and temperature. In order to quantify the micro-crack density and reveal the micro-fracture characteristics of the brittle rocks exposed to various temperatures, scanning electron microscopy (SEM) analysis was also conducted. This is highly relevant to link the excess strain energy and the main failure mechanism triggering strain burst under high-temperature condition.

The failure process of strain burst is the outcome of the unstable growth and coalescence of secondary micro-cracks. If the dissipative energy to grow pre-existing cracks and the secondary cracks is smaller than the elastic stored strain energy in rock masses, the residual strain energy will be released suddenly in the form of kinetic energy, resulting in ejecting high-velocity rock fragments. Therefore, understanding the crack initiation and propagation in rocks is of great concern for engineering stability and security. As an intrinsic property of rocks to resist crack initiation and propagation, the rock fracture toughness is the most significant material property in fracture mechanics. In this respect, the three-point bending method was applied using cracked chevron notched semi-circular bend (CCNSCB) granite specimens subjected to different temperatures under a wide range of loading rates in pure mode I. A suitable relation for the dimensionless stress intensity factor (Y^*) of SCB with chevron notch samples were presented based on the normalised crack length (α) and half-distance between support rollers ($S/2$). The minimum dimensionless stress intensity factor (Y^*_{min}) of CCNSCB specimens were determined using an analytical method, i.e., Bluhm's slice synthesis method. In this study, the influence of thermal damage and loading rate on the quasi-static mode I fracture toughness and the energy-release rate using CCNSCB method was investigated. In the deep mining process, the rock mass is subjected to a dynamic disturbance caused by blasting, and mechanical drilling resulting in dynamic fractures in the forms of strain burst, slabbing, and spalling. The dynamic rock fracture parameters, including dynamic initiation fracture toughness and fracture energy which are an important manifestation of dynamic rock failure (strain burst) in deep underground engineering and they are of great practical significance to assess the dynamic fracture behaviour of deep rock masses. Since deep rock engineering operations in high temperature and high pressure environment is prone to strain burst, the influence of thermally induced damage on the dynamic failure parameters of granite specimens was investigated. The damage evolution of granitic rocks were studied over a wide range of loading rates to reveal the rate dependency of strain burst. Dynamic fracture toughness tests were carried out on granite under different temperatures and impact loadings using a Split Hopkinson Pressure Bar (SHPB) apparatus at Monash University. With dynamic force balance achieved in the dynamic tests, the stable-unstable transition of the crack propagation crack was observed and the dynamic initiation fracture toughness was calculated from the dynamic peak load.

The thermal damage influence on strain burst characteristics of brittle rocks under true-triaxial loading-unloading conditions was investigated using the AE and kinetic energy analyses. A unique strain burst testing system enabling to simulate the creation of excavation at the State

Key Laboratory for Geomechanics and Deep Underground Engineering in Beijing (China) was used to replicate strain burst condition. Time-domain and frequency-domain responses AE waves related to strain burst were studied, and the damage evolution was quantified by *b*-values, cumulative AE energy and events rates that can be used as warning signals to rock failure. The ejection velocities of the rock fragments from the free face of the granite specimens were used to calculate kinetic energies which can be used as an indicator for quantitatively evaluating the intensity of strain burst.

Based on the energy evolution characteristics of brittle rocks under uniaxial and triaxial compression, true-triaxial loading-unloading and three-point bending, new strain burst proneness indexes and strain burst criterion were proposed. The effects of temperature, confinement and loading rate on strain burst proneness were discussed.

This study aims to advance the understanding on underlying processes that govern the macro-behaviour of brittle rocks during strain burst and make use of this insight to further advance our current predictive capabilities of strain burst with references to large-scale underground mining. Using the developed experimental methodologies in this study, fractures around an excavation to reduce the amount of excess strain energy leading to strain burst can be determined and ultimately incipient strain burst in deep mines can be predicted avoiding potential hazards. Using the methodology for forecasting of strain burst in this research can be used for enhanced understanding of the design of rock support in strain burst-prone areas in deep mining activities

The findings of this study will facilitate achieving a better and comprehensive understanding of the damage process during strain burst in deep mines. This study underpins the development of better and more efficient prediction methods for strain burst which will lead to better planning guidelines and ultimately safer deep underground working conditions.

Acknowledgements

First and foremost, I would like to express my sincere gratitude to my principal supervisor and mentor, Associate Professor Murat Karakus for his supervision, guidance and support during my Ph.D. study at the University of Adelaide. I also would like to thank him for being a great role model for me in pursuing a scientific career and for his enthusiasm in the pursuit of knowledge. Guided by his kind wisdom, I have learned much about life in general. I would like to express my gratitude to my co-supervisors Associate Professor Giang D. Nguyen and Senior Lecturer Abbas Taheri for their guidance, supervision and support during my study.

I would like to acknowledge the financial support from the Australian Research Council (ARC-LP150100539), OZ Minerals, and the principal geotechnical manager David Goodchild.

I would like to thank Professor Manchao He for allowing me to use the novel true-triaxial strain burst testing system at the State Key Laboratory for Geomechanics and Deep Underground Engineering in Beijing, China.

Many thanks to Professor Jian Zhao and Dr Qianbing Zhang for allowing me to use the Split Hopkinson Pressure Bar apparatus at Monash University.

Many thanks to Professor Michael Goodsite and Assistant Professor Mustafa Erkayaoglu for their continuous support and motivation.

I also would like to express special thanks to my mates and colleagues; Ugur Alkan and Thomas Bruning, and my amazing friends: Urmila Rosario and Amanda Niroshani Nimalasena for their continuous support and motivation.

I would like to express my special thanks to the laboratory technicians Adam Ryntjes and Simon Golding.

Last but not least, I owe my loving thanks to my family for their encouragement, great passion and kind understanding during the preparation of this study. Most of all, I would love to give my deepest gratitude to my dearest mum, Serpil Akdag. Without her continuous support, care, sacrifice and love, I could not have finished this thesis.

Publications

1. **Akdag S**, Karakus M, Nguyen GD, Taheri A, Bruning T (2019). Evaluation of the propensity of strain burst in granite based on post-peak energy analysis. Underground Space. (Accepted).

2. **Akdag S**, Karakus M, Nguyen GD, Taheri A (2019). Combined influence of increasing temperature and confining pressure on the potential intensity for strain burst (to be submitted to the International Journal of Rock Mechanics and Mining Sciences).

3. **Akdag S**, Karakus M, Nguyen GD, Taheri A (2019). Quasi-static and dynamic fracture and energy characteristics of strain burst in granite under different temperatures and loading rates (to be submitted Engineering Fracture Mechanics).

4. **Akdag S**, Karakus M, Nguyen GD, Taheri A (2019). New energy indexes for evaluating the strain burst proneness of brittle rocks and their application to real engineering problems (to be submitted to the International Journal of Rock Mechanics and Mining Sciences).

5. **Akdag S**, Karakus M, Taheri A, Nguyen GD, He M (2018). Effects of thermal damage on strain burst mechanism for brittle rocks under true-triaxial loading conditions. Rock Mechanics and Rock Engineering. 51 (6): 1657-1682.

6. Bruning T, Karakus M, **Akdag S**, Nguyen GD, Goodchild D (2018). Influence of deviatoric stress on rockburst occurrence: An experimental study. International Journal of Mining Science and Technology. 28 (5): 763-766.

7. **Akdag S**, Bruning T, Karakus M (2019). How can accumulated damage lead to a violent rock failure? An innovative experimental study for rockburst. *53rd US Rock Mechanics/Geomechanics Symposium*, New York City, USA: American Rock Mechanics Association.

8. **Akdag S**, Karakus M, Taheri A, Nguyen GD, He Manchao (2018). Effects of thermal damage on strain burst mechanics of brittle rock using acoustic emission. In Litvinenko (Ed.) *Geomechanics and Geodynamics of Rock Masses, Proceedings of the 2018 European Rock Mechanics Symposium (EUROCK)* (pp. 581-585). Saint Petersburg, Russia.

9. Karakus M, **Akdag S**, Randhawa LS, Zhao Y, Cao Z (2018). State-of-the-art damage assessment methods for brittle rock using digital image correlation and infrared thermography. In Litvinenko (Ed.) *Geomechanics and Geodynamics of Rock Masses, Proceedings of the 2018 European Rock Mechanics Symposium (EUROCK)* (pp. 525-531). Saint Petersburg, Russia.

10. **Akdag S**, Karakus M, Nguyen GD, Taheri A (2017). Influence of specimen dimensions on bursting behaviour of rocks under true-triaxial loading conditions. In J. Wesseloo (Ed.), *8th International Conference on Deep and High Stress Mining* (pp. 447-457). Perth: Australian Centre for Geomechanics.

11. Karakus M, **Akdag S**, Bruning T (2016). Rock fatigue damage assessment by acoustic emission. In P. Ranjith & J. Zhao (Ed.), *International Conference on Geo-mechanics, Geo-energy and Geo-resources, IC3G* (pp. 9-82-88). Melbourne, Australia.

Table of contents

List of abbreviations

AE	Acoustic emission
HS	High-speed
SEM	Scanning electron microscope
EDS	Energy dispersive spectrometer
LEFM	Linear elastic fracture mechanics
SIF	Stress intensity factor
ISRM	International Society for Rock Mechanics
CB	Chevron bend
SR	Short rod
CCNBD	Cracked chevron notched Brazilian disc
SCB	Semi-circular bend
NSCB	Notched semi-circular bend
CCNSCB	Cracked chevron notched semi-circular bend
CSTBD	Cracked straight through Brazilian
CSTFB	Cracked straight through flattened Brazilian disc
SNDB	Straight notched disc bend
SENRBB	Single edge-notched round bar in bending
SHPB	Split Hopkinson Pressure Bar
CT	Compact tension
WLCT	Wedge loaded compact tension
HNBD	Holed-notched Brazilian disc
SENB	Single edge notch bending
COD	Crack-opening displacement
DIFT	Dynamic initiation fracture toughness
LVDT	Linear variable differential transducer

SSM	Slice synthesis method
FE	Finite element
KE	Kinetic energy
FFT	Fast fourier transform
MSPS	Million samples per second
RT	Room temperature
In	Incident wave
Re	Reflected wave
Tr	Transmitted wave

List of symbols

σ_{UCS}	Uniaxial compressive strength
F_{peak}	Peak force
ε_a	Axial strain
ε_l	Lateral strain
U_E	Elastic stored strain energy after the point of Class II behaviour
Φ_{CW}	Energy consumption dominated by cohesion degradation
Φ_{FM}	Energy dissipated during the mobilisation of frictional failure
U_{RE}	Residual stored elastic strain energy
Φ_{EX}	Excess strain energy released during brittle failure (strain burst)
σ_A	Point of axial strain reversal
σ_B	Point of brittle failure intersection
E	Elastic stiffness
M	Post-peak modulus
v	Poisson’s ratio
ρ	Density of the rock
σ_1	Axial stress (major principal stress)
σ_2	Intermediate principal stress
σ_3	Lateral stress (minor principal stress)
v	Ejection velocity of rock fragments
T	Temperature
P	Load on specimen
S	Support span
R	Radius of specimen
D	Diameter of specimen

R_S	Saw radius
B	Thickness of specimen
R	Radius of specimen
a	Crack length
a_0	Initial crack length
a_1	Final crack length
a_m	Critical crack length
α_B	Normalised (dimensionless) specimen thickness
β	The ratio of the span to specimen diameter
α_0	Normalised (dimensionless) initial crack length
α_1	Normalised (dimensionless) final crack length
α_m	Normalised (dimensionless) critical crack length
P_{max}	Peak load
Y^*	Dimensionless stress intensity factor of specimen
Y^*_{min}	Minimum dimensionless stress intensity factor of specimen
h_c	Cutting depth of chevron notch
Δt	Thickness of slice in slice synthesis method
b	Crack front width
K_I	Quasi-static mode I stress intensity factor
Y_I	Quasi-static mode I dimensionless stress intensity factor
i	Slice number in slice synthesis method
a_i	Crack length of the *i*th slice
n	Constant in reduction factor formulation of slice synthesis method
N	Number of slices in slice synthesis method
γ	Geometry factor in slice synthesis method
u_2	Displacement of a crack face in the direction of the maximum tension

K'	Stress intensity factor for the new crack length
K_{IC}	Quasi-static mode I fracture toughness
G_I	Mode I energy-release rate
K_{Id}^i	Mode I dynamic initiation fracture toughness
$\dot{K}_I$	Loading rate of dynamic fracture toughness test
c_b	P-wave velocity of the bar
E_b	Elastic modulus of the bar
A_b	Cross-sectional area of the bar
ρ_b	Density of the bar
$\varepsilon_i, \varepsilon_t, \varepsilon_r$	Incident, transmitted, and reflected strains of the bar
P_1, P_2	Dynamic forces in the incident and transmitted bar
$\dot{\varepsilon}(t)$	Strain rate of the specimen at time *t* during loading using the SHPB
$\varepsilon(t)$	Strain of the specimen at time *t* during loading using SHPB
$\sigma(t)$	Stress of the specimen at time *t* during loading using SHPB
C	One dimensional longitudinal elastic stress wave velocity of the bar
A_0	Initial cross-sectional area of the specimen
L_0	Initial length of the specimen
$v_{striker}$	Striking impact velocity
σ_{c1}, σ_{c2}	UCS of cylindrical and rectangular prism specimen
D_{SB}	Strain burst damage variable
Ω	Cumulative amount of AE energy or number of AE hits at a certain time
Ω_m	Cumulative amount of energy or number of hits during the whole test
A_{dB}	Peak amplitude of AE events in decibels
N	Incremental frequency
$\bar{v}_i$	Initial ejection velocity of the *i*th rock fragment
m_i	Mass of the *i*th rock fragment

x_0, y_0, z_0	Initial ejection location of the fragment
x_1, y_1, z_1	Final dropping down point of the fragment
Ω_{SB}	Excess strain energy index
λ_{SB}	Released energy index
Ψ_{SB}	Energy-release rate index
W	Applied energy
σ_{SB}	Strain burst stress

List of tables

List of figures

Chapter 1: Introduction

1.1 - General background

The increasing demand for mineral resources and depletion of near-surface reserves has driven more mining applications into higher depth which has caused that stress-induced rock failure processes are inevitable. Before excavation, rock mass at depth exists in a true-triaxial state of stress equilibrium ($\sigma_1 > \sigma_2 > \sigma_3$) where σ_1, σ_2, and σ_3 are the maximum, intermediate, and minimum principal stresses, respectively. Introducing an excavation which results in forming an open free boundary condition changes the stress state of the rock mass near the excavated boundary and elastic strain energy accumulates in the surrounding rock. When the excavation-induced stress exceeds the carrying capacity of the rock mass, the stored elastic strain energy within the rock mass is abruptly released, resulting in strain burst occurrence. Strain burst is a nonlinear dynamic rock instability accompanied by violent rock ejection, which frequently occurs during the excavation of hard brittle rock masses subjected to high stress ground conditions, leading to severe rock mass damage. Strain burst can kill workers and usually results in casualties and damages to equipment as well as delays the project schedule. Due to its nature of unpredictability, destructiveness and suddenness, strain burst poses an increasing threat to the safety and production of deep engineering operations. For instance, several intense strain burst caused casualties, destruction of equipment and production delays with the maximum excavation depth of approximately 3050 m at Jinping II hydropower station in China (Li et al. 2012).

Deep mining activities for extracting deep mineral resources require an assessment of mechanical rock behaviour and damage mechanism for long-term stability. Although, considerable efforts have been devoted to the investigation of the strain burst, the fundamental mechanism of strain bursting is still not adequately understood and should be further explored. Mines under high-stress conditions are deemed to be operating at highly-stresses ground conditions and the confinement controls the rock failures. With the advancement of extraction, progressive build up stress in the rock mass takes place which may lead to the sudden violent ejection of rocks. With the increasing of excavation depth, the influence of elevated ground temperature becomes remarkably significant on triggering strain burst. The coupling of high-stressed ground conditions and thermal damage will alter the overall mechanical behaviour of hard brittle rocks which may trigger strain bursting in deep engineering operations. Therefore, an in-depth understanding the damage process of hard brittle rocks and how the overall mechanical behaviour of rock is affected by high stress and high temperature is essential to facilitate long-term stability maintenance of deep engineering constructions, reducing the tendency of strain burst, which will impact on the safety of deep mining operations.

This research focuses on investigating the mechanism of strain burst and provides an insight of this phenomenon and its relevance to deep mining operations. This research examines and addresses the challenges in the experimental investigation of strain burst mechanism related to the inherent difficulties in quasi-static and dynamic failure simulation. The strain burst phenomenon is explored and an innovative experimental methodology is adopted to investigate the underlying mechanism of strain burst and the influence of external factors such as high confining pressure, elevated temperature, and loading rate on strain burst mechanism for brittle rocks. This approach is intended to expedite in arriving at a systematic engineering methodology that evaluates the propensity of strain burst whereby severe damage conditions may exist and the excavations are vulnerable to strain burst damage.

1.2 - Research objectives

The main objective of this research is to investigate the damage mechanism of strain burst in deep mines under high stress and elevated temperature conditions and provide guidelines for the development of an effective and reliable method to forecast the propensity of strain burst. In addition, this research aims to underpin the design of appropriate rock support systems in strain burst-prone deep mines which will result in cost-effective deep mining operations under safe working environments. These goals are achieved by accomplishing a series of tasks listed below:

- Forecasting the propensity of strain burst of brittle rock based on post-peak energy analysis.
- Investigating the combined influence of confining pressure and thermal damage on the intrinsic potential for strain burst, energy evolution and mechanical behaviour of brittle granitic rocks leading to strain burst.
- Characterisation of quasi-static and dynamic fracturing and energy evolution during strain burst.

- Analysing the thermal damage and rate dependence of quasi-static and dynamic fracture toughness and energy parameters for strain burst failure process.
- Investigating the effects of thermal damage on strain burst mechanism under true-triaxial loading-unloading conditions.
- Evaluating the strain burst proneness based on the energy characteristics during strain burst.

1.3 - Thesis organisation

The starting point of this research is a brief review of the damage processes and strain burst in brittle rock, all of which are presented in Chapter 2. The emphasis in Chapter 2 is placed on presenting the efforts devoted to investigating the real damage process of strain burst under the condition of laboratory experiments within the context of damage and rock mechanics and fracture mechanics. This chapter also includes the factors that contribute to strain bursting.

Chapter 3 of this thesis addresses the post-peak energy balance of Class II behaviour at spontaneous failure and presents a newly developed energy calculation method based on the post-peak energy distributions for brittle rocks using acoustic emission (AE). The methodology used in a series of circumferentially-controlled quasi-static uniaxial and triaxial compression tests for forecasting the propensity of strain burst is presented. The intrinsic potential intensity for strain burst in granite is quantitatively assessed. Coupling influence of high confining stress and thermal damage on the overall mechanical behaviour and post-peak energy characteristics is analysed and the underlying mechanism is discussed. The crack evolution characteristics of thermally-treated granite specimens were also examined.

Chapter 4 of this thesis focuses on exploring the fracture characteristics during strain burst. Damage accumulation leading to strain burst is a static process followed by the dynamic release of stored strain energy in which stored strain energy is converted to kinetic energy in the form of rock fragment ejection. Hence, strain burst from initiation to end is a combined quasi-static and dynamic failure process. In order to estimate the onset of strain burst failure process during deep mining operations, it is significant to understand the behaviour of the rock subjected to mode I fracturing as it is assumed that the mode I fractures dominate the failure process during strain burst. Therefore, characterisation of fracture behaviour and energy evolution during strain burst by conducting quasi-static and dynamic fracture toughness tests is presented. For fracture toughness tests, cracked chevron notched semi-circular bend (CCNSCB) method is applied. Dimensionless stress intensity factor (Y^{*}_{min}) approach using a semi-analytical synthesis method is adopted to determine the fracture toughness values. Coupling effects of loading rate and temperature on quasi-static mode I fracture toughness and energy-release rate are investigated. To provide a deeper insight into dynamic fracture propagation during strain burst, Split Hopkinson Pressure Bar technique is adopted to perform dynamic fracture toughness tests over a wide range of loading rates. The dynamic mechanical behaviours of CCNSCB granite specimens at various impact velocities are studied. With the dynamic force balance across CCNSCB samples, the evolution of dynamic stress intensity factor (SIF) is analysed. Thermal damage influence and rate dependence of the dynamic mode I fracture initiation toughness (K^{i}_{Id}) are investigated. Loading rate dependent progressive fracturing and failure modes of CCNSCB granite exposed to different levels of temperature at various impact velocities are assessed by analysing the High-Speed camera images.

In Chapter 5, simulating the damage process during strain burst by conducting true-triaxial loading–unloading strain burst tests is focused. The effects of thermal damage on strain burst mechanism of brittle rocks under true-triaxial unloading conditions are investigated. The variations in strain burst stress with temperature are used as indicators of strain burst occurrence and compared with the strain bust criteria based on strength theory. The failure processes of granite specimens induced by different temperatures are discussed based on the recorded high-speed (HS) camera videos. The fracturing processes of strain burst under different temperature conditions are investigated by assessing the evolution of instantaneous and cumulative AE energy, hit, and counts characteristics. The damage caused by temperature is quantified by the variation in AE signal characteristics and a strain burst damage variable is proposed and temperature influence on damage accumulation rate is discussed. To assess the degradation of rock and strain burst process during deformation stages, b-value analysis is conducted and the influence of temperature on b-value, revealing the mechanism of micro- and macro-cracking during strain burst. The frequency-amplitude characteristics of the AE waves of thermally-treated granite are also presented. By analysing the recorded HS videos, ejection velocities of rock fragments are calculated and the kinetic energies of the rock fragments which can be used as a precursor for quantitatively evaluating the intensity of strain burst are analysed and discussed in detail.

In Chapter 6, based on the energy evolution characteristics and mechanical behaviour of brittle rocks under uniaxial and triaxial compression, true-triaxial loading-unloading and three-point bending, new strain burst proneness indexes are proposed and new strain burst criterion based on these indexes are presented to quantitatively evaluate the intensity of strain burst of brittle rocks. The combined influence of thermal damage, confining pressure and loading rate on strain burst proneness is also discussed. A methodology for forecasting of strain burst is also proposed which can be used for enhanced understanding of the design of rock support in strain burst-prone areas in deep mining activities. This chapter also draws the key conclusions of this research undertaken and proposes recommendations for future work.

Chapter 2: Damage processes and strain burst in brittle rock

2.1 - Introduction

Strain burst which is one of the major concerns in highly-stressed underground engineering, poses a serious threat to workers and construction equipment and has become a topic of increased research in the fields of rock mechanics and rock engineering. Despite there have been substantial efforts of noteworthy contributions, the mechanism of strain burst associated with the influencing factors is still unclear and a deeper insight is, therefore necessary to ensure safe constructions and operation of deep underground excavations.

Deep mining and civil engineering related deep underground operations are challenging tasks and costly projects, which need special attention and design considerations. When these deep engineering activities go deeper, the rock is subjected to high stresses and elevated temperatures leading to strain bursting. Therefore, an in-depth understanding the damage process of hard rock and how the overall mechanical behaviour of rock leading to strain burst is influenced by high confinement and temperature is of significance for facilitating cost-effective design and long-term stability maintenance of these engineering structures. In addition, rock mass is stressed dynamically during underground mining operations. Accurate characterisation of dynamic fracturing over a wide range of loading rates are thus crucial. However, to the best of our knowledge, all these features are either missing or not addressed at length in the literature.

This chapter presents a brief overview of the progression of research on representing the real damage process of strain burst under the condition of laboratory experiment in the context of rock mechanics and fracture mechanics. First, assessment of strain burst mechanism based on energy analysis under uniaxial and triaxial compression is presented and how high pressure and temperature influence overall mechanical behaviour and energy characteristics of brittle rock is analysed and discussed. The second part focuses on the quasi-static and dynamic mode I fracture toughness tests, revealing the effects of temperature and loading rate on the fracturing characteristics during strain burst. The final component of the literature review will cover the investigation of strain burst evolution mechanism under true-triaxial loading-unloading conditions. This section will identify the deficiencies of the existing methods for investigating the mechanism of strain burst and provide motivation for this research. The understanding of the underlying damage mechanism of strain burst and the mechanical characteristics under different levels of confinement, temperature and impact loads will allow the development of better support design and prediction methods for catastrophic rock failure reducing the impact of strain burst so that future deep underground working environments will ultimately be much safer.

2.2 - Assessment of strain burst mechanism based on energy analysis under uniaxial and triaxial compression

As the depth of underground engineering construction increases, there are substantial problems associated with high rock stress and high temperature leading to strain burst. The coupling of high confinement and thermal damage will influence the overall mechanical behaviour of hard brittle rock in which strain burst occurs frequently in an abrupt and violent manner accompanied by violent rock ejection during deep mining activities. Strain burst can cause severe damage to underground rock engineering applications and construction equipment as well as serious injuries and fatalities. Therefore, elimination and mitigation of strain burst hazard are one of the most challenging problems in rock engineering. Elastic strain energy stored in hard rock which is one of the key factors induces and controls the brittle failure of the rock mass, is the result of the redistribution of stresses near the underground excavation. If the resulting imbalance of the energy of the system is severe enough, the stored energy is released during a rapid post-peak strength degradation of the rock mass, displaying an unstable and violent post-peak failure (strain burst). Strain burst is an energy-driven dynamic destabilisation phenomenon, including energy accumulation, dissipation and release (Akdag et al. 2019). Therefore, the damage of highly-stressed rock during strain burst can be assessed by evaluating the dynamic energy characteristics from the energy evolution point of view. Hard brittle rocks exhibiting Class II behaviour undergo self-sustaining fracturing due to excess stored strain energy, which is accompanied by some energy release. Therefore, the principles of energy redistribution during strain burst, in some regards, can be compared with the principles involved in the spontaneous failure of brittle rocks in compression. Many researchers have investigated the variation characteristics of energy in the failure process of strain burst (Li 2001; Hua and You 2001; Xie et al. 2009; He et al. 2012c; Tarasov and Potvin 2013; Li et al. 2014; Huang and Li 2014; Li et al. 2015; Carpinteri et al. 2018; Hauqin et al. 2018). Peng et al. (2015) studied the variation in energy dissipation and release of coal under triaxial compression and proposed two parameters based on the energy evolution to reflect the coal deformation under different confinement (see Figure 2.1). Meng et al. (2016) analysed the characteristics of energy accumulation, evolution and dissipation of sandstone specimens under uniaxial cyclic loading and unloading compression, revealing the energy evolution of rock deformation and failure (see Figure 2.2). The influence of different strain rates on fracture toughness as well as the energy-release rate of gas shales under three-point bending was investigated by Mahanta et al. (2017), and it was revealed that the fracture toughness and the energy-release rate are functions of the strain rate increase with ascending strain rate, as presented in Figure 2.3. Li et al. (2017) conducted triaxial compression tests on granite specimens under different loading and unloading paths to identify the rules of energy conversion and dissipation during the triaxial failure of hard rocks. They also identified the micro-difference in the granite micro-cracks via a scanning electron microscope (SEM) combined with an energy dispersive spectrometer (EDS), as shown in Figure 2.4. Strain energy density factor approach was adopted to analyse the dynamic damage localisation behaviour of rock mass by Zhou and Yang (2018) and the onset conditions of periodic distribution cracks in a rock mass were determined. The above research results have enriched the knowledge of the energy evolution mechanism of rocks under different loading conditions. However, to the best of our knowledge, the studies mentioned above did not consider the combined influence of temperature and confining pressure, critical external factors affecting the intrinsic mechanism of strain burst, on the energy evolution and balance in the post-peak stage that occurs during strain burst failure process. Hence, it is necessary to investigate and reveal the role of energy redistribution in strain burst and how the mechanism and stored excess strain energy that is responsible for the intrinsic potential energy of strain burst are influenced with thermal damage and confining pressure from the perspective of energy. In this sense, obtaining the complete stress-strain characteristics, i.e. the pre-peak and post-peak stress-strain regimes, are of great significance for analysing the features of the post-peak energy balance in strain burst and interpreting the process of rock deformation and failure.

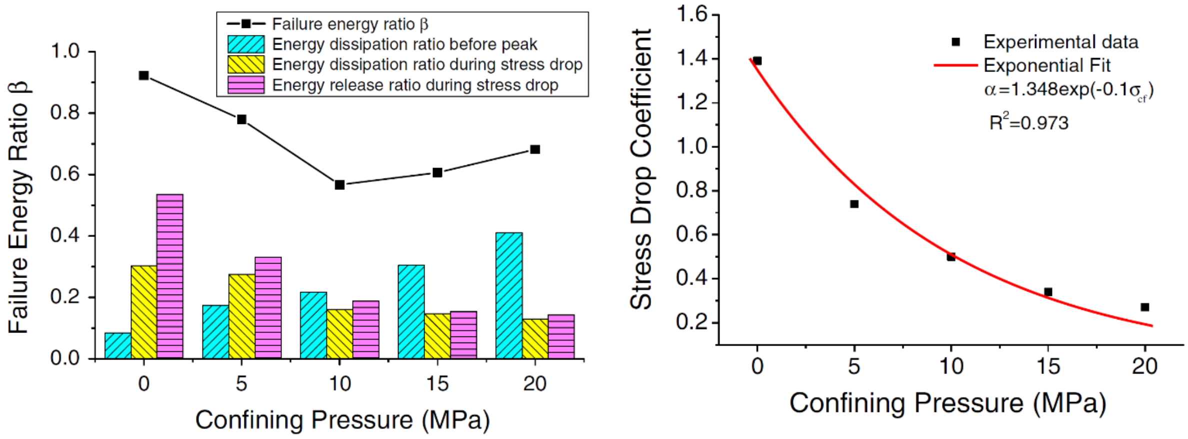

Figure 2.1 Variation in the energy based parameters under various confining pressures (Peng et al. 2015)

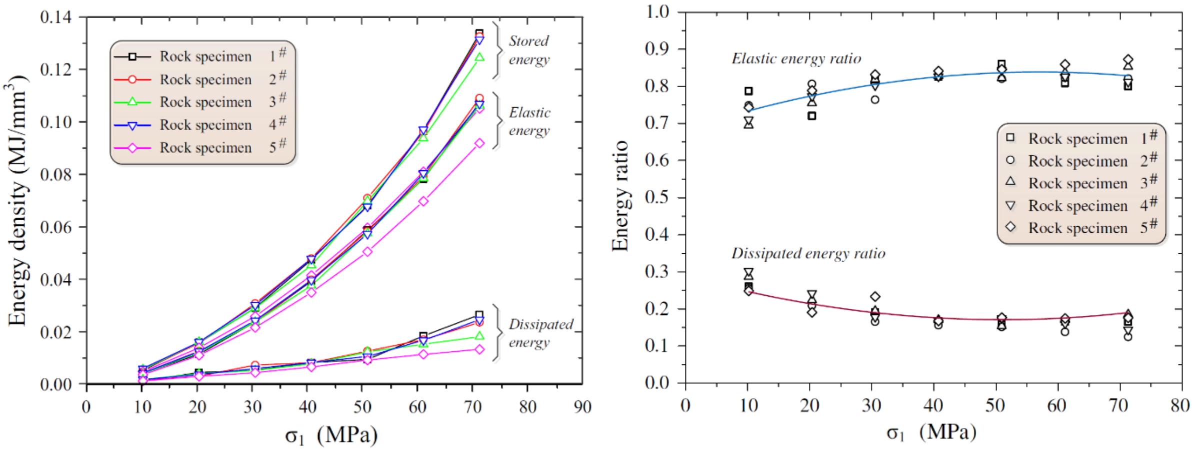

Figure 2.2 Relationships between the elastic energy density, dissipated energy density, stored energy density and the axial loading stress of rock sample and the variation of the elastic energy ratio and dissipated energy ratio of rock at a loading rate of 0.5 kN/s (Meng et al. 2016)

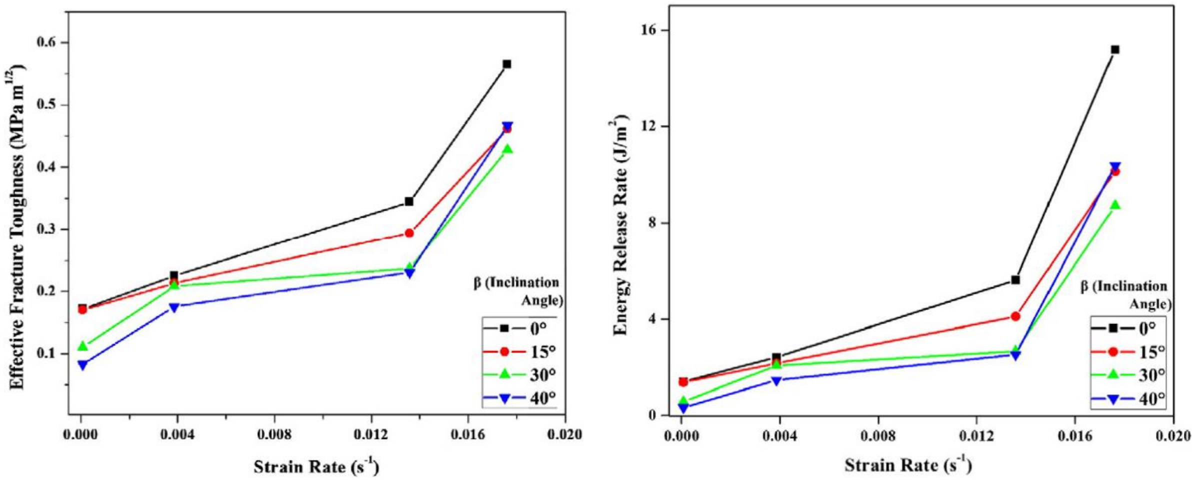

Figure 2.3 Fracture toughness and energy-release rate for the specimens with various notch angles at different strain rates (Mahanta et al. 2017)

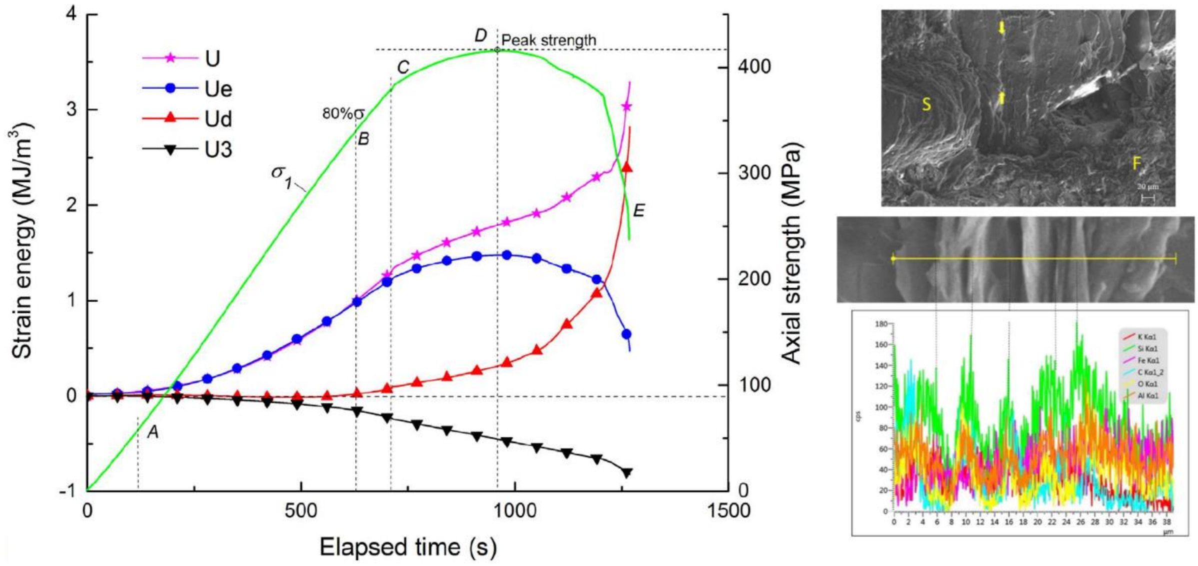

Figure 2.4 Typical time history curve of strain energy and axial stress, SEM image of typical granite and spectrum of line-scanning passing through cracks by SEM-EDS at 40 MPa confinement (Li et al. 2017)

The thermodynamic state of rock is well represented by the stress-strain behaviour of the rock which is the external manifestation of variation in energy during deformation and failure. It is, therefore, necessary to obtain the complete stress-strain response of rock which plays a paramount role in understanding the process of dynamic energy balance at the spontaneous failure (strain burst). Under quasi-static compression, the complete stress-strain behaviour of rocks can be categorised into two groups: Class I and Class II, as depicted in Figure 2.5: For Class I behaviour which is characterised by a negative post-peak slope, additional energy is required for further strength degradation. For rock exhibiting Class II behaviour or snap-back behaviour, showing positive post-peak slope, the elastic energy accumulated within the rock is sufficient to maintain the whole failure in which rock displays self-sustaining fracturing. Both classes can be distinguished from the perspective of the post-peak energy balance. Table 2.1 presents the comparison of some methods for the energy balance at three stages of deformation, energy accumulation, energy dissipation and energy release, in Class I and Class II behaviours.

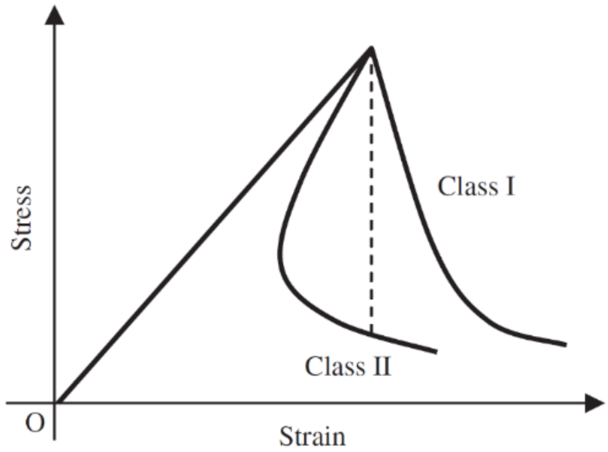

Figure 2.5 Representative illustration for complete stress-strain curves of Class I and Class II behaviour of rock failure under compression (Fairhurst and Hudson 1999)

Table 2.1 Comparison of energy evolution between Class I and Class II rocks

Explanation	Proposed energy balance for rocks exhibiting Class I and Class II behaviour
Areas of the red triangles correspond to the elastic energy stored within the specimen, grey areas represent the post-peak rupture energy and yellow areas represent the released energy. The grey area ABCD (defined by the black dotted line) corresponds to the additional amount of energy required to produce failure (Tarasov and Potvin 2013)	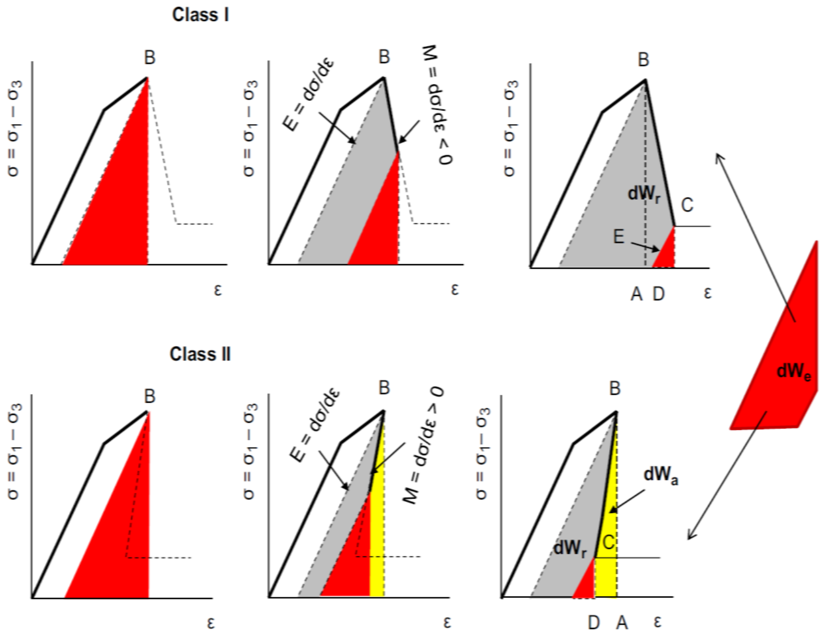

The red areas represent the elastic energy accumulated in the rock specimen before the peak stress; the green areas correspond to the pre-peak dissipation energy, blue areas represent the rock fracture energy, grey and yellow areas are corresponding to the unconsumed portion of energy and amount of released energy, respectively. The yellow dotted line represents the additional energy for the failure of the rock (Ai et al. 2016)	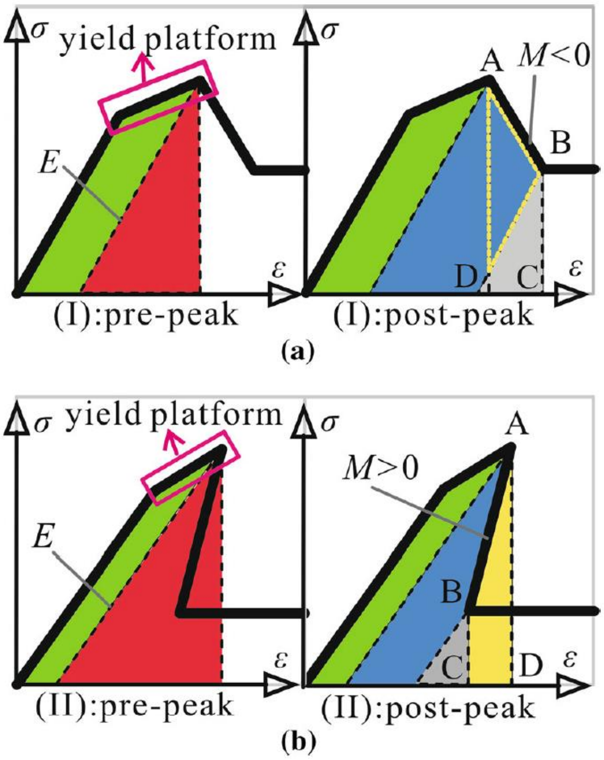
▤ Energy dissipated before peak stress ▥ Energy dissipated after peak stress ▨ Released elastic energy ▨ Residual elastic energy Peng et al. 2015	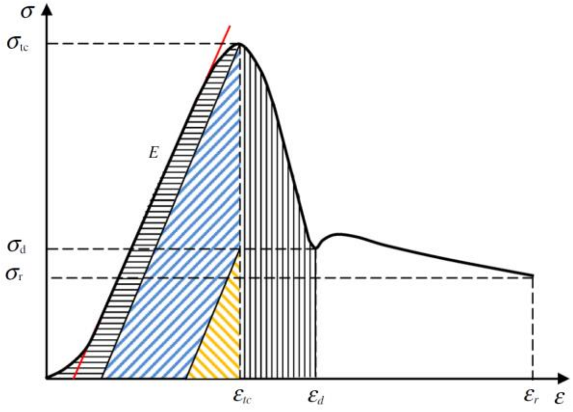

Numerous relevant attempts have been made to obtain the full stress-strain response of a rock during compression by controlling the application of load through a feedback of axial load implementing in servo-controlled compression machines (Bieniawski and Bernede 1979), axial displacement (Gowd and Rummel 1980), or axial strain rate (Rummel and Fairhurst 1970). Nevertheless, these control methods are not sufficient to measure the post-peak stage of Class II behaviour which is characterised by a strong strain localisation as axial strain no longer increases monotonically from the moment rock starts behaving as Class II (Munoz et al. 2016a). Therefore, to control the unstable failure and obtain the full stress-strain response of Class II behaviour, the surplus energy is needed to be withdrawn by reducing the axial strain. In this view, controlling the load by the circumferential-strain or lateral-strain as feedback signal has become a more appropriate method to capture the post-peak stress-strain response for brittle rocks (Wawersik and Fairhurst 1970; Fairhurst and Hudson 1999; Munoz et al. 2016b; Munoz and Taheri 2018; Bruning et al. 2018b).

In the deep mining operations, such elevated temperature and high confining pressure conditions cause dramatic alteration in the physical and mechanical properties of the surrounding rock mass which may activate strain burst. The behaviour of rock in the context of deep and high stress mining, prone to strain burst, is still not adequately understood. It is known that the mechanical behaviour of the rock depends on the confining pressure. It has been experimentally demonstrated that the rock exhibits brittle-ductile transition with an increasing confinement, which is as significant characteristic of rock deformation under high confining pressure and temperature (Wawersik and Fairhurst 1970; Yang et al. 2012; Yao et al. 2016; Walton et al. 2018). Yang et al. (2016) conducted a series of uniaxial and triaxial compression tests on marble and quantitatively analysed the internal damage of the marble using a three-dimensional X-ray micro-CT scanning system. The experimental results showed that the peak and residual strengths of marble exhibited a clear linear relationship as increasing confinement, which could be best described by the linear Mohr-Coulomb criterion (see Figure 2.6). In order to simulate various geothermal reservoir conditions, Kumari et al. (2017a) carried out a series of triaxial tests under different temperature and confining pressure conditions. They found that rock strength and shear parameters increased up to a certain temperature and then decreased with further rise of temperature due to induce-thermal cracking. With increasing confining pressure additional plastic deformation occurred, exhibiting strain-hardening characteristics in granite at high confinement. Xu and Karakus (2018) developed a thermo-mechanical damage model based on the Weibull distribution and Lemaitre’s strain-equivalent principle for granite to simulate the deformation and failure process of rocks under high temperature and pressure conditions, as depicted in Figure 2.7.The progressive process of brittle failure was studied by Renani and Martin (2018) on granite and limestone samples by damage-controlled uniaxial and triaxial tests and the evolution of cohesion and friction at different confinement levels wa analysed. However, the coupled influence of high confining stress and elevated temperature on the post-peak energy balance during strain burst has been rarely investigated. This is a serious gap in our knowledge as high stress and thermal damage will affect the overall mechanical behaviour of brittle rocks which can trigger strain bursting in deep mining operations. Therefore, this research aims to address this gap by conducting circumferential-strain controlled uniaxial and triaxial compression tests and improve the understanding of energy characteristics in the post-peak stage.

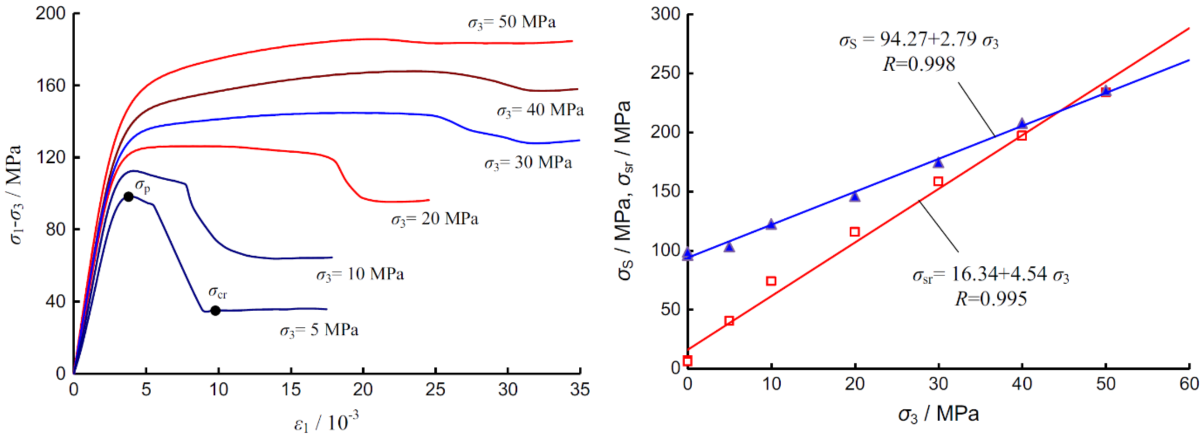

Figure 2.6 Deviatoric stress-axial strain curves and comparison of the peak and residual strength of marble at different levels of confining stress (Yang et al. 2016)

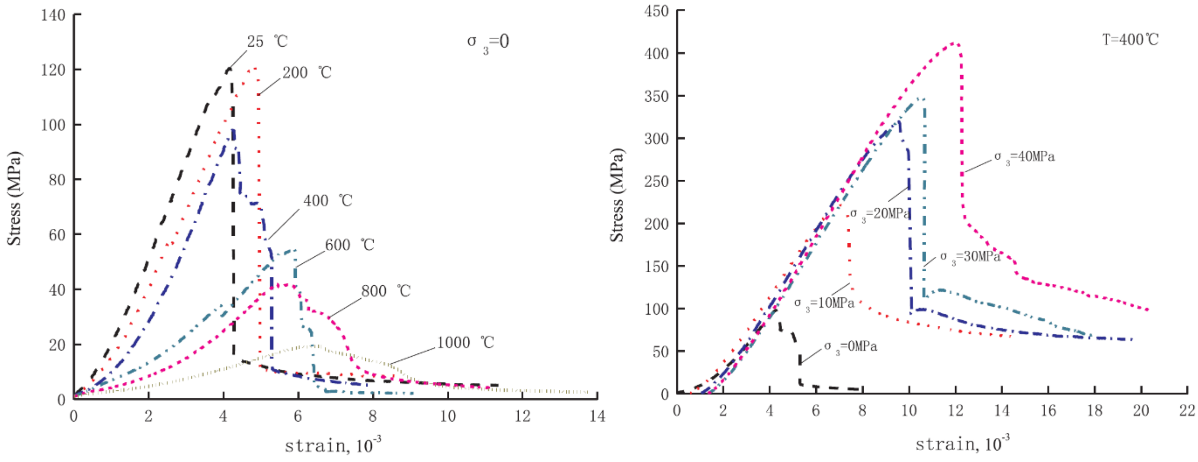

Figure 2.7 Deviatoric stress-axial strain curves and comparison of the peak and residual strength of marble at different levels of confining stress (Xu and Karakus 2018)

In the present research, to obtain the energy characteristics and analyse the post-peak energy balance of snap-back behaviour of hard brittle Australian granite demonstrating Class II behaviour in the post-peak region, a series of quasi-static circumferential strain controlled uniaxial and triaxial compression tests was conducted. The stored elastic strain energy, dissipated energy and the excess strain energy corresponding to the potential strain burst energy were calculated. A new energy calculation method was developed based on post-peak energy analysis. Acoustic emission (AE) which is an effective technique for analysing the damage evolution in rocks was adopted to evaluate the energy and crack characteristics of granite specimens. The coupled effects of elevated temperature (25 to 250 °C) and high confining pressure (0 to 60 MPa) on the energy evolution characteristics and intensity of strain burst have been systematically investigated and discussed, revealing the differences in the post-peak energy balance.

2.3 - Mode-I fracture toughness investigation

Rock masses usually contain many structural defects, including cracks, flaws, cleavages, bedding planes and natural fractures. These weaknesses can intensify the discontinuity of rock when they are subjected to further mechanical and environmental actions and finally lead to the failure of rock masses. It is thus essential to understand the load-carrying capacity of fractured rock masses and the law of crack propagation in rock, to improve the stability of rock structures under high stress concentrations that are prone to strain burst. To describe the capacity of rock to resist unstable fracturing, rock fracture toughness is defined as the most fundamental and important parameter in fracture mechanics. Rock fracture mechanics has been widely employed in many diverse areas in the rock engineering applications related to prevention of strain burst, such as rock fragmentation, cutting, drilling, rock slope stability, rock quarrying, hydraulic fracturing, tunnel boring. Brittle failure is understood as a consequence of crack propagation, and this failure pattern can be adequately described using the theory of linear elastic fracture mechanics (LEFM), which is mainly extended from the Griffith theory (Griffith 1921), and Irwin's modification (Irwin 1957) that recognises the significance of the stress intensity factor (SIF) at a crack tip. The critical value of SIF, also known as fracture toughness is a key inherent material property used in analysing brittle failure. SIF can be calculated for basic fracture modes based on the different loading: e.g. mode I (i.e., the tension/opening mode), mode II (i.e., the in-plane shear mode) and mode III (i.e., the tearing mode or out-of-plane mode), as depicted in Figure 2.8. In rock fracture mechanics, rock fractures easily occur under mode I in which the cracks tend to separate in direction normal to the crack line and thus the opening mode failure is most frequently encountered failure mode of rock against fracture. To predict the onset of catastrophic failures such as strain burst in such rock structures due to crack growth, it is essential to understand the behaviour of rock material subjected to mode I fracturing as it is assumed that the mode I fractures are dominant during strain burst. In this sense, both quasi-static and dynamic fracture toughness tests were carried out to better understand the fracture characteristics during strain burst.

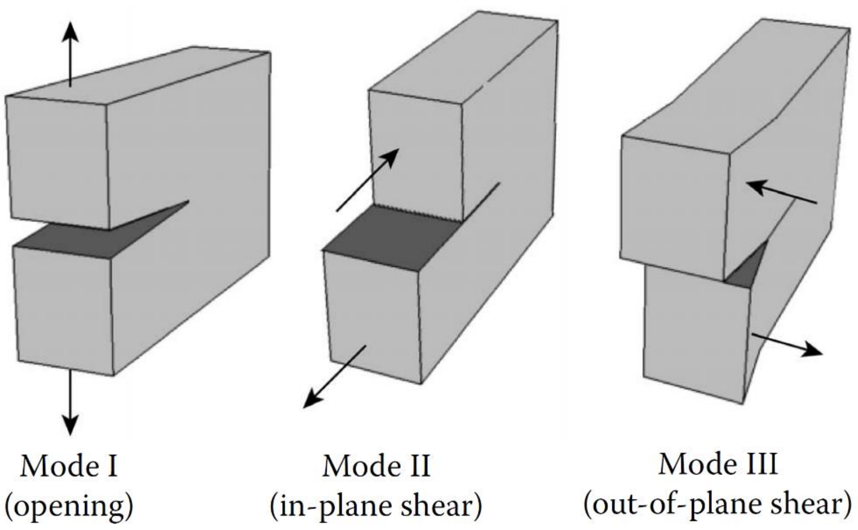

Figure 2.8 Three basic fracturing mode

2.3.1 - Quasi-static fracture tests

The strain burst is often considered as a process of crack formation and propagation in a rock mass. Fracture toughness or the critical stress intensity factor (SIF) is a significant intrinsic material property which represents the critical states of stresses or energy near the crack tip required for the initiation of brittle fracture. Therefore, assessment of fracture toughness is necessary for better understanding the mechanical behaviour of rock containing micro-cracks or flaws during strain burst.

The International Society for Rock Mechanics (ISRM) has suggested four standard testing methods, geometries and loading configurations, including chevron bend (CB) (Ouchterlony 1988), short rod (SR) (Ouchterlony 1988), cracked chevron notched Brazilian disc (CCNBD) (Fowell 1995), and semi-circular bend (SCB) (Kuruppu et al. 2014) for measuring the quasi-static mode I fracture toughness (K_{IC}) of rocks, as shown in Figure 2.9. As given in the literature, diverse testing method with various specimen geometry and loading configurations have been proposed to measure K_{IC} of rocks, some of these methods are reviewed in Table 2.2.

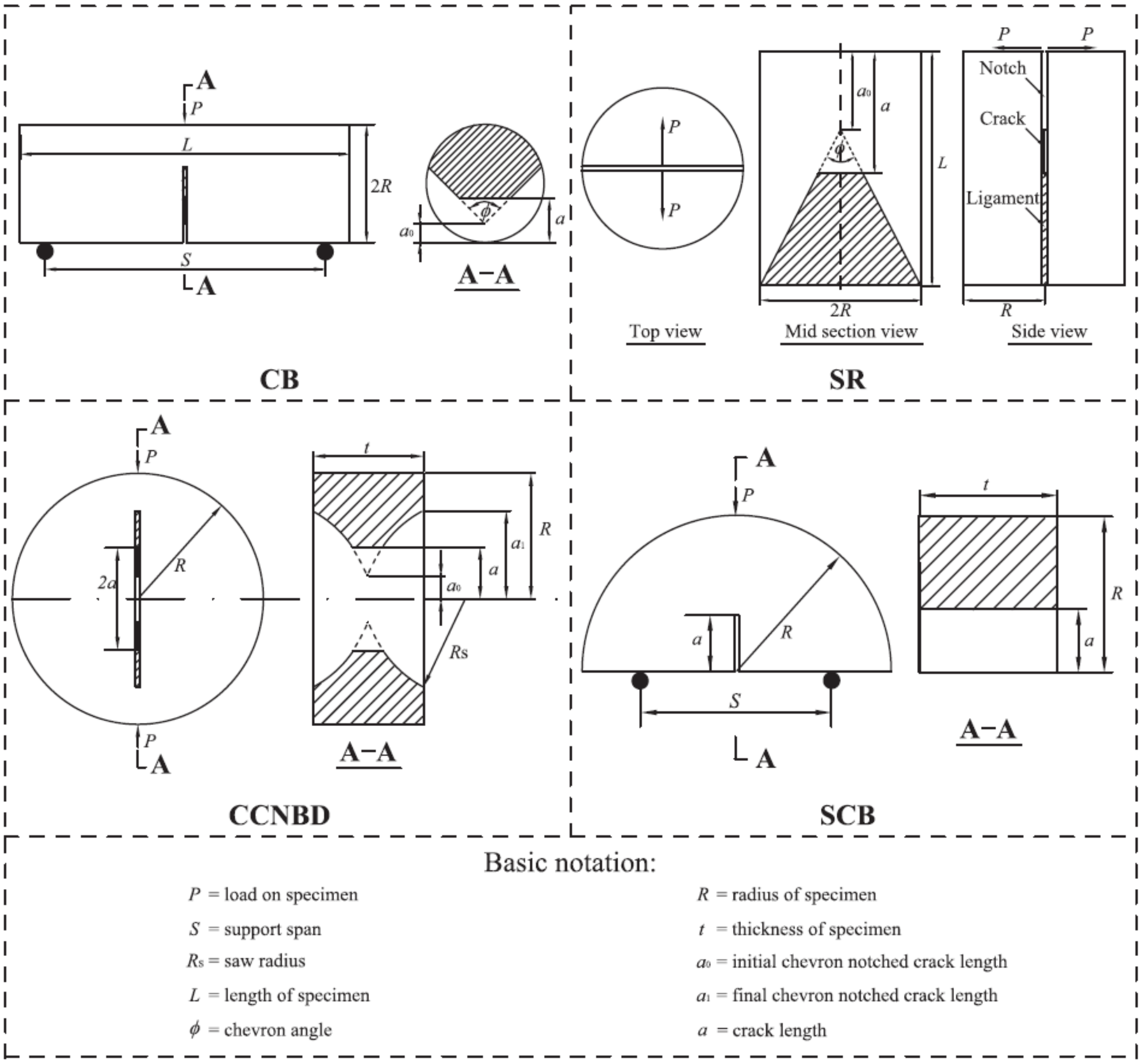

Figure 2.9 Schematic representation of four ISRM-suggested specimen geometry configurations for measuring K_{IC} of rocks

In recent years, the SCB has received broad acceptance for testing fracture parameters of rocks due to its favourable characteristics including a simple testing procedure and an easy sample preparation. Additionally, this half-disc specimen is particularly favoured in dynamic fracture toughness tests compared to full disc-type specimens as a shorter sample facilitates the dynamic force equilibrium within the sample in the Split Hopkinson Pressure Bar (SHPB) tests, and then the dynamic fracture parameters can be determined by quasi-static analysis (Zhou et al. 2012). The advantages of SCB specimen geometry and loading configuration will be discussed more in depth later in this chapter.

The methods reviewed in Table 2.2 can be categorised into two groups based on the shape of the initial crack: straight-through notch and chevron notch. According to the ISRM, the chevron notch allows a stable crack growth from the notch tip prior to the final fracture load and thus chevron notched specimen can produce reasonable, versatile and reproducible data for fracture toughness of rock. The details of the differences between chevron and straight notches will be discussed more in detail in dynamic fracture tests section (Section 2.3.2).

The cracked chevron notched semi-circular bend (CCNSCB), originally developed by Kuruppu (1997) and later developed by Dai et al. (2011) appears to have retained the merits of the ISRM-suggested CCNBD and NSCB methods. Moreover, half-disc geometry inherently circumvents the symmetrical crack propagation assumption of the CCNBD method. This chevron notched SCB specimen geometry helps to avoid the difficulty of pre-cracking or fabricating a sharp crack. Since pre-cracking is tedious, time-consuming and challenging to perform on hard rocks, chevron notch in CCNSCB specimen can induce self-precracking during the test leading to stable crack propagation along the chevron notch ligament when the specific crack length is reached. Moreover, half-disc feature of this sample geometry facilitates the dynamic force equilibrium within the specimen for the dynamic fracture toughness tests equipped with the SHPB which is the prerequisite to employ the quasi-static data reduction method. This sample geometry is also available for pure or mixed mode (mode I and mode II) fracture studies of rocks. Therefore, given its merits on both quasi-static and dynamic mode I fracture toughness measurements, the CCNSCB method was applied to more accurately determine the fracture toughness values in this research.

Table 2.2 Some typical methods for measuring the quasi-static mode I fracture toughness (K_{IC}) of rocks

Testing method	**Loading type**	**Reference**
Cracked chevron-notched Brazilian disc (CCNBD) method	Brazilian-type compression	Fowell and Xu 1994; Fowell 1995; Chang et al. 2002; Wang et al. 2003; Iqbal and Mohanty 2006; Nasseri et al. 2006; Iqbal and Mohanty 2007; Ayatollahi and Aliha 2008; Nasseri et al. 2010; Erarslan 2013; Aliha and Ayatollahi 2014; Dai et al. 2015a; Xu et al. 2016a, b; Wei et al. 2016, 2017a,b; Ghouli et al. 2018; Yu and Shang 2019
Chevron bend (CB) method	Three-point bending	Ouchterlony 1988; Funatsu et al. 2015; Dai et al. 2015b
Cracked straight through Brazilian disc (CSTBD) method	Brazilian-type compression	Aliha et al. 2010, 2012; Kuruppu et al. 2014; Ayatollahi and Sedighiani 2012; Ayatollahi and Akbardoost 2014; Akbardoost et al. 2014; Wei et al. 2017c
Flattened Brazilian disc method	Brazilian-type compression	Keles and Tutluoglu 2011
Straight notched disc bend (SNDB) method	Three-point bending	Tutluoglu and Keles 2011; Aliha et al. 2015 Aliha and Bahmani 2017
Modified ring method	Brazilian-type compression	Tutluoglu and Keles 2012

Testing method	**Loading type**	**Reference**
Straight -crack semi-circular bend (SCB) method	Three-point bending	Lim et al. 1994; Ayatollahi et al. 2009, 2016; Kuruppu and Chong 2012; Kuruppu et al. 2014; Funatsu et al. 2014; Wei et al. 2016a; Mahanta et al. 2016, 2017; Feng et al. 2017, 2018
Chevron-notched short rod (SR) method	Direct tension	Ouchterlony 1988; Dai et al. 2015b; Wei et al. 2016b
Edge-cracked triangular method	Three-point bending	Aliha et al. 2013
Cracked chevron notched semi-circular bend (CCNSCB) method	Three-point bending	Kuruppu 1997; Wei et al. 2015, 2016c, 2017b, c, d; Ayatollahi et al. 2016

2.3.1.1 - Temperature influence on the quasi-static behaviour of rocks

Due to the thermal gradient in the deep rock mass, high-temperature conditions can cause dramatic changes in the microstructures and mechanical behaviour of the rocks which are prone to strain burst As a consequence, microstructure and mineral composition of rocks will be altered due to the thermally-induced cracking. As being an inherent mechanical property of rock, researchers have revealed that temperature is a significant factor influencing fracture characteristics and rock fracture toughness. In recent years, a large number of researchers have mainly investigated the effects of temperature on the quasi-static mode I fracture toughness of rock. For instance, a study by Zhang et al. (2001) showed that the mode I fracture toughness of gabbro decreased at 20-100 °C, likely due to the different structure and mineralogy. Funatsu et al. (2004) investigated the changes in mode I fracture toughness of single-edge notched round bar bend (SENRBB) and semi-circular bend (SCB) of Kimachi sandstone and Tage tuff. The fracture toughness of Kimachi sandstone did not show significant change up to 125 °C and increased from 125 to 200 °C in which this rising trend was attributed to the drying of the clay material. For Tage tuff, the quasi-static mode I fracture toughness showed a decline with ascending temperature up to 75 °C, after which it gradually rose from 75 to 200°C. Nasseri et al. (2009) assessed the correlation between fracture toughness and fracture roughness for a series of thermally-treated CCNBD Westerly granite. The researchers concluded that fracture toughness and roughness exhibited a negative correlation as a function of temperature, on the other hand, grain-grain boundary crack density and P-wave velocity showed an opposing correlation. Research by Mahanta et al. (2016) demonstrated that mode I fracture toughness of various types of Indian rocks increased from ambient temperature condition to 100 °C, and after that diminished with increasing temperature up to 600 °C. Recently, Feng et al. (2017), investigated the influence of temperature on the mode I fracture toughness of sandstone using SCB specimens and found that the fracture toughness of sandstone decreased slowly before the temperature threshold and followed a drastic drop after crossing the threshold due to the thermal cracking. These studies have contributed to understanding the influence of temperature on the fracturing of rock. However, there is a lack of research about the coupling influence of temperature and loading rate on the quasi-static mode I fracture toughness and fracture mechanism as the mechanical response of rock during strain burst under different loading rates plays a vital role. In addition, CCNSCB method which has been considered as the most promising testing configuration for both quasi-static and dynamic mode I fracture toughness tests has yet to be investigated under the coupled influence of temperature and loading rate. In this section, I aim to fill this research gap, and focuses on the impact of elevated temperature and various loading rate on the quasi-static mode I fracture toughness behaviour, energy-release rate and fracture mechanism.

2.3.1.2 - Loading rate dependence of the quasi-static behaviour of rocks

Rock fracture toughness can be used as a threshold value to predict the imminent fractures of rocks during strain burst. The fracture mechanism and fracture parameters (fracture toughness, fracture energy) of rock under static loading rate condition are significant for a better understanding of the failure progress of rock during strain burst. A large number of studies has been devoted for investigating the mechanical properties of rock material at various strain rate or loading rate (Li et al. 2014; Liang et al. 2015). However, limited research has focused on the effects of loading rate on the fracture toughness and fracture characteristics over a wide range of loading rates. Mahanta et al. (2017), conducted experimental studies to better understand the fracture behaviour of gas shale with various strain rates and it was concluded that the fracture toughness gradually increases with increasing strain rate and the fracture toughness for all the modes are comparable but vary significantly at higher strain rates. Recently, Zhou et al. (2018) investigated the influence of loading rates on crack propagation velocity and crack initiation toughness by using a new cracked tunnel specimen and stated that crack propagation velocity and initiation toughness tend to increase with loading rate. In the current study, the quasi-static mode I fracture toughness tests were carried out using CCNSCB granite specimens exposed to different pre-heating treatments under varying loading rates. The fracture mechanism and fracture toughness and energy-release rate of thermally-treated Australian granite were investigated and the coupled influence of thermal damage and loading rate on the fracture toughness and energy-release rate was evaluated and discussed more in depth.

2.3.2 - Dynamic fracture tests

Dynamic fracture toughness test enables us to investigate the mechanical response of intact rock under dynamic loading conditions in which increased loading rate has an influence on the fracturing characteristics and mechanical behaviour. The effect of dynamic loading on rock is critical to provide insight into dynamic fracture propagation which occurs during strain burst. The typical rock dynamic problems encountered during underground engineering constructions are illustrated in Figure 2.10.

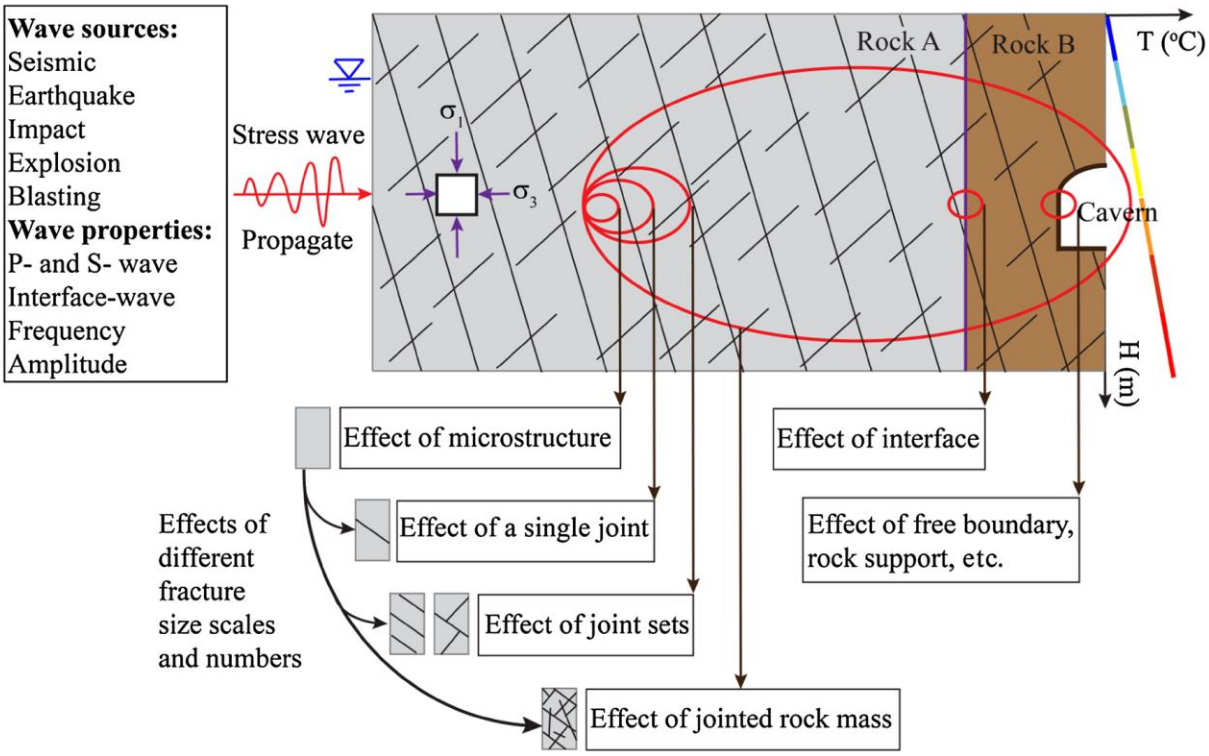

Figure 2.10 Illustration of rock dynamics problems and affecting factors in underground engineering design (Zhang and Zhao 2014)

Since rock is relatively weak in tension, the tensile/opening mode (mode I) fracture occurs more frequently than either the in-plane shear mode (mode II) or the tearing/out-of-plane shear mode (mode III), and thus, the mode I fracture toughness is of the most concern (Wei et al. 2017a).

The primary loading techniques used for investigating the dynamic mechanical properties of materials over a wide range of loading rates, including the estimate of the time to fracture are listed in Table 2.3. Amongst these dynamic loading apparatuses, the SHPB, which was initially developed by Kolsky (1949), has been considered as an ideal and effective dynamic loading device under high loading rates. The principles of the SHPB system will be discussed later in detail in Chapter 4 of this thesis.

Table 2.3 Range of loading rates and time to fracture for different dynamic experimental techniques for rock (modified after Zhang and Zhao 2014)

Loading conditions	Quasi-static	Dynamic				
		Intermediate loading rate			High loading rate	
Loading techniques	Servo-hydraulic machine	Pneumatic-hydraulic machine	Drop-weight machine	Charpy impact machine	Split Hopkinson pressure bar	Projectile impact technique
Loading rate $\dot{K}_I$ ($MPa\sqrt{m}/s$	1	$10^1 - 10^3$	10^4	10^4	$10^4 - 10^6$	$10^4 - 10^8$
Time to fracture t_f (μs)	$> 10^6$	$10^5 - 10^3$	~ 100	~ 100	$1 - 100$	$1 - 100$

Many researchers have investigated the dynamic fracture toughness and dynamic failure mechanism of rocks over a wide range of loading rates (Zhang et al. 2000; Chen et al. 2009; Dai et al. 2011; Zhang and Zhao 2013; Zhao et al. 2017; Shi et al. 2019). With the aid of SHPB testing system, Zhang et al. (2000) quantitatively analysed the energy partitioning in the dynamic fracture process of a short rod (SR) specimen over a wider range of loading rate. Dai et al. (2010) employed the SHPB technique to measure the dynamic rock fracture toughness by impacting cracked chevron notch Brazilian disc (CCNBD) specimen. A summary of typical dynamic testing methods for the determination of dynamic fracture toughness using SHPB is reviewed in Table 2.4.

Generally, an initial notch in the fracture toughness specimen is created either in a straight-through notch or a chevron notch shape, as shown in Figure 2.11. For the sample with straight-through notch, the pre-cracking through fatigue loading is required to avoid the potential errors induced by a blunt, machined crack tip (Berto et al. 2017). In reality, pre-cracking or fabricating a sharp crack is tedious, time-consuming and difficult to perform on hard rocks. Fortunately, these difficulties in sharpening or pre-cracking the notch tip can be avoided by introducing a chevron notch in the specimen. The crack initiates at the tip of the chevron notched ligament under a very low load level and grows stably to a specific length in which the critical crack associated with K_{IC} determination can be generated; thus, self-precracking can be achieved. In addition, this notch shape is particularly favoured in dynamic fracture tests due to its smaller length compared to the specimens used in the other methods. The dynamic force at the two loading ends of the sample is easily balanced for a shorter specimen, and thus, the quasi-static data reduction method can be employed to determine the dynamic fracture toughness in the SHPB tests (Zhou et al. 2012). Therefore, among the methods mentioned above, the CCNSCB method is the most promising in the dynamic fracture tests to determine the mode I fracture toughness of rocks due to its merits that will be presented in detail in Chapter 4. Only a limited number of research has focused on investigating the dynamic fracture mechanism of CCNSCB specimen. In this respect, the CCNSCB method was adopted for investigating the dynamic progressive fracturing process during strain burst in SHPB testing in this research.

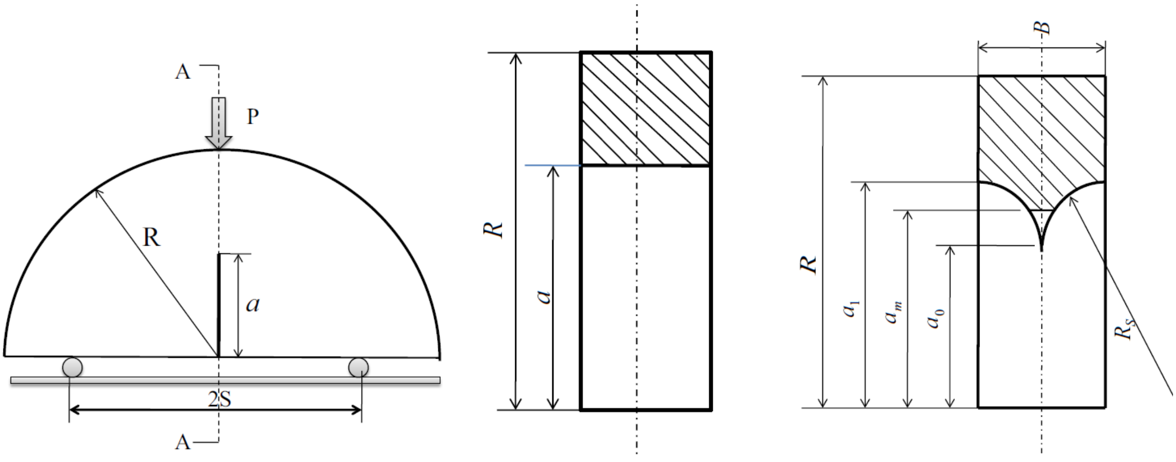

(a) (b) (c)

Figure 2.11 (a) Schematic of a semi-circular bend specimen geometry and loading scheme, (b) straight-through notch, and (c) chevron notch

Table 2.4 Summary of some typical dynamic testing methods for measuring the dynamic fracture toughness using SHPB

Loading type	Test method	Reference
Compact tension (CT)	WLCT	Klepaczko et al. 1984
	SR	Ouchterlony 1988; Zhang et al. 2000, 2001
Brazilian disc (BD)	CSTBD	Nakano et al. 1994; Wang et al. 2011; Yin et al. 2018
	HNBD	Lambert and Ross 2000; Wang et al. 2010
	CCNBD	Dai et al. 2010
Bending	SENB	Mindess et al. 1987; Tang and Xu 1990; Zhao et al. 1999; Yang et al. 2009; Zhao et al. 2013
	NSCB	Chen et al. 2009; Yin et al. 2012; Zhou et al. 2012; Dai and Xia 2013; Zhang and Zhao 2013a; Shi et al. 2019; Zhao et al. 2017; Zhou et al. 2019
	CCNSCB	Dai et al. 2011

WLCT wedge loaded CT, *SR* short rod, *CSTBD* cracked straight through BD, *HNBD* holed-notched BD, *CCNBD*, cracked chevron notched BD, *SENB* single edge notch bending, *NSCB* notched semi-circular bending, *CCNSCB* cracked chevron NSCB

2.3.2.1 - Thermal damage influence on the fracture toughness under dynamic load

The influence of temperature on rock mass becomes markedly important as the depth of underground excavation increases which may result in undesirable structural failures (Yin et al. 2012; Akdag et al. 2018). In the underground rock engineering, rock mass has to face not only the effects of temperature environment, but also is exposed to dynamic power disturbances leading to dynamic fracturing in the forms of strain burst, slabbing and spalling. We examined the dynamic fracture characteristics of rock after thermal damage exposure. A limited research in the literature has been focused on the coupled effects of temperature and loading rates on the dynamic fracture characteristics of brittle rocks. Zhang et al. (2001) carried out dynamic fracture tests on short rod (SR) Fangshan gabbro and Fangshan marble exposed to high temperature (100-330 °C) by means of the SHPB system and they concluded that the dynamic fracture toughness of the rocks mainly depends on the loading rate and it increases with loading rate as presented in Figure 2.12. Regarding the influence of temperature on dynamic fracture of rock, Yin et al. (2012) utilised a notched semi-circular bend (NSCB) method with SHPB apparatus to investigate the effect of temperature on the dynamic fracture toughness of thermally treated Laurentian granite specimens (see Figure 2.13). They reported that the dynamic fracture toughness increases with the loading rate and decreases with ascending temperature level. It was also stated that the dependence of dynamic fracture toughness on the temperature varies when temperature is below 250 °C and above 450 °C from other temperatures. Recently, the coupling effect of temperature and static pressure (a given preload) on the dynamic fracture toughness was studied (Yin et al. 2018). After performing dynamic fracture tests on cracked straight-through Brazilian disc (CSTBD) specimens with a dynamic and static coupling testing device based on the SHPB system, they reached a conclusion that the dynamic fracture toughness of the specimens showed a decreasing trend with ascending temperature.

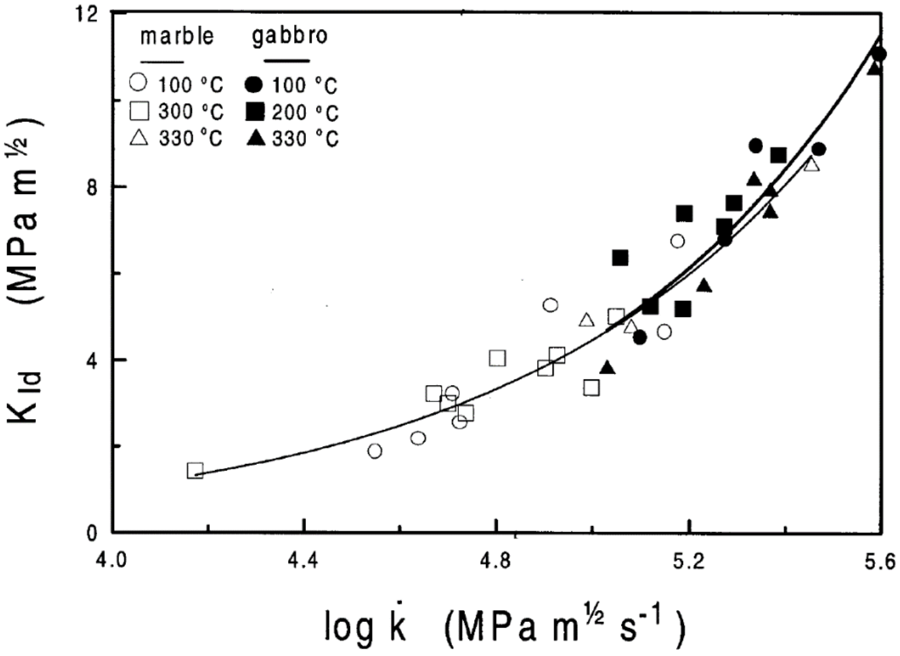

Figure 2.12 Loading rate vs the dynamic fracture toughness of gabbro and marble at various pre-heating temperatures from the dynamic SR tests (Zhang et al. 2001)

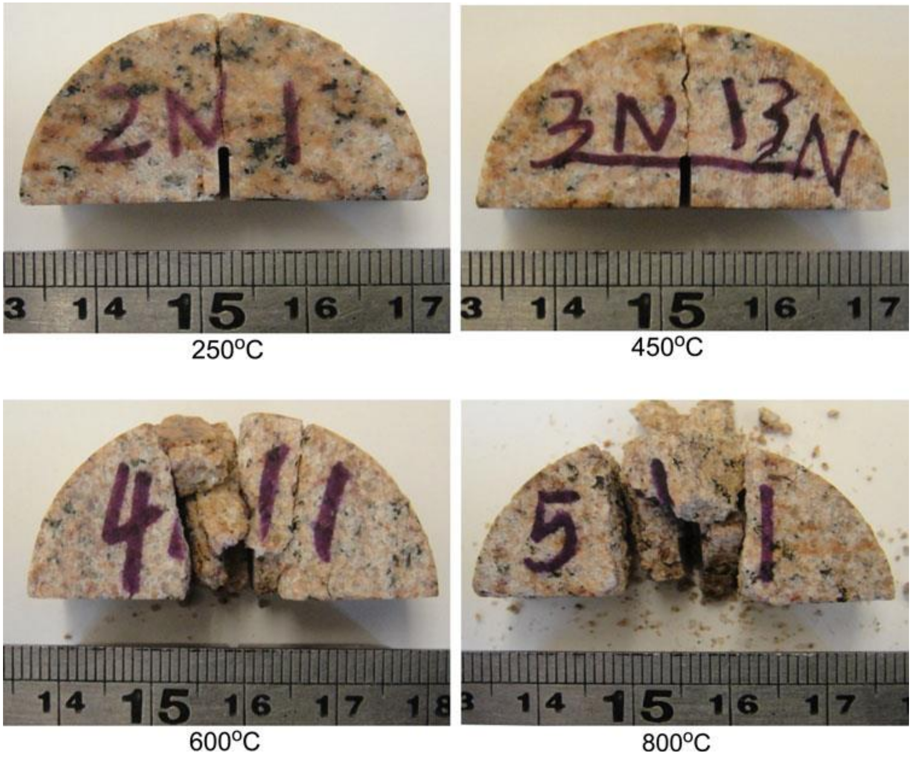

Figure 2.13 Typical recovered samples exposed to various pre-heating temperature from the dynamic NSCB test (Yin et al. 2012)

In summary, the existing studies have shown that the elevated temperature and loading rate have a remarkable influence on the dynamic fracture characteristics of the rock. However, the coupled effects of the thermal damage and the loading rate on the dynamic fracture properties of brittle rock have yet to be systematically investigated. In this sense, to investigate the effects of thermal damage and dynamic disturbance on the dynamic fracture characteristics of Australian granite during strain burst, a series of dynamic fracture toughness tests was performed by means of a SHPB system in this research. The damage evolution of thermally-treated granitic rocks over a wide range of loading rates was investigated. The mode I dynamic initiation fracture toughness (DIFT) (K_{Id}^{i}) and the rate dependency of the phenomenon were determined and compared for the pre-heated specimens at different temperatures. The CCNSCB method which is the most favoured for dynamic fracture tests was adopted under the condition of different loading rates after the action of elevated temperatures for the first time in the literature.

2.3.2.2 - Rate dependence of dynamic fracture toughness

The rock is usually fractured under dynamic loading in rock engineering applications, such as strain burst, blasting, rock cutting. It is an inherent dynamic parameter to characterise the rocks’ capability of resisting against tensile crack formation and propagation and also serves as an index for rock fragmentation processes involving fracturing in strain burst, blasting, tunnel boring, drilling and crushing. Accurate characterisation of the dynamic fracture toughness over a wide range of loading rates is thus essential. So far, to understand the loading rate dependency of the dynamic fracture toughness, a substantial amount of dynamic fracture toughness tests have been performed on various types of rock materials such as granite (Dai et al. 2010, 2011; Gao et al. 2015), marble (Wang et al. 2011; Zhang and Zhao 2014), gabbro (Zhang et al. 2000, 2001), sandstone (Wang et al. 2015; Zhou et al. 2019). A summary of some research conducted to study the loading rate influence on the dynamic fracture toughness of various rocks using different sample geometry configurations is reviewed in Table 2.5. It is concluded that the fracture toughens significantly increases with the increasing loading rate. Compared with substantial static researches regarding dynamic rock fracture characteristics of rocks under the coupled influence of different temperature and loading rate in recent decades however, researches associated with rock dynamic fracture were fewer in number, resulting in a limited understanding of dynamic fracturing characteristics of rocks. A systematic experimental investigation should be addressed to understand the combined influence of temperature and loading rate on dynamic fracture characteristics of rock. Therefore, in the present study, the mode I dynamic fracture toughness and dynamic characteristics of fracturing process of CCNSCB Australian granite specimens with various temperature exposure over a wide range of loading rates were analysed and discussed using the SHPB associated with high speed (HS) cameras.

Table 2.5 Summary of research studied the rate dependency of dynamic fracture toughness of various rocks

Rock type	Test method	Reference
Laurentian granite	SCB	Chen et al. 2009
	CCNBD	Dai et al. 2010
	CCNSCB	Dai et al. 2011
	NSCB	Yin et al. 2012; Gao et al. 2015
Barre granite	NSCB	Dai and Xia 2013a Dai et al. 2013b
Marble	SR	Zhang et al. 2000, 2001
	CSTFBD	Wang et al. 2011

	NSCB	Zhang and Zhao 2013b, 2014
Gabbro	SR	Zhang et al. 2000, 2001
Sandstone	CSTFBD	Wang et al. 2015
	NSCB	Zhang and Zhao 2014; Zhou et al. 2019

SCB semi-circular bending, *CCNBD* cracked chevron notched Brazilian disc, *NSCB* notched semi-circular bending, *CCNSCB* cracked chevron NSCB, *SR* short rod, *CSTFBD*, cracked straight through flattened Brazilian disc

2.4 - Strain burst evolution mechanism of brittle rock under true-triaxial loading/unloading conditions

Strain burst is the most common type of rock burst in the deep underground which is caused by a sudden release of stored strain energy within the surrounding rock mass near the free boundary after excavation. This dynamic rock failure in deep rock engineering occurs in an abrupt manner accompanied by a violent rock fragment ejection at high speed. With its unpredictable and violent nature, strain burst poses a major threat to the safety, construction equipment and productivity in rock engineering operations. Prior to any excavation, underground rock mass is in a true-triaxial state of stress equilibrium ($\sigma_1>\sigma_2>\sigma_3$) where σ_1, σ_2, σ_3 are the major, intermediate and minor principal stresses, respectively. Introducing an excavation in rock masses results in forming the free face boundary condition; at the same time, redistribution of stresses around underground openings takes place, i.e., the radial stress (minor principal stress, σ_3) releases suddenly, the tangential stress (the major principal stress, σ_1) increases sharply, while the intermediate principal stress (σ_2) varies slightly, as depicted in Figure 2.14. Hence, it is imperative to better understand the failure mechanism of strain burst more in-depth under true-triaxial loading-unloading condition.

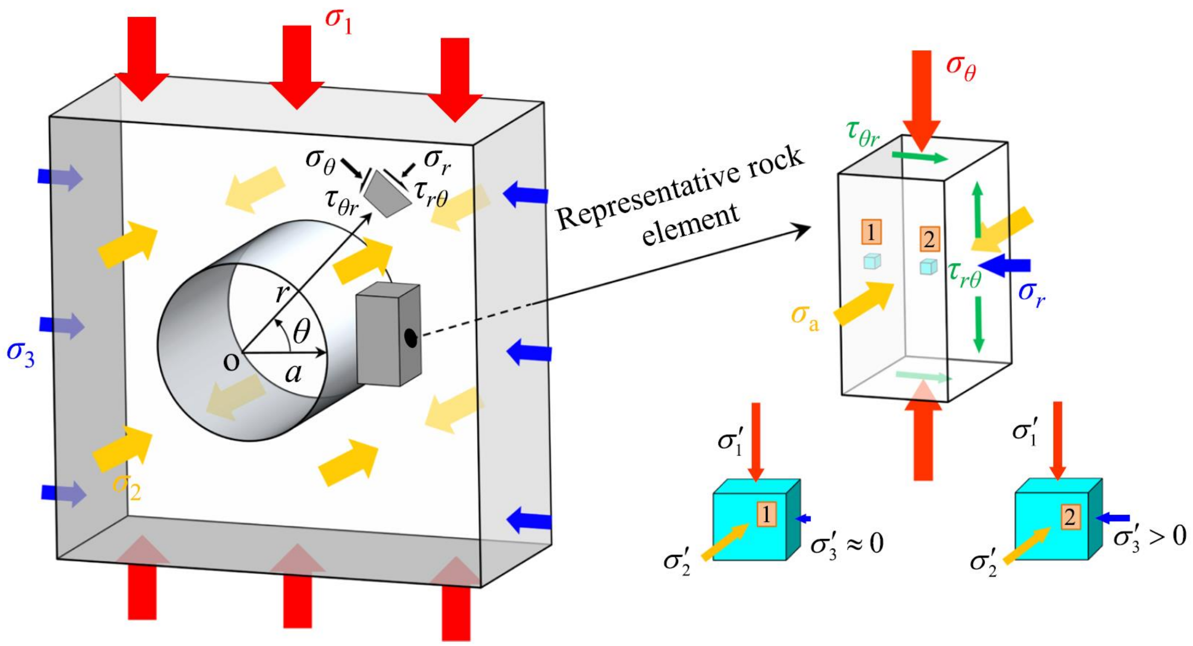

Figure 2.14 Stress state of the surrounding rock mass and the representative elementary volume after excavation: σ_1, σ_2, σ_3 are the far-field major, intermediate and minor principal stresses, respectively; σ_θ, σ_a, σ_r and $\tau_{r\theta}(\tau_{\theta r})$ are the tangential stress, axial stress, radial stress and shear stress of tunnel, respectively; θ is the angular direction measured counter-clockwise from the σ_3 direction; r is the radial distance from the axis of the hole; and a is the tunnel radius (Su et al. 2017b)

It is known that laboratory tests have a significant role in understanding the mechanism of strain burst, calibration of numerical models and assessment of mechanical parameters. Over the last decade, substantial efforts in the laboratory have been devoted to exploring the real damage process of strain burst (Wang and Park 2001; He et al. 2010, 2012a, b, c; Huang and Li 2014; Gao et al. 2018; Li et al. 2018). In recent years, simulating strain burst process using rectangular prism specimens through true-triaxial loading-unloading tests have become more prevalent (He et al. 2010, 2012a, b, c; Zhao and Cai 2014; Su et al. 2017a, 2018a, b; Akdag et al. 2018). The pioneering true-triaxial loading-unloading strain burst testing facility was firstly developed at the State Key Laboratory for Geomechanics and Deep Underground Engineering in Beijing, China by He et al. (2010) to realistically mimic the exact boundary conditions and stress paths for rocks during an excavation in which strain burst occurs. The hydraulic true-triaxial testing machine consists of a hydraulic controlling frame, a data acquisition system and an AE monitoring system and high-speed cameras are employed to monitor the fracturing behaviour and failure process during strain burst, as presented in Figure 2.16. Cai et al. (2008) emphasised that the actual stress path in a rock mass during excavation is complex and accurately simulating the stress change is of great significance to capture correct rock mass response. Hence, to simulate the stress change of rock mass during excavation using this testing system can be described in detail as follows:

- Firstly, stresses along the six surfaces of rectangular prism sample are progressively increased until reaching the in-situ stress state.
- Subsequently, to simulate the creation of an excavation, the rigid loading plate acting along σ_3 direction is abruptly dropped, while σ_2 is kept constant.
- After unloading σ3 from one of the rectangular prism's surfaces that is exposed to air, σ_1 is continuously increased until strain burst occurs (see Figure 2.15).

Hydraulic pumping systems are used to apply vertical and other two horizontal loads on a rectangular prism rock specimen with a maximum capacity of 450 kN. The data acquisition system is capable of recording 100,000 data points per second (see Figure 2.16). The largest specimen tested by this system has dimensions of 160 x 65 x 35 mm, along with the σ_1, σ_2, σ_3 directions, respectively. The loading range varies from 0.1 to 0.5 MPa/s, while the time interval for each loading is about 5 min. The image resolution of the high-speed camera is of 1024 x 1024 pixels which enables to capture the abrupt fracturing and violent rock fragment ejection, as shown in Figure 2.16. Two AE transducers with a diameter of 18 mm each are used to investigate internal damage evolution during strain burst test. The AE sensors (type WD, from the American Physical Acoustics Corp.) are mounted to the lateral side of the rock sample tested via spring clips and adhesive tape is used for reducing friction between the specimen and loading plate. The resonance frequency of the transducers is about 150 kHz with an operating frequency range of 100 kHz – 1 MHz. The amplitude threshold for pre-amplification of two AE sensors is set to 40dB to amplify the AE signals during loading. A PIC-2 AE system is used to monitor the characteristic of cracking with a sampling rate of 10 msps (million samples per second).

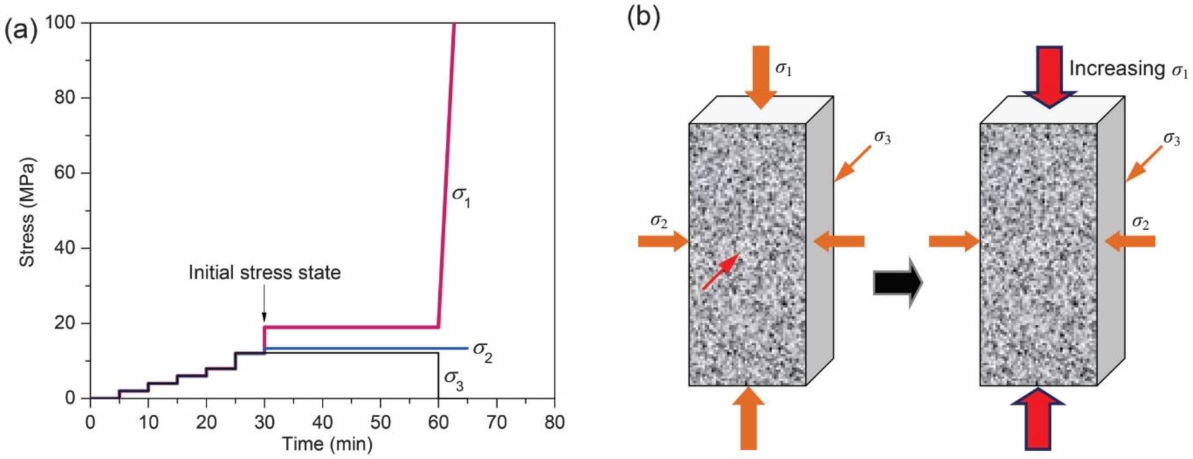

Figure 2.15 (a) Designed loading-unloading stress path and (b) schematic illustration of the stress state of the rock specimen in strain burst test (Zhao and Cai 2014)

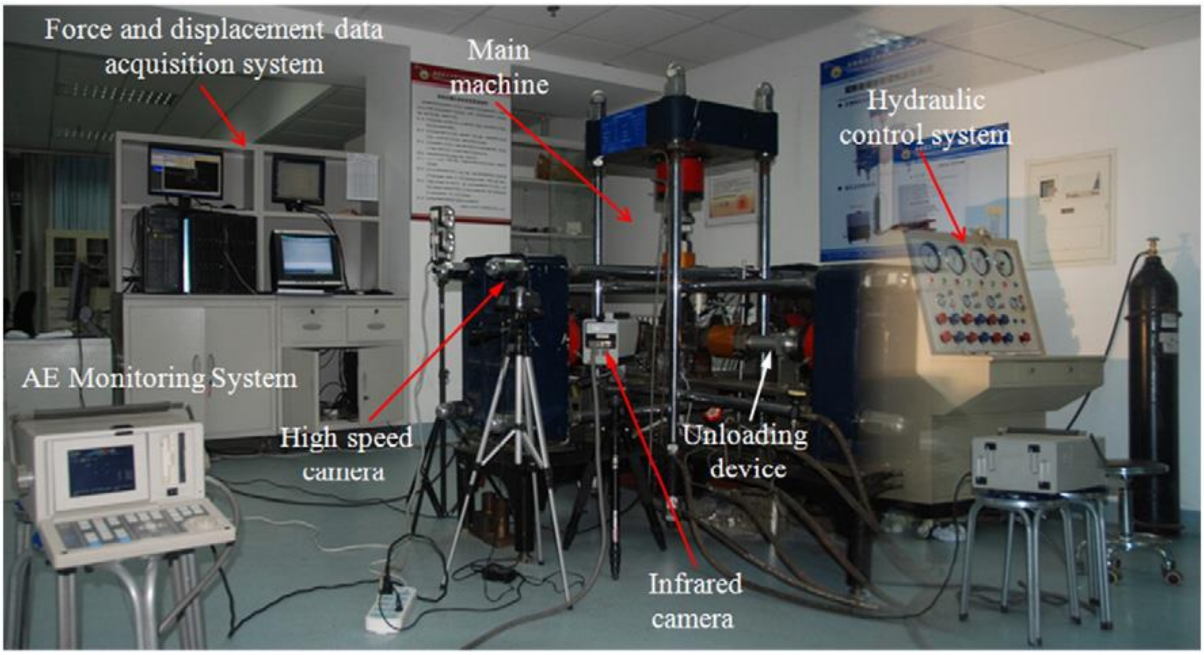

Figure 2.16 Illustration of true-triaxial strain burst testing system (He et al. 2015)

Based on this testing system, many scholars have performed strain burst tests using different types of rocks under different stress paths for gaining deeper understanding of strain burst under true-triaxial loading/unloading conditions (Coli et al. 2010; He et al. 2010, 2012a, b, c; Gong et al. 2015; Li et al. 2015; Sun et al. 2017). Based on a comprehensive database for strain burst tests, Akdag et al. (2017) studied the influence of specimen dimensions on bursting characteristics of rocks and revealed that the failure mode changes from strain burst to local spalling when the height to width ratio of rock specimen is reduced from 2.5 to 1 (see Figure 2.17). Hence, all specimens with a height to width ratio of 2.5 were used in the present study.

Zhao et al. (2014) investigated the effects of unloading rate on the strain burst behaviours of brittle rock under true-triaxial unloading conditions and reported that the rock tends to strain burst more often when the unloading rate is high and the failure mode changes from strain burst to non-violent spalling as the unloading rate decreases. Sun et al. (2017) analysed the mechanism of strain burst based on the infrared thermography and AE monitoring and concluded that the infrared temperature declines prior to strain burst, including obvious anomaly bands in AE and anomaly temperature differentiation in a different area. Su et al. (2017) investigated the influence of tunnel axis stress on strain burst by using modified true-triaxial rock burst testing apparatus. The experimental results indicated that intensive strain burst is more likely to occur when the tunnel axis stress is high. Recently, to investigate the failure process and mechanism of strain burst in a deep circular cavern under high stresses, Gong et al. (2018) conducted true-triaxial tests on cubical specimens with a pre-fabricated circular hole, as depicted in Figure 2.18. A wireless micro-camera was utilised to monitor the bursting process on the sidewalls of the hole, and the entire bursting process was split into four stages: calm period, pellet ejection period, rock fragment exfoliation period and rock bursting period. The researchers also revealed that the intensity of rockburst varies with the stress condition; when the vertical stress is constant, and the horizontal axial stress is low, the rockburst severity decreases with the ascending horizontal radial stress. In summary, the true-triaxial loading and unloading tests to assess the failure characteristics of different rocks are reviewed in Table 2.6.

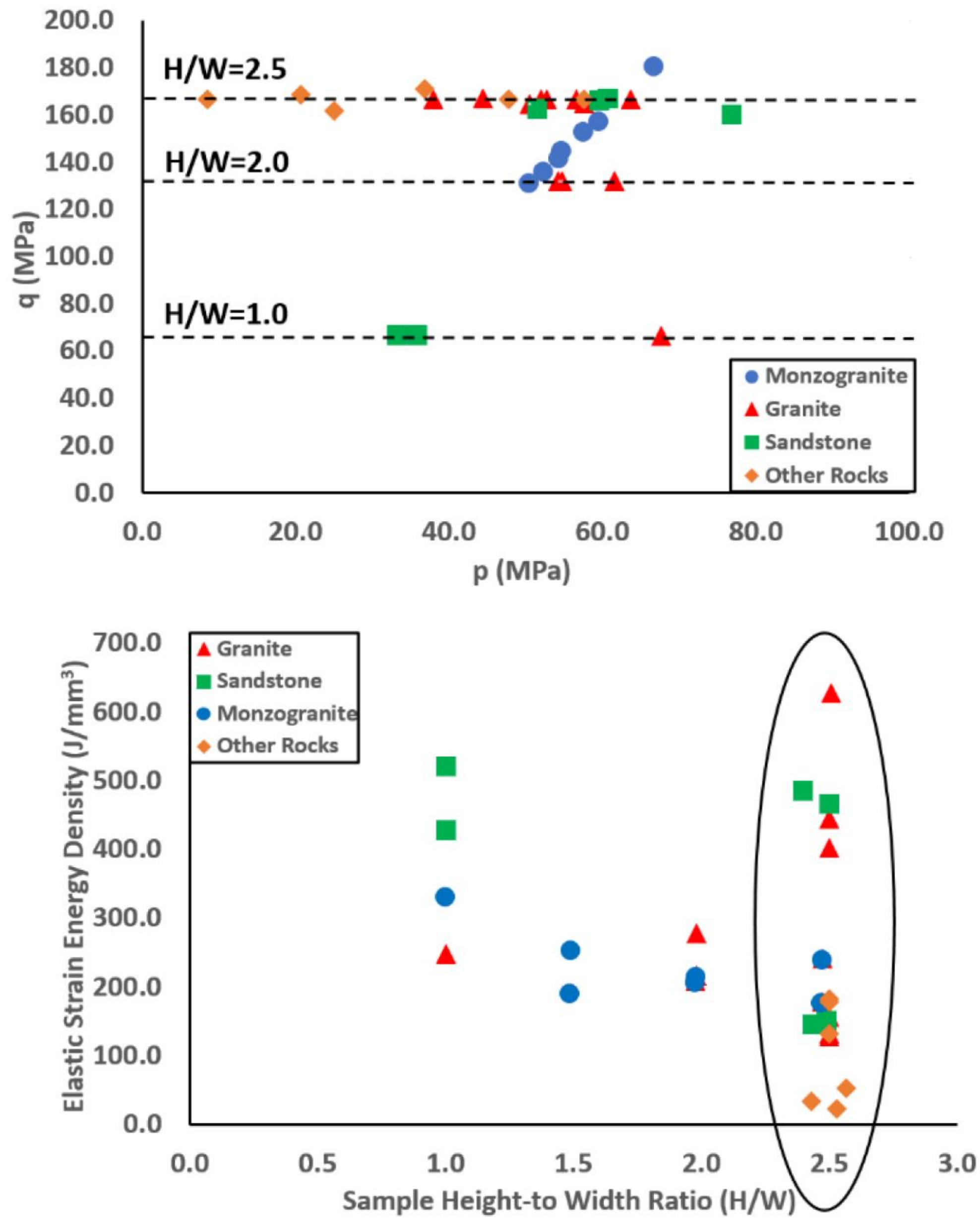

Figure 2.17 Stress state change on the sidewall of an underground opening, and a representative elementary volume before and after excavation (Akdag et al. 2017)

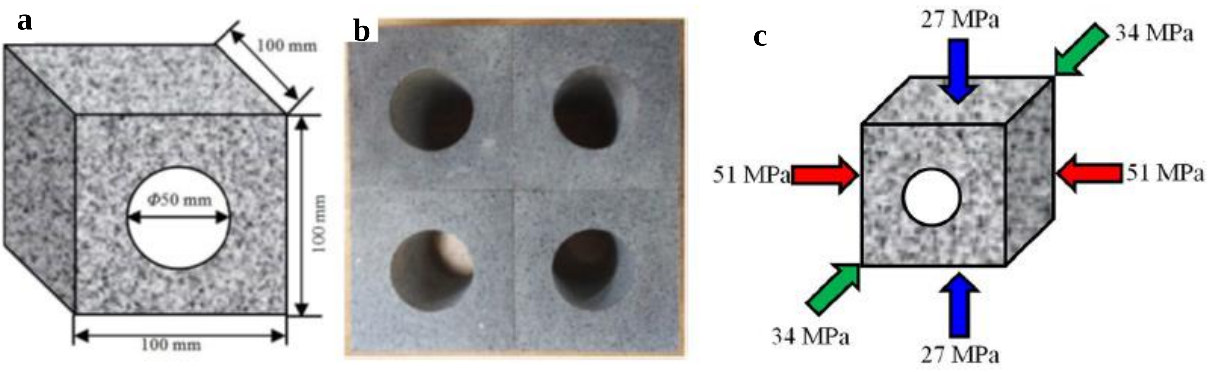

Figure 2.18 (a) Sketch of specimen geometry tested, (b) photo of a granite specimen, and (c) schematic of 3D stress condition in strain burst test (modified after Gong et al. 2018)

Table 2.6 Summary of true-triaxial loading and unloading tests to characterise the failure type of rocks (modified after Akdag et al. 2018)

Type	Loading step	Specimen size (mm x mm xmm)	Rock type	Failure mode	References
Loading	(1) apply σ1, σ2, σ3 (2) keep σ2 and σ3 (3) increase σ1	15 x 15 x 30	Dolomite	Fracturing & ductility	Mogi (1971)
		50 x 50 x 100	Marble		Michelis (1985)
		50 x 50 x 100	Sedimentary rocks		Takahashi & Koide (1989)
		57 x 57 x 125	Sandstone		Wawersik et al. (1997)
		19 x 19 x 38	Granite		Haimson & Chang (2000)
		80 x 80 x 80	Sandstone		Nasseri et al. (2014)
		50 x 50 x 100	Granite		Feng et al. (2016)
		60 x 60 x 110		Mixed tensile and shear fractures	Xu et al. (2019)
		50 x 50 x 100	Marble	Brittle & ductile failure	Zhao et al. (2018)
		50 x 50 x 100		V-shaped secondary fractures	Zheng et al. (2019)
		50 x 50 x 100	Granite, marble, sandstone	Spalling, brittle transgranular fractures	Gao et al. (2018)
		50 x 50 x 100	Sandstone	Stable-unstable fracturing	Kong et al. (2018)
Unloading	(1) apply σ1, σ2, σ3 (2) keep σ2 (3) Unload σ3 (4) Increase σ1	30 x 60 x 150	Limestone, granite, sandstone, marble	Rockburst	He et al. (2010, 2012a, 2012b, 2012c)
		20 x 40 x 100	Marble	Spalling	Coli et al. (2010)
		30 x 60 x 150		Rockburst and slabbing	Gong et al. (2012)
		30 x 60 x 150		Rockburst	Zhao et al. (2014)
		30 x 60 x 150		Rockburst	
		30 x 60 x 120	Granite	Slabbing	Zhao and Cai (2014)
		30 x 60 x 90		Shearing	
		30 x 60 x 150		Rockburst	Gong et al. (2015)

	100 x 100 x 100	Granite, sandstone, cement mortar	Splitting, slabbing, spalling	Li et al. (2015)
	100 x 100 x 100	Sandstone	Slabbing	Du et al. (2016)
	25 x 50 x 125	Granite	Rockburst (strain burst)	Akdag et al. (2018)
	50 x 50 x 100		Rockburst and slabbing	Li et al. (2018)
	50 x 50 x 50			
	25 x 50 x 50			
	30 x 60 x 150	Tuffaceous sandstone	Rockburst	Sun et al. (2017)
	100 x 100 x 200	Granodiorite	Rockburst	Su et al. (2017, 2018a, b)

At increasing depths, rock mass surrounding underground excavations becomes vulnerable to the effects of temperature. Due to the thermal gradient in the deep rock mass, elevated temperature conditions can cause dramatic changes in the microstructure and mechanical behaviour of rocks which are prone to strain burst. As a consequence, microstructure and mineral composition of rocks will alter due to the thermally-induced cracking under the action of high temperatures which will directly influence the long term safety and stability of underground rock structures. In recent years, a large number of researchers have investigated the effects of temperature on the physical and mechanical properties of various rocks under quasi-static loading (Keshavarz et al. 2010; Zhang et al. 2015; Peng et al. 2016; Xu and Karakus 2018; Xu et al. 2018). Liu and Xu (2015) studied the mechanical response of marble under the combined effects of high temperature and mechanical load under uniaxial compression and the mechanical damage and thermal damage caused by mechanical load and temperature respectively were discussed. The researchers established a high-temperature damage constitutive equation of rock based on the macroscopic damage mechanics and nonequilibrium statistical methods. Kumari et al. (2017) carried out a series of unconfined compressive strength tests on granite exposed to various temperatures up to 800 °C, followed by two cooling methods (rapid and slow cooling). They found that the influence of rapid cooling is much higher than that of slow cooling due to the abrupt thermal shock and the failure mode of the granite specimens changed from brittle to quasi-brittle fracturing with increasing temperature. To reveal the coupled effect of temperature and confining pressure on the failure mechanism of deep rocks, a new statistical constitutive model of rock thermal damage under triaxial compression was established by Xu et al. (2018). Besides, as being an intrinsic mechanical property of rocks, researchers have revealed that temperature is a significant factor influencing fracture characteristics and fracture toughness in the recent years (Yin et al. 2012; Mahanta et al. 2016). Using semi-circular bend (SCB) method, Yin et al. (2012) studied the effect of thermal treatment on dynamic fracture toughness of Laurentian granite and concluded that fracture toughness increases with the loading rate, whereas decreases with the treatment temperature. Mahanta et al. (2016) measured the static mode I fracture toughness of SCB Indian sandstone specimens and revealed that fracture toughness increased between the room temperature and 100 °C, thereafter decreased from 100 °C to 600 °C. However, to the best of our knowledge, the influence of temperature on the energy release during strain burst and the dynamic energy balance at spontaneous failure are still missing in the existing literature. However, the aforementioned studies did not consider the influence of thermal damage on strain burst mechanism under true-triaxial loading-unloading conditions. There is only a limited number of research focusing on exploring the influence of temperature on strain burst characteristics. Therefore, it is essential to investigate how strain burst mechanism is affected with elevated temperature which provides the very motivation for the study presented for accurate and better understanding of rock behaviour when strain burst occurs under high ground temperature condition.

Additionally, sudden ejection of rock fragments is a unique failure behaviour of strain burst. The kinetic energy of the rock fragments ejected from the free face of rock specimen in the strain burst test can be used as a precursor to quantitatively express the potential intensity of a burst event. A few studies in the available literature have addressed the kinetic energy characteristics of strain burst failure. Therefore, detailed kinetic energy analysis may allow the accurate interpretation of precursory information contained in strain burst damage and the accurate prediction of strain burst under high-temperature condition.

In this research, the process of strain burst in deep hard rock excavations was effectively reproduced by conducting true-triaxial strain burst tests and failure characteristics of strain burst damage were analysed more in-depth and the influence of thermal damage on strain burst mechanism and dynamic failure process was discussed. To quantify rock damage and monitor the evolution of damage within a thermally-treated rock, AE technique was adopted and time-domain, frequency-domain and b-value analyses were conducted to systematically study the evolution of AE due to thermal damage influence on strain burst. A high-speed camera was employed to observe and track the ejection of rock fragments during strain burst and kinetic energy analysis was carried out based on the velocity of ejected rock particles.

2.5 - Summary and discussion

As the depth of mining and underground engineering construction increases, strain burst which is a dynamic rock failure in highly-stressed ground, occurs more prevalently in an abrupt manner accompanied by violent rock fragment expulsion at a high speed. Due to its unpredictability, destructiveness and sudden nature, strain burst has become a serious disaster for safety and production during deep mining operations. Therefore, it is an urgent problem to better understand the underlying mechanism of the rock engineering disasters occurring in deep underground working environments for deriving strategies to eliminate or mitigate and reduce the potential intensity of strain burst.

Laboratory tests play a vital role for exploration the mechanism of strain burst, assessment the mechanical parameters and behaviour and identification of the stress states in which a spontaneous dynamic instability initiates. The primary goal for researches related to the physical modelling of strain burst phenomenon including the triggering factors is to replicate failure process of strain burst in the laboratory in a realistic manner and to mimic the stress conditions under which strain burst occurs. Over the past few decades, significant progress has been achieved in the characterisation of strain burst by conducting laboratory tests. However, existing studies have not been thoroughly evaluated the damage evolution during strain burst under the effects of different temperature, confinement and loading rate in various loading (and unloading) conditions. This section briefly presents the efforts on representing the real damage process of strain burst under the condition of laboratory tests within the framework of rock mechanics and fracture mechanics. The following key conclusions can be drawn:

1. The manifestation of strain burst is related to the elastic strain energy accumulated within the rock or rock mass and how this stored energy is released during energy-driven spontaneous failure. From the perspective of energy, strain burst is a nonlinear dynamic destabilisation failure process in which the energy is converted into kinetic energy by the ejected rock fragments. Therefore, the principles of energy release during strain burst, in some regards, can be compared with the principles involved in the spontaneous failure in hard brittle rock exhibiting Class II behaviour under compression. Strain burst is frequently encountered during the excavations in hard rock, which can store substantial amount of strain energy prior to failure and can release the energy during a rapid post-peak strength loss, displaying an unstable spontaneous and violent post-peak failure mode. In this respect, it is necessary to obtain the complete stress-strain characteristics for assessing the dynamic post-peak energy balance in strain burst. In addition, high rock stresses (confinement) and elevated temperatures have a significant influence on leading to strain burst as the underground excavations go deeper and extensive. Hence, it is also essential to investigate the coupling effects of thermal damage and confining pressure on the energy characteristics and potential intensity for strain burst.

2. The phenomenon of strain burst is mainly characterised by the nucleation, growth and coalescence of micro-cracks in rock or rock mass. Rock fracture toughness which is the critical SIF is an important intrinsic material property to resist fracturing can be used as a threshold for estimating the imminent fractures of rock structures during strain burst.

Therefore, to predict the onset of catastrophic failures such as strain burst in rock engineering structures due to crack growth, it is necessary to better understand the fracture characteristics and fracture parameters (fracture toughness, fracture energy) of rock during strain burst. In this sense, quasi-static and dynamic fracture and energy evolution characteristics in strain burst can be revealed by conducting fracture toughness tests. Rock mass is exposed to not only different loading rate disturbances, but also is vulnerable to the effects of elevated temperature as the depth of underground opening increases. Coupling impact of various loading rate and thermal damage will affect the overall mechanical behaviour of brittle rock which can trigger strain bursting in deep rock engineering operations. Therefore, rate dependence and the influence of temperature on quasi-static and dynamic fracture characteristics during strain burst are of great importance for reinstating the thermally damaged deep underground engineering constructions under the action of various loading rates.

3. Simulating the stress change and boundary of rock mass after excavation successfully is crucial importance to investigate the occurrence and mechanism of strain burst near the excavation boundary. In this respect, true-triaxial strain burst test has been conducted to mimic the failure process of strain burst, demonstrating the progressive stress concentration process during strain burst under true-triaxial loading-unloading condition. Since the rock mass is vulnerable to the effects of temperature at increasing depths, it is needed to explore the influence of thermal damage on strain burst characteristics under true-triaxial loading-unloading condition.

Rock properties, particularly rock strength, fracture toughness, have a significant control influence on the extent of strain burst mechanism and its propensity and severity. Rock strength determines the amount of elastic stored strain energy within the rock before critical strain burst stress level is reached, and rock fracture toughness determines the capacity of rock to insist unstable fracturing. Therefore, in terms of the laboratory evaluation of rock strength and rock fracture toughness, strain burst vulnerability can be initially identified.

It should also be noted that most of the experimental studies mentioned above are conducted on limited rock specimen sizes as compared to most of the natural processes operated in the field scale. Although some mechanisms of strain burst such as damage evolution and energy redistribution during strain burst, which were well documented in the laboratory studies, have been successfully used to account for certain brittle deformations of rock mass, the scaling effect still remains as a puzzle for the rock mechanics and structural geology research communities.

The brief review in the preceding sections and above summary have shown the need to conduct experimental research to better understand the mechanism of strain burst in a rigorous way. The combination of different experimental methodologies within the first law of thermodynamics and fracture mechanics will be focused on in the next chapters.

Further research is required to address these deficiencies and to determine improved methodologies for analysing the expression of strain burst using laboratory experiments.

Chapter 3: Forecasting the propensity of strain burst of brittle rock based on the post-peak energy analysis

3.1 - Introduction

The magnitude of strain burst, amount of kinetic energy released, the volume of ejected rock, ejection velocity and degree of rock fragmentation can show a considerable variation due to the mineral composition of the brittle rocks. The manifestation of strain burst is related to the elastic stored strain energy and how this stored energy is released during unstable spontaneous failure (Tarasov and Potvin 2013; Akdag et al. 2018; Bruning et al. 2018). The first law of thermodynamics states that the energy transformation process of strain burst in rock mass involves energy storage, dissipation, and release. Hence, it is significant to investigate the energy state during strain burst from the viewpoint of energy theory. Indeed, the failure of rock is driven by energy activities, including absorption, evolution, dissipation, and the release of strain energy (Huang and Li 2014; Peng et al. 2015; Li et al. 2017; Weng et al. 2017). Rocks exhibiting Class II behaviour undergo self-sustaining fracturing due to excess stored strain energy which is accompanied by some energy release. Hence, principles of the energy redistribution during strain burst, in some regards, can be compared with principles involved in the spontaneous failure of Class II, which implies that the role of energy in strain burst can be better understood by analysing the energy characteristics of rock in compression. In this respect, a series of quasi-static circumferential strain controlled uniaxial and triaxial compression tests were conducted on Class II rocks exposed to various temperatures up to 250 °C over a wide range of confinement to capture the post-peak reaction of Class II rock or ‘snap-back’ behaviour and calculate stored strain energy, dissipated energy, and the excess strain energy that is the intrinsic potential energy for strain burst in the rock. A novel energy calculation method associated with acoustic emission (AE) was developed based on the post-peak energy analysis. Combined effects of thermal damage and confining pressure on the mechanical properties of granite including the post-peak behaviours, energy redistribution at the post-peak regime, failure characteristics, strength and deformation parameters, characteristics stresses in the progressive failure process have been systematically investigated.

In this chapter, an introduction to the relevant researches conducted to gain a better understanding of the mechanism of strain burst, energy evolution characteristics of rocks under different loading paths, and the thermal damage influence on mechanical behaviour of rocks tests is presented. This is then followed by the experimental work included for estimating the energy redistribution characteristics of brittle rock during strain burst. A novel energy calculation method associated with AE to investigate the post-peak regime of rocks exhibiting Class II behaviour was developed. Intrinsic potential intensity for strain burst in the rock was quantitatively assessed. Coupling influence of thermal damage and confining pressure on the post-peak energy redistribution and crack evolution characteristics of thermally treated Australian granite specimens that ranged from ambient conditions (25 °C) to 250 °C was analysed. In order to reveal the microstructural changes due to thermal effects, scanning electron microscopy (SEM) analysis was also performed. This is highly relevant to link the excess strain energy and the main failure mechanism triggering strain burst under high temperature condition.

3.2 - Experimental methodology

Experimental work includes the investigation of the propensity of strain burst of rocks exhibiting Class II behaviour under the coupling influence of high confining pressure and high temperature. The main objective of this chapter is to quantitatively estimate the energy redistribution characteristics of brittle rock based on a newly developed energy calculation method, conducting circumferential strain controlled uniaxial and triaxial compression tests of granite. Two groups of tests were carried out in this study: Group (1) was the circumferential strain controlled uniaxial compression tests to quantitatively examine the potential intensity of strain burst, and Group (2) was the circumferential strain controlled triaxial compression tests to develop a new energy calculation methodology based on the post-peak energy balance of snap-back behaviour and investigate the combined effects of increasing temperature and confining pressure on the post-peak energy evolution characteristics. In order to support the findings, SEM analysis was also performed to provide a better understanding of the associated failure mechanism and the corresponding micro-structure alteration in granite.

3.2.1 - Specimen preparation and heating process

The granite specimens were collected from a borehole located in South Australia at depth ranging from 1020 m to 1345 m. The grain size of the granite varies between 0.5 and 3 mm within a coarse-grained matrix. The granite selected for testing mainly comprised of quartz, feldspar, chlorite and potassium.

The granite specimens were sub-cored from 63-mm diameter drill cores and cut using diamond coring and cutting apparatus to obtain cylindrical samples of 42 mm in diameter and 100 mm in length in which the aspect ratio (i.e. length to diameter ratio) was maintained at 2.4 (Fairhurst and Hudson 1999). The diameter of the specimens was more than 20 times bigger than the rock grain size satisfying ISRM recommendations (Fairhurst and Hudson 1999). Both ends of the specimens were then finely ground flat and parallel to each other within approximately 0.01 mm and polished to minimise the end effect during loading. The average uniaxial compressive strength (UCS) of the granite samples is 158 MPa with a density of 2871 kg/m^3, the average elastic modulus is 38.6 GPa, and the average P-wave velocity of the specimens before thermal damage is 5764 m/s.

The granite specimens were divided into four groups based on temperature exposure. In the present study, the heating process of the rock samples was carried out in a high-temperature tube furnace in the Mining Engineering Research Laboratory at The University of Adelaide. Samples were first heated up to the target temperatures (25, 100, 175, and 250 °C) at a modest-constant heating rate of 5 °C/min to avoid the development of cracks due to the thermal shock during the heating process. Once the designated temperature was reached, the temperature remained constant at the pre-determined level for about 12 h, to ensure uniform heating inside the specimens. They were then allowed to cool down naturally to room temperature (25 °C) prior to mechanical testing.

3.2.2 - Circumferential strain controlled uniaxial and triaxial compression tests

It is well-understood that the stress-strain behaviour of rock is the external manifestation of energy evolution during deformation and failure. Therefore, the complete stress-strain response of rock, importantly post-peak failure stage, is the fundamental information to describe the processes of energy redistribution, evolution and rock deformation as strain burst takes place at the post-peak failure stage. Numerous relevant attempts have been made by researchers to obtain the full stress-strain response of rock in compression by controlling the application of load through a feedback of axial load (Bieniawski and Bernede 1979), axial displacement (Gowd and Rummel 1980), or axial strain rate (Okubo et al. 1990). However, these control methods are only sufficient to measure pre-peak behaviour, not to capture post-peak stage of

Class II rocks which is characterised by a strong strain localisation as axial strain no longer monotonically increases from the moment that rock exhibits Class II behaviour (Munoz & Taheri, 2017). In this sense, the circumferential- or lateral-strain controlled method is more appropriate to measure post-peak stress-strain response for brittle rocks (Wawersik and Fairhurst 1970; Fairhurst and Hudson 1999; Munoz et al. 2016a, b). In this research, full stress-strain behaviour and energy evolution characteristics of brittle rock were analysed by performing circumferential strain controlled uniaxial and triaxial compression tests.

A series of uniaxial and triaxial compression tests were carried out on Australian granite. Compression tests compiled with circumferential-strain controlled method in order to capture the post-peak response of rock. To reveal the influence of temperature on rock energy evolution characteristics, and post-peak energy distribution of Class II behaviour under self-sustaining failure, a number of granite specimens exposed to different temperatures were tested. For UCS tests, rock samples were subjected to a quasi-static monotonic axial loading by a closed-loop servo-controlled Instron 1282 hydraulic compression machine, with a loading capacity of 1000 kN, which was stiff enough not to allow the elastic energy accumulated in the machine. (see Figure 3.1). The applied axial load was initially controlled at an axial-strain feedback at a rate of 0.001 mm/mm/s until reaching approximately 70% of the expected peak force (0.07 F_{peak}) and then the control mode was switched to circumferential control, in a way keeping lateral-strain rate constant by the circumferential extensometer outlined in the ISRM method (Fairhurst and Hudson 1999). In this sense, the electronics and computer program allowed the hydraulic system to be adjusted continuously and automatically to ensure the load to respond accordingly with the feedback signal and with the damage extent to the specimen.

In UCS test, each granite specimen was instrumented by a pair of strain gauges (30 mm in length) oriented in the axial direction to measure the corresponding axial strain, ε_a, as depicted in Figure 3.1. Additionally, the vertical displacement of the granite specimens was measured externally by a pair of LVDTs, which were mounted on both sides of the specimens. Besides, direct-contact lateral ring-shaped extensometer was mounted along the perimeter and at the mid-length of the specimens which eliminated the end-edge friction influence. This setup was used to both control the axial load by lateral-strain feedback and record lateral strain, ε_l. Figure 3.1 shows the arrangement of the instrumentation and experimental setup for uniaxial compression tests under quasi-static monotonic loading conditions.

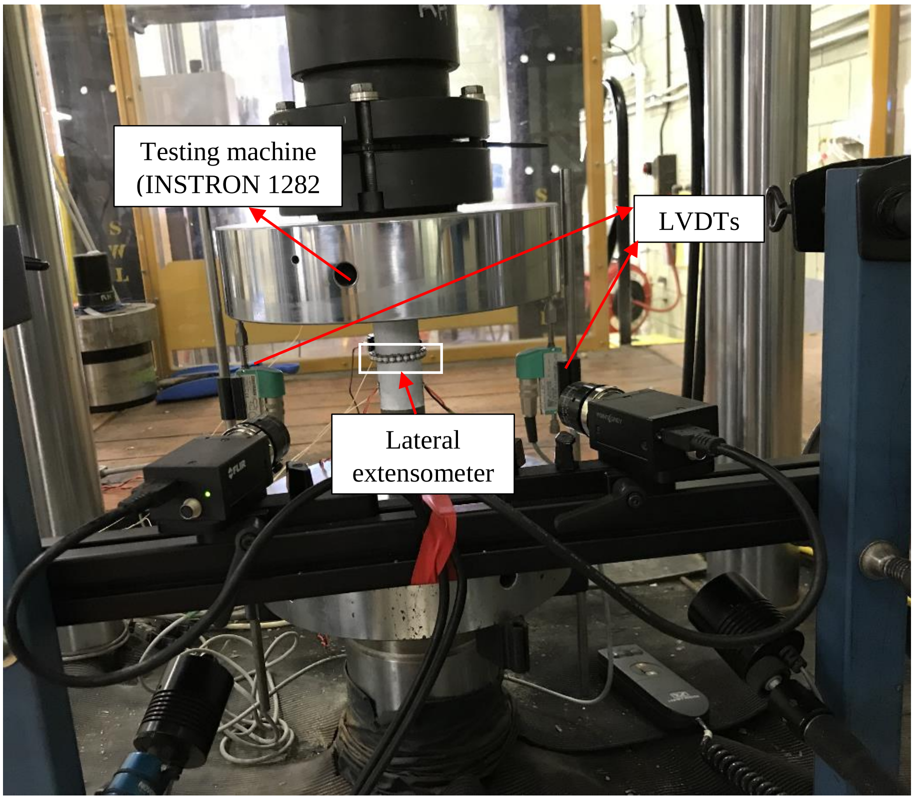

Figure 3.1 Experimental setup: servo-controlled closed-loop testing system and rock instrumentation in uniaxial compression loading

To investigate the coupling influence of thermal damage and confining pressure on energy evolution, circumferential strain controlled triaxial tests were conducted on the granite specimens exposed to temperatures up to 250 °C over the confining pressures up to 60 MPa. Triaxial compression tests were carried out using Instron 1282 with an axial loading capacity of 1000 kN under three groups of confining pressures (20, 40, and 60 MPa). A Hoek cell with a capacity up to 65 MPa was used to apply confining pressure in these tests. Circumferential strain control was utilised by means of a Hoek cell membrane fitted with four strain gauges internally within the cell, as depicted in Figure 3.2. The circumferential strain method suggested by ISRM for obtaining the complete stress-strain curve was adopted in these tests. The specimen was loaded axially with a constant growth of lateral strain of 1×10^{-6} mm/mm/s. The first step of the test was to apply hydrostatic pressure on the rock specimen until the pressure reached the required magnitude of the confinement. After that, the axial loading was applied using the circumferential strain control method while keeping the confining stress constant.

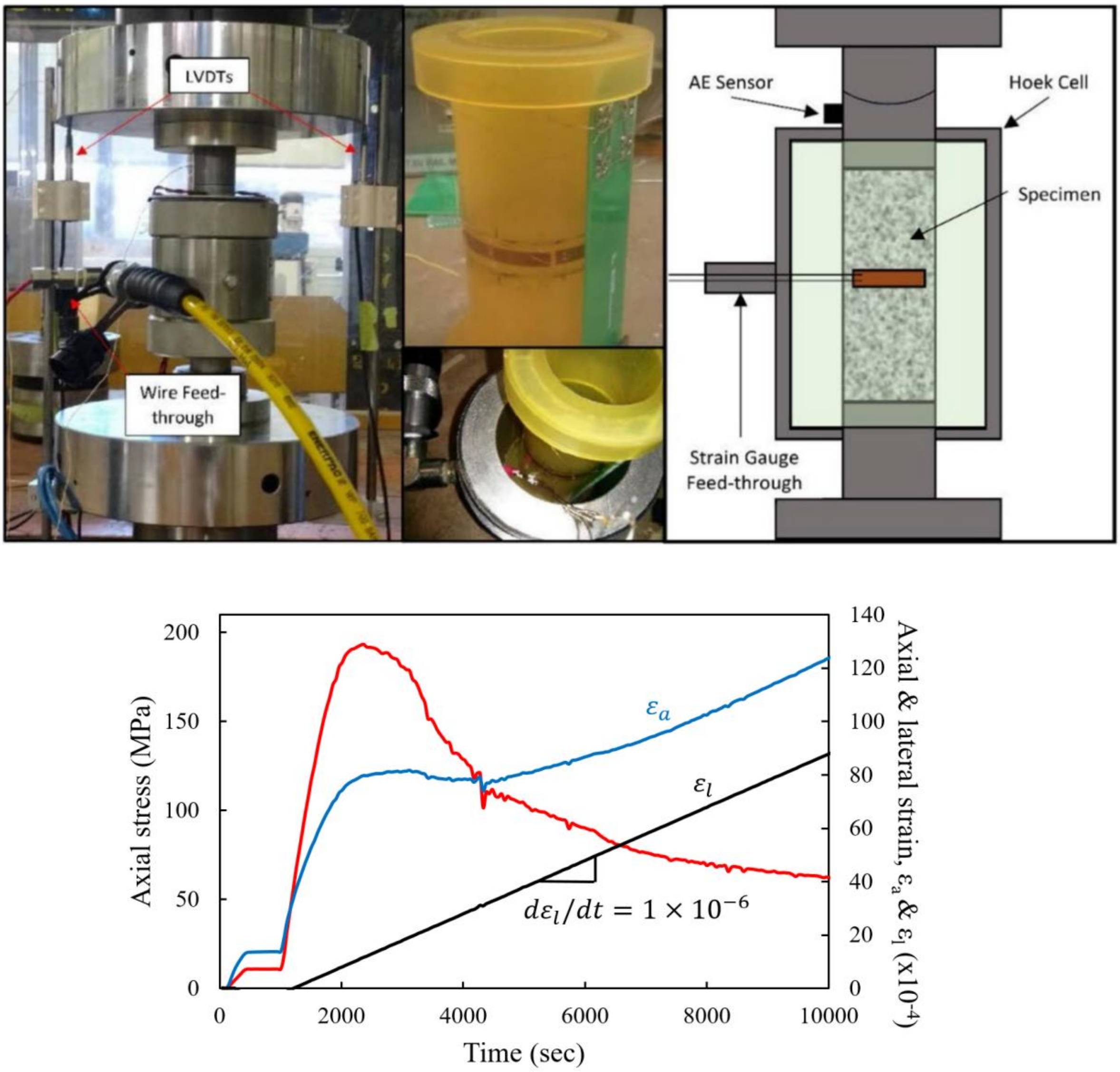

Figure 3.2 (a) Testing setup for circumferential strain controlled triaxial compression tests and strain gauged membrane to control the application of load through a feedback loop of circumferential strain and (b) Typical time history of a loading and strains in circumferential-strain control feedback triaxial compression test in the present study

3.2.3 - Acoustic emission monitoring

During experiments, in order to analyse fracturing characteristics, and damage evolution mechanism of the thermally-treated deforming specimens, the output of AEs was continuously monitored. It is known that acoustic emission can be defined as the transient elastic waves induced by the rapid release of localised energy due to crack formation and propagation within a material (Carpinteri et al., 2013; Karakus et al., 2016; Akdag et al., 2018; Bruning et al., 2018). In the present study, the AE system was started simultaneously with the uniaxial compression loading and the pre-amplifiers of two AE sensors were set to 60 dB to amplify the AE signals during loading. The resonance frequency of the AE transducers was 125 kHz, associated with an operating frequency ranging from 100 kHz to 1 MHz. A PCI-2 AE system was used to monitor the damage within the granite specimens during compression tests, and the sampling rate was set to 2MSPS. The amplitude threshold for AE detection was set to 45 dB to ensure environmental noise was no longer registered during data acquisition.

3.3 - Evaluation of the experimental results

In this part, a new energy calculation method associated with AE for evaluating the post-peak energy characteristics of brittle rock is introduced. According to the proposed formulas and tests results, energy evolution during strain burst of Class II rock is analysed with the change of temperature and confining pressure, and the underlying mechanism of strain burst is also discussed. The combined influence of thermal damage and confinement on the mechanical properties, failure modes and AE characteristics of Australian granite is investigated. Kinetic energy analysis is conducted for quantitatively evaluating the intensity of strain burst, and the effects of temperature on the severity of strain burst is studied. The fracturing mechanism of granite under the combined effects of temperature and confining pressure is also discussed.

3.3.1 - New energy calculation method based on the post-peak energy balance of snap-back behaviour

The stress-strain response is the phenomenological manifestation of the energy evolution during rock failure. Under compression, the stress-strain curves of the post-peak behaviour of rocks can be classified as Class I and II. Class I behaviour is characterised by a negative post-peak slope which means that loading must be applied to generate additional energy for maintaining the entire fracture process until the failure of the rock to occur. Class II rock behaviour, on the other hand, shows positive post-peak slope and the elastic stored strain energy in the rock specimen is sufficient to display self-sustaining failure which is accompanied by some energy release. The post-peak behaviour is a reflection of some intrinsic material properties which allows estimating the dynamic energy balance at spontaneous failure. Therefore, full stress-strain behaviours of rock undergoing uniaxial and triaxial compression play a significant role to describe the total energy evolution and rock deformation. In this respect, the full stress-strain and the post-peak characteristics of hard brittle granite samples exhibiting Class II behaviour under uniaxial and triaxial compression, which can be compared with the stress state of a strain burst, were obtained by utilising the circumferential-strain controlled loading method.

Figure 3.3 shows the complete stress-strain curve of a granite tested at a confinement of 10 MPa. Area of the green triangle (dU_E) corresponds to the elastic stored strain energy within the specimen before it displays ‘snap-back’ behaviour, which is the energy source for fracturing and spontaneous failure (strain burst).

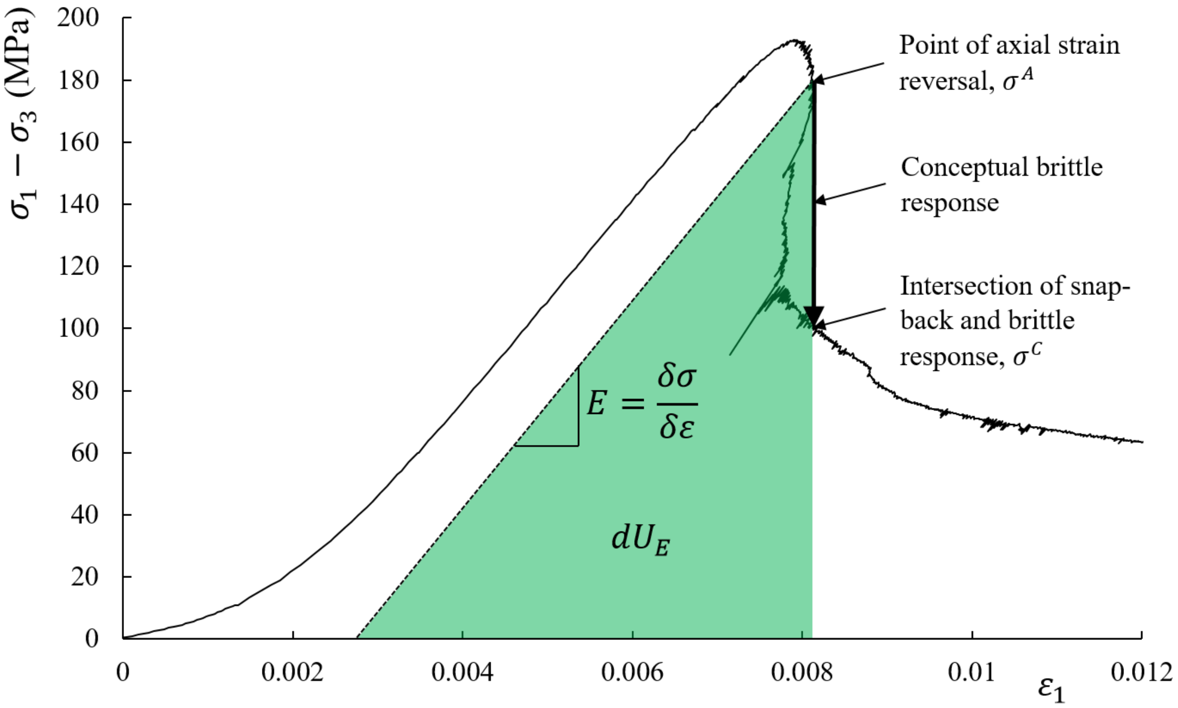

Figure 3.3 Class II behaviour and elastic stored strain energy of granite under 10 MPa confinement

Tarasov and Potvin (2013) assessed rock brittleness under triaxial compression and established a corresponding brittleness index based on the energy balance of the post-peak stage of the full stress-strain curve. However, this energy calculation framework did not take into account the energy dissipation due to cohesion loss and frictional failure and the excess strain energy released during brittle failure (bursting). Herein, a new energy calculation method to investigate the post-peak regime of rocks exhibiting Class II behaviour is proposed. Using the AE characteristics during compression tests, fracture energy was split into two classes: 1) energy consumed due to gradual loss of dominating cohesive behaviour and 2) energy dissipated during the mobilisation of frictional failure (as shown in Figure 3.4). In Figure 3.4, blue and yellow areas represent the energy consumed by cohesion weakening during stable fracturing ($d\Phi_{CW}$) and the energy dissipated during the mobilising frictional sliding ($d\Phi_{FM}$), respectively. The green area is corresponding to the residual stored elastic strain energy (dU_{RE}). For Class II rock behaviour, the elastic strain energy accumulated within the rock is sufficient to maintain the entire failure of the rock which indicates that rocks exhibiting snap-back behaviour are close to absolute brittleness. In this case, self-sustaining fracturing forces rock failure which is accompanied by some energy release. The red area (subtended by snap-back part) represents the excess strain energy released during brittle failure (energy in excess, $d\Phi_{EX}$) which is responsible for the intrinsic potential energy for strain burst in the rock. The above assumptions on unloading without stiffness change and different stages of failure based on the measured macro behaviour facilitate the calculation of energies in this study. I am aware that they may not always truly reflect the underlying failure modes that are a combination of microcracking and friction between microcrack surfaces. The links between macro behaviour and underlying micro-structural processes require advanced experimental techniques that can track the evolution of these processes in real time, given the very fast failure in rocks under uniaxial/triaxial compression condition. This is beyond the scope of this study.

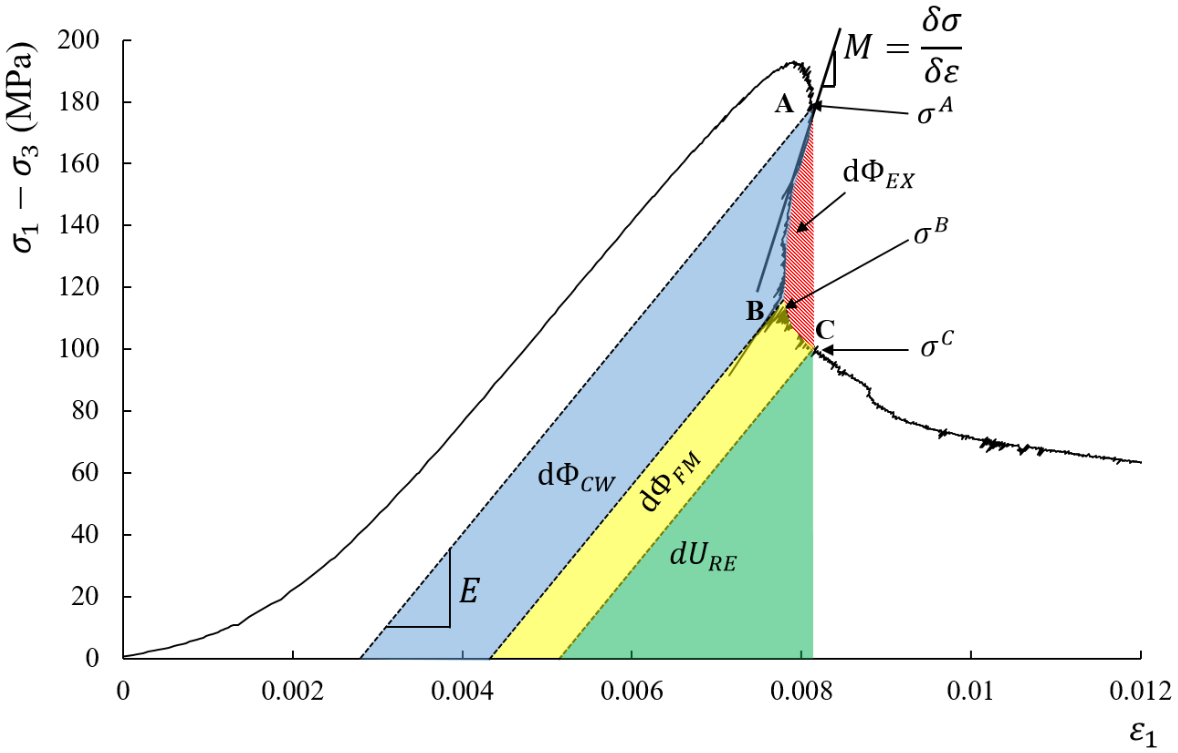

Figure 3.4 Schematic diagrams of energy calculation during Class II behaviour of granite under 10 MPa confinement

The Class II failure process between points A and C can be characterised by the following types of specific (per unit volume) energy calculations (Equations 3.1-3.5):

$$dU_E = \frac{(\sigma^A)^2}{2E} \tag{3.1}$$

$$\mathrm{d}\Phi_{CW} = \sum_{i=A}^{B} \frac{(\sigma^i)^2 - \left(\sigma^{i+1}\right)^2 (M - E)}{2EM} \tag{3.2}$$

$$\mathrm{d}\Phi_{FM} = \sum_{i=B}^{C} \frac{(\sigma^i)^2 - (\sigma^{i+1})^2 (M - E)}{2EM} \tag{3.3}$$

$$dU_{RE} = \frac{(\sigma^C)^2}{2E} \tag{3.4}$$

$$\mathrm{d}\Phi_{EX} = dU_E - \mathrm{d}\Phi_{CW} - \mathrm{d}\Phi_{FM} - dU_{RE} \tag{3.5}$$

where U_E is the elastic stored strain energy after the point of Class II behaviour, Φ_{CW} is the energy consumption dominated by cohesion degradation during stable fracturing, Φ_{FM} is the energy dissipated during the mobilisation of frictional failure, U_{RE} is the residual stored elastic strain energy, Φ_{EX} is the excess strain energy released during brittle failure (bursting), σ^A is the point of axial strain reversal, σ^B is the point of brittle failure intersection, E is the elastic stiffness of the specimen and M ($M = \delta\sigma/\delta\varepsilon$) is the post-peak modulus between two incremental stress points.

The AE detection technology is a powerful non-destructive technique to investigate the failure process and crack evolution mechanism in brittle rocks (Lockner, 1993). When a brittle rock is under stress, strain energy is released during the development of new cracks or the widening of existing cracks. This energy is released in the form of elastic waves from the crack tips, and can be captured and amplified by an AE system. Therefore, AE detection technique has been widely used in a number of previous researches to study the crack development mechanism in brittle rocks (Carpinteri et al., 2013; Karakus et al., 2016; Kumari et al., 2017; Akdag et al., 2018; Bruning et al., 2018; Weng et al., 2018). In this study, the AE technique was adopted to assess the post-peak energy evolution characteristics of the granite specimens under various confining pressures. Figure 3.5 shows axial stress-strain and AE hits characteristics for rocks with Class II behaviour tested in triaxial compression ($\sigma_3 = 10\ MPa$). From near peak (pre-peak) to the point of axial strain reversal (σ^A), some microcracking is mobilised that facilitates fracture process, e.g. creating more surfaces to facilitate sliding. In Zone (1), the energy dissipation of the rock specimen is provided by the initiation and further opening of microcracks in the specimen. In this energy dissipation process, cohesion degradation and frictional sliding facilitates simultaneously in which cohesion weakening is dominant, but the energy needed to further fail the specimen is below the storage. During this process, further degradation of cohesive strength leads to more fracture surface created and hence gradually shows stronger interlocking. This is typified by the increasing AE activities as more microcracks are opened. Once a certain level of microcrack generation is reached, the fractures start to coalesce and propagate forming macrocracks (Zone 2). This allows frictional sliding to dominate the fracture energy dissipation process. More energy is gradually required to further fail the specimen, due to friction strengthening and also lower energy storage. At this stage the sliding plane has formed in rock and a more constant rate of AE energy is recorded. Therefore, with fracture propagation, dominating cohesion loss (Zone 1) is gradually substituted by the mobilisation of frictional failure (Zone 2) which is accompanied by the decrease in bearing capacity of the specimen from the cohesive strength to the frictional (residual) strength (Bazant, 1996; Landis et al., 2003; Tarasov & Potvin, 2013; Munoz & Taheri, 2018; Renani & Martin, 2018). This new method for determining the energy dissipation of compressive tests avoids the grouping of all energy into the term ‘energy lost due to stable fracturing’. This is significant when considering phenomena like strain burst as frictional processes are not likely to occur at the excavation face due to the sudden ejection of rock fragments and spalling type of failure. Therefore, these energy measures can be further studied to determine their role in strain burst prediction and mechanism investigation.

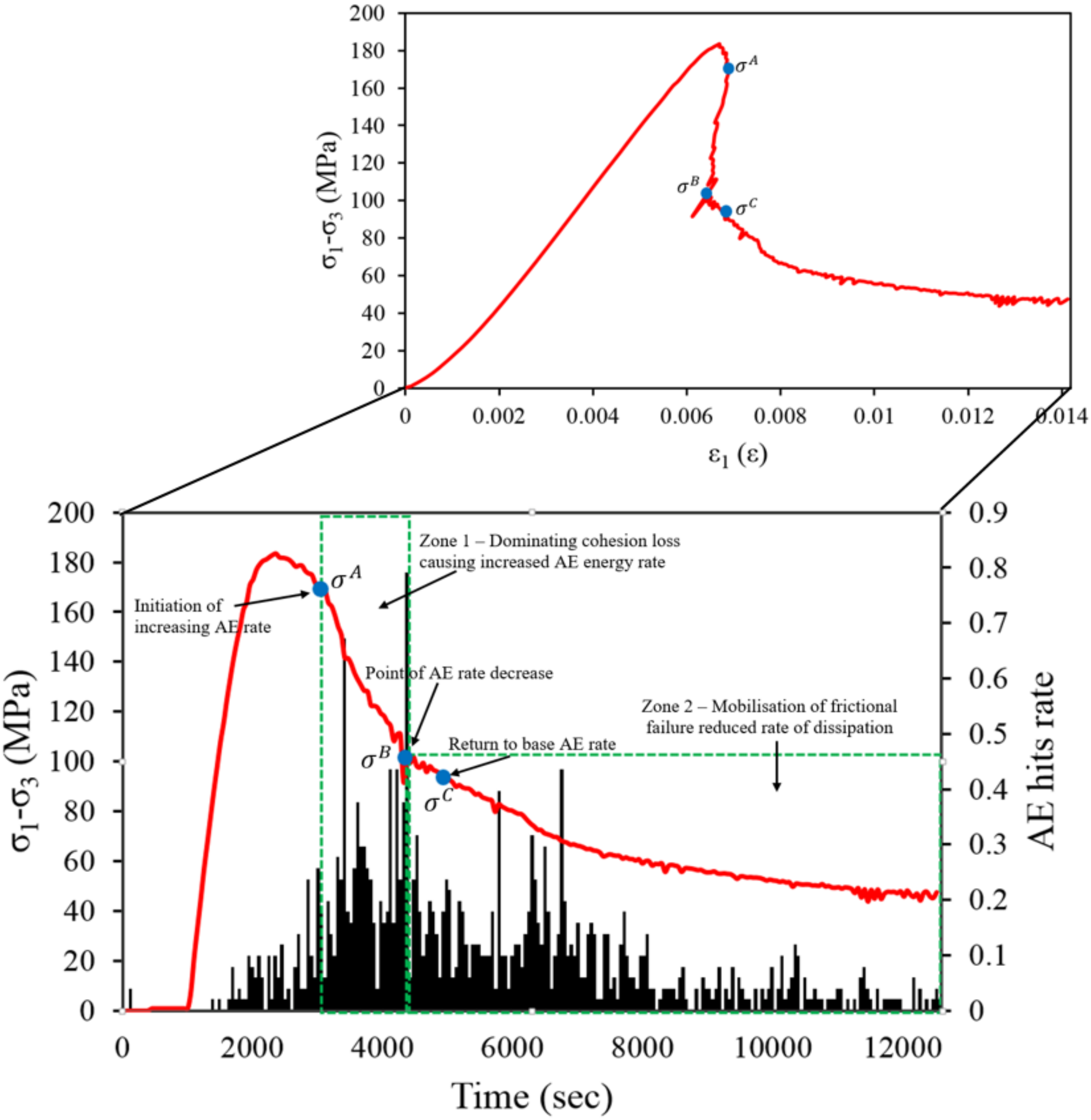

Figure 3.5 Stress-strain and AE energy characteristics for Class II rock under 10 MPa confinement

3.3.2 - Coupled temperature and confinement influence on the mechanical behaviour of Australian granite

To further understand the temperature effect on the overall mechanical behaviour of Australian granite, the stress-strain characteristics were considered first and the results are given in Table 3.1. Figure 3.6 presents the relationship between deviatoric stress and axial strain curves for granite after different thermal treatments under the confining pressure levels of 0, 20, 40 and 60 MPa. It can be seen that the post-peak behaviour of granite is strongly affected by the coupled thermal damage and confining pressure. At low confining pressure, granite exhibited

Class II failure mode, characterised as a self-sustaining failure, and showed a transition to Class I behaviour. Based on the experimental results, peak stress at 250 °C declined by 10% when compared with the results at room temperature (25 °C) under unconfined conditions. With the increase of confining pressure (20-60 MPa), the peak stresses decreased by 16, 18 and 27% as increasing temperature, respectively. The main reason for this descending trend was that a large amount of thermally induced micro-cracks caused mechanical degradation weakening the bonding among mineral grains due to the differences in the thermal expansion properties of constituent rock minerals. This observation is consistent with the existing literature (Yin et al. 2012; Yao et al. 2016; Yang et al. 2017; Xu and Karakus 2018).

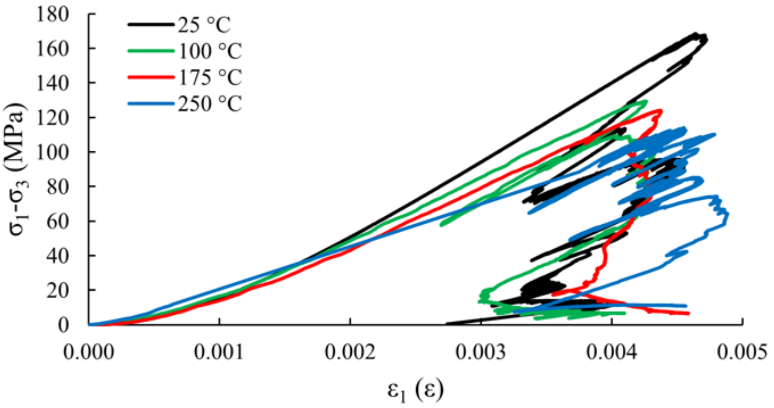

0 MPa

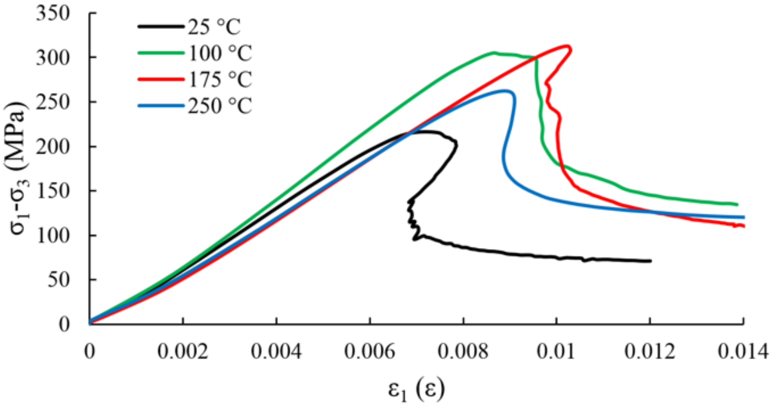

20 MPa

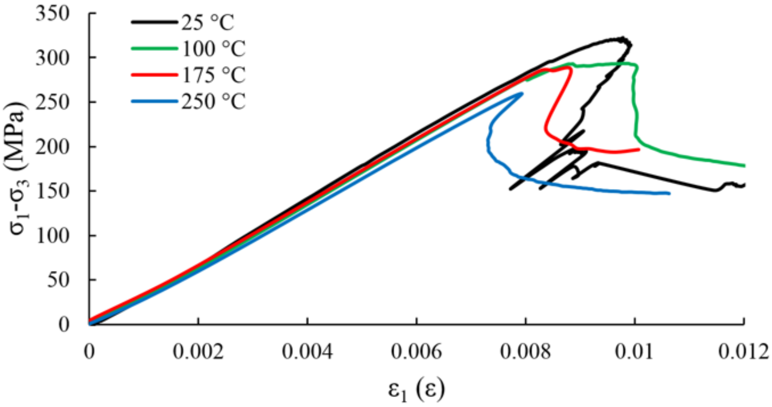

40 MPa

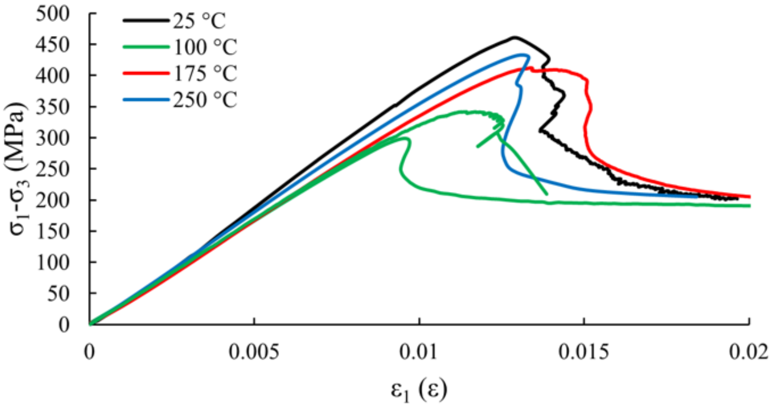

60 MPa

Figure 3.6 Stress-strain curves of granite at different temperatures under various levels of confinement

The variations of peak stress, peak strain and Young's modulus with confinement and temperature are depicted in Figure 3.7. It can be expected that with the rise of confining pressure, the peak strength increased (see Figure 3.7a). At low confinement, the peak strength of thermally treated Australian granite was mainly controlled by the micro-cracks; however, with increasing confining pressure, the effects of micro-cracks on the strength diminished as the initial micro-cracks began to close due to the application of confinement. As shown in Figure 3.7b, the peak strain increased by 26% as the temperature increased from 25 to 250 °C due to the compaction of more micro-cracks inside high-temperature treated specimen produced larger strain. The trend of the elastic modulus of granite specimen with increasing temperature was similar to that of the peak strength. With the increase of temperature from 25 to 250 °C, the elastic modulus of Australian granite decreased by approximately 17% due to the fact that different levels of fragmentation rendered the rock relatively weaker after heating treatment (see Figure 3.7.c). This phenomenon can be attributed to the increased crack density due to induced thermal crack development (Kumari et al. 2017a). This trend was consistent with the temperature-dependent strength behaviour of the granite described above.

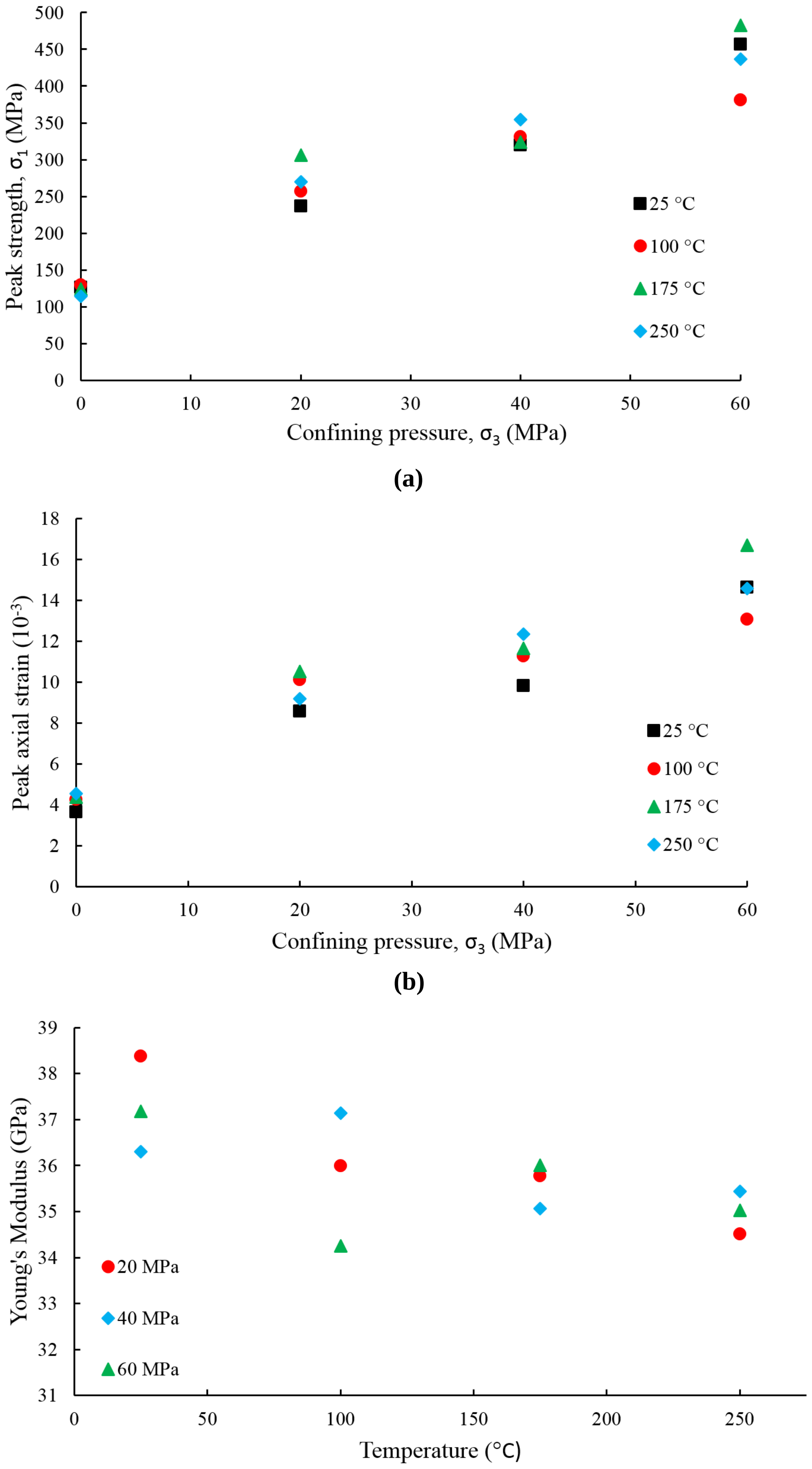
500
450
400
350
300
250
200
150
100
50
0
Peak strength, σ_1 (MPa)
0
10
20
30
40
50
60
Confining pressure, σ_3 (MPa)
■ 25 °C
● 100 °C
▲ 175 °C
◆ 250 °C
18
16
14
12
10
8
6
4
2
0
Peak axial strain (10^{-3})
0
10
20
30
40
50
60
Confining pressure, σ_3 (MPa)
■ 25 °C
● 100 °C
▲ 175 °C
◆ 250 °C
39
38
37
36
35
34
33
32
31
Young's Modulus (GPa)
0
50
100
150
200
250
Temperature (°C)
● 20 MPa
◆ 40 MPa
▲ 60 MPa

(a)

(b)

(c)

Figure 3.7 Stress-strain curves of granite at different temperatures under various levels of confinement

The failure modes of the granite specimens under the combined conditions of elevated temperature and confinement are presented in Figure 3.8. The main feature is the multiple longitudinal splitting failure pattern accompanied by local shear failure when $\sigma_3 = 0$ MPa. The formation of extension cracks oriented in the direction of principal stress is the prevailing pattern of macroscopic fracturing in uniaxial compression. In moderate confining pressures, the granite specimens mainly failed by shear localisation along an inclined macroscopic shear band. Under high confinement, a conjugate shearing or ductile failure was observed in which the thermal heating could also enhance the ductility of the rock samples, as depicted in Figure 3.8. Confining pressure restricts the propagation and coalescence of longitudinal cracks which helps to the expansion of the inclined cracks at an angle to the direction of the major principal stress, and hence the failure mode changed. The longitudinal splitting cracks is a type of tensile crack, which is easily opened and has a small displacement between crack surfaces. Therefore, the dissipated energy needed to initiate and propagate the longitudinal splitting cracks is small. However, granite specimens will slide along the surfaces after shear failure under a high confinement. This process requires the testing apparatus to provide more energy to overcome the friction and maintain the propagation of the macro-cracks.

Table 3.1 Mechanical properties of Australian granite at different temperatures and confining pressures

Temperature (°C)	**Confining pressure, σ_3 (MPa)**	**Peak stress, σ_1(MPa)**	**σ_1-σ_3 (MPa)**	**Peak strain, ε_1 (x10^{-3})**	**Elastic modulus (GPa)**
RT (25)	0	126.581	126.581	3.647	44.815
	20	236.387	216.387	8.401	34.857
		305.410	285.410	8.794	38.375
	40	275.042	235.042	8.692	35.393
		363.875	323.875	10.984	37.211
	60	522.490	462.490	16.278	40.158
		391.239	331.239	12.985	34.193
100	0	129.563	129.563	4.259	36.420
	20	214.654	194.654	8.707	34.060
		299.164	279.164	11.513	37.930
	40	328.393	288.393	11.139	38.264
		333.432	293.432	11.437	36.027
	60	358.858	298.858	12.475	33.690
		403.321	343.321	13.660	34.803
175	0	124.171	124.171	4.367	35.577
	20	332.640	312.640	12.166	34.665
		279.156	259.156	8.880	36.890
	40	326.534	286.534	11.357	35.853
		321.228	281.228	11.939	34.269
	60	472.587	412.587	18.088	35.438
		493.006	433.006	15.313	36.567
250	0	114.059	114.059	4.551	25.138
	20	281.859	261.859	10.288	33.659
		257.320	237.320	8.079	35.353
	40	300.300	260.300	11.239	34.830
		409.417	369.417	13.459	36.056
	60	493.644	433.644	16.411	36.666
		380.037	320.037	12.761	33.375

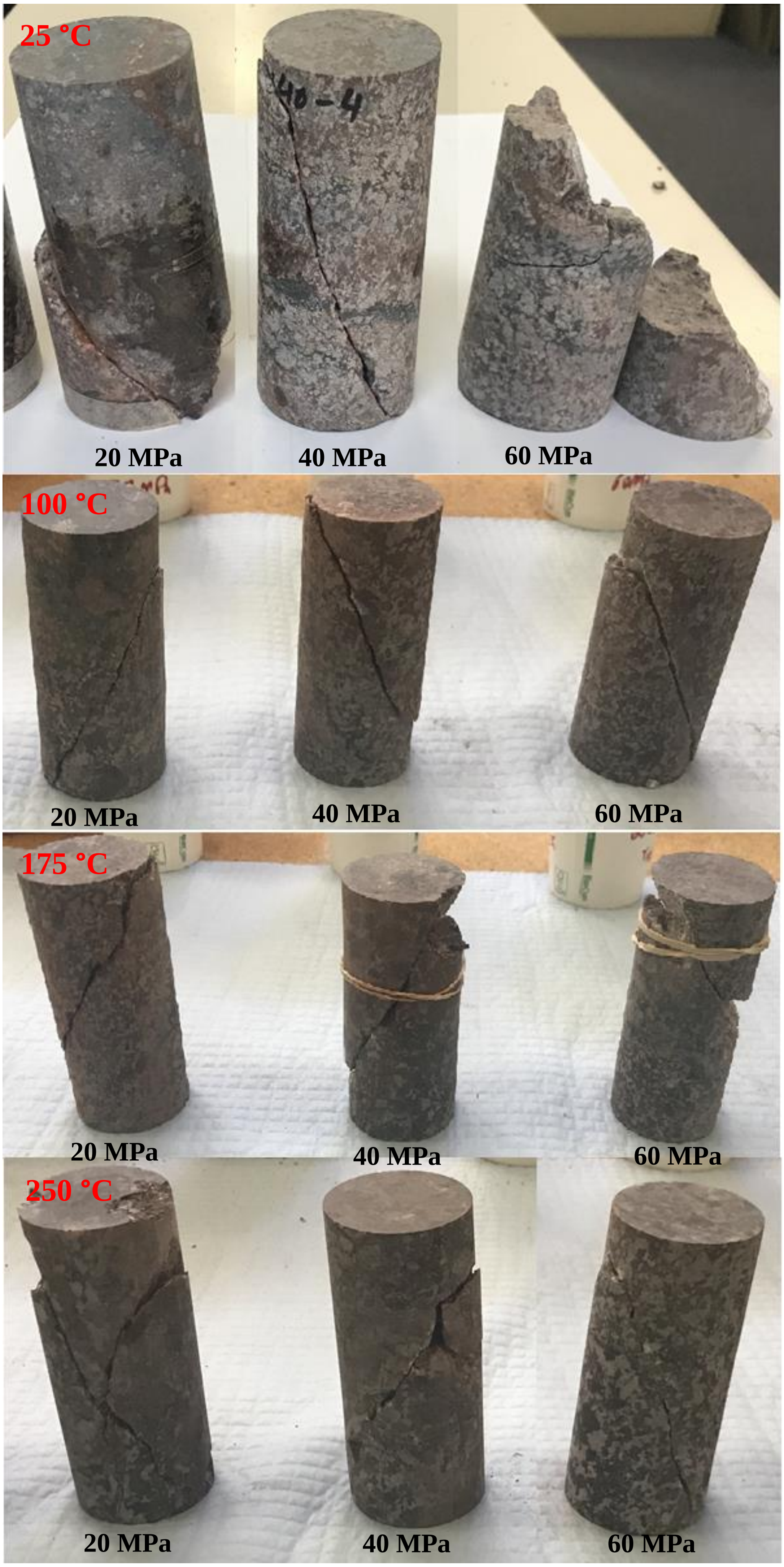
25 °C
40-4
20 MPa
40 MPa
60 MPa
100 °C
20 MPa
40 MPa
60 MPa
175 °C
20 MPa
40 MPa
60 MPa
250 °C
20 MPa
40 MPa
60 MPa

Figure 3.8 Fracture patterns of granite specimens after heating to different temperatures under different confining pressures

Progressive damage evolution and fracturing behaviour in Australian granite under uniaxial and triaxial loading conditions were investigated by using AE monitoring technique in this study. As indicated that cumulative AE energy characteristics reflect the damage evolution better as the size of micro-cracks is related to the magnitude of the AE events, cumulative AE responses were analysed in this study (Akdag et al. 2018). Figure 3.9 shows the cumulative AE energy evolution for granite specimens at different levels of temperature for each confinement. Based on the AE characteristics, the evolution of AE behaviour underwent two typical stages, i.e. quiet stage and active stage. The quiet stage corresponds to the closure of pre-existing cracks or other defects and linear elastic deformation in which AE energy responses were rare when compared with the active stage. It can also be observed that the AE characteristics at the quiet stage for brittle rocks are not dependent on temperature. With the increase of axial deformation, stable and unstable crack propagation took place which contributed to the progressive degradation of the inherent rock strength and thus resulted in a dramatic increase of cumulative AE energy. In relation to the thermal damage influence, the accumulated AE energy curves became smoother with the rising temperature which resulted in a delay in damage evolution. Due to the thermally-induced micro-cracks, a delay in damage evolution occurred which indicates that at higher temperatures, the granite specimens tended to burst in a more intense manner.

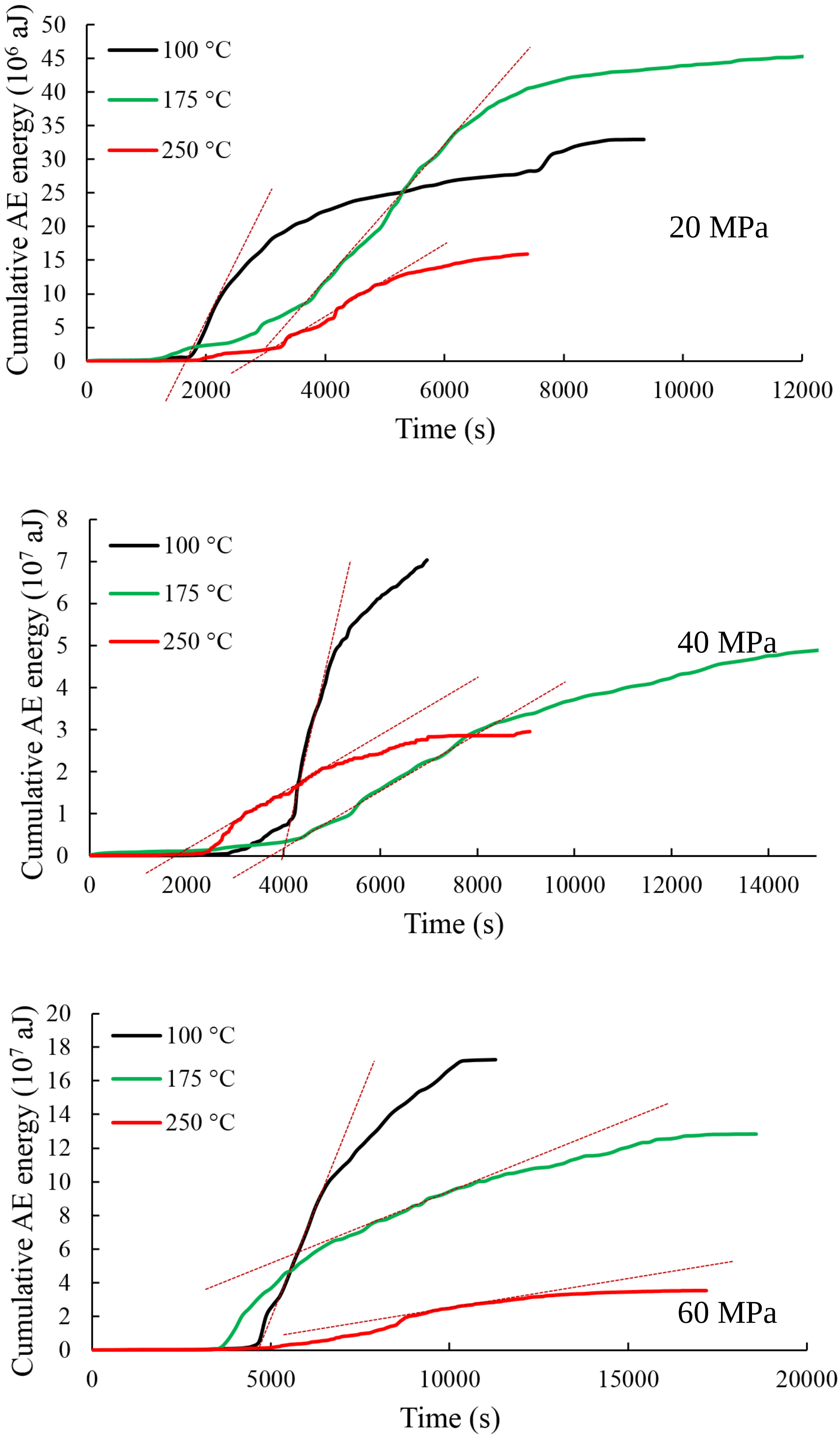

Figure 3.9 Evolution of accumulated AE energy for granite specimens after different thermal treatments.

3.3.3 - The energy balance of Class II at spontaneous failure under the combined conditions of elevated temperature and confining pressure

The release of excess strain energy and the increase of dissipated fracture energy caused a reduction in the energy storage capacity of the rock so that rock deformation increased gradually and tended to fail. The formation of macrocracks and failure surfaces in the rock promoted the conversion of the accumulated elastic strain energy into the forms of energy to be dissipated and released which resulted in spontaneous bursting. Due to the aggravation of dramatic internal fracture expansion, further strength loss took place with a transition into the residual stage in which some amount of strain energy was stored within the specimen (see Figure 3.4).

In general, the higher the peak stress, the higher the elastic stored strain energy, with higher excess strain energy which is the intrinsic potential energy for strain burst in the rock associated with faster rock fragment ejection. The material strength drops along the increase of pre-heating temperature. An increase in the temperature can exacerbate the fragmentation degree of the sample that can weaken the interaction force between the particles and aggravate the fragmentation degree. The results demonstrated that thermal damage affects strain burst behaviour of brittle rock. Figure 3.10 shows the variations of elastic stored strain energy, total fracture energy, excess strain energy by temperature. When the temperature increased from 25 to 250 °C, elastic stored strain energy, total fracture energy, excess strain energy decreased by 80, 82 and 43%, respectively (see Figure 3.10). Increasing temperature resulted in an alteration of the grain-to-grain contacts in the rock matrix, which led to reduced cohesion at higher temperatures.

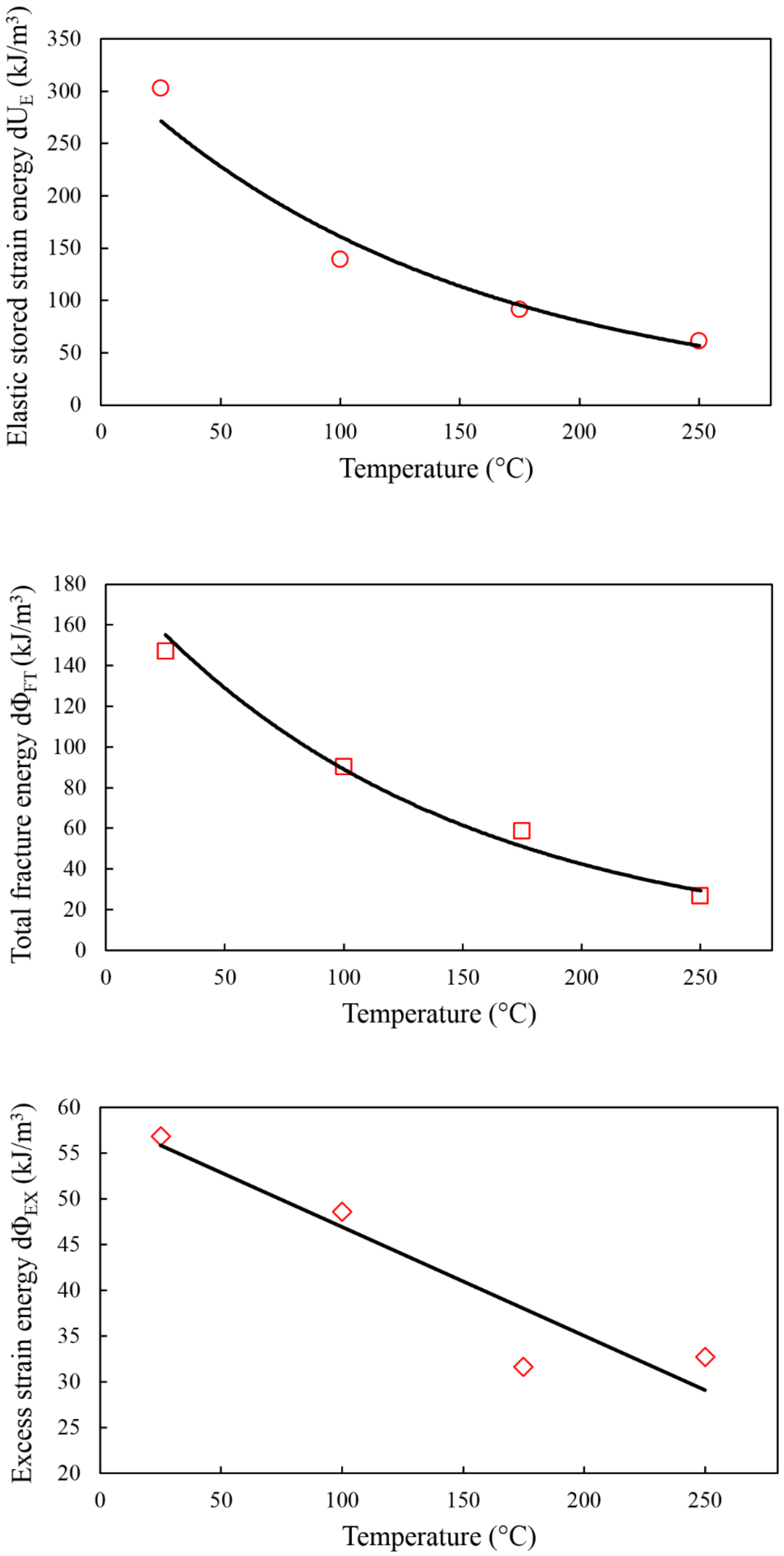

Figure 3.10 Evolution of accumulated AE energy for granite specimens after different thermal treatments

The influence of confinement on the elastic stored strain energy, the energy consumed by dominating cohesion weakening, the energy dissipated during mobilisation of frictional failure and the excess strain energy of the granite specimens are depicted in Figure 3.11. It can be seen that the energy redistribution characteristics and material behaviour of Australian granite under different levels of confinement are strongly dependent on confining pressure. When the confining pressure increased to 60 MPa, elastic stored strain energy, energy consumed by dominating cohesion weakening, energy dissipated during mobilisation of frictional sliding were 8.74, 2.53 respectively, and 12.1 times the values at unconfined condition indicating that the elastic energy accumulates more rapidly as the depth of an underground excavation rises up, resulting in a more severe strain burst (see Figure 3.11a-c). At the pre-peak stage, the growth of the accumulated elastic strain energy was faster than the dissipated energy, indicating that the energy evolution behaviour of granite prior to the onset of ‘snap-back’ behaviour was mainly dominated by the elastic energy accumulation. This phenomenon implies that the ability of granite specimens to store elastic strain energy was enhanced by the higher confining pressure. In the post-peak regime, the accumulation of elastic energy began to slow down and ultimately became stable and the dissipated fracture energy increased by the development and further openings of micro-cracks leading to internal damage of rock progressively with a loss of cohesive strength. The expansion, coalescence and propagation of micro-cracks to form macro-cracks led frictional failure to dominate the fracture energy dissipation process in which the sliding plane was formed. The excess strain energy diminished by 46% as the confining pressure increased up to 60 MPa, as depicted in Figure 3.11d. As rising the level of confinement, the frictional strength component was easily mobilised, which caused an increase in frictional resistance to crack propagation. Thus, greater dissipated energy consumption is required to promote crack propagation, revealing that the damage of deep granite is more severe from the viewpoint of energy evolution.

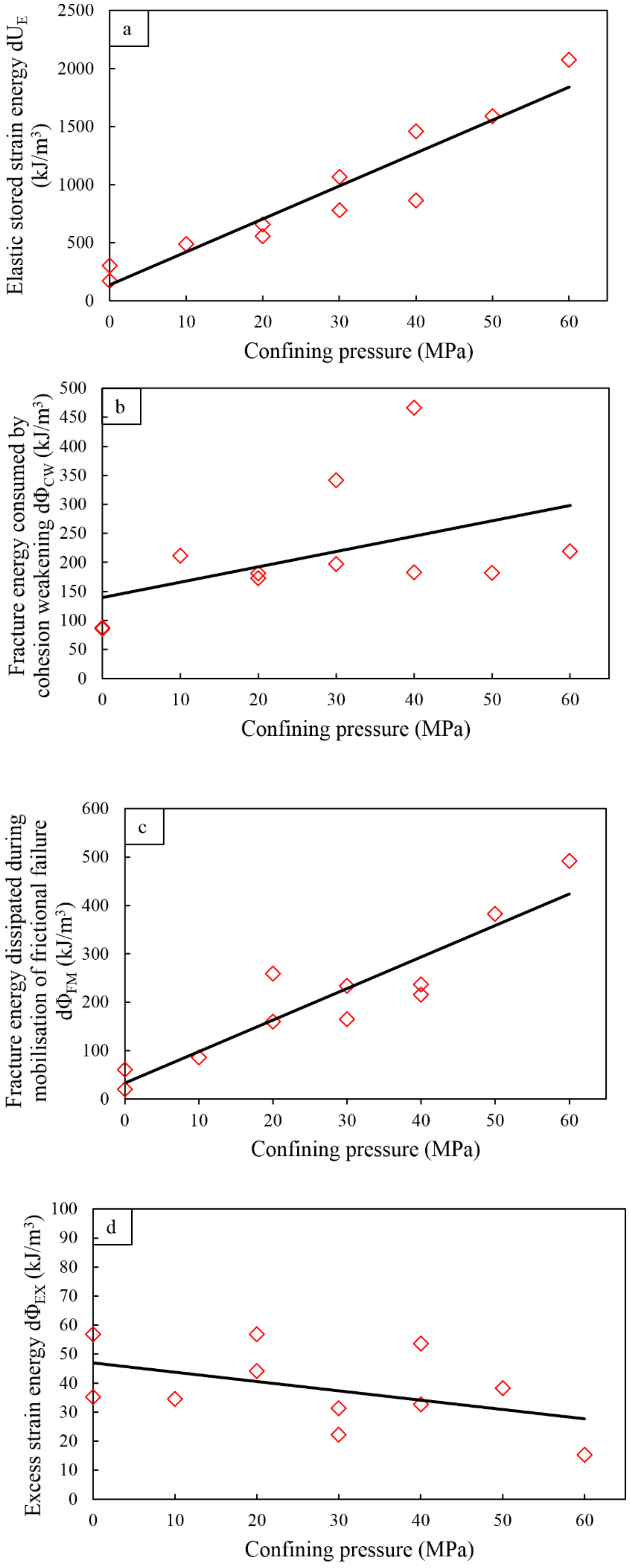
a
Elastic stored strain energy dU_E (kJ/m^3)
0
500
1000
1500
2000
2500
0
10
20
30
40
50
60
Confining pressure (MPa)
b
Fracture energy consumed by cohesion weakening $d\Phi_{CW}$ (kJ/m^3)
0
50
100
150
200
250
300
350
400
450
500
0
10
20
30
40
50
60
Confining pressure (MPa)
c
Fracture energy dissipated during mobilisation of frictional failure $d\Phi_{FM}$ (kJ/m^3)
0
100
200
300
400
500
600
0
10
20
30
40
50
60
Confining pressure (MPa)
d
Excess strain energy $d\Phi_{EX}$ (kJ/m^3)
0
10
20
30
40
50
60
70
80
90
100
0
10
20
30
40
50
60
Confining pressure (MPa)

Figure 3.11 Variations of (a) elastic stored strain energy (b) energy consumed by dominating cohesion weakening (c) energy dissipated during mobilisation of frictional sliding (d) excess strain energy

3.3.4 - Kinetic energy analysis for strain burst due to thermal damage

Another parameter to quantitatively express the potential intensity of a burst event is the ejection velocity of rock fragments (Akdag et al., 2018). The ejection velocity, denoted as v, refers to the velocity of rock fragments in a burst event, which is caused by the excess strain energy Φ_{EX} released during rock fragmentation. Assuming that the excess strain energy is completely converted to kinetic energy to eject the rock fragments, one can obtain the following expression for the ejection velocity:

$$v = \sqrt{\frac{2}{\rho}\Phi_{EX}} \tag{3.6}$$

where v is in m/s, Φ_{EX} in kJ/m^3 and ρ is the density of the rock in kg/m^3.

The influence of temperature on the potential ejection velocity of rock fragments of the granite specimens treated with various temperatures is depicted in Figure 3.12. It can be seen that the energy redistribution characteristics of Australian granite under uniaxial compression are strongly dependent on the pre-heating temperature. When the temperature increased from room temperature (25 °C) to 250 °C, potential rock ejection velocity decreased by 25% (see Figure 3.12).

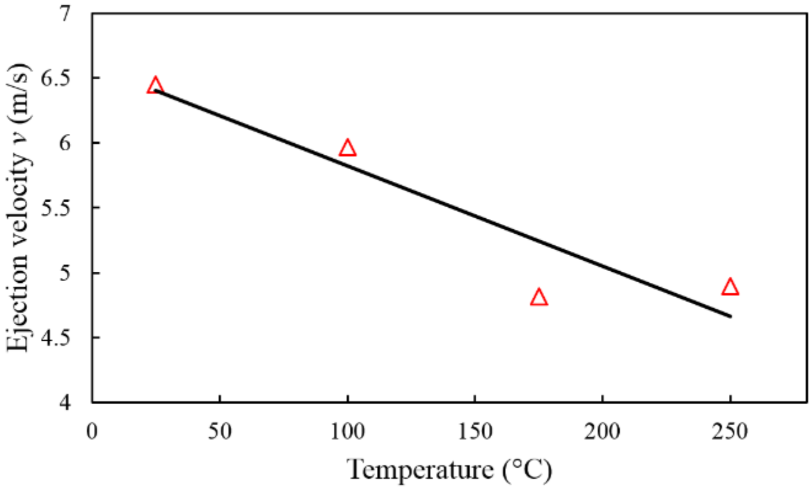

Figure 3.12 Potential rock fragment ejection velocity at different temperatures

The ejection velocity of the rock fragments showed a decline from 6.5 m/s to 4.8 m/s by gradual treatment at elevated temperatures. Due to the anisotropy in the thermodynamic properties of different rock minerals, the amount and width of the microcracks inside the specimen increased, and this triggered the rapid thermal damage accumulation and bursting. In other words, the fundamental reason for the decrease of peak stress and energy values is the thermally induced damage by microcracking. Thermally induced damage caused less elastic strain energy accumulation and hence the excess strain energy which is a measure for the intensity of the intrinsic strain burst in the rock decreased with increasing temperature. The findings of this weakening influence are in accordance with the previous studies (Zuo et al. 2014; Kumari et al. 2017b).

3.3.5 - Corresponding alterations in granite micro-structure

After the pre-heating treatment, the damage created by external forces was assessed by analysing the properties of the fracture. This analysis can help in to reveal the microscopic characteristics and fracture modes of rock. The SEM images of the fractured surface of the granite are shown in Figure 3.13. The SEM results indicated that microcracks are almost invisible at room temperature which is due to the weaker effect at lower temperatures. When the temperature was less than 100 °C, cracks mainly propagate along the boundary of mineral particles, i.e. intergranular fracture mechanism, as depicted in Figure 3.13. SEM images for the specimens exposed to temperatures of 100-250 °C showed coupled intergranular and transgranular, the formation of cracks within the mineral grain, thermally induced microfracturing was the primary mechanism triggering strain burst in the rock. Thermal influence gradually became more significant, and the fracture surface also became increasingly cluttered as the temperature increased, indicating that plastic deformation occurred.

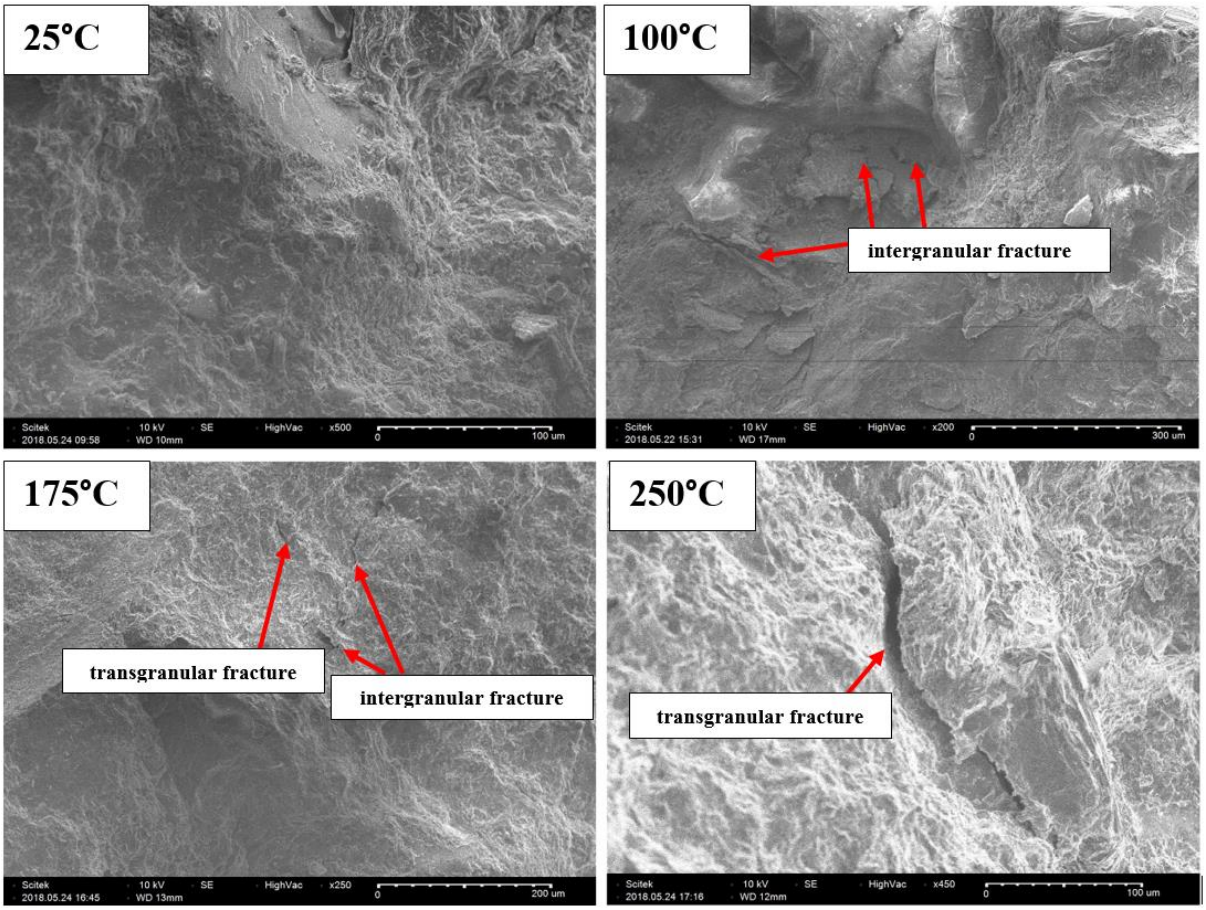

Figure 3.13 SEM images of granite specimen exposed to elevated temperatures

3.4 - Summary and discussion

In this chapter, the coupling influence of thermal damage and confining pressure on the energy characteristics and potential intensity for strain burst was investigated by conducting circumferential strain controlled tests on Australian granite. The energy evolution during strain burst of Class II rocks was analysed and the underlying mechanism was discussed. Based on the acoustic emission, stress and kinetic energy analyses carried out on granite samples exposed to various temperatures the following conclusions can be drawn:

1. An energy calculation method was developed based on the post-peak energy analysis. AE responses during compression tests were used to assess the energy and crack evolution characteristics of the granite under different confinement. Using AE characteristics,

fracture energy was split into two class: 1) energy consumed dominantly by gradual weakening of cohesive behaviour and 2) energy dissipated during the mobilisation of frictional failure. A portion of elastic energy, released from the Class II rock, was defined as excess strain energy which is a measure for the propensity of the intrinsic strain burst in the rock. It directly determines the ejection velocity of the rock fragments when a bursting event occurs. Therefore, this methodology can be used for quantitative predictions of bursting strain energy in the field which could facilitate improving the early warning efficiency and provides a comprehensive guideline for the mitigation methods to reduce strain burst intensity.

2. Confinement has significantly affected the post-peak energy redistribution characteristics and fracture mechanism of granite. The elastic stored strain energy, energy consumed by dominant cohesion weakening, and energy dissipated during mobilisation of frictional failure were 8.74, 2.53 respectively and 12.1 times the values at the unconfined condition, resulting in more severe strain burst indicating that increase in the confining pressure improved the efficiency of energy accumulation. This explains why the damage degree of deep granite is more prominent in the process of deep mining operations.

3. Temperature has significantly affected the post-peak energy redistribution characteristics and fracture mechanism of granite. The elastic stored strain energy, total fracture energy, excess strain energy diminished by 80, 82 and 43%, respectively when the temperature increased from room temperature to 250 °C. This declining trend was attributed to the development of micro-cracks that were induced by elevated temperatures. Thermally induced damage caused less strain energy accumulation and hence the excess strain energy decreased with increasing temperature. Another parameter to express the intensity of a burst event, ejection velocity, decreased as the gradual increase of temperature. The proposed energy-based strain burst propensity forecasting approach can provide an early warning of brittle rock instability, which is significant for strain burst assessment in deep mining operations.

4. The fracturing mechanism of granite was influenced by both confining pressure (excavation depth) and temperature. The dominant failure pattern of granite changed from multiple splitting failure to splitting-shear composite failure as the level of confinement

increased. When the temperature was less than 100 °C, granite samples experienced more induced intergranular thermal fracturing. Coupled fracture mechanism of intergranular and transgranular thermally induced cracking was the main fracture mechanism triggering strain burst when the temperature exceeded 100 °C.

Chapter 4: Quasi-static and dynamic fracture toughness tests: The influence of loading rate and thermal damage on strain burst

4.1 - Introduction

Rock masses are natural complex geological bodies which contain different scales of fractures, defects from microns to kilometres. Since these natural fractural structures play a vital role in the failure process and mechanical properties of rocks, rock fracture mechanics has been employed as a useful and practical tool to solve different rock engineering problems. It has been diversely applied to investigate brittle breakage and fracturing mechanism such as rockburst, strain burst, hydraulic fracturing in the broad area of tunnelling, rock cutting, underground excavation, rock slope stability, oil exploration and deep burial of nuclear waste. Thus, understanding the crack initiation and propagation in rocks is of great concern for engineering stability and safety.

As it was discussed in Chapter 3 and indicated that, strain burst is induced by the unstable growth and coalescence of micro-cracks to form macro-cracks. Based on the post-peak energy analysis conducted by Akdag et al. (2019), when the elastic stored strain energy in rock masses is larger than the dissipated fracture energy to grow micro-cracks, the excess strain energy will be transformed into the kinetic energy in the form of rock fragments at a certain speed, leading to strain burst. As an intrinsic property of rocks to resist crack initiation and propagation, the rock fracture toughness is the critical value of stress intensity factor (SIF) which is the most significant material property in fracture mechanics. Since brittle rock is relatively weaker in tension, the mode I (the tensile/opening mode) fracture is the most frequently encountered failure mode of rocks against fracture (Tutluoglu and Keles 2011; Funatsu et al. 2015; Wei et al. 2017a). As can be seen in Figure 4.1, the damage process is dominantly initiated by tensile fracturing in hard brittle rock mass in deep underground openings leading to strain burst (Diederichs et al. 2004). Therefore, extensive experimental and numerical studies were conducted on granite to determine the mode I fracture toughness (K_{IC}), which is known as the critical mode I stress intensity factor at the onset of fracture, in this study.

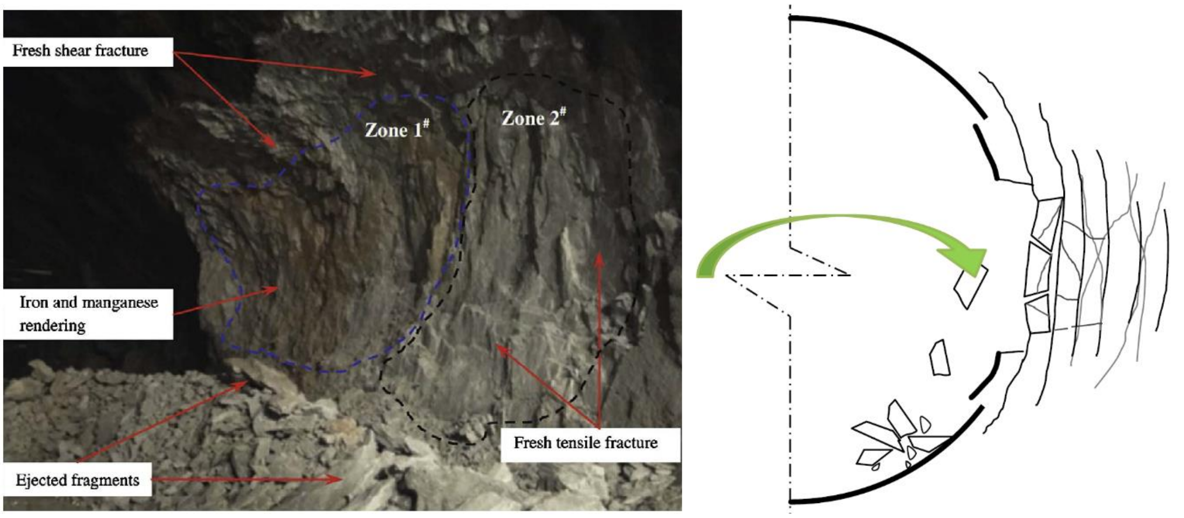

Figure 4.1 Schematic illustration of strain burst induced by tensile fracturing and an example of strain burst at the headrace tunnel at Jinping II hydropower station (Chen et al. 2015)

During underground mining operations, rock mass is highly subjected to dynamic disturbance caused by blasting, mechanical drilling and earthquakes resulting in dynamic fractures in the forms of strain burst, slabbing and spalling. The dynamic fracture is a significant manifestation of rock failure in deep underground engineering, and it is of great importance to assess the dynamic fracture behaviour of the rock mass under high-stress and high-temperature conditions. A good understanding of the dynamic behaviour of brittle rock under dynamic loading is required for the prediction of the damage extent during strain burst, and proper design as well as control of the underground rock structures. In this sense, dynamic fracture tests of pure mode I were carried out to reveal the fracture mechanism of granite specimens subjected to different loading rates using a Split Hopkinson Pressure Bar (SHPB) apparatus at Monash University. The damage evolution of granitic rocks was studied over a wide range of loading rates to reveal the rate dependency of strain burst.

Myriads of methods with different sample geometries have been proposed in the literature to measure K_{IC} of rocks under quasi-static loading conditions including short rod (SR) and chevron bend (CB) (Ouchterlony 1988), cracked straight-through Brazilian disc (CSTBD) (Ayatollahi and Akbardoost 2014; Wei et al. 2017b), cracked chevron notched Brazilian disc (CCNBD) (Fowell 1995; Wei et al. 2018), flattened Brazilian disc (Keles and Tutluoglu), straight-crack semi-circular bend (SCB) (Ayatollahi and Aliha; Dai et al. 2015), cracked chevron notched semi-circular bend (CCNSCB) (Kuruppu 1997; Ayatollahi et al. 2016; Wei et al. 2017). Among them, CCNSCB specimen which inherently combines the merits of both the SCB specimen and CCNBD specimen. This specimen configuration also overcomes major shortcomings by avoiding the fabrication of a sufficiently sharp crack as self-precracking from the chevron notch tip can inherently be induced during testing. Note that sufficient crack tip sharpness is needed for the straight-through cracked specimens to be able to accurately determine the fracture toughness and this process is tedious on hard rocks. Moreover, the CCNSCB method is more promising in determining the dynamic mode I fracture toughness (K_{Id}), of rocks as the dynamic force at the two loading ends of the specimen is easily balanced due its relatively shorter dimension in the loading direction compared with the full-disc (Dai et al. 2011). The halved disc geometry also circumvents the symmetrical crack propagation assumption of the CCNBD method. Therefore, due to the mentioned merits above, the CCNSCB method was chosen for determining the mode I fracture toughness (K_{IC}), and energy release rates of granite specimens and critical/minimum dimensionless SIFs (Y^*_{min}) of the CCNSCB granite specimens were determined using slice synthesis method (SSM).

In the underground rock engineering, rock masses not only suffer from dynamic loading but also are vulnerable to the effects of high temperatures. Such high-temperature conditions cause dramatic changes in the physical and mechanical properties of the surrounding rocks which are prone to strain burst. As a consequence, microstructure and mineral composition of rocks will be altered due to the thermally-induced cracking under the action of high temperatures which will directly influence the long-term safety and stability of underground rock structures. In recent years, a large number of researchers have investigated the effects of temperature on the mode I fracture toughness of various rocks under quasi-static and dynamic loading conditions (Mahanta et al. 2016; Feng et al. 2017; Liu and Xu 2013; Yin et al. 2018). Funatsu et al (2004) evaluated the static fracture toughness of single edge-notched round bar in bending (SENRBB) and SCB specimens of Kimachi sandstone and Tage tuff and showed that the fracture toughness decreased from room temperature to 75 °C due to the thermally-induced microcracks, and then increased from 75 °C to 200 °C which was attributed to the drying of the clay materials. Using SCB method, Yin et al. (2012) studied the effect of thermal treatment on the dynamic fracture toughness of Laurentian granite and concluded that fracture toughness increases with the loading rate, whereas decreases with the treatment temperature. Mahanta et al. (2016) measured the static mode I fracture toughness of SCB Indian sandstone specimens and revealed that fracture toughness increased between the room temperature and 100 °C, thereafter decreased from 100 °C to 600 °C. To our knowledge, there is not any attempt to investigate the influence of thermal damage on the mode I fracture toughness using CCNSCB method and energy-release rate in pure mode I.

The Chapter 4 is organised as follows. Section 2 presents the experimental methodology conducted. Section 3 discusses the rate dependence and influence of temperature on quasi-static fracture behaviour during strain burst in brittle rocks. Dynamic characteristics of strain burst in brittle rocks exposed to thermal damage are analysed in Section 4. Section 5 includes the summary and conclusion of the chapter.

4.2 - Experimental methodology

4.2.1 - The principles of cracked chevron notched semi-circular bend (CCNSCB) method

The detailed CCNSCB specimen geometrical configuration and the valid range of the geometric parameters including the specimen used in this study are schematically shown in Figure 4.2. This specimen geometry can be fabricated by notching a semi-circular bend specimen with a chevron notch or by cutting a CCNBD sample into two halves along the diametrical plane which is perpendicular to the chevron notch plane.

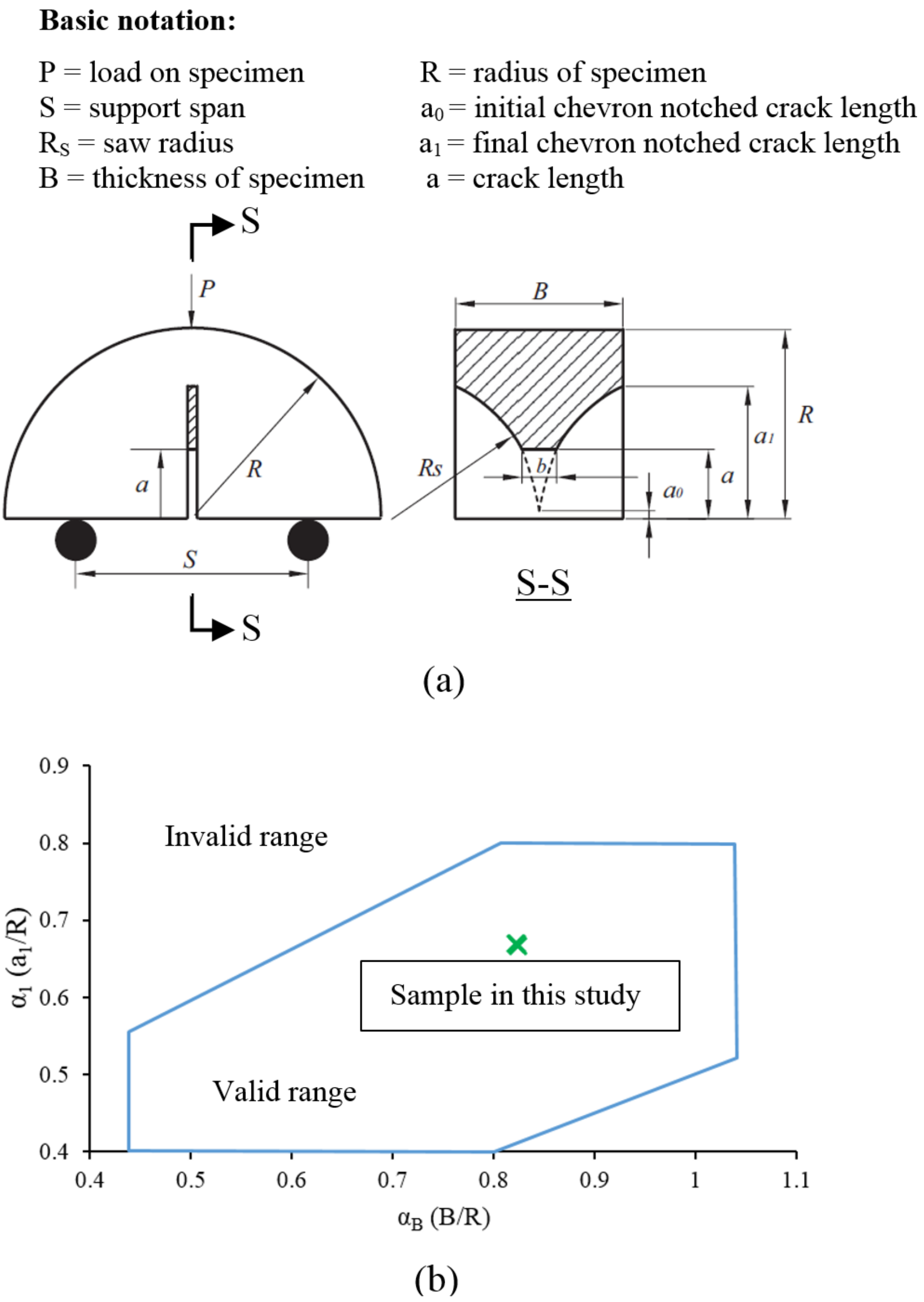

Figure 4.2 (a) Schematics of CCNSCB specimen configuration, (b) the valid geometrical range

R and B are the radius and thickness of the specimen; P is the compressional load which was applied at the central loading roller of the three-point bend loading device; α is the crack length;

a_0, a_m, and a_1 denote the initial, critical, and final crack length, respectively which are also used in their normalised (dimensionless) forms: thus, α_0 (=a_0/R), α_m (=a_m/R), and α_1 (=a_1/R) are the normalised (dimensionless) initial, critical, and final crack length; α_B (=B/R) is the normalised (dimensionless) specimen thickness; S is the span between two supporting rollers and β (=S/2R) is the ratio of the span to specimen diameter; and α_S (=R_S/R) is the normalised (dimensionless) radius of rotary saw. Note that the following dimensional restrictions should be satisfied to guarantee consistent testing results in the plain strain condition (Equation 4.1):

$$\begin{array}{ll} \alpha_1 \geq 0.4 & \alpha_1 \leq 0.8 \\ \alpha_1 \geq \alpha_B/2 & \alpha_B \geq 1.1729 \times \alpha_1{}^{1.6666} \\ \alpha_B \leq 1.04 & \alpha_B \geq 0.44 \end{array} \tag{4.1}$$

The typically experimental CCNSCB specimen and its normalised (dimensionless) geometrical parameters with the ISRM-suggested standards are given in Figure 4.3 and geometric parameters of the CCNSCB specimen used in this investigation are tabulated in table 4.1, respectively.

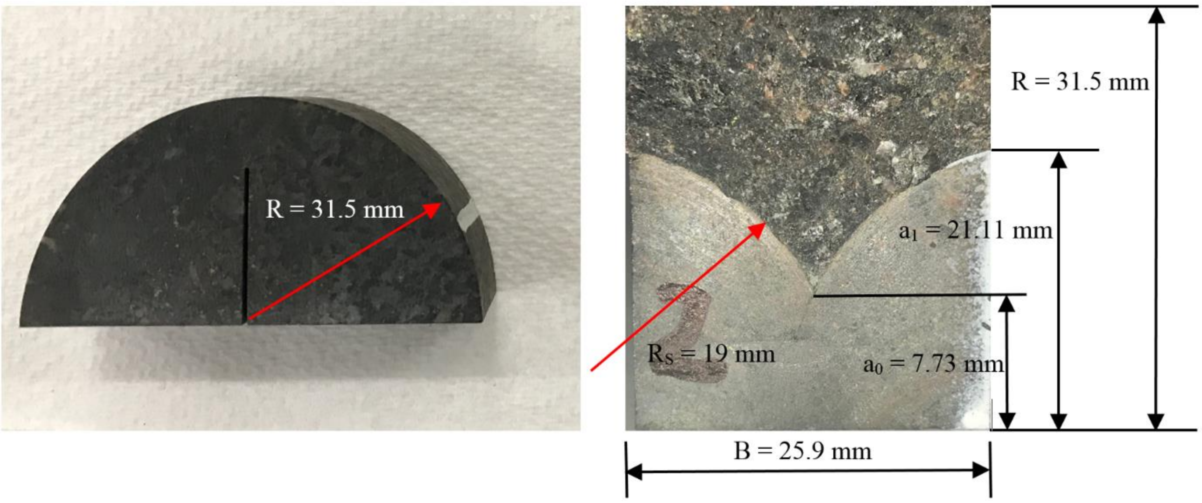

Figure 4.3 Demonstration of typical CCNSCB specimen used in this study

Table 4.1 Geometric parameters of the CCNSCB specimen used in this study

Description	Value (mm)	Dimensionless value
Radius, R	31.5	-
Thickness, B	25.9	$\alpha_B = B/R = 0.82$
Initial crack length, a_0	10.57	$\alpha_0 = a_0/R = 0.336$
Final crack length, a_1	21.11	$\alpha_1 = a_1/R = 0.67$

Saw radius, R_S	19	$\alpha_s = R_S/R = 0.603$
Supporting span, S	36.8-50	$\beta = S/D =$ 0.6-0.8

According to LEFM, the fracture toughness K_{IC} of CCNSCB specimen can be determined by using equation 4.2:

$$K_{IC} = \frac{P_{max}}{B\sqrt{R}} Y^*_{min} \tag{4.2}$$

in which K_{IC} denotes the mode I fracture toughness of rock material, P_{max} is the experimentally determined peak load, B and R the thickness and radius of CCNSCB specimen, respectively, and Y^*_{min} which is the most significant value of the rock material refers to the minimum value of the dimensionless stress intensity factor (SIF) of the CCNSCB specimen, which can be determined as in equation 4.3:

$$Y^*{}_{(CCNSCB)} = K_I / \frac{P}{B\sqrt{R}} \tag{4.3}$$

where K_I is the mode I SIF. Up to now, many analytical and finite element analyses have been used to determine Y^*which relies upon α_0, α_1, and α_B. In this study, an analytical method, i.e., slice synthesis method (SSM) was adopted to assess Y^*_{min} of the CCNSCB specimen.

Within the framework of LEFM, crack growth process can be considered in two stages: stable crack growth and unstable crack growth. In the stable crack growth stage, it is usually assumed that primary crack initiates from the tip of the chevron notched ligament (shaded area in Figure 4.1), and then propagates stably toward the apex of the semi-circular specimen with a perfect straight-through crack front, as illustrated in Figure 4.4a-c. In addition, crack grows along the centre of the notch width h, as shown in Figure 4.4. Subsequently, when the loading force reaches is peak value (P_{max}), unstable crack growth/propagation stage starts (point B in the figure. 4.4d). At this moment, the normalised (dimensionless) SIF $Y^*$is assumed to meet its minimum value of Y^*_{min} (point B in the Figure 4.4e) in which crack length is the critical crack length a_m. As can be seen in Figure 4.4e-d, the applied load and Y^* exhibit opposite trends during stable and unstable crack growth stages. The transition point between stable and unstable crack growth stages is critical for determining the fracture toughness (Equation 4.2).

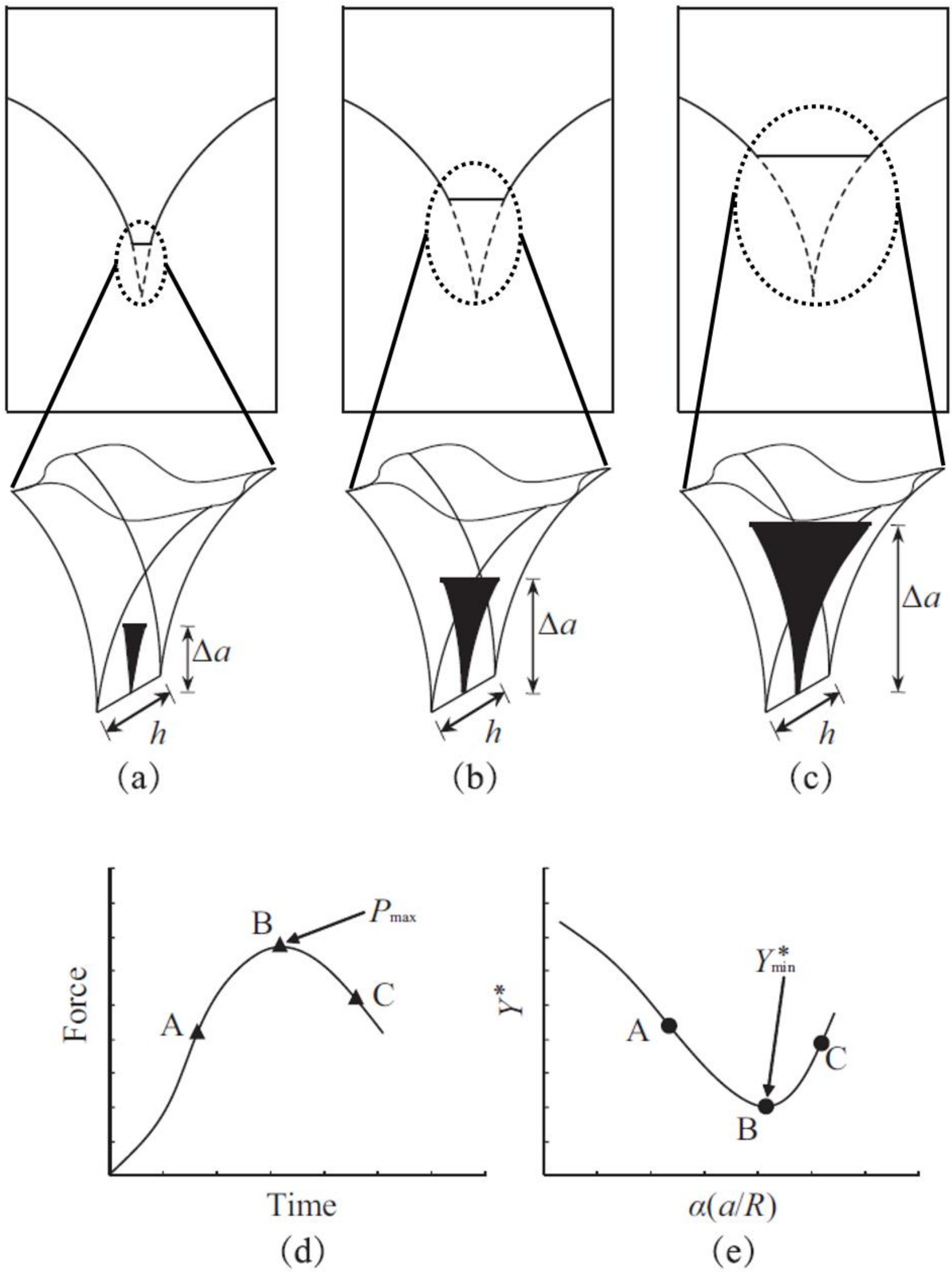

Figure 4.4. Schematics of the ideal postulation of the chevron notched ligament about fracture initiation and growth

4.2.2 - Specimen preparation and heating process

The fabrication procedure of the CCNSCB specimen is illustrated in Figure 4.5. First, the rock cores were sliced into circular discs with a thickness of 25.9 mm (Table 4.1), and both ends of the specimens were then carefully ground using a grinding machine to ensure perfectly smooth faces (Figure 4.5a). The polished discs were diametrically cut into two halves at the centre of the discs to form SCB specimens using a circular saw in which the discs were clamped with a holding apparatus to stay stable during sawing (Figure 4.5b-c). The surfaces of the SCB specimens were carefully polished to produce flat regular surfaces via a face grinder prior to notching (Figure 4.5d-e). A 3D-printed rig was designed and fabricated to hold the SCB specimens stable while notching (Figure 4.5f-g). For CCNSCB specimens, chevron notches of less than 1 mm were machined to the centre of each semi-circular half-disc in two cuts by moving a rotary diamond-impregnated saw (with a radii $R_S = 19$ mm and a thickness less than 1 mm) to meet the requirements of the permissible notch width in the ISRM suggested method (Kuruppu et al. 2014). First, the semi-circular half-disc was hold in a 3D-printed fixture and clamped, the rotary diamond-impregnated saw was located in the designed chevron notch plane and moved to touch the edge of the specimen surface. Then the saw was moved to the designed cutting depth h_c from one side along the axial direction of the CCNSCB specimen, as depicted in Figure 4.5g. Subsequently, the first cut was made by moving the rotating diamond-impregnated saw into the rock sample with a horizontal displacement. Finally, the second cut was made by following the similar procedure after aligning the saw in the first chevron notch plane, a desired CCNSCB specimen was thus prepared (Figure 4.5h). Special care was taken during grinding and notch preparation to avoid any damage to the CCNSCB specimens.

The granite specimens were divided into four groups based on temperature exposure. In the present study, the heating process of the rock samples was carried out in a high-temperature tube furnace in the Mining Engineering Research Laboratory at The University of Adelaide. Samples were first heated up to the target temperatures (25, 100, 175, and 250 °C) at a modest-constant heating rate of 5 °C/min to avoid the development of cracks due to the thermal shock during the heating process. Once the designated temperature was reached, the temperature remained constant at the pre-determined level for about 12 h, to ensure uniform heating inside the specimens. They were then allowed to cool down naturally to room temperature (25 °C) prior to mechanical testing.

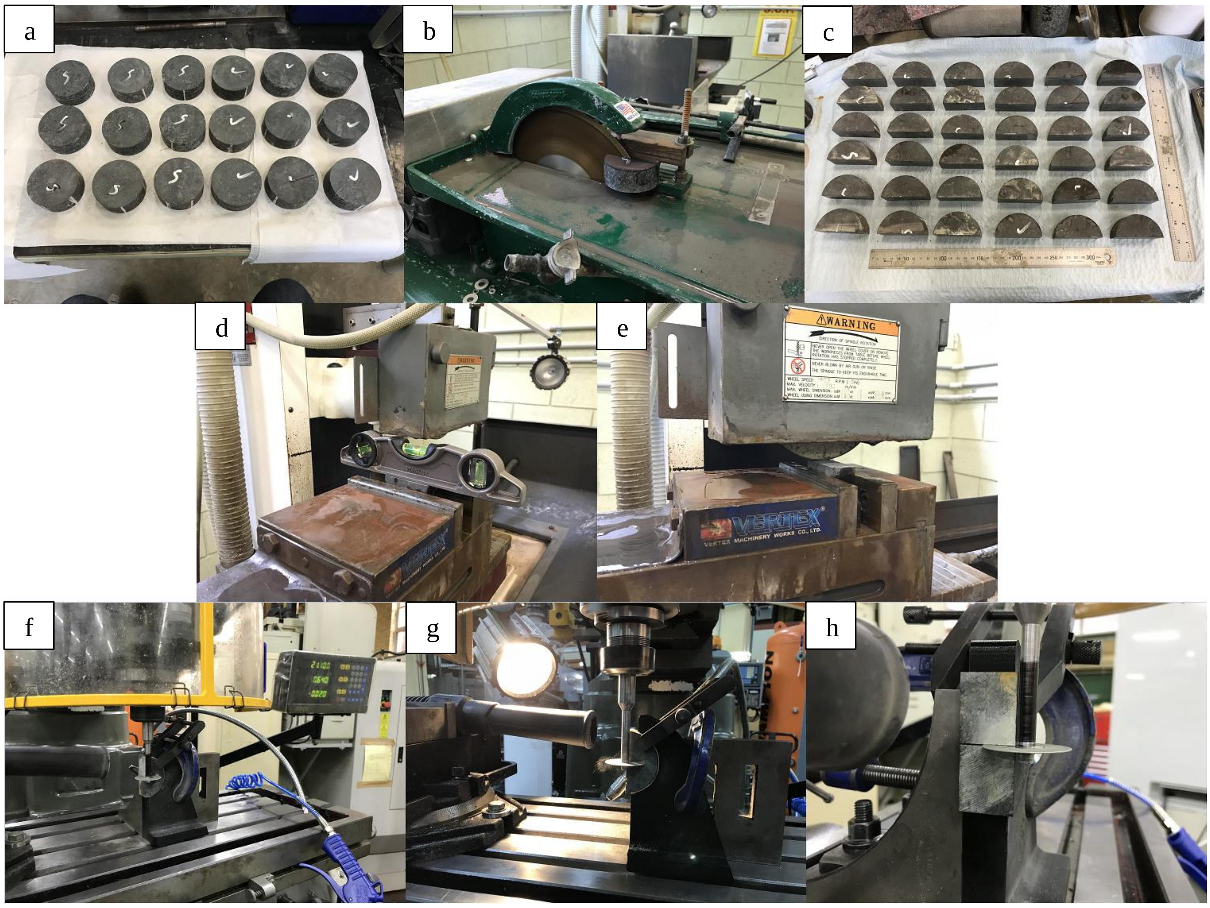

Figure 4.5 CCNSCB specimen preparation

4.2.3 - Determination of Y^* in CCNSCB using slice synthesis method (SSM)

To determine the minimum value of the dimensionless stress intensity factor (SIF) Y^*_{min} of the CCNSCB specimen, a semi-analytical slice synthesis method (SSM) was proposed first by Bluhm (1975) to evaluate the fracture problems with curved crack fronts was used in this study. When using this method, the thickness of the specimen is initially divided into a number of slices each having a thickness Δt as shown in Figure 4.6. Each slice is considered as a cracked straight-through (CST) specimen to simplify the complex configuration of chevron notched specimens for the analysis. Based on the equilibrium principle, an analytical equation for the entire specimen can be obtained by combining the equations for each slice which enables researchers to be able to extract appropriate analytical relations for the specimens with complex configuration. In this method, the compliance function which is used for measuring SIF is the most important output. Since it is tedious to obtain the compliance function in a geometrically complicated specimens, i.e. CCNBD or CCNSCB, a new SSM was proposed by Wang et al. (2004) as a constant term attributed to the corresponding part of the specimen without crack was ignored for determining SIF of CCNBD specimen in Bluhm's study (Bluhm 1975). In this new procedure the output is directly related to the SIF, not the compliance, which has a better accuracy for a wide-range of geometric parameters of CCNBD specimen with slight corrections of an empirical factor.The same procedure was used for CCNSCB specimen.

At first, CCNSCB specimen, as depicted in Figure 4.6, was divided into many slices along its thickness. Each slice could be considered as a SCB with straight-though crack with thickness, Δt. In fact, there is no need to divide the central part of CCNSCB specimen with the straight crack front thickness b into thin slices since it is itself can be considered as a SCB specimen with a straight crack front of width b.

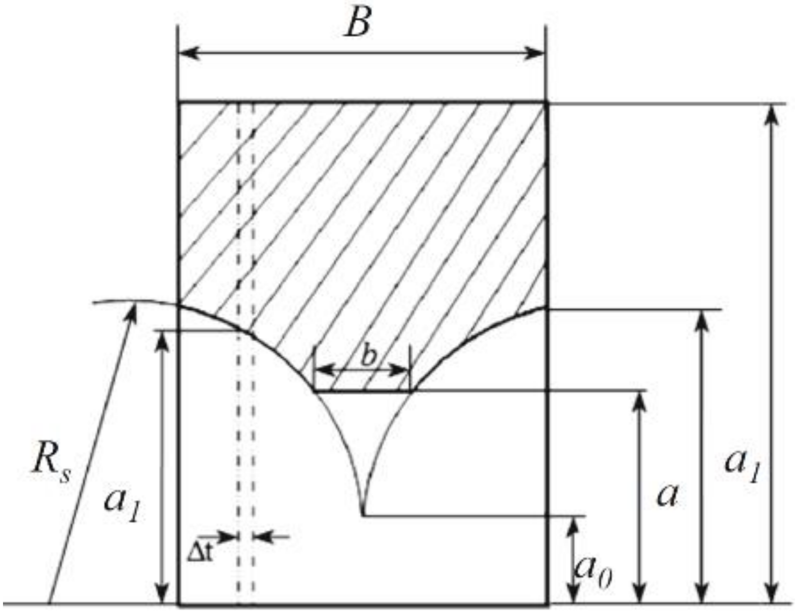

Figure 4.6 Slice synthesis method for CCNSCB specimen

Note that Equation 4.2 has been suggested for a crack, whereas, as can be seen in Figure 4.6, only the central part of the specimen that is formed due to the crack growth is a real crack, thus, the SIF of the central part is considered as K_I. However, the SIFs of two lateral chevron parts which are not real cracks have lower value than K_I. Therefore, a reduction factor for the slices other than the central part can be employed as:

$$K_I' = \begin{cases} K_I & \text{central part} \\ K_I/\beta & \text{other sides} \end{cases} \tag{4.4}$$

in which β is an empirical factor that has a value of always greater than one and depends on the chevron geometry.

It should be noted that the normalised (dimensionless) SIF Y_I was derived from Equation 4.2. Since each slice is considered as straight-through cracked specimen in SSM method, to calculate Y_I of CSTSCB specimen Equations 4.5 and 4.6 were used (Kuruppu et al. 2014):

$$\begin{aligned} Y_I = &\left(0.4122 + 5.06355\left(\frac{S}{R}\right)\right) + \left(-16.65 + 3.319\left(\frac{S}{R}\right)\right)\alpha + \left(52.939 + 76.910\left(\frac{S}{R}\right)\right)\alpha^2 \\ &+ \left(-67.027 - 257.726\left(\frac{S}{R}\right)\right)\alpha^3 + (29.247 + 252.8\left(\frac{S}{R}\right))\alpha^4 \end{aligned} \tag{4.5}$$

As can be seen in Equation 4.5, Y_I has a linear relationship with S/R and is of fourth degree or quadric function in terms of α. Equation 4.6 which is a quadratic equation in terms of α ($0.2 \leq \alpha \leq 0.6$) was also used to calculate the normalised (dimensionless) minimum of Y_I.

$$Y_{I_{alt}} = -1.297 + 9.516\left(\frac{S}{R}\right) + \left(-0.47 - 16.457\left(\frac{S}{R}\right)\right)\alpha + (1.071 + 34.401\left(\frac{S}{R}\right))\alpha^2 \tag{4.6}$$

Using equations 4.2 and 4.4 and summing up the loads applied on each slice, the total load can be calculated as:

$$P = \frac{K_I 2Rb}{\sqrt{\pi a} Y_I(\alpha)} + \sum_{i=1}^{N} \frac{K_I(2R\Delta t)}{\beta\sqrt{\pi a} Y_I(\alpha_i)} \tag{4.7}$$

where Δt and N are the thickness of each slice and the number of slices, respectively. Y_I is the normalised (dimensionless) SIF of the CSTSCB and α_i= a_i/R, where a_i is the crack length of the *i*th slice. The first term in Equation 4.7 is associated with the central part of the specimen with normalised (dimensionless) crack length α and the crack width b, and the second term is related to the lateral slices with different normalised (dimensionless) crack lengths α_i.

The thickness of the central part can be calculated as shown in Equation 4.8:

$$b = 2R\left(\sqrt{\alpha_S^2 - \alpha_0^2} - \sqrt{\alpha_S^2 - \alpha^2}\right) \tag{4.8}$$

The thickness, Δt and the normalised (dimensionless) crack length $\alpha_i$of each slice can also be calculated as below:

$$\left[\begin{array}{l} \Delta t = \dfrac{B-b}{N} \\ \alpha_i = \sqrt{\alpha_s^2 - \left(\sqrt{\alpha_s^2 - \alpha_0^2} - \dfrac{b}{2R} - \dfrac{i.\Delta t}{R}\right)^2} \end{array}\right. \tag{4.9}$$

in which i is the slice number from the centre of the specimens apart of the central part having the flat notch.

The normalised (dimensionless) SIF of CCNSCB specimen can be calculated by substituting Equation 4.7 into Equation 4.3 as follows:

$$Y^* = \left[\frac{2b/B}{\sqrt{\pi A} Y_I(\alpha)} + \sum_{i=1}^{N/2} \frac{4\Delta t/B}{\beta\sqrt{\pi\alpha_i} Y_I(\alpha_i)}\right]^{-1} \tag{4.10}$$

The empirical factor β, reflecting the difference between the SIF of central part and the lateral parts of the CCNSCB specimen, can be determined as in Equation 4.11:

$$\beta = 1 + \gamma \frac{\alpha_1 - \alpha}{\alpha_B} \tag{4.11}$$

Calculation of the empirical reduction factor β that is one of the most significant and difficult part of the SSM method, was employed by three-dimensional finite element (FE) analysis and the coefficient γ in Equation 4.11 was predicted as 0.9 for the CCNSCB specimen (Wang et al. 2004).

Based on the FE analysis results, the obtained value of Y^*_{min} is not sufficient, and thereby a new form of Equation 11 was proposed to predict the coefficient β as follows (Ayatollahi et al. 2016):

$$\beta = 1 + \gamma \left(\frac{\alpha_1 - \alpha}{\alpha_B}\right)^n \tag{4.12}$$

Comparing the results from three-dimensional FE analysis and SSM for the CCNSCB specimen in mode I loading, the coefficient γ and the power n were predicted as 0.9 and 0.5, respectively (Ayatollahi et al. 2016). The minimum value of Equation 4.10 was obtained by putting its derivative with respect to the normalised (dimensionless) crack length α equal to zero as the mode I fracture toughness can be calculated using the minimum value of the SIF. Therefore, one can obtain the normalised (dimensionless) SIF and corresponding critical value of the normalised (dimensionless) crack length α by utilising SSM for CCNSCB specimen. In this study, for the CCNSCB specimen; $\alpha_0 = 0.245, \alpha_1 = 0.67, \alpha_S = 0.6, \alpha_B = 0.8,\ and\ S/D = 0.8$, the minimum SIF and critical value of normalised (dimensionless) crack length were obtained as $Y^*_{min} = 5.00144\ at\ \alpha_m = 0.512$ (Figure 4.7). It can be seen in Figure 4.7, the SIF for CCNSCB specimen initially decreases and subsequently increases as crack grows. It can be stated that due to the high stress concentration at the tip of the chevron notch, crack growth can be observed, and then, it propagates stably within the trajectory of chevron notch until the crack length meets its critical value, i.e., $\alpha \leq \alpha_m$. Following the decreasing trend of the force, unstable crack growth occurs rapidly and the final failure takes place in the specimen. In this specimen geometry configuration, the chevron notch that is efficient for stabilising the crack growth, allows to develop higher accuracy SIFs. In this sense, CCNSCB method is suitable for determining the fracture toughness and investigating the mechanism of crack growth postulation of rock masses and brittle materials.

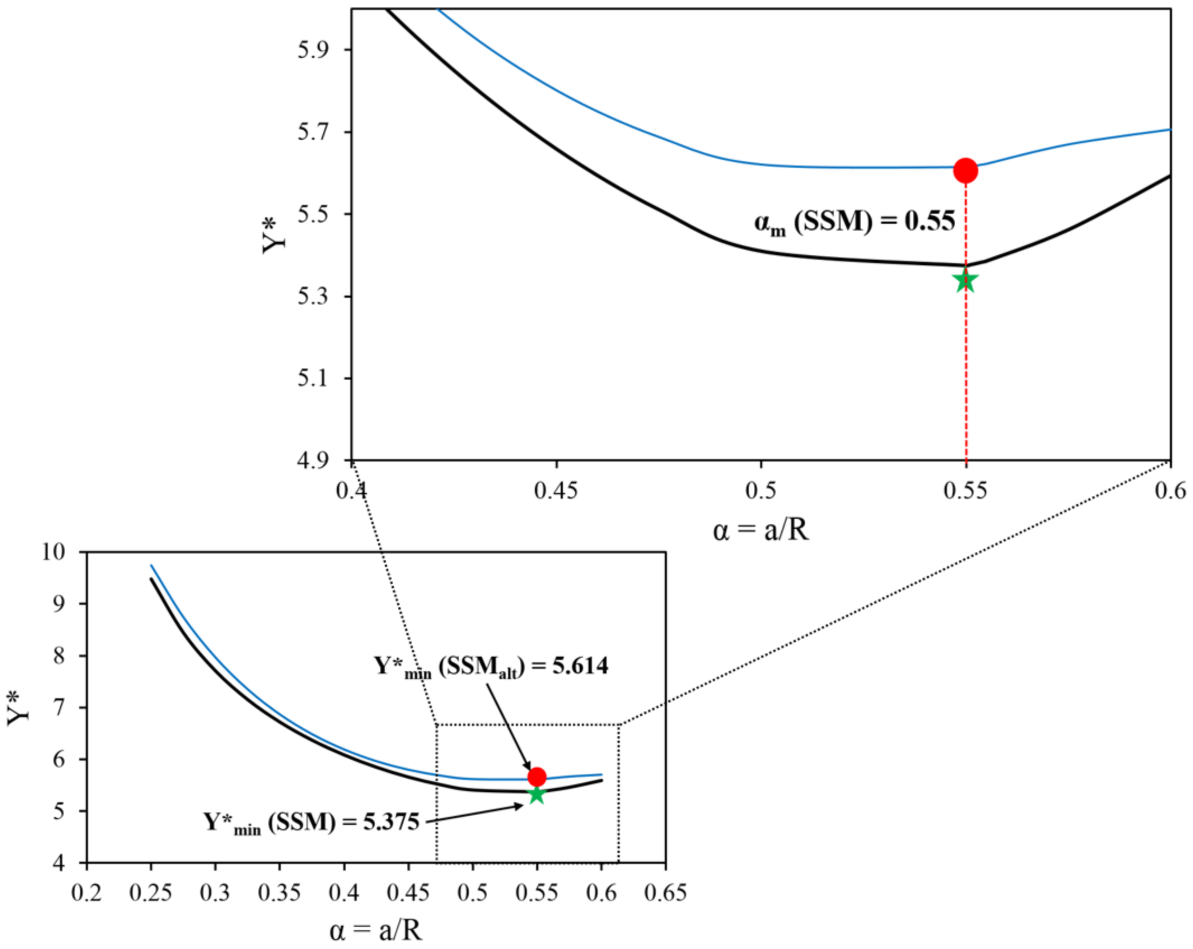

Figure 4.7 Mode-I dimensionless stress intensity factor of CCNSCB determined by SSM method

In table 4.2, the discrepancies of Y^*_{min} and α_m by two different methods are presented. As can be seen from the table, the results obtained from both methods are closely related with a small discrepancy of 5%. Therefore, it can be concluded that these methods are capable of assessing the process of crack growth in CCNSCB specimen.

Table 4.2 The values of Y^*_{min} and α_m for the CCNSCB specimen obtained from Equations 4.5 and 4.6

SSM	Y^*_{min}	α_m
Equation 4.5	5.375	0.55
Equation 4.6	5.614	0.55
% Discrepancy	4.4	-

4.3 - Influence of the loading rate and the temperature on quasi-static fracture behaviour during strain burst in brittle rocks

4.3.1 - Experimental setup

A hydraulic servo-controlled MTS Criterion^{TM} Model 45 with a load-applying capacity of 300 kN was used to conduct the quasi-static loading experiments on the pre-heated and cooled CCNSCB granite specimens. The specimens were placed on the loading platform such that the span ratio S/R was 0.8 and make the pre-chevron cracking in the middle of the specimen coincide with the centreline of the loading roller to provide mode I loading conditions and then loaded under a three-point bending load configuration until failure. A constant displacement-controlled testing manner was adopted for the compressive load on the specimens and the load-displacement data was recorded by a data-acquisition system. During the tests, crack-opening displacement (COD) was measured by a strain gauge with a length of 10 mm, which was mounted in CCNSCB specimen and the crack mouth displacement was continually recorded. Figure 4.8 shows the loading configuration and the experimental setup for the mode I CCNSCB tests. The compression load on the specimen was applied in displacement control in which the displacement rate was varied in the range of 0.02 mm/min to 0.1 mm/min.

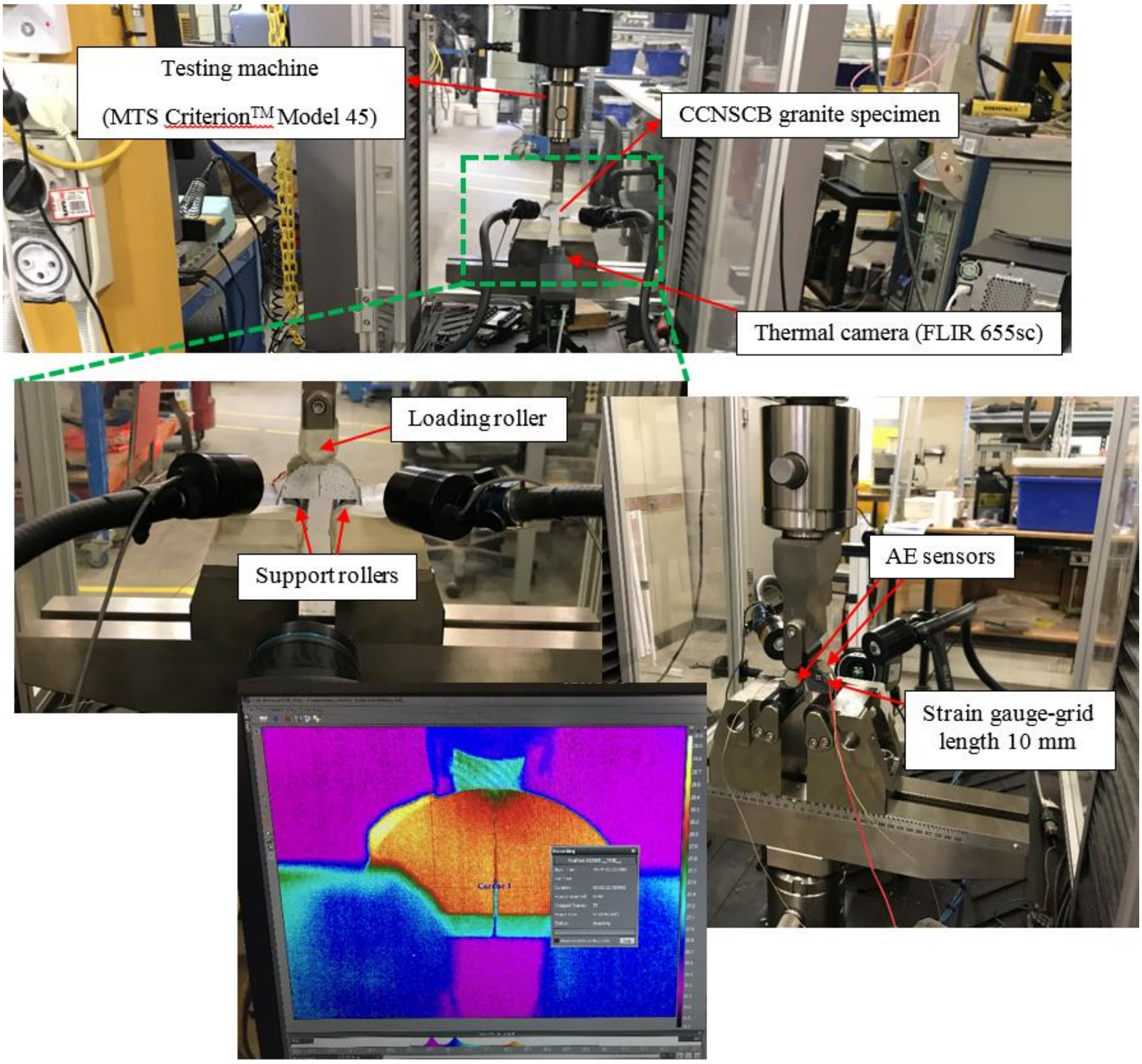

Figure 4.8 Experimental setup: Loading configuration and rock instrumentation of the mode I CCNSCB tests in the MTS machine

4.3.2 - Determination of energy-release rate

As proposed by Griffith (1921), the strain energy release rate is a measure of the energy that is dissipated per unit increase in an area during crack growth and is represented by G.

According to Westergaard's approach (1939), the displacement field in the vicinity of the crack tip for plane stress condition in the direction of maximum tension can be obtained using Equation 4.13 as shown below:

$$u_2 = \frac{K_I}{\mu}\sqrt{\left(\frac{r}{2\pi}\right)}\, sin\frac{\theta}{2}\left(\frac{2}{(1+v)} - cos^2\frac{\theta}{2}\right) \tag{4.13}$$

where r, θ are polar coordinates of the point.

Considering a crack of initial length a, with the application of load the cracks starts to propagate and the initial crack length is extended by an incremental length of Δa (see Figure 4.9). The new crack length is $a' = a + \Delta a$ and the stress intensity factor for the new crack length is $K'(K' = K + \Delta K)$. At a distance x from the previous crack tip, that is at a distance $\Delta a - x$ from the extended crack tip, the displacement of a crack face in the direction of the maximum tension for $\theta = 180°$ is given in Equation 4.14:

$$u_2(x) = \frac{K_I'}{\mu}\sqrt{\left(\frac{\Delta a - x}{2\pi}\right)}\frac{2}{1+v} \tag{4.14}$$

Each crack face in the portion of Δa has moved a distance of $u_2(x)$ due to the influence of the normal stress, σ_{22} equal to:

$$\sigma_{22}(x) = \frac{K_I}{\sqrt{2\pi x}} \tag{4.15}$$

According to Irwin (1957), the total elastic work required by σ_{22} to close the crack is equal to the energy released.

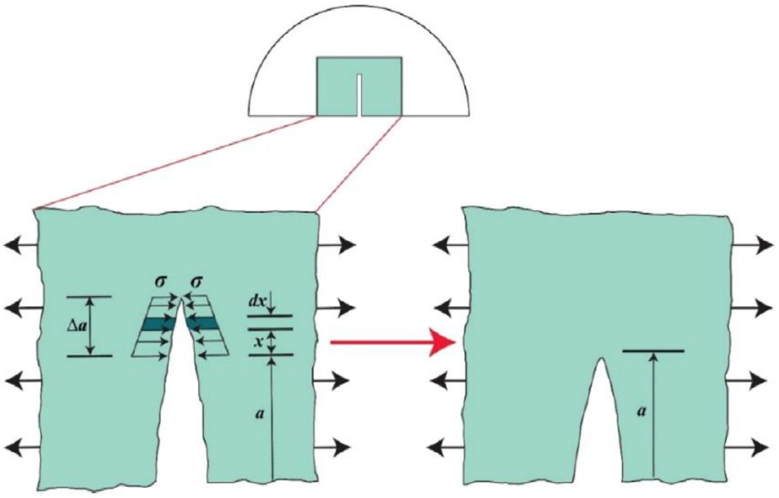

Figure 4.9. Closure of the crack to find the relation between G_I and K_I (Mahanta et al. 2017)

$$G_I B \Delta a = 2\int_0^{\Delta a} \frac{B\sigma_{22}u_{22}}{2}dx \tag{4.16}$$

where B is the thickness of the specimen. By taking the limit $\Delta a \rightarrow 0$:

$$G_I = \lim_{\Delta a \to 0} \frac{2}{(1+v)\mu \Delta a} \int_0^{\Delta a} \frac{K_I}{\sqrt{2\pi x}} \frac{K_I' \sqrt{(\Delta a - x)}}{\sqrt{2\pi}} dx \tag{4.17}$$

Δa can be very small, such that $\Delta K'$ can be made small enough in comparison to K_I, and as a result of which $\Delta K'$ can be neglected.

$$G_I = \lim_{\Delta a \to 0} \frac{K_I^2}{(1+v)\mu \Delta a} \int_0^{\Delta a} \frac{\sqrt{\Delta a - x}}{x} dx \tag{4.18}$$

In order to solve the integral, putting $x = \Delta a sin^2 \alpha$. When $x = 0$ and $\alpha = 0$ and when $x = \Delta a, \alpha = \frac{\pi}{2}$ $and\ dx = \Delta a\ 2sin\alpha\ cos\alpha\ d\alpha$

$$G_I = \lim_{\Delta a \to 0} \frac{K_I^2}{(1+v)\pi\mu \Delta a} \int_0^{\pi/2} \sqrt{\frac{(\Delta a - \Delta a sin^2 a)}{\Delta a sin^2 a}} \Delta a 2 \mathrm{sin} a cosada$$

$$\begin{aligned} G_I &= \frac{K_I^2 \Delta a}{(1+v)\pi\mu \Delta a} \int_0^{\pi/2} 2cos^2 ada \\ G_I &= \frac{K_I^2}{(1+v)\pi\mu} \int_0^{\pi/2} 2cos^2 ada \\ G_I &= \frac{K_I^2}{(1+v)\pi\mu} \frac{\pi}{2} \end{aligned} \tag{4.19}$$

$$G_I = \frac{K_I^2 2(1+v)}{(1+v)\pi E} \frac{\pi}{2} \tag{4.20}$$

$$G_I = \frac{K_I^2}{E} \tag{4.21}$$

4.3.3 - Quasi-static mode I fracture toughness test results

The load-displacement curves of granite which represent the rock characteristics were directly obtained from SCB fracture toughness tests. Figure 4.10 shows the typical load-displacement curves of Australian granite with different loading rates at various temperatures obtained in this study. After the elastic stage, the rock suddenly broke in a typical brittle failure. Each load-displacement curve exhibits a slowly increasing portion until a peak followed by a dramatically falling post-failure portion indicating a brittle fracture. The turning point at the peak force in Figure 4.10 denotes the stable-unstable fracture transition of the specimen. Figure 4.11 illustrates typical failed specimens for each temperature group and fracture surface of a recovered specimen. The specimens were completely split into two roughly identical halves by a damage zone enclosing the main crack along the notch.

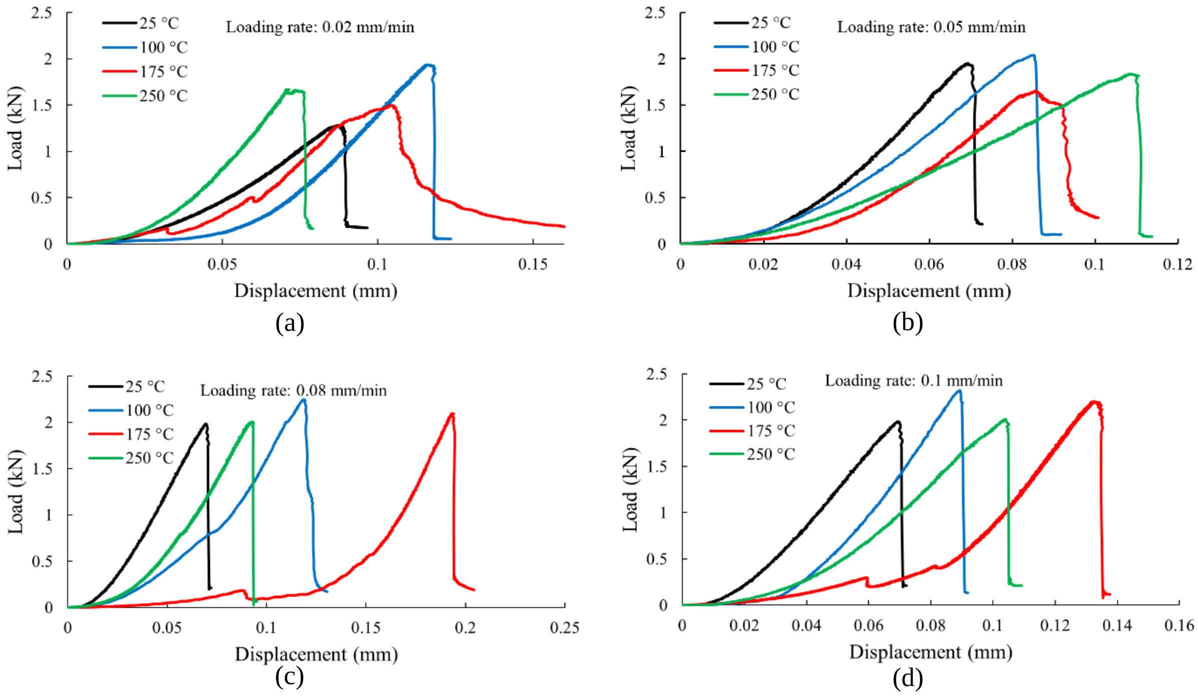

(a) (b)

(c) (d)

Figure 4.10 Load-displacement curves of granite under different loading rates and temperatures

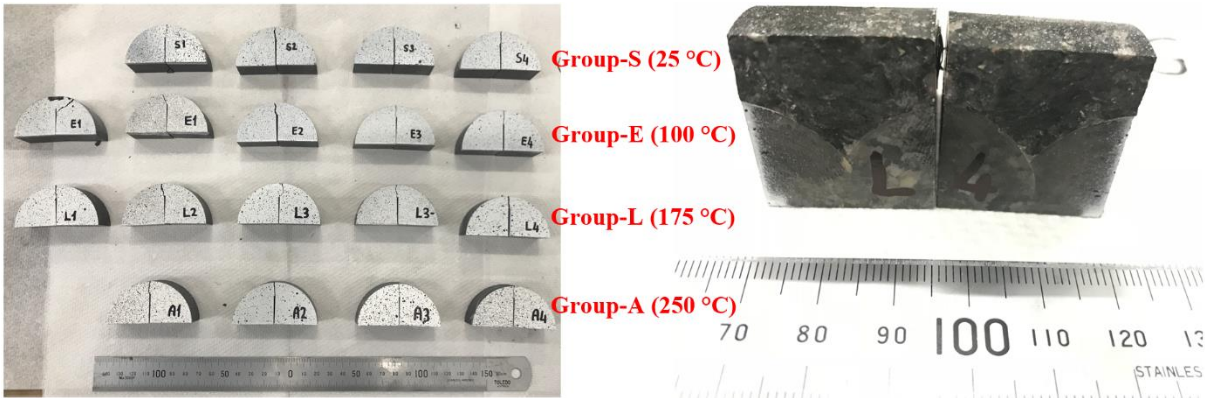

Figure 4.11 Typical CCNSCB granite specimens after mode I fracture toughness tests under quasi-static loading conditions

4.3.4 - The effects of temperature and strain rate on quasi-static mode I fracture toughness and energy-release rate of granite

The details of the geometric parameters of all the tested samples in this research which satisfy ISRM-proposed restrictions for valid tests are listed in Table 4.3. The

Y_{min}^{*} values of the CCNSCB specimens were determined in previous calculations as well as based on the work by Wei et al. (2017a).

Table 4.3 Geometric dimensions of the CCNSCB specimens

Temperature (°C)	**Loading rate (mm/min)**	**Specimen no**	**R (mm)**	**B (mm)**	**a_0 (mm)**	**a_1 (mm)**	α_0	α_1	α_B	Y^*_{min}
RT (25)	0.02	S1	30.87	25.97	10.33	20.2	0.335	0.654	0.8	6.0922
	0.05	S2	30.83	25.93	10.75	20.39	0.349	0.661	0.8	6.2755
	0.08	S3	30.83	25.92	10.56	20.52	0.343	0.666	0.8	6.3118
	0.1	S4	30.93	25.91	10.59	20.43	0.342	0.661	0.8	6.2336
100	0.02	E1	30.82	25.93	11.19	20.71	0.363	0.672	0.8	6.5321
	0.05	E2	31.16	25.91	10.77	20.47	0.346	0.657	0.8	6.1994
	0.08	E3	30.76	25.9	10.46	20.38	0.340	0.663	0.8	6.2502
	0.1	E4	30.87	25.91	10.83	20.6	0.351	0.667	0.8	6.3763
175	0.02	L1	30.96	25.9	10.17	20.09	0.328	0.649	0.8	5.9826
	0.05	L2	30.94	25.94	10.73	20.44	0.347	0.661	0.8	6.2635
	0.08	L3	30.86	25.9	10.65	20.32	0.345	0.658	0.8	6.2079
	0.1	L4	30.91	25.91	10.34	20.52	0.335	0.664	0.8	6.2342
250	0.02	A1	30.98	26.11	10.47	20.34	0.338	0.657	0.8	6.1524
	0.05	A2	30.59	25.93	10.94	20.62	0.358	0.674	0.8	6.5277
	0.08	A3	30.84	25.95	11.1	20.81	0.360	0.675	0.8	6.5566
	0.1	A4	30.96	26.04	10.86	20.81	0.351	0.672	0.8	6.4499

Table 4.4 summarises the failure loads and the corresponding fracture toughness values for all sets of the specimens at different temperatures and loading rates. More detailed results of the fracture toughness are depicted in Figure 4.12a. The relation between the mode I quasi-static fracture toughness, loading rate and temperature for CCNSCB specimens treated at various temperatures and under different loading rates is depicted in Figure 4.12b. It can be seen from Figure 4.12 that the quasi-static mode I fracture toughness and energy-release rate (given by Equation 4.21) at the same heat-treatment temperature increased linearly with the loading rate. As in the case with increasing loading rate, the load required to fail the specimen increased which resulted in a rising trend of the fracture toughness of the rock as they are dependent on each other. The cracks which were mostly formed by intergranular fractures under low loading rates caused rougher fracture surfaces, when compared to that of the samples failed under high loading rates. However, transgranular fractures became dominant which consumed more energy than intergranular fractures and resulted in more straight fracture path and less rough fracture surface at high loading rates as supported by Zhang and Zhao (2013). Due to the increased number of activated micro-cracks at high loading rates and that absorbed more energy when compared to a single macro crack, resulting in an increase in the fracture energy as parallel to the findings by Dai and Xia (2013).

Table 4.4 Summary of the failure loads and the fracture toughness results and their average with standard deviations

Temperature (°C)	**Loading rate (mm/min)**	**P_{max} (kN)**	**Average of P_{max} (kN)**	**K_{IC} (MPa·m$^{0.5}$)**	**Average of K_{IC} (MPa·m$^{0.5}$)**
RT (25)	0.02	1.28	1.93±0.49	1.70	2.56±0.65
	0.05	1.95		2.59	
	0.08	1.98		2.63	
	0.1	2.49		3.30	
100	0.02	1.94	2.14±0.18	2.57	2.84±0.24
	0.05	2.04		2.69	
	0.08	2.25		2.99	
	0.1	2.32		3.08	
175	0.02	1.50	1.88±0.34	1.99	2.49±0.45
	0.05	1.65		2.19	
	0.08	2.10		2.79	

	0.1	2.20		2.92	
250	0.02	1.67	1.88±0.16	2.20	2.49±0.21
	0.05	1.84		2.45	
	0.08	2.01		2.66	
	0.1	2.01		2.65	

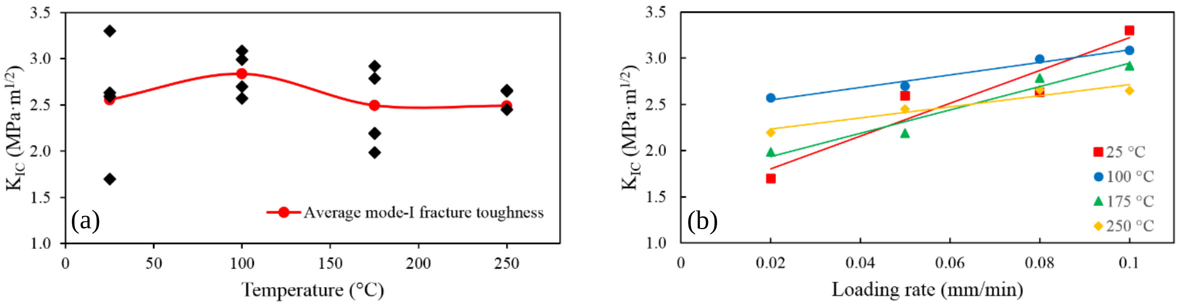

Figure 4.12 (a) Pure mode-I fracture toughness variation with temperature (b) relationship of mode-I fracture toughness with loading rate under different temperatures

In addition, the quasi-static mode I fracture toughness and energy-release rate of pre-heated Australian granite are dependent on temperature as depicted in Figure 4.12. Under the same loading rate, K_{IC} and G_I of granite presented a decreasing trend by a total of approximately 17% and 30%, respectively with ascending temperature from ambient temperature (25 °C) to 250 °C. The fundamental reason for the decrease of fracture toughness is micro-cracks induced by thermal damage resulting in degradation of the tensile stress resistance which indicates that the rock's ability to resist fracture deteriorated with increasing temperature. These results were interpreted with the support of microscopic observations of the micro-cracks within the specimens along with the help of SEM analysis (see Figure 3.13 in Chapter 3.3.5). This is also in accordance with the findings of Yin et al. (2012), Mahanta et al. (2016) and Feng et al. (2017). Therefore, it is shown that both the loading rate and temperature have significant influence on the quasi-static mode I fracture toughness and energy-release rate of granite in this study. These findings of this investigation will be useful for better understanding of the strain burst mechanism such as application of a combination of favourable measures for thermal damage and loading rate during deep excavations over 1000 m.

4.4 - Dynamic characteristics of strain burst in brittle rocks exposed to thermal effect

Rock fracture in explosion, excavation and strain burst tends to occur at high loading rates of about 104-106 MPa·m$^{1/2}$/s (Zhang and Zhao 2014), which is close to the loading rates in SHPB tests. Hence, the SHPB apparatus is suitable for investigating the dynamic responses in rock during strain burst. To explore the topic of coupled influence of thermal damage and loading rate on the dynamic fracture properties and behaviour of Australian granite during strain burst, a series of dynamic fracture toughness tests was conducted on thermally-treated CCNSCB specimens over a wide range of loading rates by the SHPB setup. The dynamic mechanical behaviour of granite after high-temperature treatment under different loading rates was examined and discussed. The dynamic stress intensity factor (SIF) of the CCNSCB specimen was obtained by the extended quasi-static calculation under the dynamic force equilibrium condition. The dynamic initiation fracture toughness (DIFT) (K_{Id}^{i}) and the rate dependency of the phenomenon were determined and also compared for the specimens exposed to different temperatures. The fracturing processes were recorded by a high-speed (HS) camera, and the crack propagation speeds were estimated by HS image analysis. In addition, the dynamic fracture process and the coupled influence of temperature and loading rate on the dynamic fracture modes were identified by HS image analysis.

4.4.1 - Split Hopkinson Pressure Bar (SHPB) system

Dynamic fracture tests were performed by means of a 50 mm-diameter SHPB system at Monash University as shown in Figure 4.13. The testing system comprises of a gas gun generating the impact speed of the bullet up to 15 m/s, a cylindrical striker bar (500 mm in length), an incident bar (2500 mm in length), a transmission bar (2000 mm in length) and an absorbed bar (damper) (1000 in length), and were made from 50 mm diameter high strength 45CrMo steel, with a nominal yield strength of 1.1 GPa. The main parameters of the SHPB setup used in this research are shown in Table 4.5. A steel platen with two pins was introduced to achieve a three-point bending load to the specimen (see Figure 4.13).

Table 4.5 The main parameters of the SHPB system (Subscript b stands for bar)

Diameter of bars (mm)	**Incident bar length (mm)**	**Transmission bar length (mm)**	**Absorbing bar length (mm)**	**P-wave velocity c_b (m/s)**	**Elastic modulus E_b (GPa)**	**Density ρ_b (kg/m^3)**
50	2500	2000	1000	5170	210	7800

During the tests, the stress-wave pulses were captured by two sets of strain gauges located diametrically opponent attached on the incident and transmission bars. An eight-channel digital oscilloscope was used to record and store the strain gauge signals collected from the Wheatstone bridge circuits after amplification (by means of a differential amplifier), together with the signal from the strain gauge mounted on the CCNSCB specimen. The CCNSCB specimen was sandwiched between the incident and transmission bars, with three point-contacts to transfer dynamic loads: one between the incident bar and the top of the specimen, the other two contacts formed by two supporting pins between the transmission bar and the specimen, as depicted in Figure 4.13. To capture the fracture characteristics of Australian granite under dynamic loading, a high-speed camera (CMOS camera, Phantom V2511) at the frame rate of 200,000 fps with a resolution of 256 × 256 pixels in conjunction with the SHPB system, located on the front side of the specimen, was utilised in this research (see Figure 4.13). The focus of the ultra-high speed camera was manually adjusted under focused mode to capture images with optimal quality.

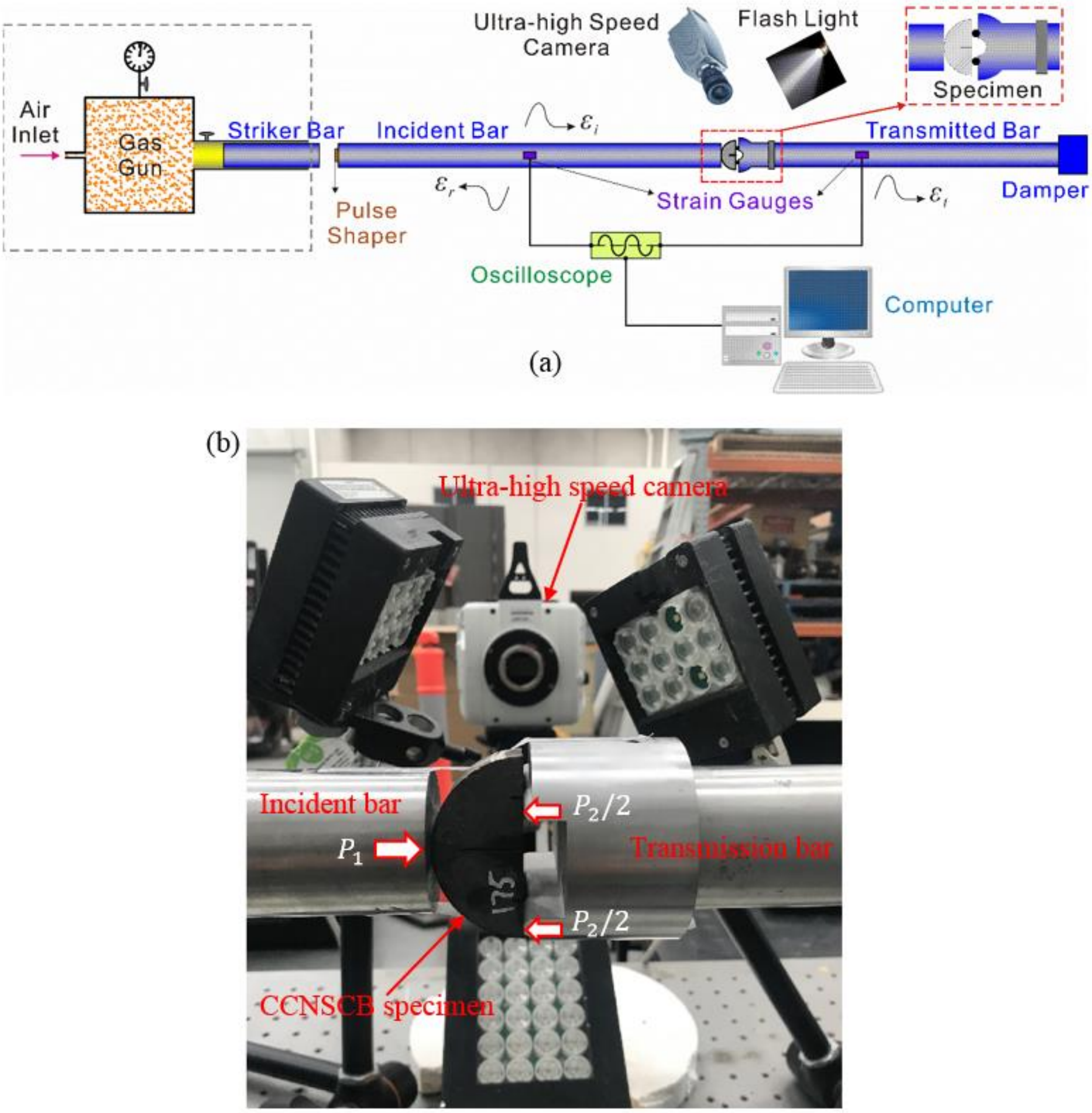

Figure 4.13. (a) Schematics of the split Hopkinson pressure bar (SHPB) system (ε denotes strain and the subscripts i, r, and t refer to the incident, reflected and transmitted waves, respectively) (b) close-up view of the partial SHPB bars and a CCNSCB specimen

4.3.2.1 - Working principles of SHPB system

As depicted in Figure 4.14, the striker bar is launched by the gas gun, and impact of the striker upon the free end of the incident bar induces a longitudinal compressive wave propagating in both directions. The left-propagating wave is fully released at the free end of the striker bar and forms the trailing end of the incident compulsive stress wave (incident wave ε_i) in which the duration of ε_i depends on the length and longitudinal wave velocity in the striker, as shown in Figure 4.14. Due to the wave impedance mismatch between the incident bar and the specimen, a part of the incident stress wave is reflected back into the incident bar as the reflected wave ε_r upon reaching the bar-specimen interface, and the remaining portion of the wave passes through the specimen to the transmission bar and becomes the transmitted wave ε_t. Strain gauges mounted on the incident and transmission bar surfaces capture the time of passage and magnitude of these elastic stress-wave pulses through the incident and transmission bars during the test.

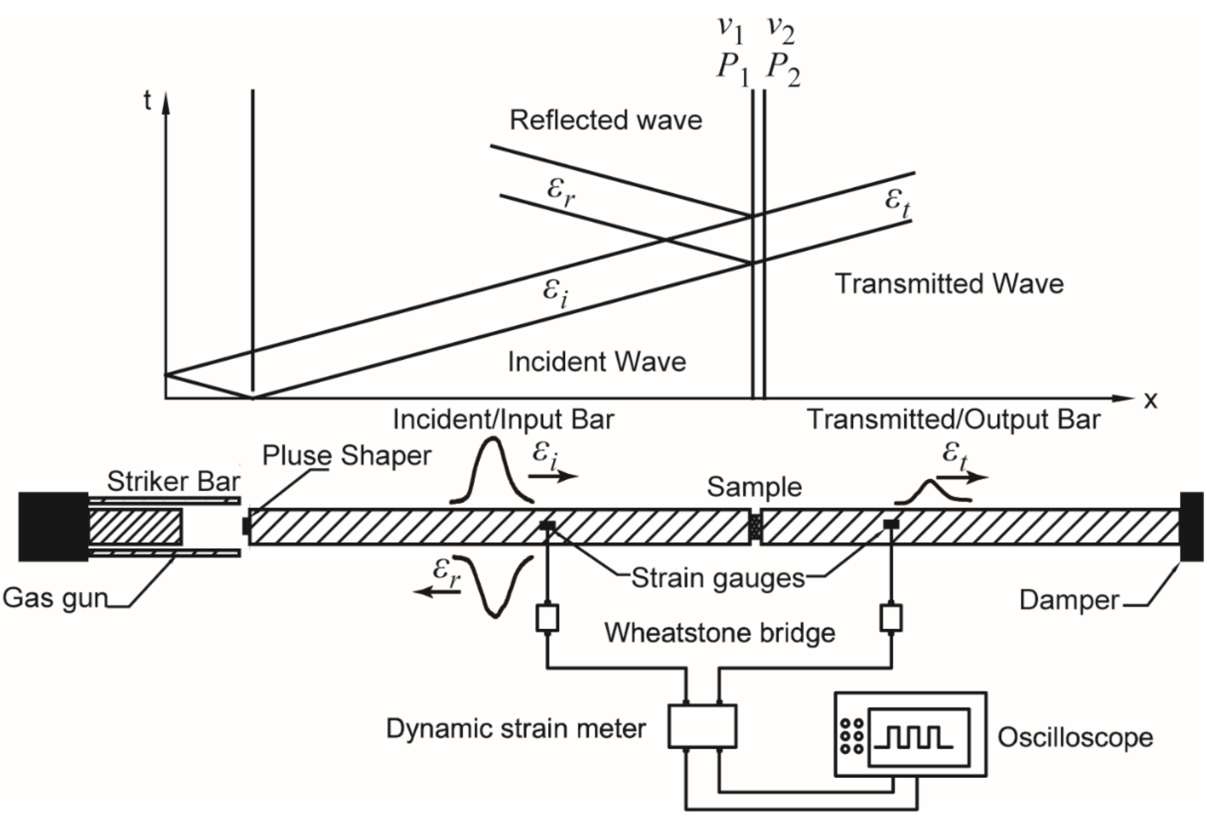

Figure 4.14. The x-t diagram of stress waves propagation in SHPB (Xia et al. 2011)

Denoting the incident wave, the reflected wave and the transmitted wave by ε_i, ε_r and ε_t, respectively, and based on one-dimensional elastic wave theory with the SHPB experimental data the dynamic forces on the incident end (P_1) and the transmitted end (P_2) of the specimen can be calculated as (Kolsky 1953) (see Figure 4.9b):

$$P_1 = A_b E_b (\varepsilon_i + \varepsilon_r) \tag{4.22}$$

$$P_2 = A_b E_b \varepsilon_t \tag{4.23}$$

where A_b and E_b the cross-sectional area and Young's modulus of the bars, respectively.

The histories of strain rate $\dot{\varepsilon}(t)$, strain $\varepsilon(t)$ and stress $\sigma(t)$ of the specimen in the dynamic tests can be determined as:

$$\dot{\varepsilon}(t) = \frac{C}{L_0}(\varepsilon_i - \varepsilon_r - \varepsilon_t) \tag{4.24}$$

$$\varepsilon(t) = \frac{C}{L_0}\int_0^t (\varepsilon_i - \varepsilon_r - \varepsilon_t)dt \tag{4.25}$$

$$\sigma(t) = \frac{A_b}{2A_0}E_b(\varepsilon_i - \varepsilon_r - \varepsilon_t) \tag{4.26}$$

where A_0, and L_0 are the initial cross-sectional area and the initial length of the specimen, respectively. C is the one dimensional longitudinal elastic stress wave velocity of the bar. Therefore, based on the Equations 4.24-4.26, the dynamic stress-strain curve of the specimen can be determined.

4.3.2.2 - Pulse shaping technique

The induced stress wave is an approximately trapezoidal shape accompanied by high-frequency oscillation and a steep rise of the incident wave when the striker bar directly impacted on the incident bar. Without a proper pulse shaping, it is difficult to achieve dynamic stress equilibrium which leads to premature failure of rock and unbalanced forces at the front and rear interface of the rock sample (Zhou et al. 2012). In order to eliminate this problem, the pulse shaping technique was adopted to facilitate the dynamic force balance of the CCNSCB specimen which is a requirement for all the equations deduced in the SHPB test in this study.

4.4.2 - Dynamic fracture tests

The damage evolution of Australian granite was investigated by conducting dynamic tests over a wide range of loading rates to reveal the rate dependency of strain burst. Dynamic fracture toughness tests were performed on thermally-treated granite specimens up to 250 °C under different impact velocity ranging from 2 to 8 m/s using a SHPB device at Monash University.

4.4.3 - Evaluation of the experimental results

CCNSCB granite specimens were successfully tested for dynamic fracture toughness mechanical behaviour in the SPHB experiments. For all the SHPB tests, the dynamic force balance of the granite specimen is inspected,and the results meet the criterion recommended by the ISRM (Zhou et al. 2012). The influence of temperature and rate dependence of the dynamic fracture toughness of Australian granite are analysed and discussed. The dynamic fracturing process and failure patterns of CCNSCB samples in different temperature and loading rate conditions are observed using a high-speed camera.

4.3.2.1 - Dynamic force balance

Dynamic force equilibrium is the prerequisite of any effective dynamic fracture tests. It must be ensured that the time-varying dynamic forces on both loading sides of the specimen are roughly balanced prior to failure and the sample must be in a state of stress equilibrium through the time to fracture and thus the quasi-static equation could be employed to determine the dynamic fracture toughness. According to the suggested method by ISRM, the dynamic force equilibrium was achieved for each sample by means of the pulse shaping technique in this research (Zhou et al. 2012). Taking a typical test as an example, the captured incident, reflected and transmitted strain waveforms of a typical CCNSCB sample are displayed in Figure 4.15a. The time-zero of the incident and reflected waves was shifted to the incident bar/specimen interface, and the time-zero of the transmitted wave was shifted to the transmitted bar/specimen interface. As shown in Figure 4.15b, the curve of the sum of the incident and reflected stresses almost overlapped ($P_1 = P_2$) with that of the transmitted stress, indicating that the external forces on both sides of the sample was nearly identical. The dynamic forces P_1 and P_2 were calculated and checked by equations 4.22 and 4.23, and the dynamic loading history on both ends of a specimen is shown in Figure 4.15b. It can be observed that the uniformity of the dynamic stress across the specimen was well achieved in the impact direction, and thus the inertial effect was reduced to a negligible level. Although there exists inevitably dynamic friction at the interfaces between the rock sample and the bars, the achieved dynamic stress equilibrium also demonstrated that 1D stress wave propagation theory could be employed to calculate the stress-strain history of rock specimen in dynamic tests.

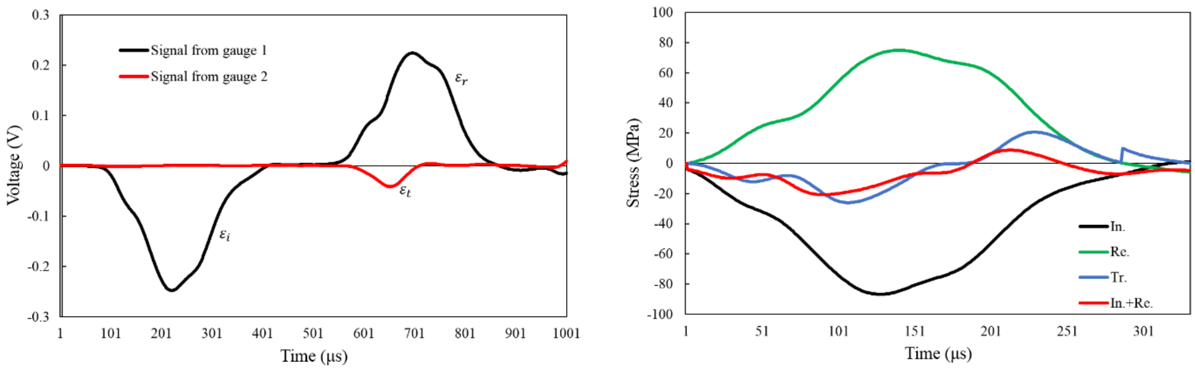

(a) (b)

Figure 4.15 (a) Typical signals recorded by strain gauges of a dynamic test with thermally-treated (100 °C) CCNSCB specimen at $v_{striker}$ of 5 m/s and (b) dynamic force equilibrium. In., Re., Tr. denote the incident, reflected and transmitted waves, respectively

4.3.2.2 - Dynamic data interpretation

Figure 4.16a presents a typical dynamic stress-strain curve of a granite specimen in dynamic CCNSCB test. The stress and strain were calculated from the incident and transmission bar signals using Equations 4.25 and 4.26. These signals provide not only the deformation information of the specimen, but also contain energy release during rock fracturing. The evolution of stress and strain on the rock specimen during impact are shown in Figure 4.16b. It should be noted that the stress of the peak point can be used to calibrate dynamic constitutive models. Figure 4.16c depicts a typical dynamic SIF-time history curve of CCNSCB specimen which can be used for determining the loading rate in the dynamic experiment.

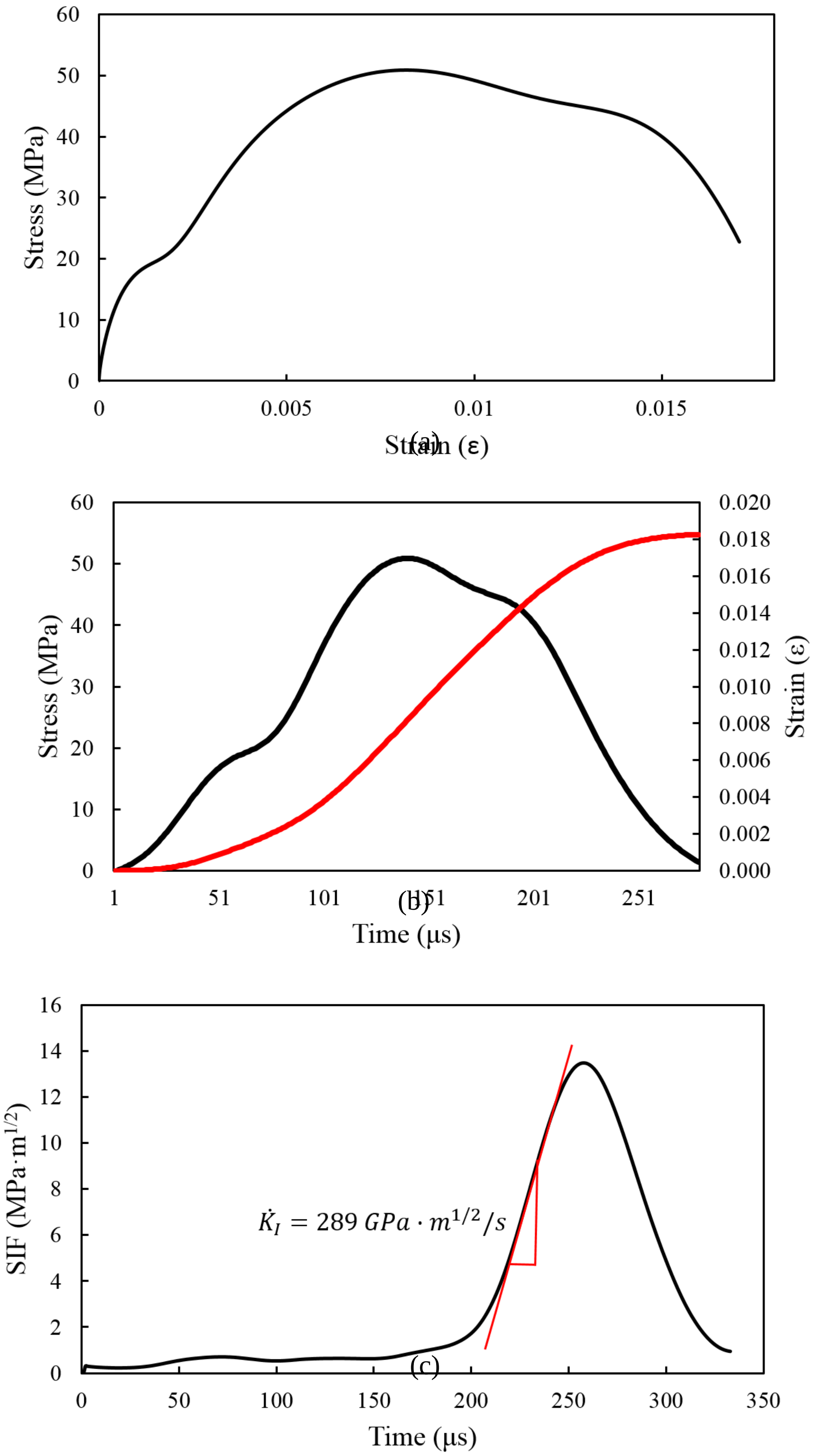

Figure 4.16. (a) Stress-strain curve (b) stress and strain as a function of time and (c) the history of the SIF in a typical CCNSCB specimen

Using the signals of the incident, reflected and transmitted waves recorded by the strain gauges, the stress-strain curves of granite were obtained under the coupling effects of temperature (25, 100, 175 and 250 °C) and impact velocity, $v_{striker}$, (2, 3, 5, 7 and 8 m/s), as presented in Figure 4.17. It can be seen that the curves underwent into three stages: elastic deformation, yielding and failure. In the elastic deformation stage, the rate of increase in the stress decreased more slowly compared with that in the initial loading. Meanwhile, the micro-cracks within the rock began to increase in size under the action of the dynamic loading, resulting in a decrease in the curve slope. In the yielding stage, the rate of increase in the stress was lower than that in the elastic stage, mainly due to the rapid expansion of the micro-cracks within the specimen unde the stress wave. When the curve reached the peak strength, the maximum load-bearing capacity was reached, which would led to macroscopic damage. In the failure stage, due to the formation of macroscopic fracture surfaces the failure of rock occurred which resulted in the decrease in the load-bearing capacity of the specimen. The stress decreased, while the strain continued to increase in this stage. With an increase in the impact velocity, the loading rate strengthening influence became more remarkable and the stress of the granite increased under all temperatures. At a high impact velocity, the loading was fast and plastic strain component may not get enough time to develop fully until the next incremental load was applied. Consequently it appeared that the material had stiffened due to the incomplete development of the plastic strain which then led to the increase of the dynamic strength of granite.

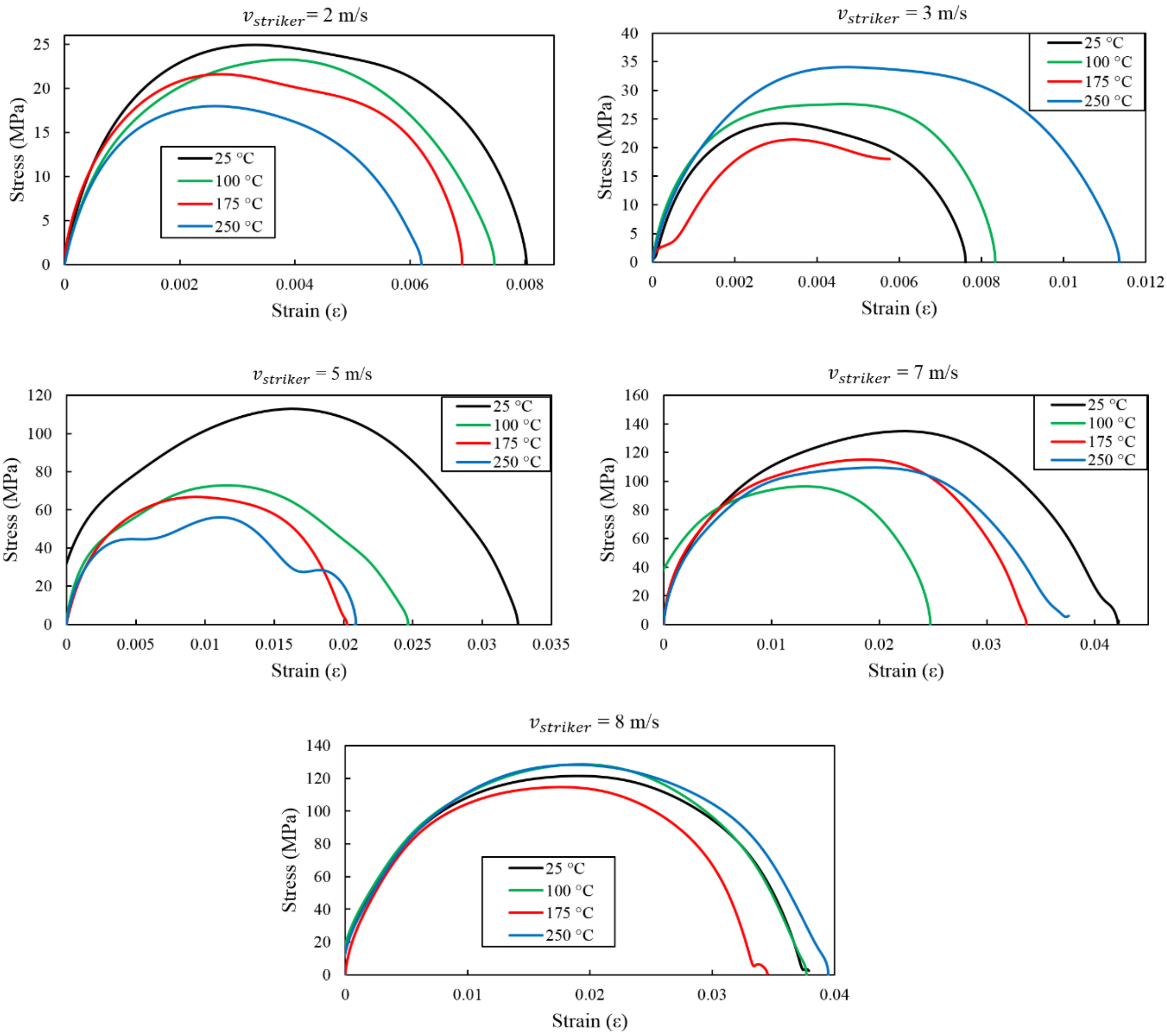

Figure 4.17. Dynamic stress-strain curves of granite under different temperatures and impact loadings

Figure 4.18 presents the relationship between the dynamic strength and the loading rate under various temperatures. It can be seen that the loading rate has a significant effect on the dynamic strength of granite under each temperature level, however the degree of the influence varies. At a given loading rate or impact velocity, the value of dynamic strength for the same level of deformation tended to decrease as the pre-heating temperature rose over the range from room temperature (25 °C) to 250 °C due to degradation influence of thermal damage on the overall rock strength in which high temperature aggravated the cumulative damage of the rock. Similar results were observed by Yin et al. (2012) and Wang et al. (2018) who studied the mechanical properties of granite by conducting dynamic tests using the SHPB technique. Taking $v_{striker} = 5\,m/s$ as an example, the dynamic strength of granite showed a decline by 33% when the temperature increased from 25 °C to 250 °C because of the thermally-induced micro-cracks in the rock.

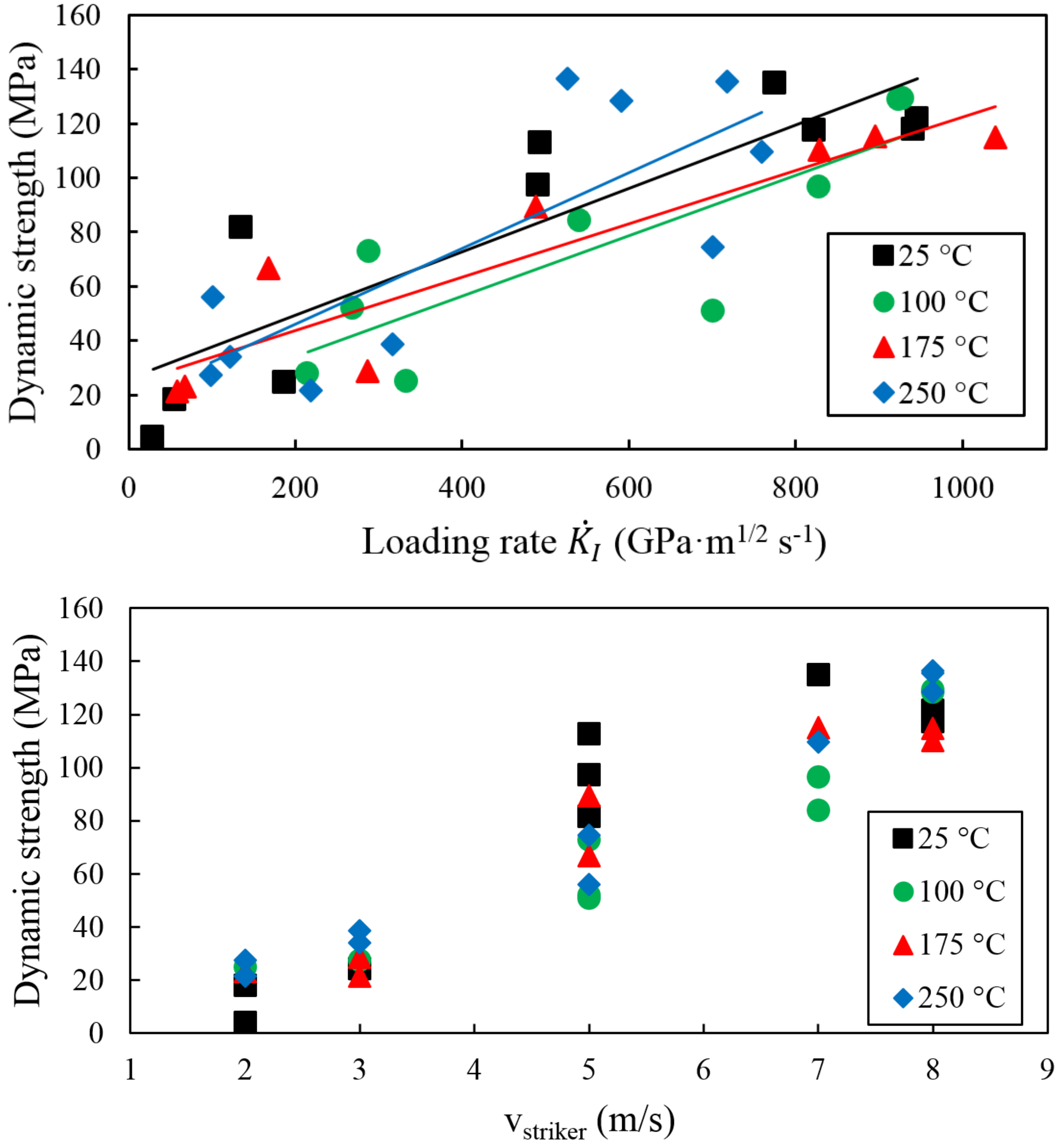

Figure 4.18 The dynamic strength versus loading rate for CCNSCB specimens treated at different temperatures

4.3.2.3 - Determination of loading rate

With the dynamic force equilibrium across CCNSCB sample, the dynamic stress intensity factor (SIF) for mode I fracture was calculated by using Equation 4.2. Based on the recommended method by ISRM to determine the dynamic fracture toughness of rocks (Zhou et al. 2012), the loading rate ($\dot{K}_I$) of CCNSCB specimen was calculated by the evolution of the dynamic SIF obtained from the dynamic CCNSCB test. Figure 4.16c shows a typical dynamic SIF-time history curve of CCNSCB specimen. There exists an approximately linear-increasing regime in the SIF history, indicating the dynamic SIF in the CCNSCB specimen increased steadily during this stage. The slope of this region is defined as the loading rate in which the unit of the loading rate is GPa·m$^{1/2}$ s^{-1} based on the suggested method by ISRM (Zhou et al. 2012). In this study, the loading rates of all specimens in dynamic CCNSCB tests were determined using this method. Typical dynamic SIF-time curves including the loading rate in the CCNSCB specimens at room temperature (25 °C) are depicted in Figure 4.19.

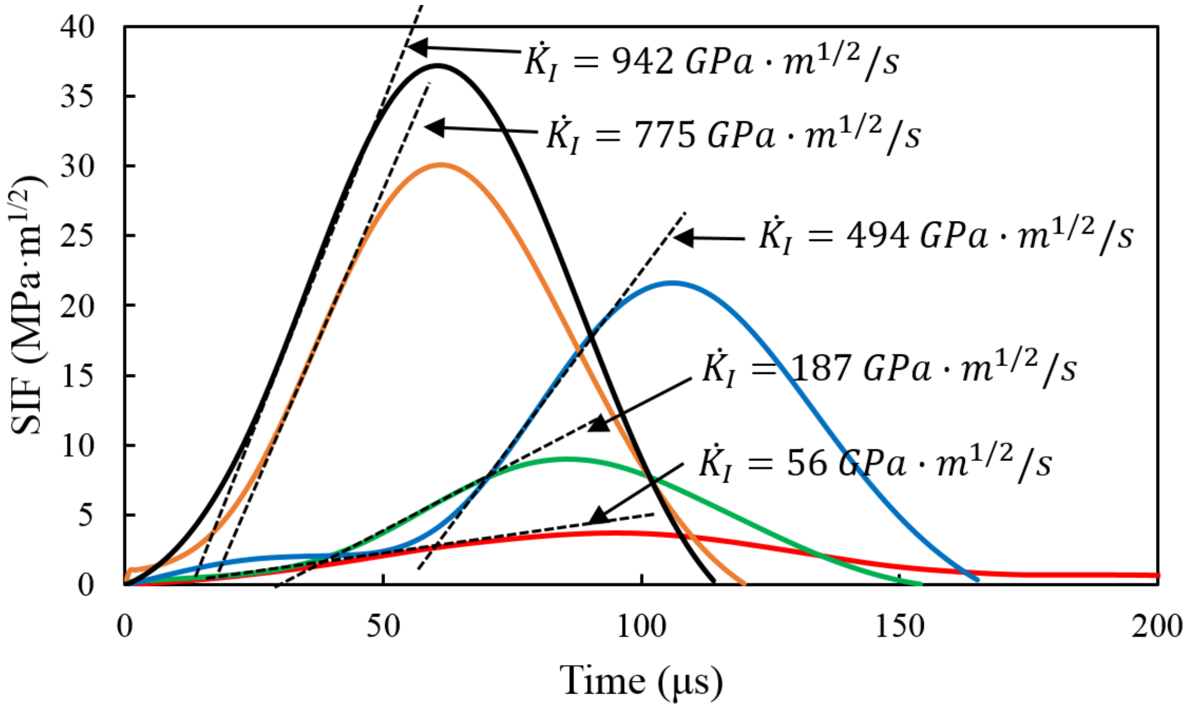

Figure 4.19. Typical SIF-time curves for determining loading rate in dynamic CCNSCB tests at room temperature (25 °C)

4.3.2.4 - Thermal damage influence and rate dependence of dynamic initiation fracture toughness (K_{Id}^i)

The dynamic initiation fracture toughness (DIFT) (K_{Id}^i) which is the ability of the material to fracture was determined by using the maximum value of SIF in this research. The fracture properties were deduced using a quasi-static theory as the dynamic stress balance was substantially achieved during the dynamic test using pulse shaping technique, eliminating the inertial effects (Chen et al. 2009; Zhou et al. 2012). The DIFT of CCNSCB specimen was calculated by using Equations 4.2 and 4.3, provided that the dynamic force balance was satisfied at both ends of specimens. Figure 4.20 shows the variation of DIFT with the loading rate and temperature. It can be concluded from Figure 4.20 that the DIFT of granite is obviously both loading rate and temperature dependent. The DIFT are close to each other at lower loading rates (less than 400 GPa·m$^{1/2}$ s^{-1}), whereas, showed a certain degree of dispersion at higher loading rates. For the CCNSCB specimen under the same loading rate, the DIFT values of granite showed a decline compared with those at 25 °C. The obtained DIFT values of thermally-treated granite under various impact velocities from dynamic CCNSCB tests are listed in Table 4.6. For instance, the DIFT under the impact velocity of 5 m/s, decreased by 29% as the temperature increased from 25 °C to 250 °C. This phenomenon was mainly caused by the increase of the thermal damage induced by the micro-cracks which eventually led to the continuous decrease of fracture toughness. This viewpoint was further verified with the SEM analysis conducted to observe the microstructure of the granite after treatment at various temperatures in Chapter 3.

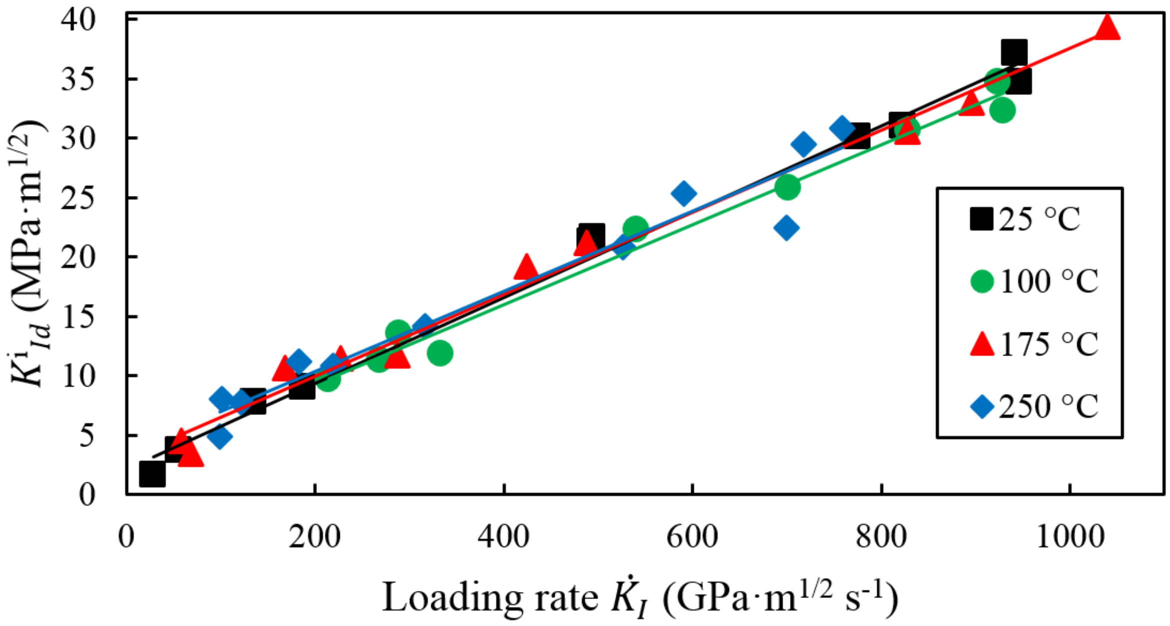

Figure 4.20. The DIFT versus loading rate for granite specimens treated at various temperatures

In order to systematically investigate the coupling effects of loading rate and thermal damage on the DIFT of granite, the linear regression method was utilised and the linear fitting of each group was obtained. Figure 4.21 presents the rate dependency of DIFT for four groups of thermally-treated granite. It was found that the DIFT of granite showed an increasing trend with the rise of impact velocity under all heat-treatment temperatures. This was due to the multiple cracks formed by transgranular fractures around the crack tip and their interaction with the main crack tip delayed the onset of crack initiation, thereby leading to an increase of the DIFT of granite. These findings are also consistent with results of other researchers' studies (Zhang et al. 2001; Yin et al. 2012; Dai and Xia 2013; Wang et al. 2018) which indicates that the coupling influence of loading rate and temperature affects the dynamic properties of granite.

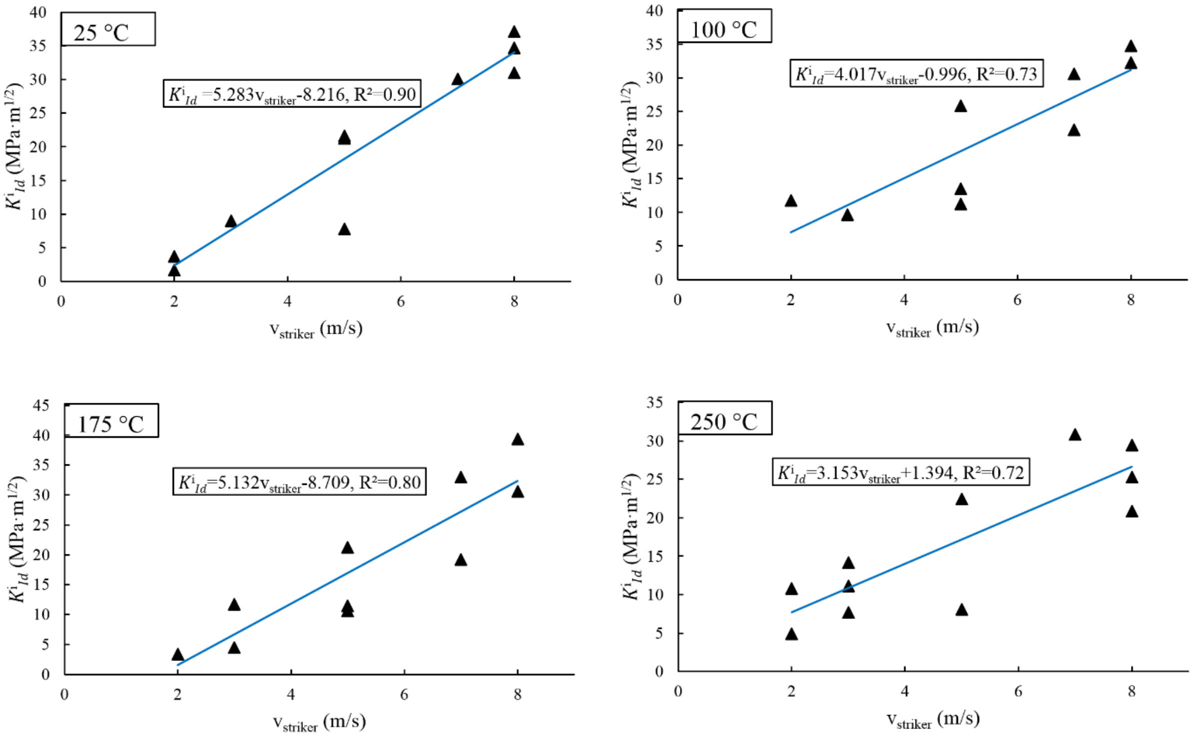

Figure 4.21. Relationship between DIFT and striker impact velocity for four different temperatures of granite specimens

Table 4.6 Dynamic initiation fracture toughness of pre-heated CCNSCB granite specimens for dynamic tests

Specimen no	**$v_{striker}$ (m/s)**	**Loading rate $\dot{K}_I$ (GPa·m$^{1/2}$ s^{-1})**	**K_{Id}^{i} (MPa·m$^{1/2}$)**	**Specimen no**	**$v_{striker}$ (m/s)**	**Loading rate $\dot{K}_I$ (GPa·m$^{1/2}$ s^{-1})**	**K_{Id}^{i} (MPa·m$^{1/2}$)**
		T = 25 °C (RT)				**T = 100 °C**	
DT25-2-1	2	29	1.64	DT100-2-2	2	334	11.78
DT25-2-2	2	56	3.67	DT100-3-1	3	215	9.67
DT25-3-1	3	187	9.01	DT100-5-1	5	269	11.22
DT25-5-1	5	135	7.75	DT100-5-2	5	702	25.81
DT25-5-2	5	494	21.65	DT100-5-3	5	289	13.49
DT25-5-3	5	492	21.25	DT100-7-1	7	541	22.27
DT25-7-2	7	775	30.07	DT100-7-2	7	829	30.62
DT25-8-1	8	823	30.96	DT100-8-1	8	924	34.72
DT25-8-2	8	942	37.15	DT100-8-2	8	929	32.28
DT25-8-3	8	946	34.68				
Specimen no	**$v_{striker}$ (m/s)**	**Loading rate $\dot{K}_I$ (GPa·m$^{1/2}$ s^{-1})**	**K_{Id}^{i} (MPa·m$^{1/2}$)**	**Specimen no**	**$v_{striker}$ (m/s)**	**Loading rate $\dot{K}_I$ (GPa·m$^{1/2}$ s^{-1})**	**K_{Id}^{i} (MPa·m$^{1/2}$)**
		T = 175 °C				**T = 250 °C**	
DT175-2-2	2	68	3.39	DT250-2-1	2	219	10.79
DT175-3-1	3	58	4.48	DT250-2-2	2	99	4.91
DT175-3-2	3	287	11.70	DT250-3-1	3	316	14.17
DT175-5-1	5	488	21.20	DT250-3-2	3	183	11.15
DT175-5-2	5	168	10.61	DT250-3-3	3	122	7.71
DT175-5-3	5	227	11.44	DT250-5-1	5	101	8.05
DT175-7-1	7	895	32.96	DT250-5-2	5	700	22.44
DT175-7-2	7	424	19.19	DT250-7-1	7	759	30.81
DT175-8-1	8	828	30.56	DT250-8-1	8	591	25.27
DT175-8-2	8	1040	39.36	DT250-8-2	8	526	20.84
				DT250-8-3	8	718	29.46

4.3.2.5 - Dynamic fracturing process and failure patterns of CCNSCB specimens

To study the progressive dynamic failure of thermally treated granite, a high-speed (HS) camera with 200,000 fps was utilised to capture the dynamic fracturing process in dynamic tests. The representative examples of typical dynamic mode I failure processes of CCNSCB granite specimens induced by different temperature conditions at impact velocity of 8 m/s are depicted in Figure 4.22, demonstrating the initiation and propagation of the cracks. The time zero corresponds to a specific time when the incident pulse has just arrived at the incident bar/specimen interface. The first one or two snapshots exhibit the typical CCSCNB specimen prior to macro fracture onset. It can be seen that the cracks initiated from the tip of notch and propagated along the impact loading, and then the tensile failure along the dynamic loading direction dominated the failure. For instance, after around 154 μs, a small macroscopic crack ahead of the notch tip became visible, indicating that crack initiation occurred, and then the crack propagated along the pre-notched direction. Subsequently, the primary crack run throughout the specimen at about 189 μs, and the CCNSCB specimen was split into two almost identical halves and each fragment showed a rotation motion around the contact points between the incident bar and the sample (see Figure 4.22, the last snapshot).

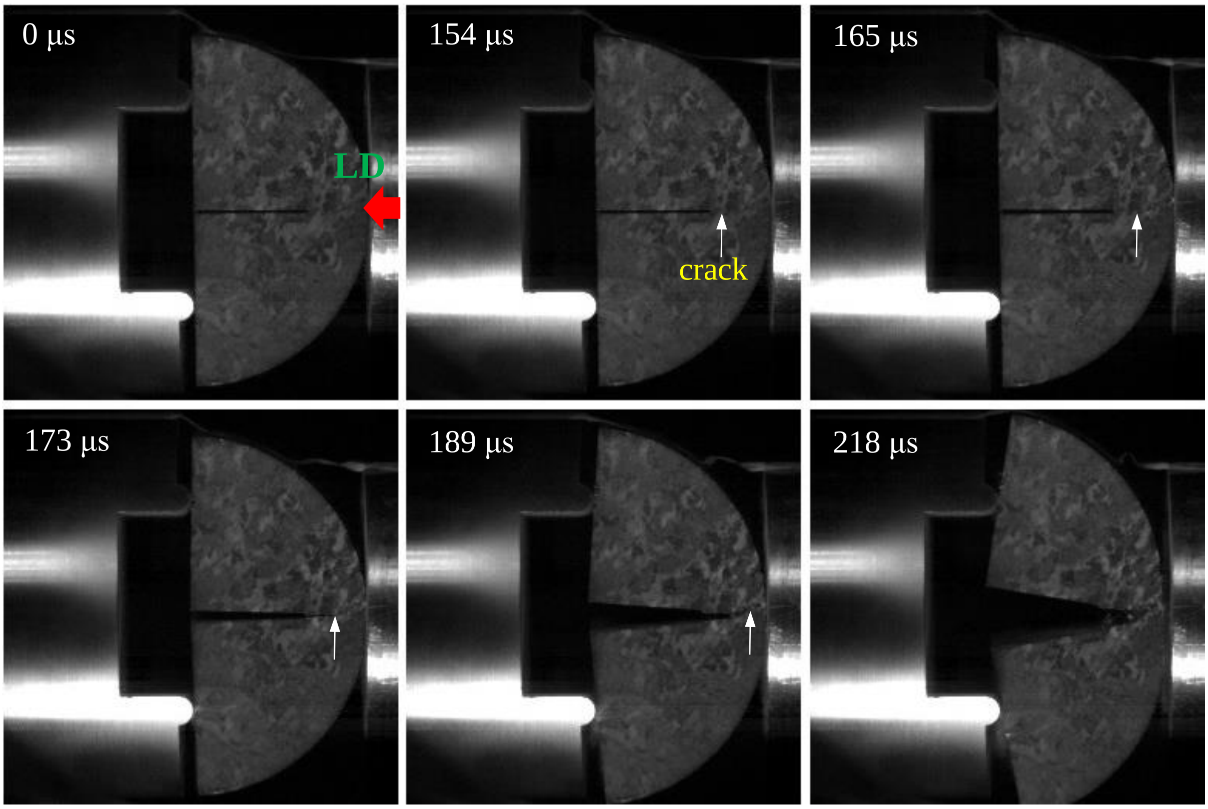

(a) T = 25 °C

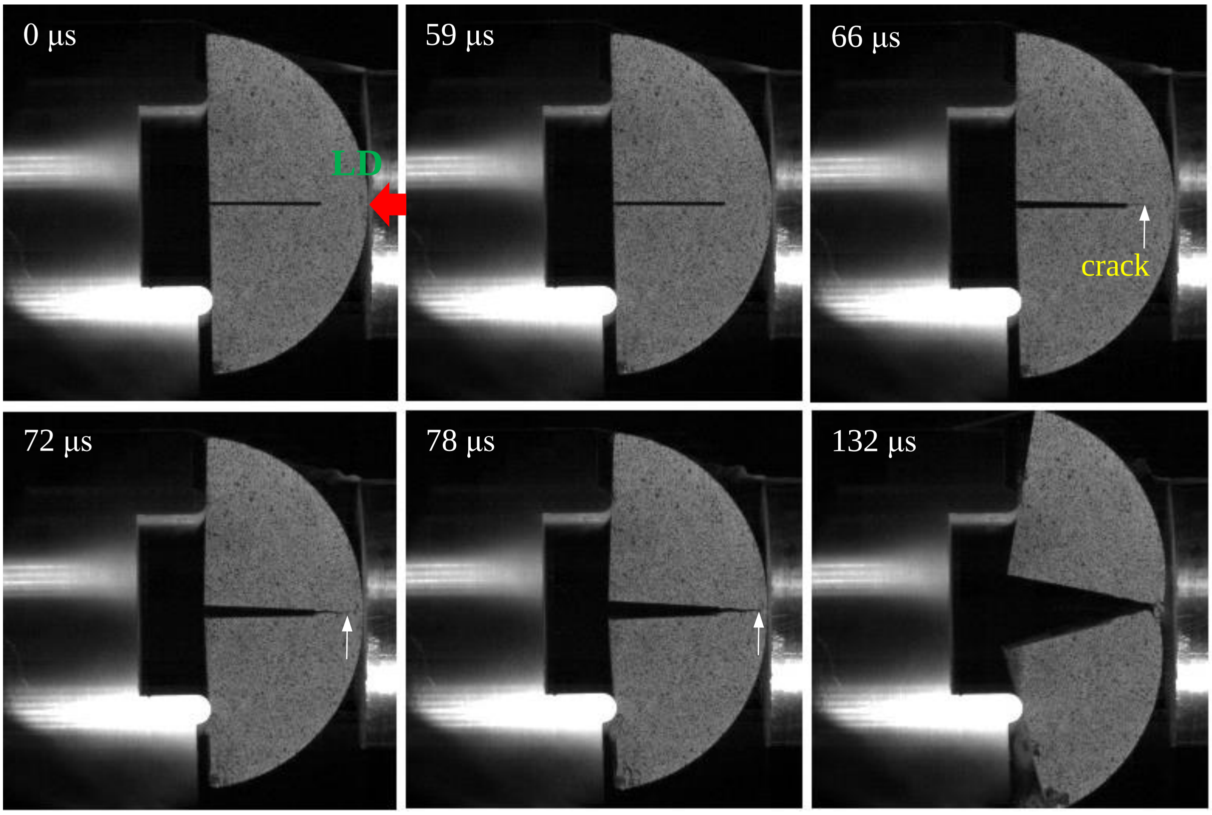

(d) T = 250 °C

Figure 4.22. HS camera images showing dynamic fracturing process of thermally treated granite (a) 25 °C (RT) and (b) 250 °C at an impact velocity of 8 m/s in dynamic CCNSCB tests (LD-loading direction)

The failure mechanism of rocks can be revealed by assessing the failure mode. The failure patterns of Australian granite exposed to various temperatures at five different impact velocities can be seen in Figure 4.23. Along with the increased impact velocity, the failure modes of the pre-heated granite changed from tensile splitting (characterisation of class I) to pulverisation in which the samples were pulverised by excess energy in class II loading, indicating that the stress concentration at both ends became more serious, and thus the crashed area was greater. The fundamental reason for this failure mode was that the elastic modulus of the bar was quite different from that of the specimen, resulting in that the pressure of contact surface was concentrated and thus the specimens were broken into many smaller fragments or pulverised in which more cracks were activated and expanded.

It can be seen in Figure 4.23 that the increased level of thermal damage within the specimen resulted in a wider damage zone which was due to the thermally-induced micro-cracks with the treatment temperature. This can be attributed to the weakening of the minerals' bonding causing a mechanical degradation. Moreover, under the same dynamic loading rate, an increase in the temperature exacerbated the fragmentation degree of the granite.

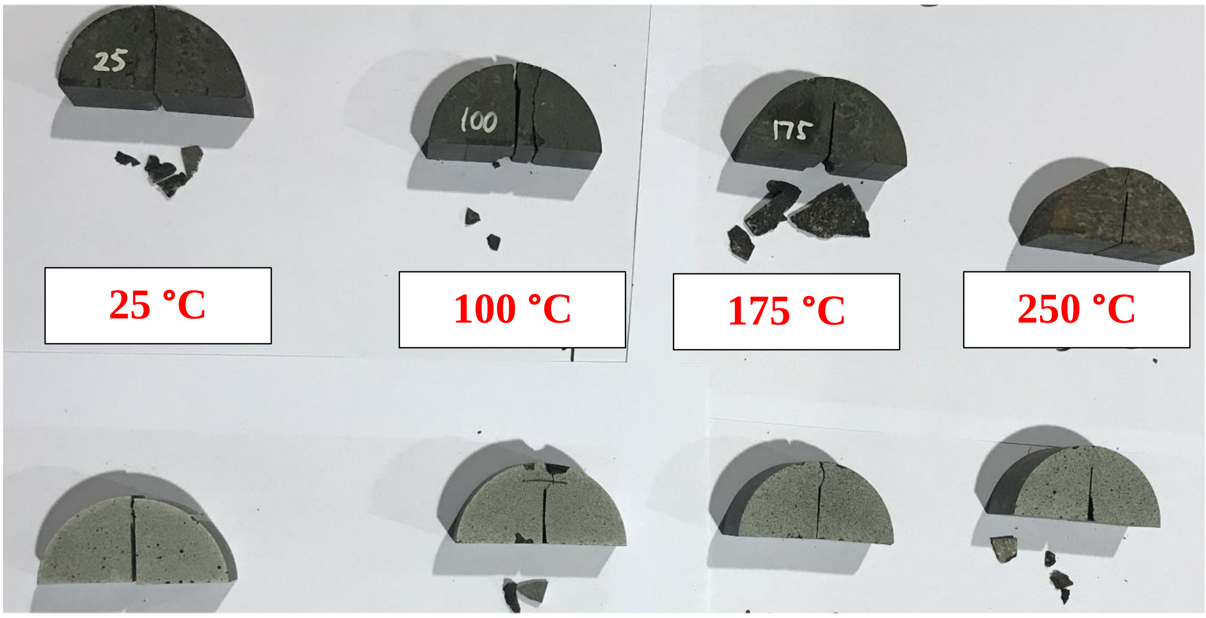

(a) Impact velocity ($v_{striker}$) = 2 m/s

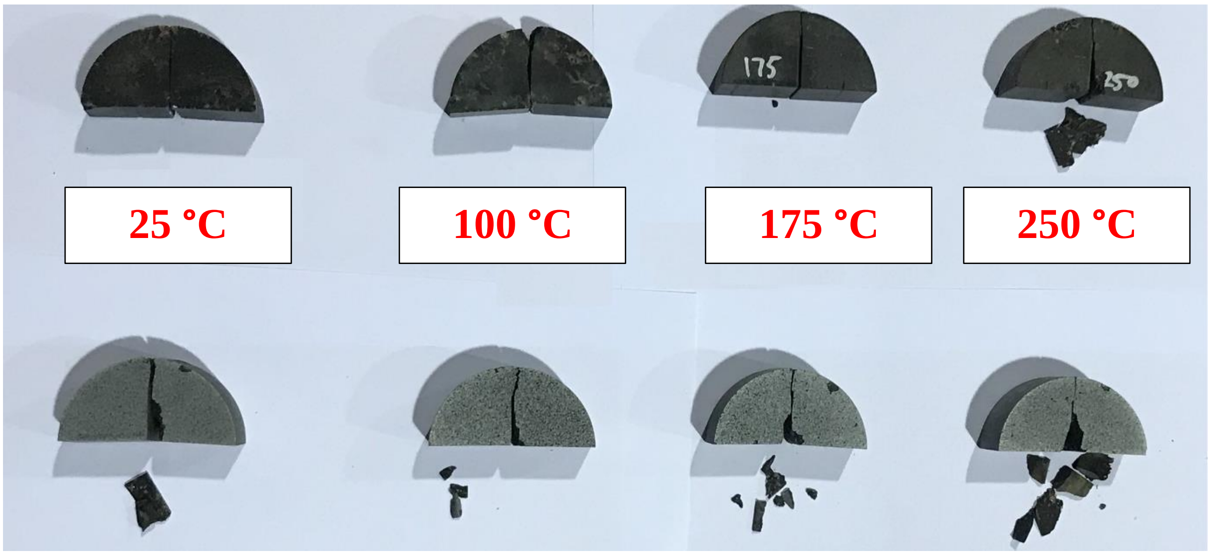

(b) Impact velocity ($v_{striker}$) = 3 m/s

(c) Impact velocity ($v_{striker}$) = 5 m/s

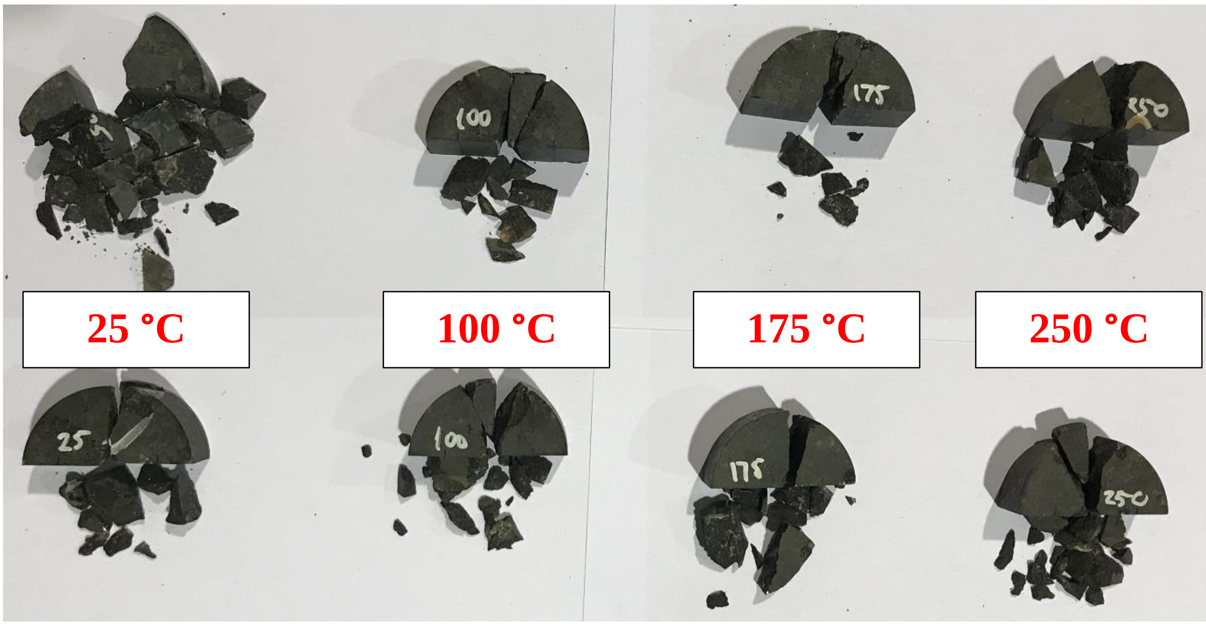

(d) Impact velocity ($v_{striker}$) = 7 m/s

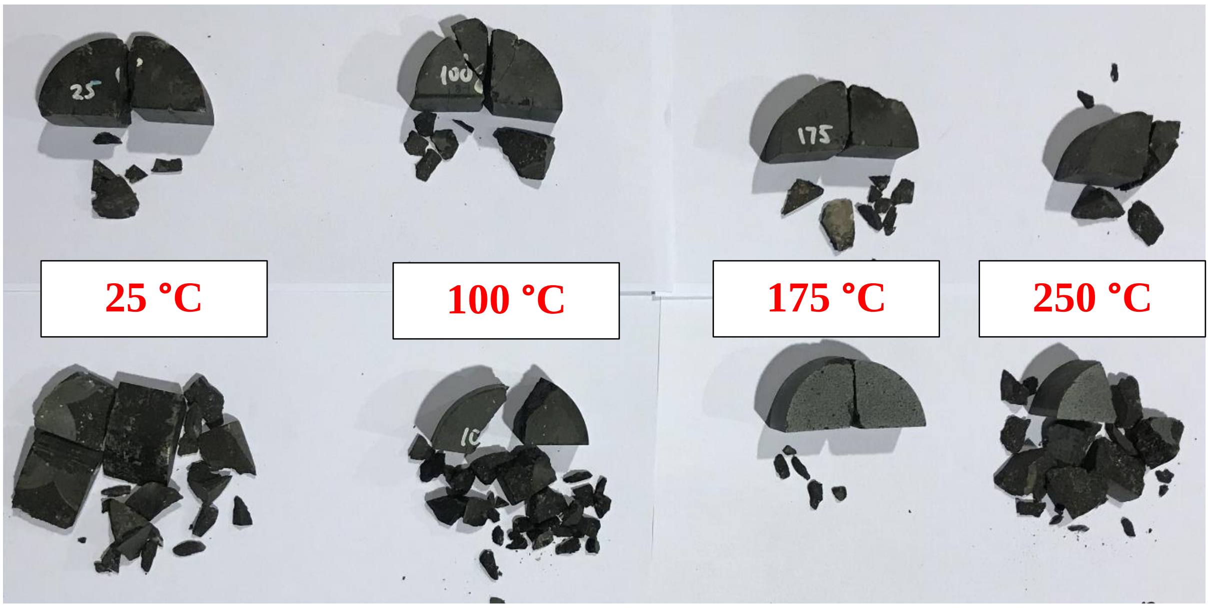

(e) Impact velocity ($v_{striker}$) = 8 m/s

Figure 4.23. Failure modes of recovered specimens under different impact velocities and temperatures

4.5 -Summary and discussion

In this chapter, the effects of the thermal damage and loading rate on both quasi-static and dynamic mechanical, fracture characteristics and quasi-static (K_{IC}) and dynamic initiation (K_{Id}^{i}) mode I fracture toughness and energy-release rate of thermally treated Australian granite specimens at various pre-heating treatments up to 250 °C under different loading rates were explored. The CCNSCB specimens were adopted in the quasi-static and dynamic mode I fracture toughness measurements of the rocks. A servo-hydraulic testing machine and a dynamic testing apparatus SHPB were utilised to conduct the quasi-static and dynamic fracture toughness tests. The fracturing characteristics during strain burst under various temperature conditions and loading rates were assessed and discussed in detail. The following key conclusions can be drawn:

1. The CCNSCB specimen combines the merits of two ISRM-suggested methods (CCNBD and NSCB methods), and thus it allows accurate determination of the mode I fracture toughness of granite under quasi-static and dynamic loadings.

2. The experimental results indicated that the quasi-static fracture toughness and energy-release rate in mode I are a function of loading rate and they presented a rising trend with

increasing loading rate. At high loading rates, transgranular fractures became dominant which consumed more energy than intergranular fractures; this in turn, resulted in more straight fracture path and posed a less rough fracture surface when compared to the low loading rate condition (Zhang and Zhao 2013).

3. Under the same loading rate, the quasi-static mode I fracture toughness and energy-release rate of granite showed a gradual decrease (17% and 30%, respectively) with ascending temperature from 25 °C to 250 °C due to the thermally-induced micro-cracks within the rocks. These findings of this investigation will be useful in achieving a better understanding of initiation of fracturing during strain burst under various temperature and loading rate conditions.

4. The stress-strain curves of granite under various impact velocities and temperatures showed the same deformation stages; elastic deformation, yielding and failure. When the impact velocity was high, the loading rate strengthening effect became more remarkable and the strength of granite increased under all temperatures. The failure modes of Australian granite also exhibited rate dependence at the same temperature level. Along with the high impact velocity, the failure mode of the pre-heated granite changed from tensile splitting (characterisation of Class I) to pulverisation or breaking into many small pieces in which the specimens were pulverised by the excess energy in Class II loading. Under the same dynamic impact, an increase in the treatment temperature weakened the interaction force between the particles and aggravated the fragmentation degree of granite.

5. The DIFT of Australian granite was obtained by the quasi-static analysis that was evidenced by the dynamic force balance until the time to fracture. The DIFT of the granite presented an ascending trend with the loading rate at a given heat-treatment temperature and decreased with increasing temperature, revealing the deterioration of the ability to resist fracturing with the rise of temperature. Therefore, in order to effectively and safely excavate the rock in deep underground conditions, a favourable measure should be applied to reduce the intensity of strain burst by considering a combined application of thermal treatment and impact with a proper loading rate.

6. Observations of the dynamic fracturing process of CCNSCB specimens using a high-speed camera indicated that the cracks initiated from notch crack tips. It was also observed that the specimens were separated into two roughly identical halves.

Chapter 5: Effects of thermal damage on strain burst mechanism for brittle rocks under true-triaxial loading conditions

Strain burst is a common problem encountered in brittle rocks in deep, high-stress mining applications. Limited research focuses on the effects of temperature on the strain burst mechanism and the kinetic energies of rocks. This study aims to investigate the effects of thermal damage on the strain burst characteristics of brittle rocks under true-triaxial loading conditions using the acoustic emission (AE) and kinetic energy (KE) analyses. The Time-domain and frequency-domain analyses related to strain burst were studied, and the damage evolution was quantified by *b*-values, cumulative AE energy and events rates. The ejection velocities of the rock fragments from the free face of the granite specimens were used to calculate kinetic energies. The experimental results showed that thermal damage resulted in a delay in bursting but increased the bursting rate at ~95% of normalised stress level. This is believed to be due to the microcracks induced by temperature exposure and thus the accumulated AE energy (also supported by cumulative AE counts) at the initial loading stage was reduced, causing a delay in bursting. The strain burst stress, initial rock fragment ejection velocity, and kinetic energy decreased from room temperature (25 °C) to 100 °C, whereas they resulted in a gradual rise from 100 °C to 150 °C demonstrating more intense strain burst behaviour.

Keywords Strain burst · Rock burst · True-triaxial loading · Thermal damage · Temperature · Acoustic emission · *b*-value · Kinetic Energy

Rock burst is a typical unstable rock failure associated with the violent ejections of rock fragments from the free face/sidewall/roof of an underground excavation. A serious threat, rock bursts can kill workers and cause severe injuries and damage. They can also cause mining and tunnelling operations to cease either temporarily or permanently. Rock bursts are classified into three types: Strain burst, fault-slip burst, and pillar burst (Hedley 1992). Strain burst is the most prevalent type of rock burst. It occurs due to the sudden release of stored strain energy within the rock mass when the induced major principal stress (σ_1) exceeds the rock mass strength (σ_{cm}). This type of detrimental failure process has been observed in deep, hard rock mines and tunnels in different locations all around the world, and is considered to be the biggest unsolved problem in deep underground excavations (He et al. 2016). Underground rock mass is in a state of stress equilibrium prior to any excavation ($\sigma_1 > \sigma_2 > \sigma_3$). Introducing an excavation in rock masses results in the redistribution of stresses around underground openings (see Figure 5.1) and accumulation of elastic strain energy in the surrounding rock mass.

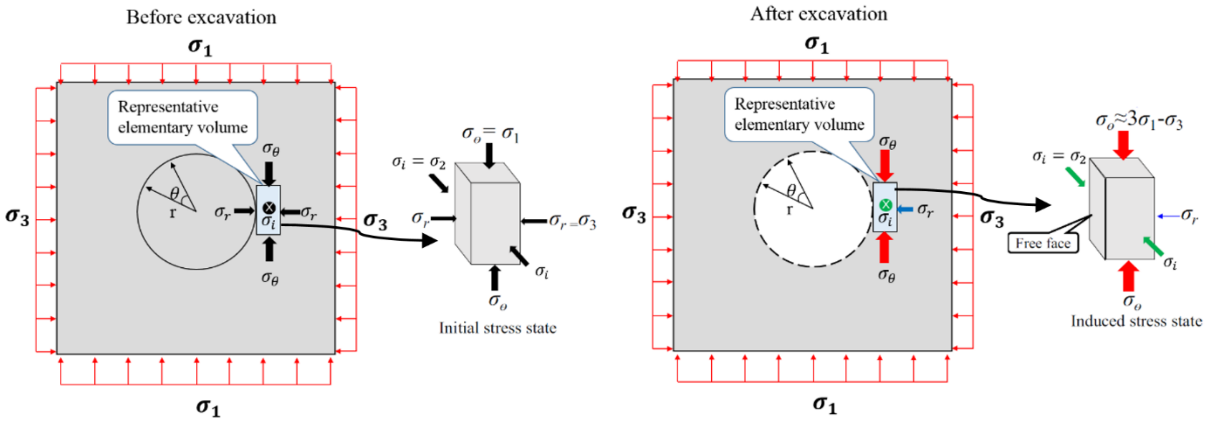

Figure 5.1 Stress state change on the sidewall of an underground opening, and a representative elementary volume before and after excavation (“modified from Su et al. 2017a”)

Additionally, rock mass surrounding underground excavations is vulnerable to the effects of high ground temperatures, especially at increasing depths. The physical and mechanical behaviours of the rock mass are influenced by the thermal effects which threaten both the safety of the working environment and the efficiency of engineering projects (Chen et al. 2012; Liu and Xu 2013). For instance, a number of intense strain bursts occurred during the excavation of tunnels in the Jinping II Hydropower Station, which caused casualties and fatal injuries, damaged equipment and ceased operations at the increasing depth due to the high geo-stress and high temperature (Zhang et al. 2012; Li et al. 2012; Feng et al. 2015). Understanding thermally induced rock damage is, therefore, of utmost importance for the safety and long-term stability of underground excavations. For this purpose, a realistic experimental testing system needs to be used for the assessment of thermal damage on the behaviour of strain burst.

Many researchers have investigated the influence of temperature on the mechanical and physical behaviour of rocks under uniaxial compression (Heuze 1983; Dwivedi et al. 2008; Sun et al. 2015), and under triaxial compression (Masri et al. 2014; Ding et al. 2016; Yao et al. 2016; Mohamadi and Wan 2016). Ding et al. (2016), studied damage evolution in sandstone after exposure to high-temperature treatment in unloading conditions, and found that both peak ductile deformation and peak effective stress changed after a critical temperature level. Kong et al. (2016) investigated the AE characteristics and physical-mechanical properties of sandstone after high-temperature exposure under uniaxial compression conditions and found that AE parameters can be used for evaluating the thermal stability of rocks and for analysing crack development. These existing works clearly show considerable thermal effects on the mechanical behaviour of rocks, and the need to consider damage due to thermal effects in investigating strain burst in deep mining. In this sense, a true-triaxial condition that better reflect stress states in deep mining, along with the effects of thermal damage on strain burst behaviour of rocks should be considered. However, to the best of our knowledge, all these features are either missing or not addressed at length in previous works.

A considerable amount of research in the laboratory has been conducted to mimic the failure process of strain burst. These experimental efforts have mainly conducted under uniaxial compression (Nemat-Nasser and Horii 1982; Wang and Park 2001), conventional triaxial compression (Huang et al. 2001; Hua and You 2001;), and true-triaxial compression (Mogi 1971; Atkinson and Ko 1973; Michelis 1985; Takahaski and Koide 1989; Wawersik et al. 1997; Haimson and Chang 2000; Nasseri et al. 2014; Feng et al. 2016). However, none of the aforementioned testing methods were able to realistically simulate the exact boundary conditions and stress paths for rocks during an excavation in which strain burst occurs. Hence, to characterise strain burst process in the laboratory, a novel true-triaxial strain burst testing system was developed by He et al. (2010) at the State Key Laboratory for Geomechanics and Deep Underground Engineering in Beijing, China. This hydraulic testing facility enables researchers to simulate the creation of an excavation by abruptly unloading σ_3 from one of the rectangular prism's surfaces that is exposed to air. Using this testing system, a considerable number of tests have been conducted on various types of rocks exposed to different stress paths to provide a better understanding of the behaviour of strain burst under true-triaxial loading/unloading conditions (He et al. 2010, 2012, Gong et al. 2015; Li et al. 2015). Few studies in the available literature have addressed the kinetic energy characteristics of strain burst failure. The influence of the unloading rate on strain burst behaviours of brittle rock under true-triaxial unloading conditions was studied by Zhao et al. (2014) concluding that the rock tends to strain burst more often when the unloading rate is high and the failure mode changes from strain burst to non-violent spalling as the unloading rate decreases. After creating a comprehensive database on the true-triaxial unloading tests, Akdag et al. (2017) discussed the influence of specimen dimensions on the bursting behaviour of rocks and indicated that the failure mode changes from strain bursting to local spalling when the height to width ratio of the rock sample is reduced from 2.5 to 1. For this reason and my focus on rock burst in the present study, all specimens with height to width ratio of 2.5 were used. Su et al. (2017) investigated the influence of tunnel axis stress on strain burst by using modified true-triaxial rock burst system. The experimental results indicated that intensive strain burst is more likely to occur when the tunnel axis stress is high. Table 1 summarises the true-triaxial loading and unloading tests to assess the failure characteristics of different rocks. However, the aforementioned studies did not consider the temperature influence on strain burst behaviours. Therefore, it is essential to investigate how strain burst mechanism is affected by high-temperature conditions.

This chapter investigates the influence of temperature on strain burst. A true-triaxial loading-unloading experimental set up was used to replicate strain-burst condition. In the following sections, the basic properties of the rock samples are described first. The strain burst testing methods and the experimental procedure are then introduced. This is followed by the analysis of the influence of temperature on strain burst stress and dynamic failure processes of strain burst. Subsequently, time-domain, frequency-domain and *b*-value analyses were conducted to systematically investigate the evolution of AE due to thermal damage influence on strain burst. Finally, the kinetic energies of the ejected rock fragments due to thermal damage are discussed.

Table 5.1 Summary of true-triaxial loading and unloading tests to characterise the failure type of rocks

Loading type	Loading method	Specimen size (mm x mm x mm)	Rock type	Failure mode	Reference
Loading	(1) apply σ_1, σ_2, σ_3 (2) keep σ_2 and σ_3 (3) increase σ_1	15 x 15 x 30	Dolomite	Fracturing & ductility	Mogi (1971)
		50 x 50 x 100	Marble		Michelis (1985)
		50 x 50 x 100	Sedimentary rocks		Takahashi & Koide (1989)
		57 x 57 x 125	Sandstone		Wawersik et al. (1997)
		19 x 19 x 38	Granite		Haimson & Chang (2000)
		80 x 80 x 80	Sandstone		Nasseri et al. (2014)
		50 x 50 x 100	Granite		Feng et al. (2016)
Unloading	(1) apply σ_1, σ_2, σ_3 (2) keep σ_2 (3) Unload σ_3 (4) Increase σ_1	30 x 60 x 150	Limestone, granite, sandstone, marble	Rock burst	He et al. (2010, 2012)
		20 x 40 x 100	Marble	Spalling	Coli et al. (2010)
		30 x 60 x 150	Marble	Rock burst and slabbing	Gong et al. (2012)
		30 x 60 x 150	Granite	Rock burst	Zhao et al. (2014)
		30 x 60 x 150	Granite	Rock burst	Zhao and Cai (2014)
		30 x 60 x 120	Granite	Slabbing	
		30 x 60 x 90	Granite	Shearing	
		100 x 100 x 100	Granite, sandstone, cement mortar	Splitting, Slabbing, Spalling	Li et al. (2015)
		100 x 100 x 200	Granite	Rock burst	Su et al. (2017)
		25 x 50 x 125	Granite	Strain burst	Akdag et al. (2018)

2

5.1 -Experimental methodology

5.1.1 - Rock properties

The rock samples used in this study were collected from a borehole located in South Australia at a depth of 1020 – 1345 m. The collected rock was coarse-grained granite with weak to moderate alteration and occasional weak gneissic foliation. The grain size of this brittle granite rock ranges from 0.5 mm to 3 mm and is composed of potassium feldspar, quartz and chlorite. Therefore, the diameter of the specimens was more than 10 times bigger than the rock grain size required to satisfy ISRM recommendations (Fairhurst and Hudson 1999).

Uniaxial compression tests were performed on both cylindrical granite specimens that had a diameter of 42 mm, were sub-cored from 63 mm diameter drill cores, and were 100 mm long (Fairhurst and Hudson 1999). The tests were also performed on rectangular prism samples (125 mm × 50 mm × 25 mm). The granite specimens were loaded axially with an axial displacement rate of 0.1 mm/min and LVDTs and strain gauges were attached to measure both axial and lateral strains. Rocks were also equipped with AE sensor to capture the cracking and damage behaviour during the tests (see Figure 5.2). The test results and basic mechanical properties of the granite samples are listed in Table 5.2.

Figure 5.2 Instrumentation of granite specimens for UCS tests

Table 5.2 Mechanical properties of rectangular prism granite specimens for UCS (σ_{c2}) tests

Specimen Number	Dimensions			Density (g/cm^3)	UCS, σ_{c2} (MPa)	Young's modulus, E (GPa)	Poisson's ratio, ν
	Height (mm)	Width (mm)	Thickness (mm)				
B1 #5	124.87	50.10	25.02	2.89	175.8	55.3	0.19
B1 #8	124.99	50.23	25.14	2.82	184.4	27.9	0.11
B3 #3	125.04	49.97	25.00	2.87	137.1	28.5	0.10

5.2 - Experimental procedure for strain burst tests

5.2.1 - Sample preparation and strain burst testing system

A total of sixteen rectangular prism granite samples were prepared from the drill cores of 63 mm diameter for the strain burst tests (see Figure 5.3a). Each sample size was approximately 125 mm × 50 mm × 25 mm. All six surfaces of the samples were carefully polished to minimise the end effect during loading. The samples' average flatness was 0.009 mm. Nine flatness measurements were taken from the surfaces of each specimen using digital dial gauge. Sample hardness was measured with the Leeb rebound method, using an Equotip 3 hardness tester (see Figure 5.3b-c). The Leeb number (L value) is used to express the hardness of the material, which can be used as an indicator of rock strength (Aoki and Matsukara, 2008). The average Leeb hardness of the granite specimens used for this study was 746 and the average density was 2871 kg/m^3. The average P-wave velocity of the specimens before thermal damage was approximately 5764 m/s. All the granite specimens were divided into six groups (i.e. groups I, II, III, IV, V and VI) based on temperature. Specimens were then kept at room temperature of 25 °C (i.e. group I) or heated up to the following temperature levels of 50, 75, 100, 125, and 150 °C (i.e. groups II, III, IV, V and VI respectively).

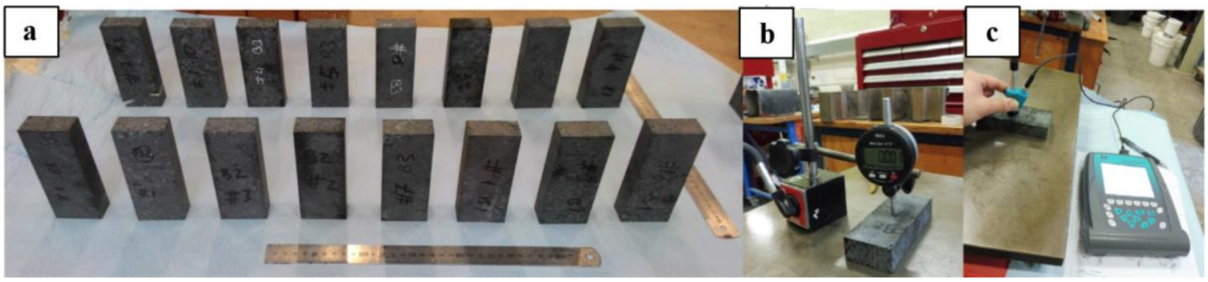

Figure 5.3 (a) Overview of granite specimens, (b) flatness measurement by digital dial gauge, (c) hardness measurement via Equotip hardness tester

The strain bursts tests were performed using the deep underground true-triaxial strain burst testing system developed by He et al. (2010) at the University of Mining and Technology in Beijing, China. The strain burst test facility consists of a hydraulic controlling unit, a data acquisition system for stress and deformation, and also equipped with an AE monitoring system, a high-speed digital video camera system to monitor the instantaneous strain bursting process and linear variable differential transducers (LVDT) to measure the displacements during testing (see Figure 5.4). To mimic and characterise the stress distribution near an excavation boundary in the laboratory, this testing system enables loading a rectangular rock specimen independently in three principal stress directions (σ_1, σ_2, σ_3) progressively to the pre-determined in-situ stress level, and suddenly removing σ_3 by dropping a rigid loading plate, while maintaining σ_2 constant and then increasing σ_1 until strain burst occurs (see Figure 5.4d-e). The hydraulic loading unit has a maximum force capacity of 450 kN which is used to apply vertical and horizontal loads on the six surfaces of a rectangular rock specimen. The data acquisition system is capable of recording 100,000 data points per second (see Figure 5.4a). The high-speed digital camera records at 1,000 fps with a resolution of 1024 × 1024 pixels, which enables the capture of sudden cracking as well as the violent ejection of rock fragments (see Figure 5.4e).

The AE technique is a useful, non-destructive testing method used to investigate the onset and evolution of micro-cracking. It is also used to analyse the damage mechanism of rocks (Karakus et al. 2016). In the present study, two AE sensors with a diameter of 18 mm to investigate the AE characteristics of granite samples were used. The AE transducers (type WD, from the American Physical Acoustics Corp.) were attached to the lateral side of the rock specimens by means of spring clips and adhesive tape to minimise friction between the specimen and the loading plate and to prevent sensor failure due to rock ejection (see Figure 5.4f). A petroleum jelly was smeared on the sensors and the steel plates to ensure good acoustic coupling. The resonance frequency of the AE transducers was 125 kHz, associated with an operating frequency range from 100 kHz to 1 MHz. A PCI-2 AE system was used to monitor the damage within the granite specimens during strain burst tests and the output voltage of the AE was amplified to 40 dB gain. The amplitude threshold for AE detection was set to 35 dB with an AE sampling rate of 10 msps (million samples per second) for each test.

5.2.2 - Strain burst test

Granite specimens were first heated up to the target temperatures (25, 50, 75, 100, 125 and 150 °C) at a rate of 5 °C/min in a high-temperature furnace. Once the corresponding temperature was reached, the temperature was kept constant for about 12 h, to ensure the specimens were sufficiently heated. Finally, the granite specimens were allowed to cool down naturally to room temperature. Strain burst tests were then performed on the cooled granite samples.

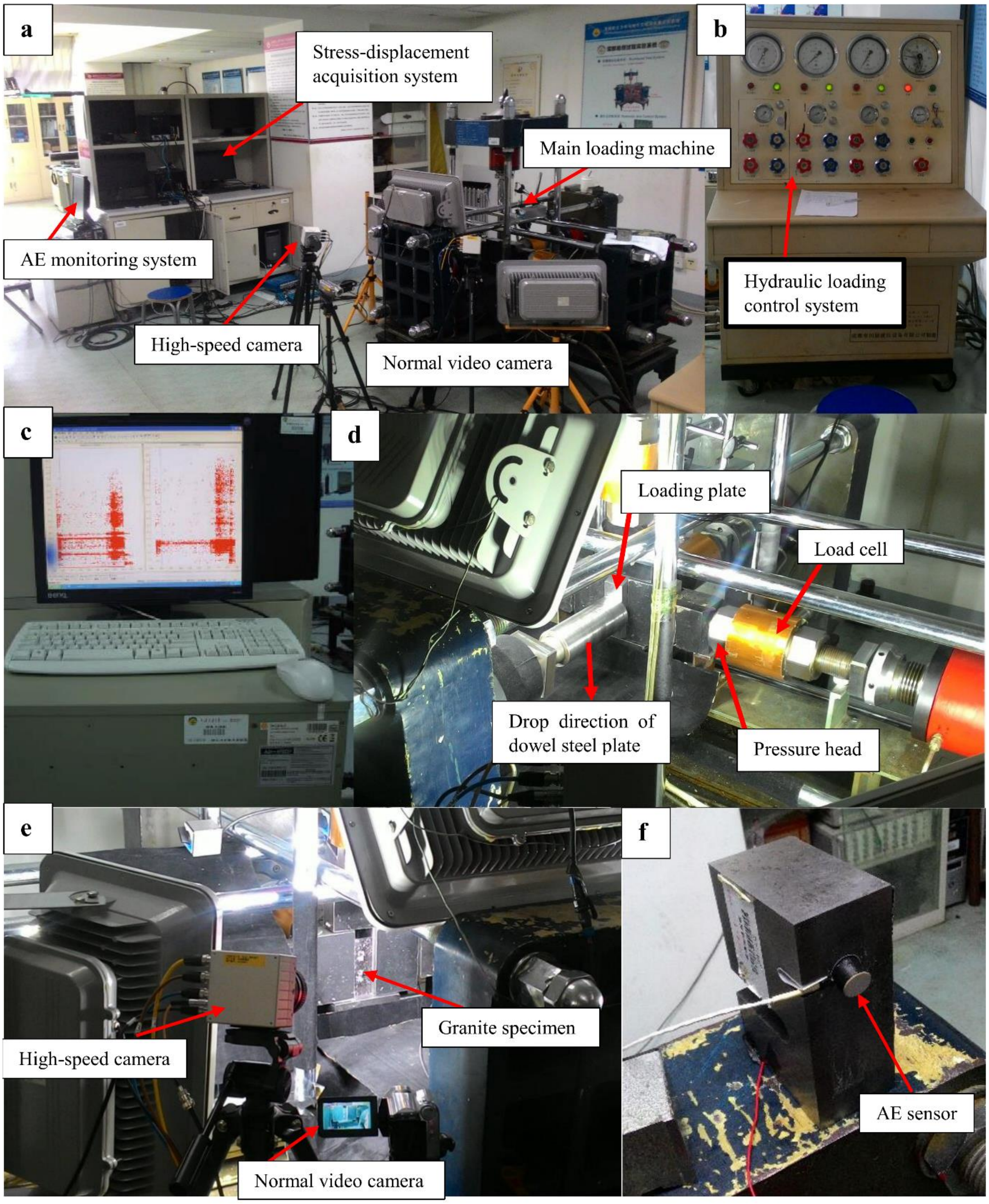

Figure 5.4 Laboratory set-up for strain burst test: (a) the testing machine, data acquisition system and cameras, (b) independently controlled hydraulic loading system, (c) the AE monitoring system, (d) loading and unloading steel plates, (e) granite specimen after unloading the plate from one face, (f) AE sensor position

Cai (2008) stated that it is significant to be able to capture the correct rock mass behaviour during excavations, because the actual stress path in a rock mass is complex and has an important role in the failure or damage process. Hence, accurate excavation responses depend on the unloading paths. The in-situ stress test results were used as a guideline for determining the stress loading conditions used to simulate strain burst in the laboratory. Figure 5.5 plots the designed stress path and the applied loading-unloading directions on a rock specimen during strain burst testing. All surfaces of the rectangular prism granite specimen were loaded independently, in three principal stress directions. The loads were progressively applied until all six surfaces reached the minimum principal stress. Subsequently, while the loads on two surfaces, where σ_3 was acting, were kept constant, the loads on the other four surfaces were increased simultaneously until they reached the intermediate principal stress level. Finally, while keeping the loads on the other lateral four surfaces constant, the load at the top surface was increased to the pre-determined maximum principal stress level in two steps. Therefore, the in-situ stress level of $\sigma_1/\sigma_2/\sigma_3$ = 43/23/11 MPa was reached and the loads were retained for about 5 minutes to make sure the stress was distributed uniformly. In order to mimic the stress redistribution and concentration after an excavation, σ_3 was removed quickly with an unloading rate of around 17 MPa/s while σ_2 was kept constant. Then to generate a strain burst σ_1 was increased at a constant rate of 0.25 MPa/s until strain burst occurred. Meanwhile, when unloading of σ_3 began, recording of the high-speed digital video camera was started to capture the strain burst process.

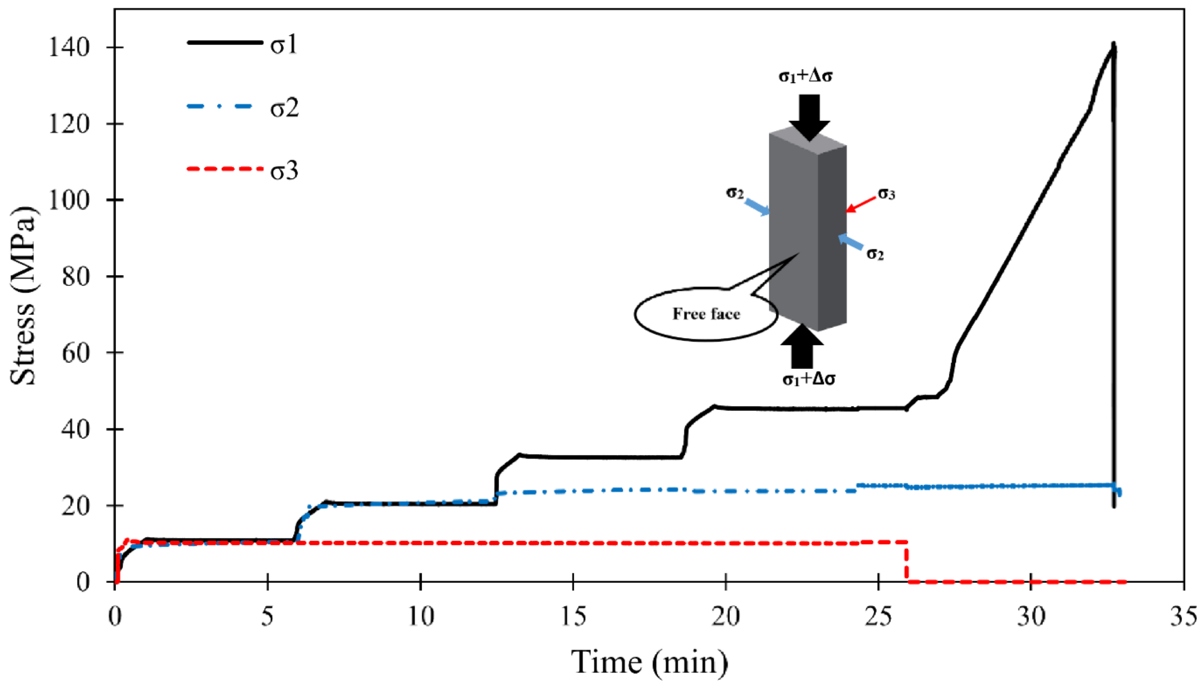

Figure 5.5 Designed loading-unloading stress path and illustration of stress conditions on rock specimen for strain burst tests

5.3 -Evaluation of the experimental results

5.3.1 - Influence of thermal damage on strain burst stress

The principal stresses applied to the granite samples just before unloading, and at failure, under various temperature conditions are summarised in Table 5.3. The table shows the ratios of major principal stress σ_1, the sum of major and intermediate principal stresses, and the deviatoric stress to the UCS $(\sigma_{c1}, \sigma_{c2})$ of both cylindrical and rectangular prism granite specimens. Note that σ_{c1} is the average value of UCS of cylindrical granite specimens (42 mm × 100 mm), which is equal to 155 MPa and σ_{c2} corresponds to the average UCS value of rectangular prism specimens (25 mm × 50 mm × 125 mm), which is 180 MPa. The major principal stress σ_1 at failure varies in the range of 0.65–1.87 times σ_{c1}, and 0.56–1.61 times σ_{c2}. It is also shown that the ratio of deviatoric stress of σ_1 and σ_2 to σ_{c1} and σ_{c2} is between 0.49–1.70 and 0.42–1.46 respectively. The ratios indicated in Table 5.3 can be used as indicators of strain burst occurrence by comparing them to the rock burst criteria based on strength theory. Figure 5.6 presents the actual stress paths and cumulative AE energy, which was calculated after AE analysis, of the granite specimens from each group under different temperature conditions. As the testing system was not servo-controlled, you will see in Table 3 some discrepancies can be conserved between the recorded principal stresses and the designed values during the loading-unloading processes. Note that only one representative result from each group is presented in Figure 5.6 to avoid providing similar results. However, the variations in strain burst stress and cumulative AE energy are shown separately in Figures 5.8 and 12a, to represent the whole dataset.

Table 5.3 Principal stresses just before unloading and at strain burst of granite specimens with different temperature conditions

Specimen	**Temperature (°C)**	**Critical principal stresses before unloading**			**Critical principal stresses at strain burst**			$\frac{\sigma_1}{\sigma_{c1}}$	$\frac{\sigma_1+\sigma_2}{\sigma_{c1}}$	$\frac{\sigma_1-\sigma_2}{\sigma_{c1}}$	$\frac{\sigma_1}{\sigma_{c2}}$	$\frac{\sigma_1+\sigma_2}{\sigma_{c2}}$	$\frac{\sigma_1-\sigma_2}{\sigma_{c2}}$
		σ_1 (MPa)	**σ_2 (MPa)**	**σ_3 (MPa)**	**σ_1 (MPa)**	**σ_2 (MPa)**	**σ_3 (MPa)**						
B1 #1	25	42.96	25.30	10.85	259.21	26.53	0	1.67	1.84	1.50	1.44	1.59	1.29
B1 #2		43.24	24.47	10.63	232.53	23.71	0	1.50	1.65	1.35	1.29	1.42	1.16
B2 #1	50	45.54	24.99	10.46	141.01	25.42	0	0.91	1.07	0.75	0.78	0.92	0.64
B2 #2		45.76	23.79	10.65	191.52	23.91	0	1.24	1.39	1.08	1.06	1.20	0.93
B2 #3		43.13	23.82	10.82	289.23	25.90	0	1.87	2.03	1.70	1.61	1.75	1.46
B1 #3	75	45.43	23.59	10.81	157.95	24.07	0	1.02	1.17	0.86	0.88	1.01	0.74
B1 #4		43.74	24.35	10.42	175.29	23.27	0	1.13	1.28	0.98	0.97	1.10	0.84
B1 #6	100	43.65	24.91	10.21	164.66	24.65	0	1.06	1.22	0.90	0.91	1.05	0.78
B1 #7		42.75	23.90	11.02	143.19	23.93	0	0.92	1.08	0.77	0.80	0.93	0.66
B3 #1		42.71	25.09	10.92	101.15	24.84	0	0.65	0.81	0.49	0.56	0.70	0.42
B3 #2	125	45.07	24.96	10.87	172.04	25.66	0	1.11	1.28	0.94	0.96	1.10	0.81
B3 #4		43.91	24.70	10.94	151.71	24.32	0	0.98	1.14	0.82	0.84	0.98	0.71
B3 #5		42.49	24.54	11.25	148.97	24.86	0	0.96	1.12	0.80	0.83	0.97	0.69
B3 #6	150	43.82	23.58	10.99	164.21	22.45	0	1.06	1.20	0.91	0.91	1.04	0.79
B3 #7		44.50	24.87	10.98	258.97	26.67	0	1.67	1.84	1.50	1.44	1.59	1.29
B3 #8		41.52	24.56	10.92	197.60	24.73	0	1.27	1.43	1.12	1.10	1.24	0.96

It can be observed that the cumulative AE energy for the six granite specimens shows similar evolutionary characteristics to the initial stress state, unloading and failure. The evolution process of cumulative AE energy can be divided into three typical periods. At the initial loading period, a sharp increase occurred due to seating, loading adjustment and the natural compaction of microcracks and voids. Relatively low AE activities were observed in the second stage, showing that the rock samples went into elastic deformation.

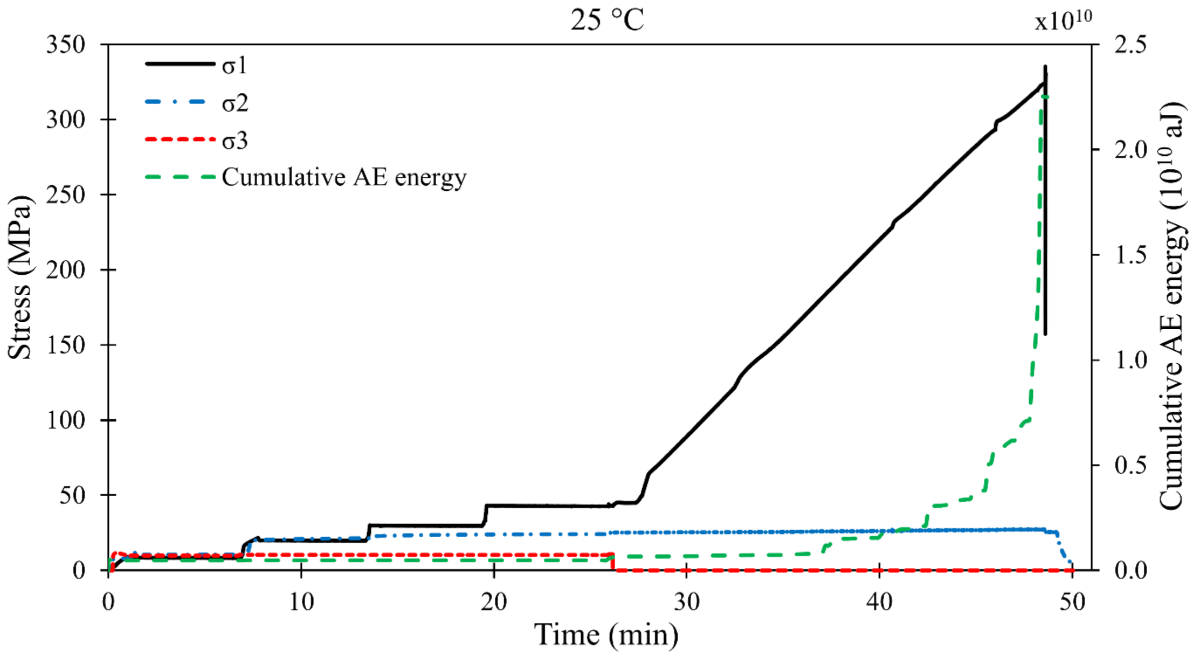

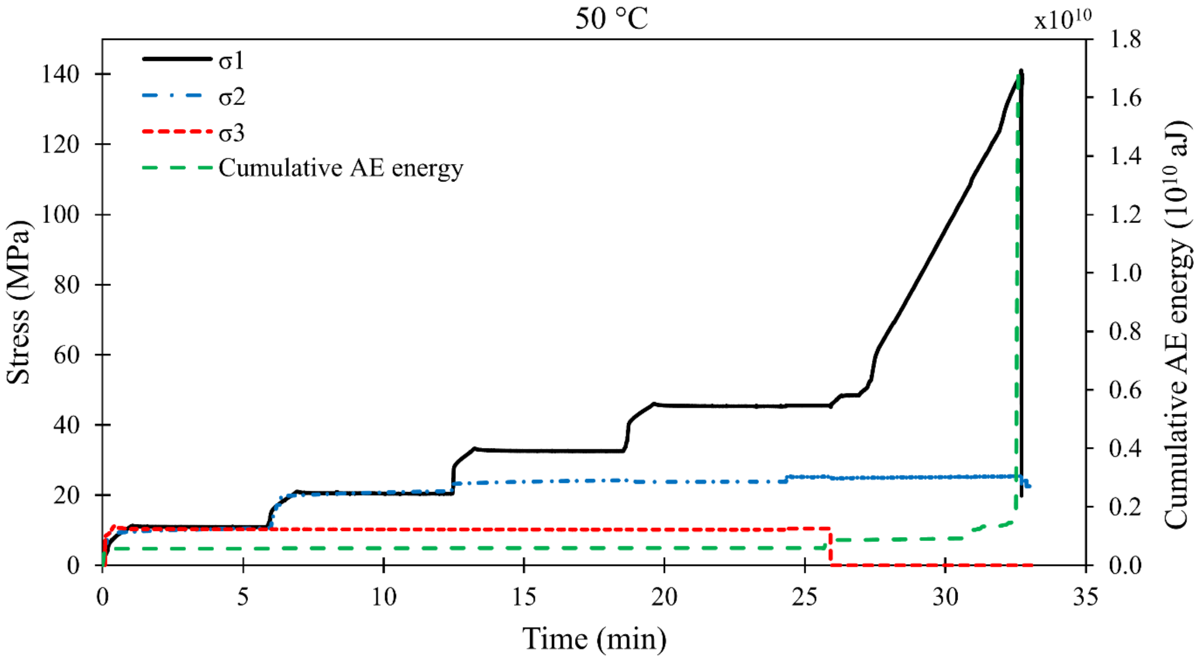

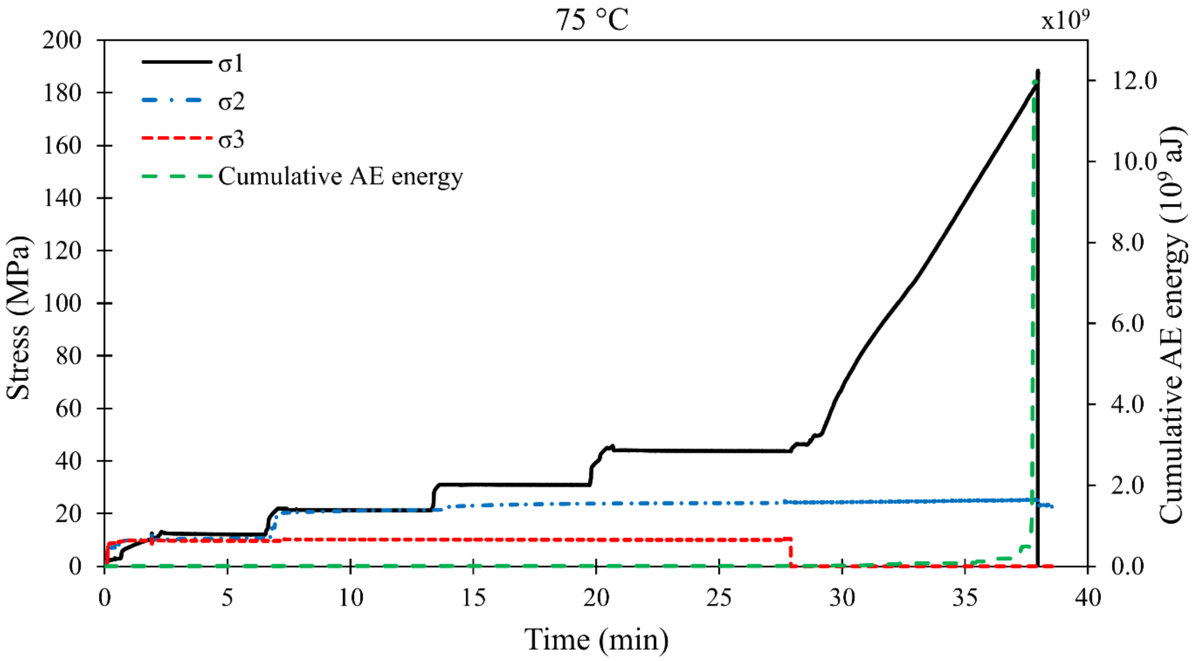
75 °C
x10⁹
Stress (MPa)
200
180
160
140
120
100
80
60
40
20
0
σ1
σ2
σ3
Cumulative AE energy
12.0
10.0
8.0
6.0
4.0
2.0
0.0
Cumulative AE energy (10⁹ aJ)
0
5
10
15
20
25
30
35
40
Time (min)

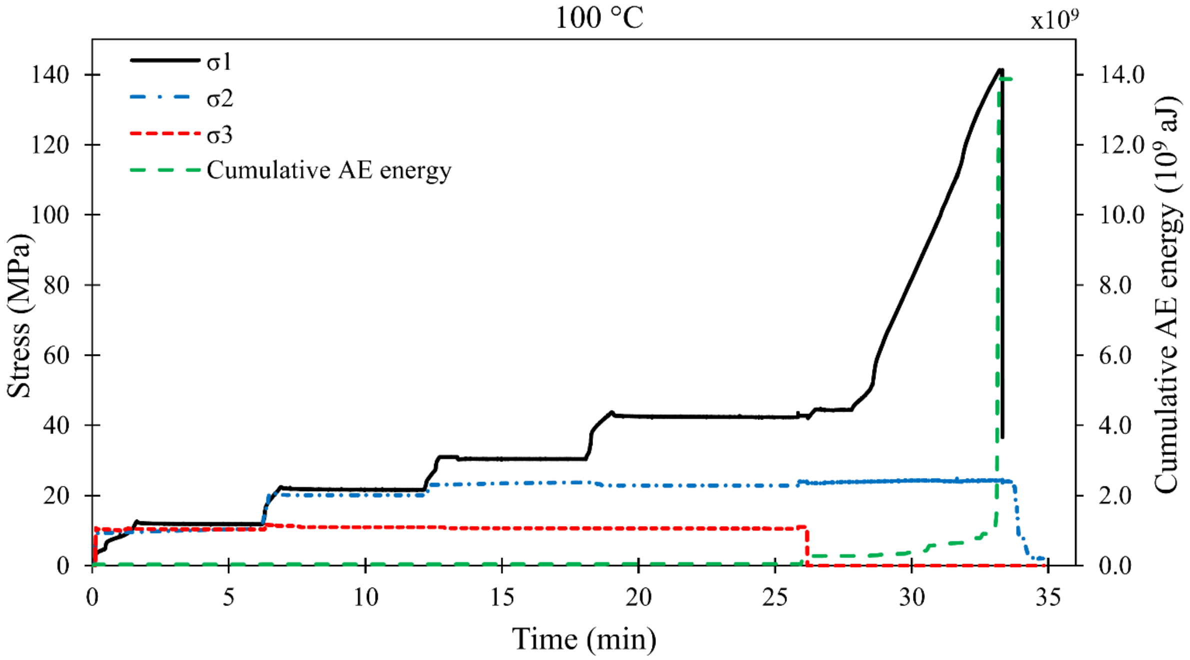
100 °C
x10⁹
Stress (MPa)
140
120
100
80
60
40
20
0
σ1
σ2
σ3
Cumulative AE energy
14.0
12.0
10.0
8.0
6.0
4.0
2.0
0.0
Cumulative AE energy (10⁹ aJ)
0
5
10
15
20
25
30
35
Time (min)

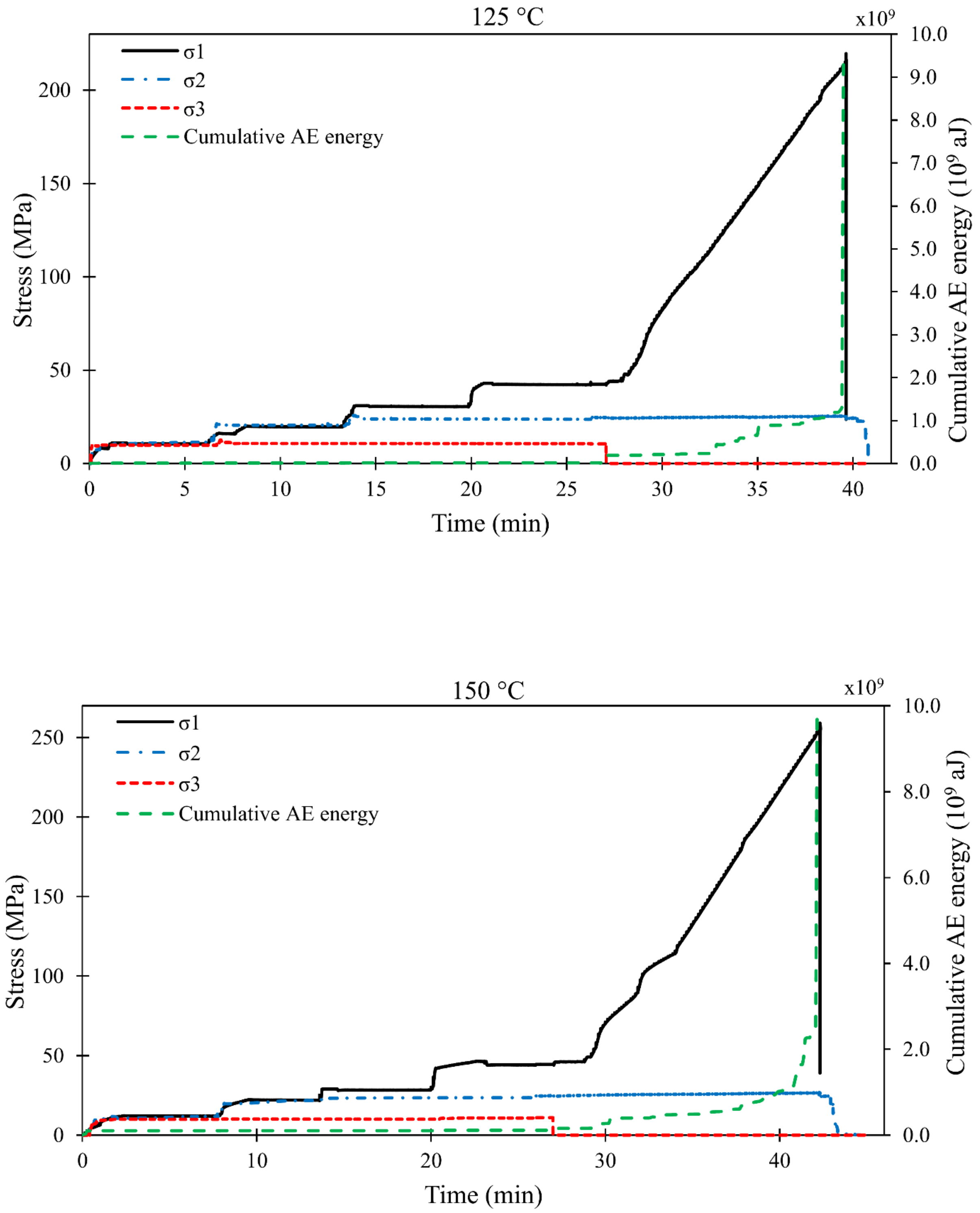

Figure 5.6 Actual stress paths and cumulative AE energy of the granite rock specimens under different temperature conditions

When σ_3 was removed, the stepwise increase in the cumulative AE energy can be seen, and then a gradual increase due to new stable micro-crack generation and coalescence. In the final period, a rapid increase of AE activities was observed, due to the developments of unstable macro-cracks, and coalescence until failure (see Figure 5.6).

Profiles of the six surfaces of the granite specimen B1#1 after strain burst testing are presented as the representative results in Figure 5.7. The profiles of all the specimens after strain burst tests are given in Appendix A. The orientation of the tensile fractures near the free face is almost parallel to σ_1. It can be seen from Figure 5.8 that strain burst stress changes with temperature. Strain burst stresses were normalised with respect to the average UCS value of rectangular prism specimens (25 mm × 50 mm × 125 mm) as it would be more consistent to compare the results of UCS from rectangular prism than the cylindrical ones. Note that strain burst stress refers to the stress level where the first rock fragments were ejected from the free face of the specimens. As shown in Figure 5.8, the strain burst stress decreased when the temperature increased from 25 °C to 100 °C since the thermally induced microstructures may lead to the degradation of mechanical strength (Sirdesai et al. 2017). For the granite specimens treated with temperatures 50 °C, 75 °C and 100 °C, the average strain burst stress decreased by 15.7%, 32.2% and 44.6% respectively in reference to the samples at room temperature 25 °C. The average normalised strain burst stress level also decreased from 1.37 to 0.76. When the temperature was increased from 100 up to 150 °C, strain burst stress showed a gradual increase. The normalised strain burst stress varied from 0.76 to 1.15. It is believed that this can be attributed to the thermal expansion of mineral grains by temperature which improved the compactness of the rocks. This observation is consistent with those stated by Yin et al. (2012) who investigated the effect of thermal treatment on granite samples.

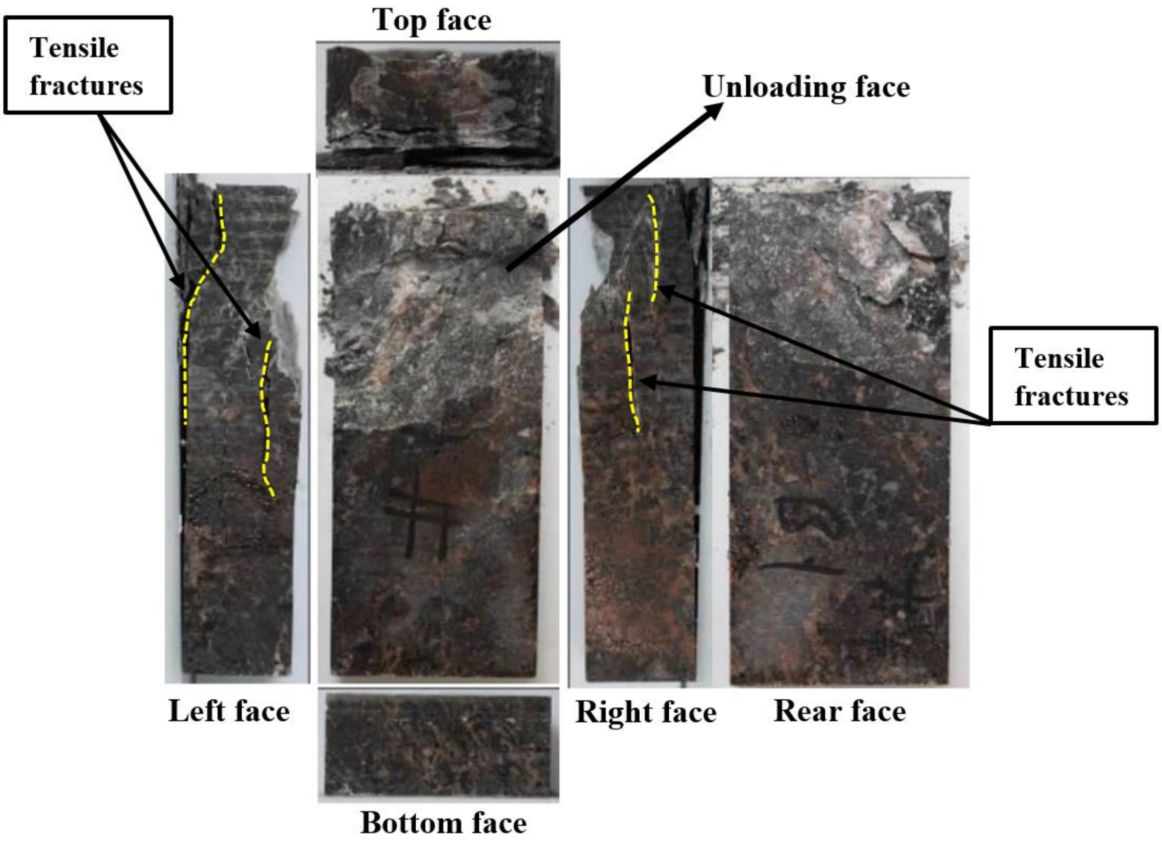

Figure 5.7 Six surfaces for granite specimen B1#1 after strain burst test

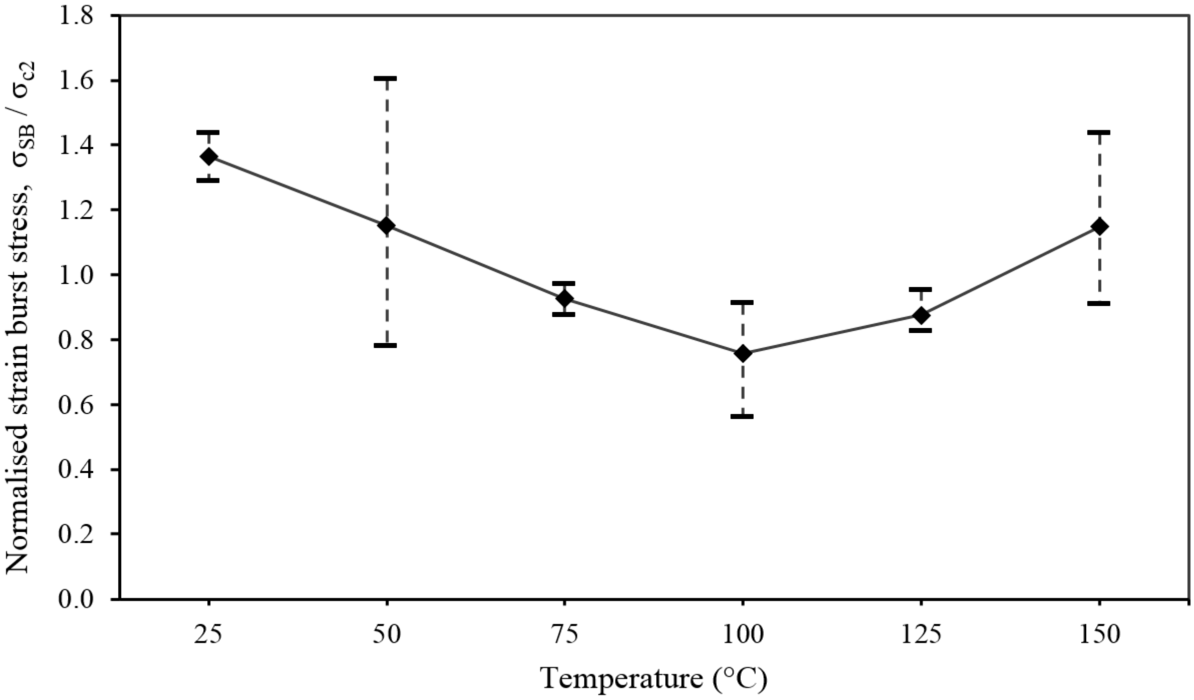

Figure 5.8 Influence of temperature in strain burst stress

5.3.2 - Observations on the influence of thermal damage on strain burst behaviour

In order to capture the failure processes of the granite samples induced by the different temperature conditions, a high-speed camera was used. Using a frame rate of 1000 f/s (frames per second), the dynamic failure characteristics of the tested samples, including the crack growth and fragment ejection were observed. A series of images for the samples were captured to investigate the influence of temperature on the rock failure process. These are presented in Figure 5.9. The numbers at the bottom-left corner of the snapshots indicate time in h:m:s:ms. It should be noted that regardless of the temperature, strain bursts occurred in all specimens. A common strain burst development process for all of the specimens was as follows: Splitting of rock into rock plates, bending of the rock plates, ejection of rock fragments, and rock plates at high speeds accompanied by a loud explosion sound after the rock plates break off. It can be observed from Figure 5.9 that the intensity of the strain burst differs moderately in different temperature conditions. For granite specimen tested at the temperature of 25 °C, (see Figure 5.9a), where the specimen did not experience any thermal damage, the upper part of the free face split into rock plates, and small fragments were ejected at high speed. After the upper rock plate broke off, a large number of fragments and rock plates were suddenly ejected outward, and this activity was associated with a loud sound. The final strain burst pit area was around half of the whole free surface of the specimen and tensile cracks near the free face occurred parallel to σ_1 on both lateral sides. When the temperature was increased up to 100 °C (see Figure 5.9d), strain burst further became less violent. This may be caused by the thermal damage due to the deteriorated bonding among mineral grains that rendered the rock relatively weaker after temperature. Tensile cracks are observable at the free face of the sample. As the temperature increased from 100 °C to 150 °C, more violent strain burst characteristics were observed, as shown in Figure 5.9e-f. This gradual change can be attributed to the compaction of the rock samples due to the closure of pre-existing micro-cracks (Kumari et al. 2017a).

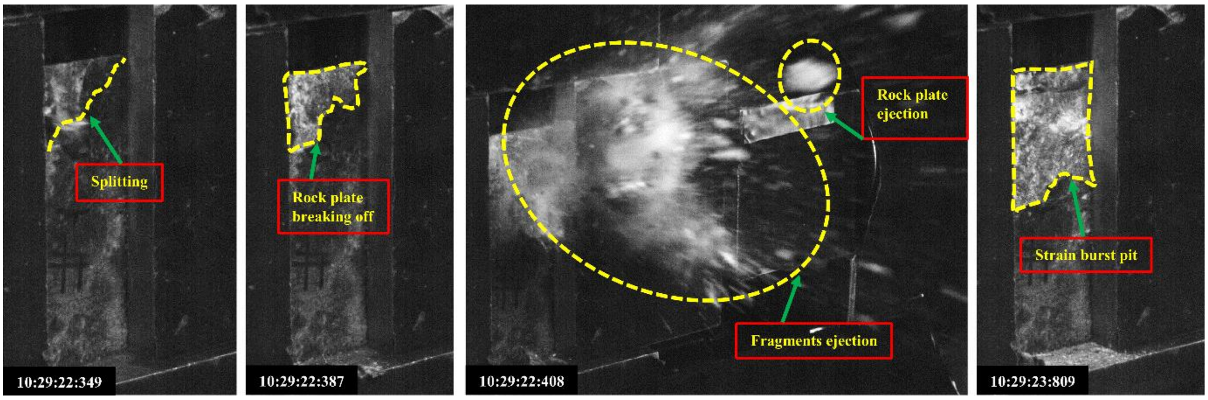
Splitting
10:29:22:349
Rock plate breaking off
10:29:22:387
Rock plate ejection
Fragments ejection
10:29:22:408
Strain burst pit
10:29:23:809

(a)

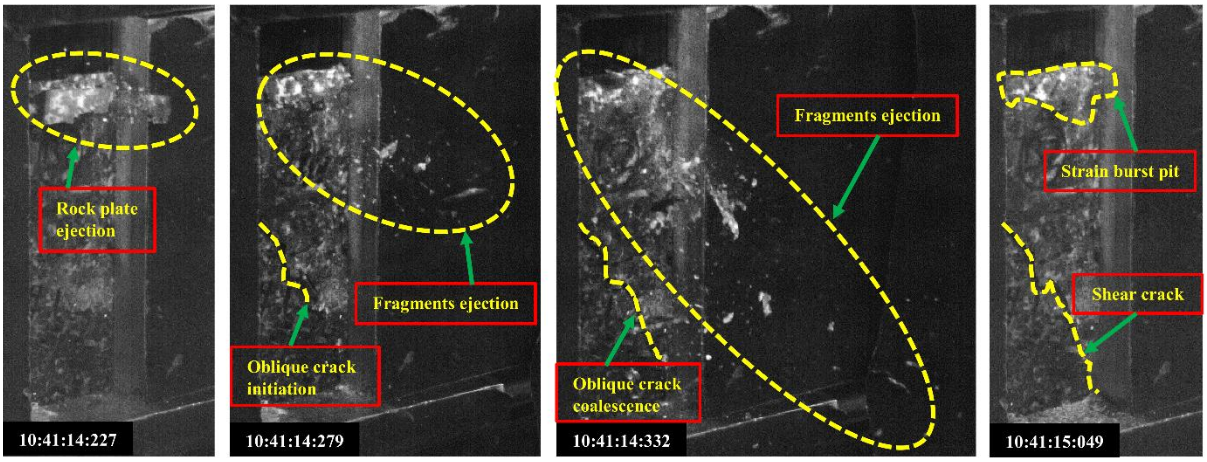
Rock plate ejection
10:41:14:227
Fragments ejection
Oblique crack initiation
10:41:14:279
Fragments ejection
Oblique crack coalescence
10:41:14:332
Strain burst pit
Shear crack
10:41:15:049

(b)

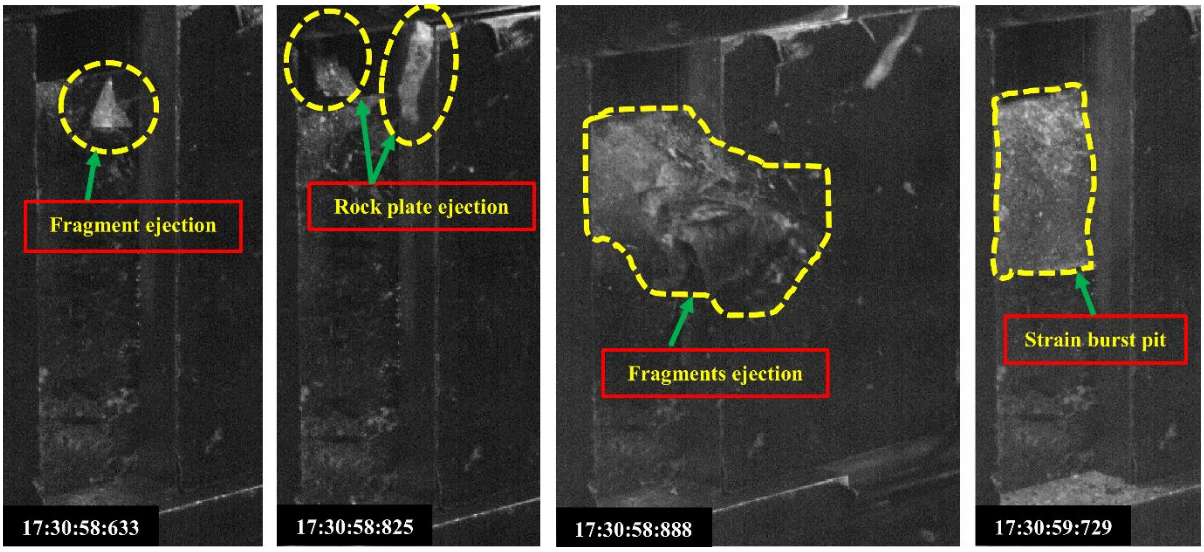
Fragment ejection
17:30:58:633
Rock plate ejection
17:30:58:825
Fragments ejection
17:30:58:888
Strain burst pit
17:30:59:729

(c)

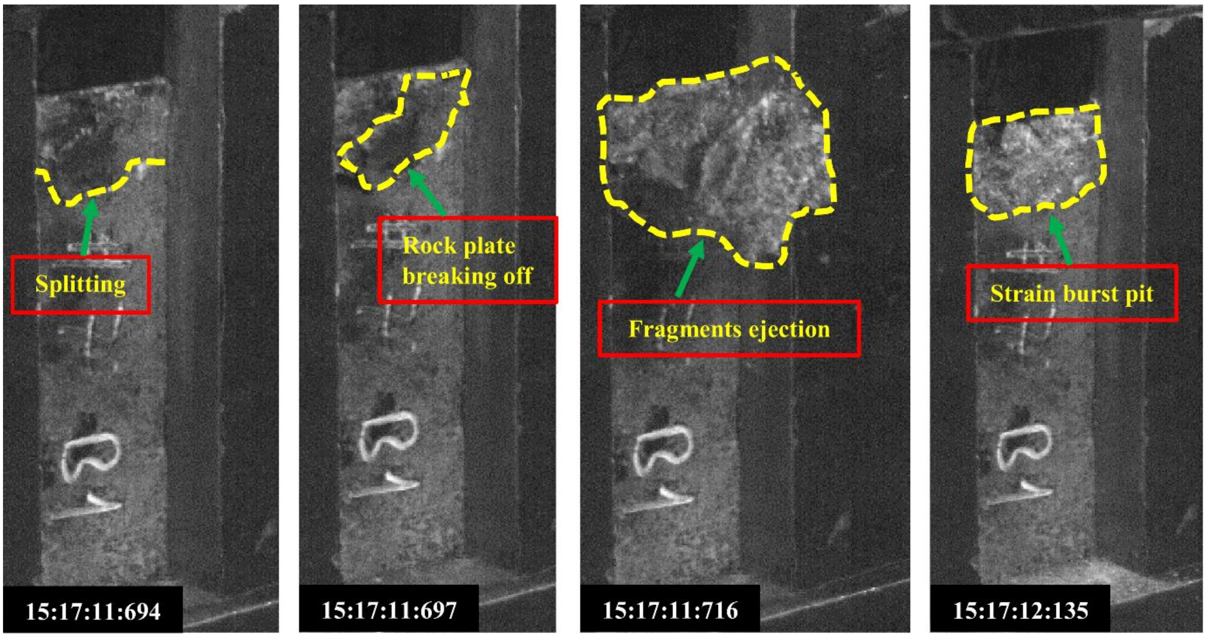
Splitting
15:17:11:694
Rock plate breaking off
15:17:11:697
Fragments ejection
15:17:11:716
Strain burst pit
15:17:12:135

(d)

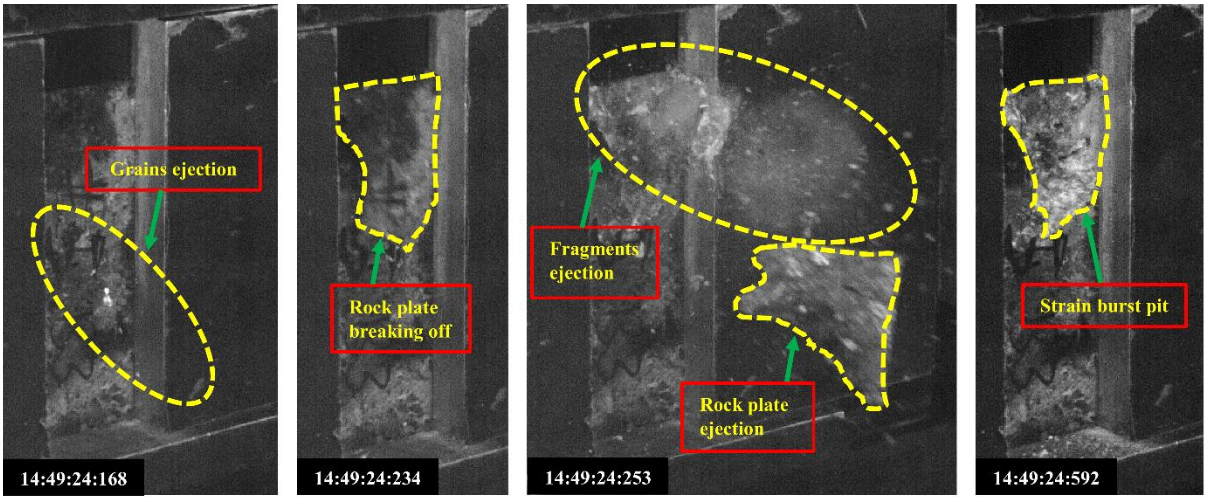
Grains ejection
14:49:24:168
Rock plate breaking off
14:49:24:234
Fragments ejection
Rock plate ejection
14:49:24:253
Strain burst pit
14:49:24:592

(e)

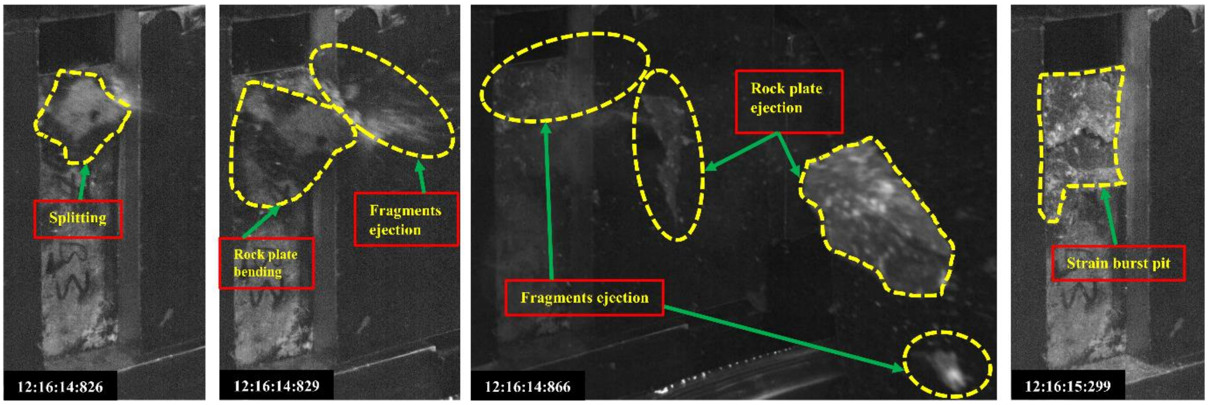
Splitting
12:16:14:826
Rock plate bending
Fragments ejection
12:16:14:829
Rock plate ejection
Fragments ejection
12:16:14:866
Strain burst pit
12:16:15:299

(f)

Figure 5.9 Rock failure process of the granite specimens treated with different temperatures captured by the high-speed camera: (a) T = 25 °C; (b) T = 50 °C; (c) T = 75 °C; (d) T = 100 °C; (e) T = 125 °C; (f) T = 150 °C

5.3.3 - AE analysis for thermal damage assessment

It is well understood that rock failure is accompanied by the release of energy. Elastic waves propagating from a source within a material by the rapid release of localised energy can be defined as an acoustic emission. The AE method has been widely used to investigate brittle rock failure, and to quantify rock damage in many engineering applications (Lockner 1993, Grosse and Ohtsu, 2008; Nicksiar and Martin 2012; Carpinteri et al. 2013; Zhao et al. 2015; Karakus et al. 2016). As shown in Figure 5.4, the AE technique was used to monitor the evolution of damage inside the granite samples at various temperatures.

Time-domain analysis

AE parameters such as counts, hits, energy, amplitude and frequency were obtained from the AE monitoring system and the fracturing processes of strain burst under different temperature conditions were investigated. While the number of cracks is manifested by AE hits, the magnitude of the micro-cracking is related to the AE energy. Cumulative AE energy was therefore used to assess the energy release characteristics of the granite specimens subjected to various temperatures under true-triaxial unloading conditions. Figure 5.6 illustrates the evolution of cumulative AE energies of the samples. It can be seen that although temperature conditions were different, the evolution features of cumulative AE energy for the six specimens underwent a similar trend from the beginning of loading until strain burst. Based on the cumulative AE energy characteristics, the evolution of AE behaviour was divided into three typical stages, i.e., the AE quiet linear elastic deformation stage, the AE growth stage and the AE active strain burst stage. Figures 5.10a and 5.11a depict the rate and cumulative plots of the AE energy and hits versus the time and also corresponding normalised strain burst stress in which the three deformation stages of strain burst are also demonstrated. The damage caused by temperature was quantified by changes in AE signal characteristics. Therefore, thermal damage for strain burst (D_{SB}) can be calculated for the granite specimens treated with different temperature conditions by using Equation 5.1.

$$D_{SB} = \frac{\Omega}{\Omega_m} \tag{5.1}$$

where Ω is the cumulative amount of AE energy or number of hits at a certain time during the damage evolution and Ω_m is the cumulative amount of energy or number of hits during the whole testing period. Note that it is also significant that $0 \leq \Omega \leq \Omega_m$ and $0 \leq D_{SB} \leq 1$, in which 0 corresponds to the initial undamaged state of the rock and 1 corresponds to the strain burst.

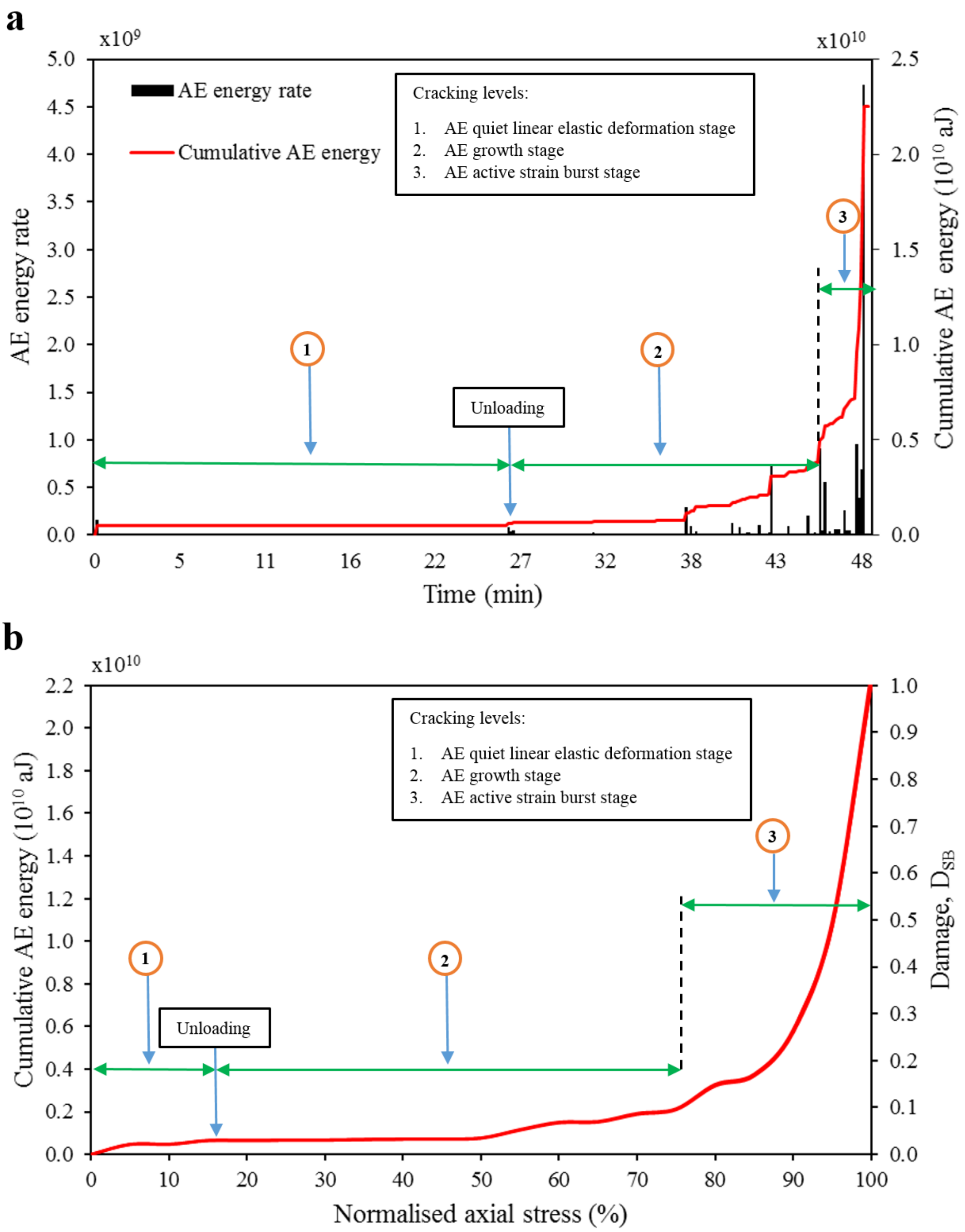

Figure 5.10 Plots of (a) AE energy rate and (b) cumulative AE energy and damage evolution by AE energy versus normalised strain burst peak stress at corresponding stages shown in part a for the rock at temperature of 25 °C

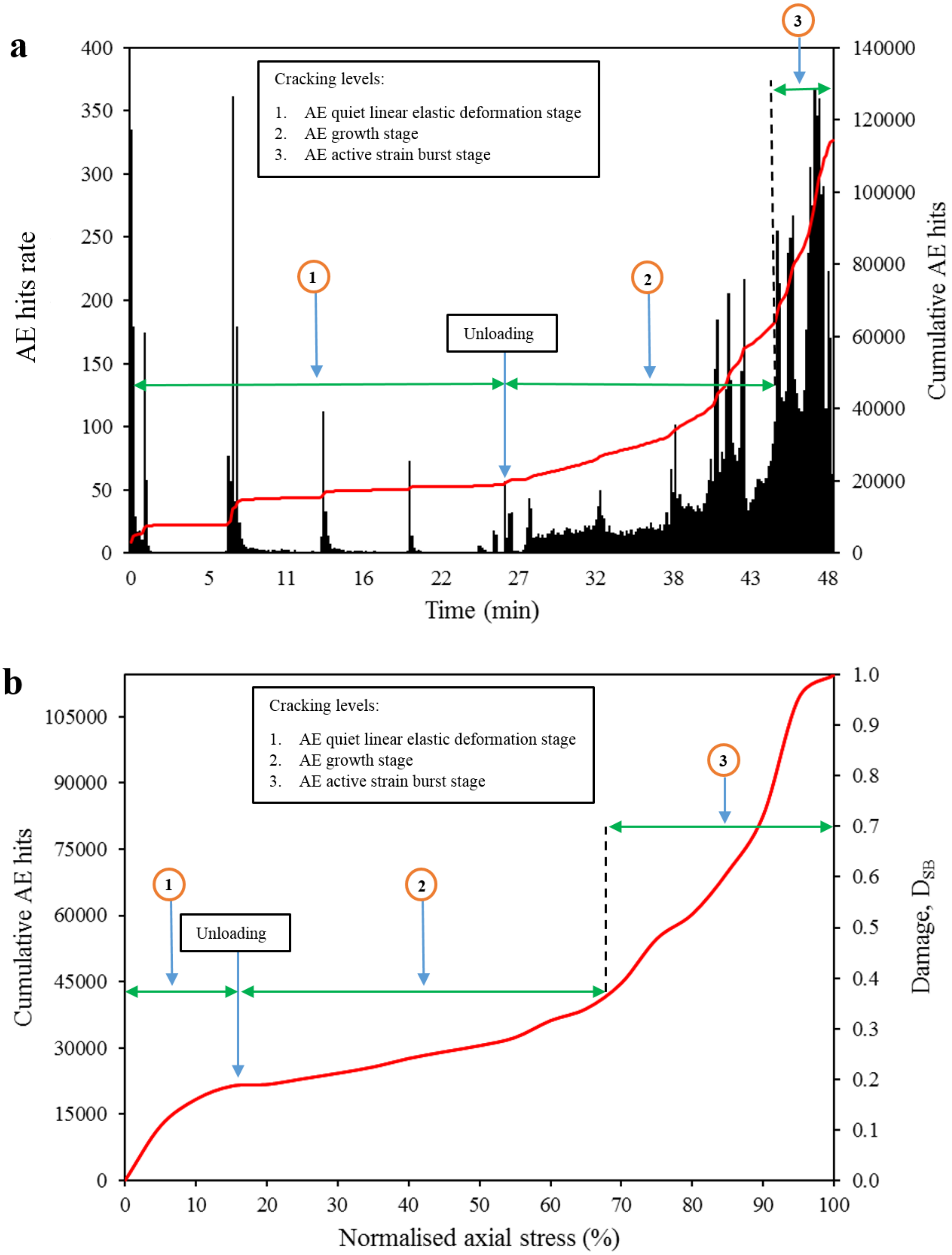

Figure 5.11 Plots of (a) AE hits rate and (b) cumulative AE hits and damage evolution by AE hits versus normalised strain burst peak stress at corresponding stages shown in part a for the rock at temperature of 25 °C

At the initial stage, a sudden increase can be observed due to the closure of pre-existing cracks, voids or other defects. After the majority of the natural cracks compacted, the rocks went into a linear elastic deformation period. During the stress maintenance phase, the cumulative AE energy rate changed little indicating that no micro-cracking inside the rocks was observed. During this phase, stiffness started to decrease, and it was associated with signifying tensile or shear movements between the faces of closing or closed cracks (Eberhardt et al. 1998). Upon the unloading of the minimum principal stress σ_3, the cumulative AE energy gradually increased, revealing that new micro-cracks generated and started to grow. However, their low AE energy indicates that they have limited influence on decreasing the overall strength of the rock and thus cannot cause strain bursting. As the maximum principal stress σ_1 was further increased while intermediate principal stress σ_2 was maintained constant, the micro-cracks began to propagate to a few large cracks, to coalescence and to form macro-cracks. This increasingly contributed to the degradation of the inherent rock strength, which was revealed by a high amount of cumulative AE energy. At AE active strain burst stage, due to the unstable coalescence of macro-cracks and the ejection of rock fragments from the free face, cumulative AE energy associated with higher amplitudes rapidly increased at a high rate until strain burst occurred. Figure 5.12 presents variations on the cumulative AE energy and cumulative AE counts with the temperature for all granite specimens. In general, increasing the number of micro-fractures caused a decline in both cumulative AE energy and counts. Nevertheless, as observed in this work, this trend is only correct for sufficiently high temperatures. For example, when the temperatures reached 100 °C and 150 °C, the cumulative AE energy of the samples decreased by 14%-20%, and the cumulative AE counts declined by 20%-55%, compared with the values at 25 °C.

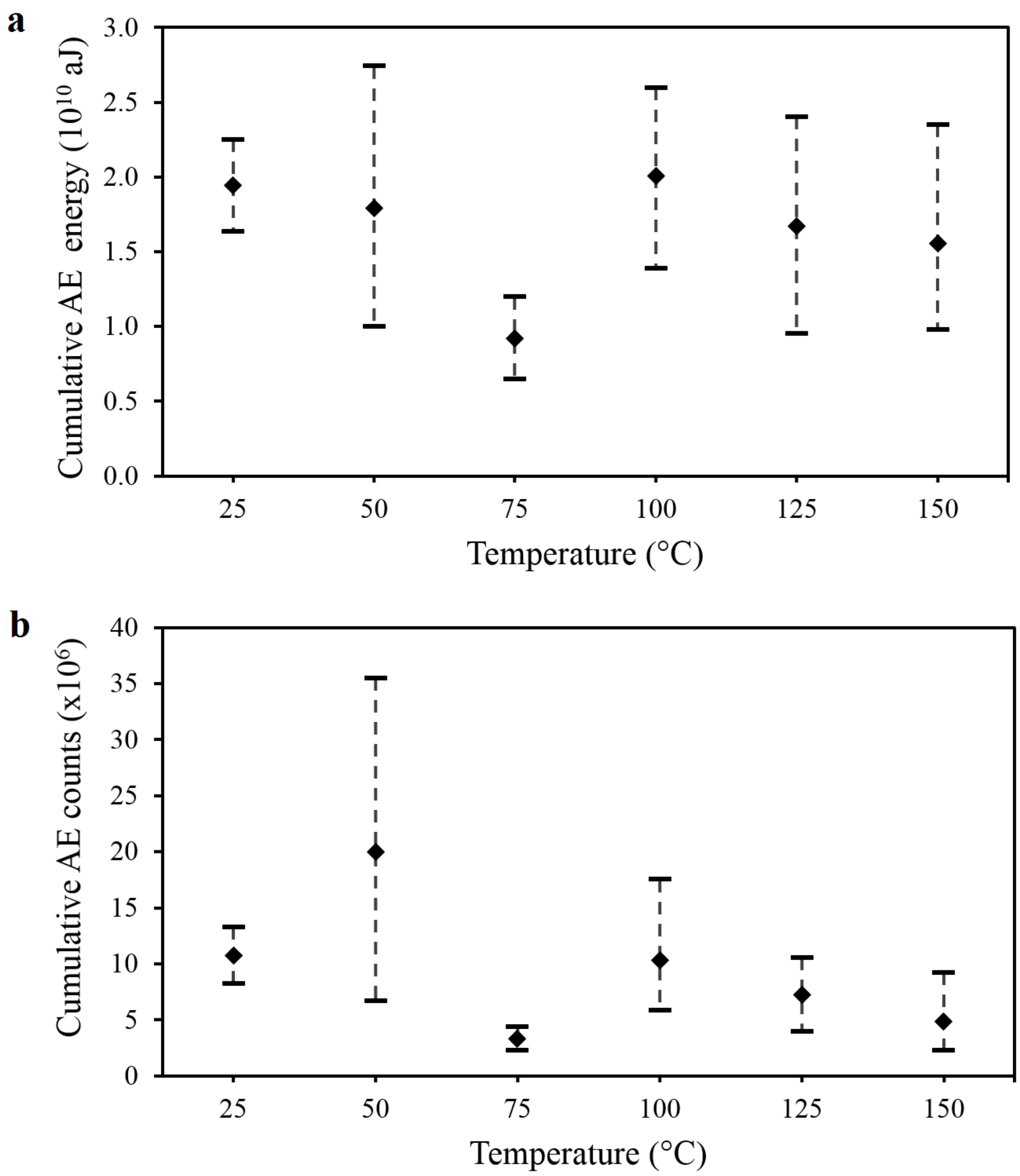

Figure 5.12 Influence of temperature on (a) cumulative AE energy (b) cumulative AE counts

The thermal damage influence on strain burst intensity was investigated by estimating the bursting rates. The evolution of damage was divided into 4 stages, and the slopes of these stages were calculated (see Figure 5.13a). It can be stated that the slope of the damage and cumulative AE energy in the last stage drastically increases the normalised stress level of 90-95%. This is associated with accumulated energy inside the rock. As displayed in Figure 5.13b, thermal damage has a significant influence on the damage accumulation rate and on bursting. When the temperature was increased up to 100 °C, the accumulation rate of thermal damage increased. It is believed that thermally induced microcracks triggered the accumulated damage inside the samples which also influenced the intensity of the strain burst. Therefore, the specimens treated with temperatures from room temperature 25 °C to 100 °C exhibited less intense strain bursts due to the rapid damage accumulation (see Figure 5.14).

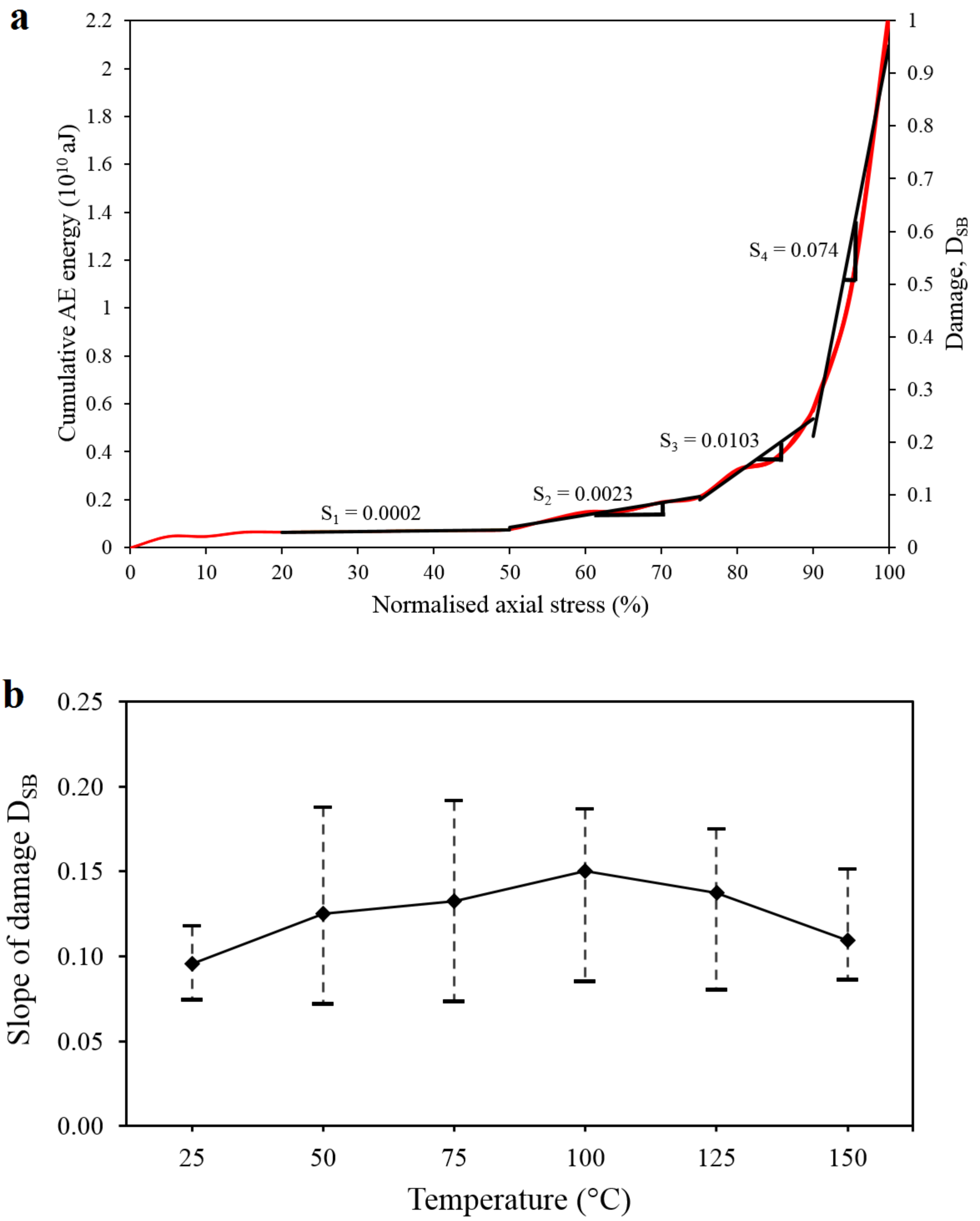

Figure 5.13 (a) Slopes of the strain burst damage, D_{SB}, evolution stages (b) influence of temperature on damage accumulation

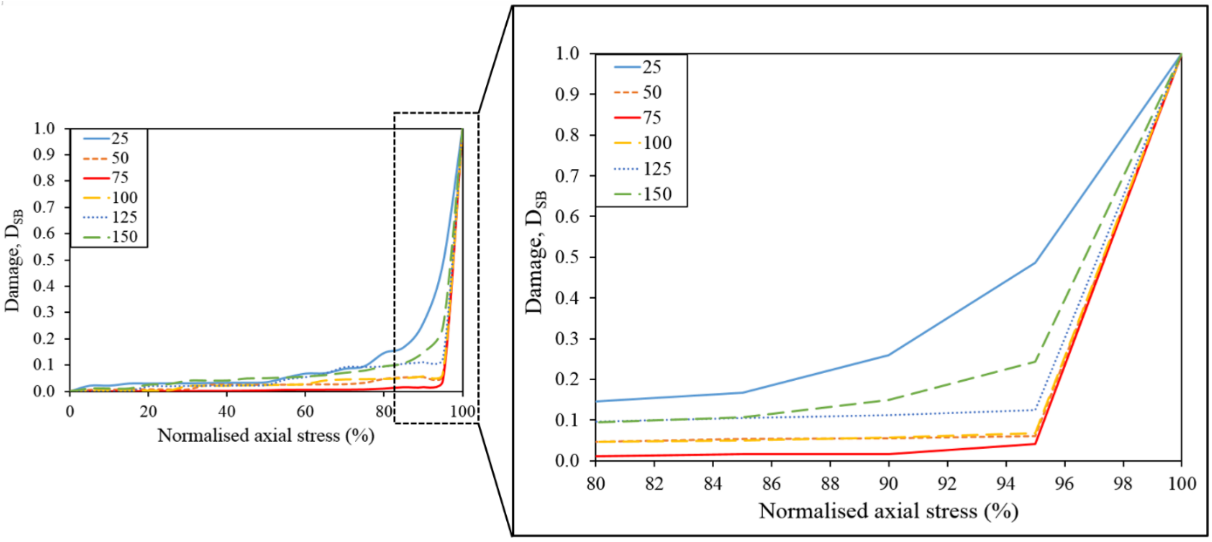

Figure 5.14 Thermal damage influence on damage accumulation rate

b-value analysis

The *b*-value from Gutenberg-Richter's equation (Gutenberg and Richter 1956) has been widely used to assess the internal damage evolution of rock (Grosse and Ohtsu 2008; Carpinteri et al. 2009; Sagar et al. 2012; Kim et al. 2015). The Gutenberg-Richter relation between the cumulative frequency-magnitude distributions of AE data is given in seismology by Equation. 5.2.

$$log_{10}(N) = a - b\left(\frac{A_{dB}}{20}\right) \tag{5.2}$$

where A_{dB} is the peak amplitude of AE events in decibels, N is the incremental frequency which can be defined as the number of AE hits with an amplitude greater than A_{dB} and the *b*-value is the negative slope of the log-linear plot between frequency and amplitude.

For three deformation stages, *b*-values were calculated by plotting the cumulative AE hits, peak amplitude distribution, and fitting curve (an example of calculation of *b*-values can be seen in Figure 5.15a). Fracture density can be represented by the y-intercept of the fitting line and as can be observed that y-intercepts of the three deformation stages decrease from the initial AE quiet stage to the AE active stage.

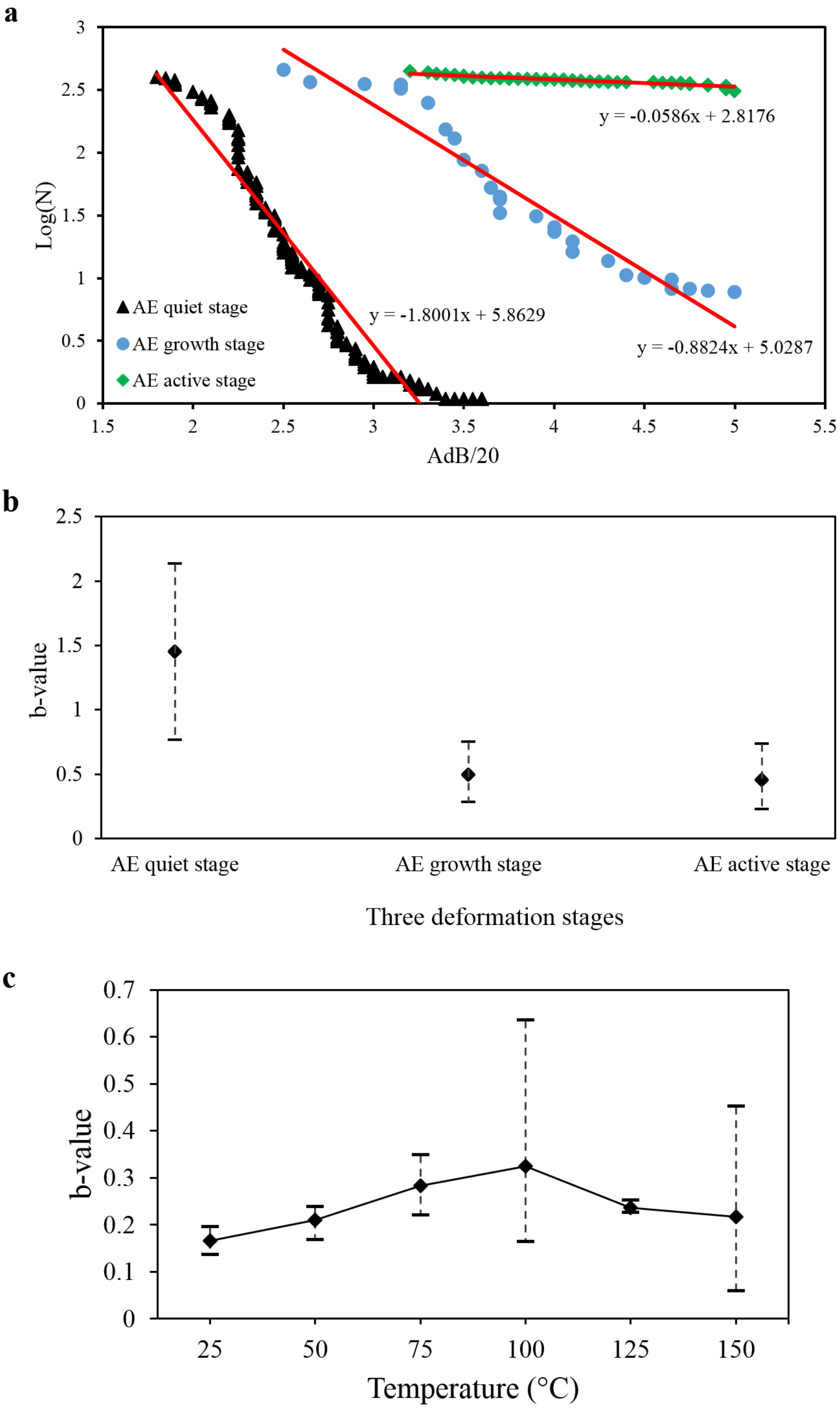
a
Log(N)
AdB/20
3
2.5
2
1.5
1
0.5
0
1.5
2
2.5
3
3.5
4
4.5
5
5.5
▲ AE quiet stage
● AE growth stage
◆ AE active stage
y = -0.0586x + 2.8176
y = -1.8001x + 5.8629
y = -0.8824x + 5.0287
b
b-value
2.5
2
1.5
1
0.5
0
AE quiet stage
AE growth stage
AE active stage
Three deformation stages
c
b-value
0.7
0.6
0.5
0.4
0.3
0.2
0.1
0
25
50
75
100
125
150
Temperature (°C)

Figure 5.15 Example of calculation of *b*-values (a) AE incremental frequency and amplitude distribution and *b*-value calculation, (b) average *b*-values and standard deviations in three deformation stages for the granite specimen at temperature level of 150 °C (c) temperature influence on *b*-value at AE active stage

Figure 5.15b presents the estimated b-values in three deformation stages and at the evolution. At the initial stage, the closure and compaction of pre-existing microcracks, voids or other defects resulted in high *b*-values. This is evidenced by a large number of AE events with low magnitude. During the generation of new micro-cracks, and also during the stable growth of micro-cracks (no macro-crack formation), a few AE events were observed. In the AE active stage, *b*-values decreased sharply. This indicates that AE events with higher amplitudes were detected due to the accelerated unstable crack growth, and coalescence until strain burst. This sudden change in the *b*-value also indicates that the damage accumulated inside the rock is increasing. Therefore, the higher *b*-value trend suggests that micro-crack growth, whilst lower *b*-value trend implies that macro-cracks have formed inside the rock that can be used as a damage alert.

Figure 5.15c presents the influence of temperature on the *b*-value at AE active stage. Although, Carpinteri et al. (2009) indicated that *b*-value changes systematically from 1.5 (in which damage in the material is still uniform at a condition of criticality) to 1.0 when the final failure is imminent characterised by a strong damage localisation, *b*-values in Figure 5.15c are less than 1.0 since they were calculated for AE active stage. When the temperature increased to 100 °C, *b*-values show an increasing trend. This indicates that thermal damage reduced the macro-cracking process due to the mechanical degradation of the samples which in turn resulted in less intense strain bursting. As the temperature increased from 100 °C to 150 °C, *b*-values gradually declined which can reveal more intense strain burst characteristics. Therefore, *b*-value analysis can be used to assess the type of deterioration of the rock and to quantify the damage degree.

Frequency-domain analysis

The frequency-amplitude characteristics of the AE waves of the six granite specimens treated different temperatures are presented in Figure 5.16. The frequency-amplitude behaviours of the AE signals showed trends similar to the total cumulative AE energy responses. Increasing the temperature led to a low-frequency band of and higher amplitudes (see Figure 5.16). When the frequency-amplitude distribution was higher, significant energy release and intense cracking and bursting evolution were observed. Moreover, the amplitudes gradually increased and reached the maximum values during strain burst except during the initial loading period.

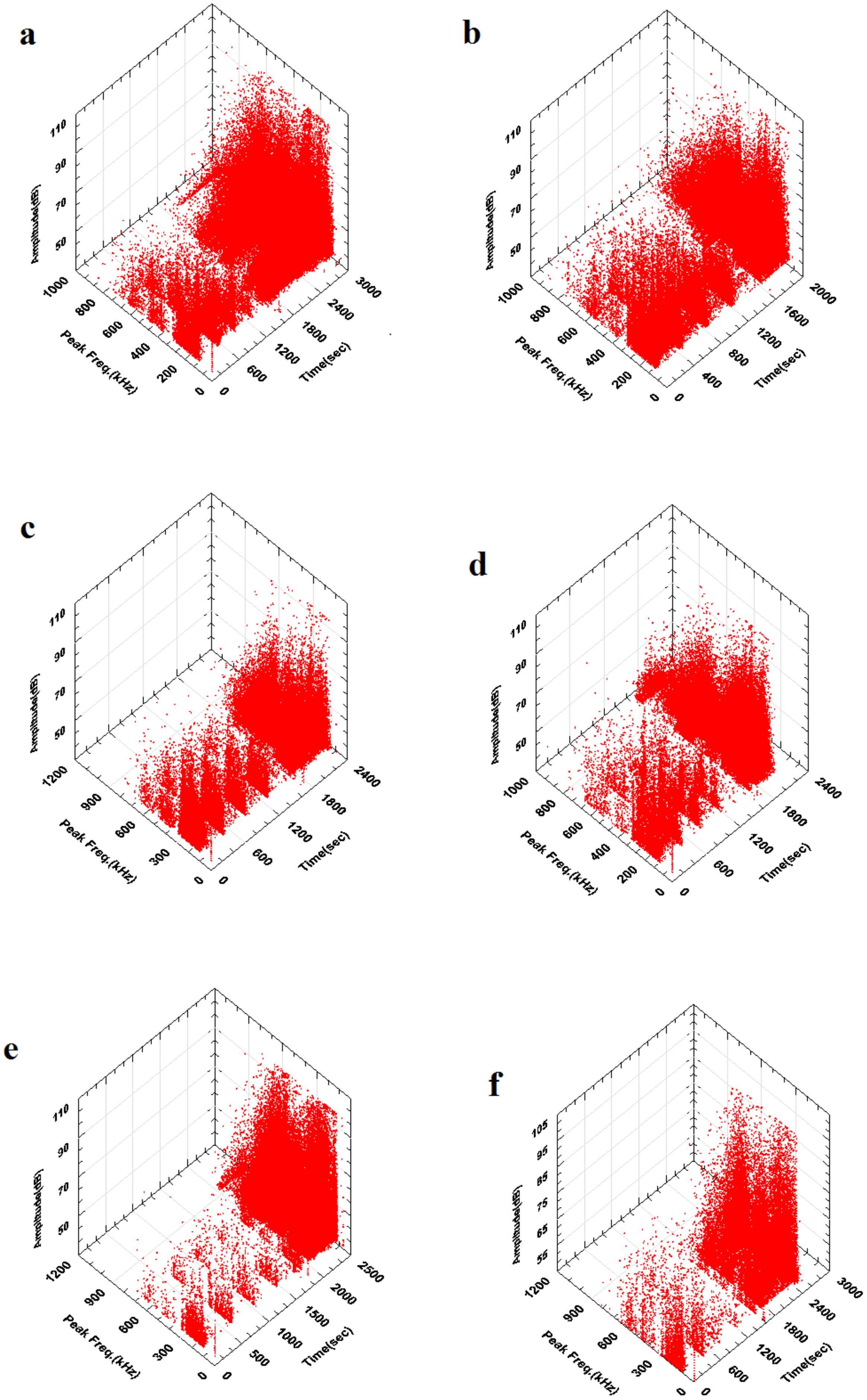
a
Amplitude(dB)
110
90
70
50
Peak Freq.(kHz)
1000
800
600
400
200
0
Time(sec)
0
600
1200
1800
2400
3000
b
Amplitude(dB)
110
90
70
50
Peak Freq.(kHz)
1000
800
600
400
200
0
Time(sec)
0
400
800
1200
1600
2000
c
Amplitude(dB)
110
90
70
50
Peak Freq.(kHz)
1200
900
600
300
0
Time(sec)
0
600
1200
1800
2400
d
Amplitude(dB)
110
90
70
50
Peak Freq.(kHz)
1000
800
600
400
200
0
Time(sec)
0
600
1200
1800
2400
e
Amplitude(dB)
110
90
70
50
Peak Freq.(kHz)
1200
900
600
300
0
Time(sec)
0
500
1000
1500
2000
2500
f
Amplitude(dB)
105
95
85
75
65
55
Peak Freq.(kHz)
1200
900
600
300
0
Time(sec)
0
600
1200
1800
2400
3000

Figure 5.16 AE frequency-amplitude features of the six granite specimens treated with different temperatures: (a) T = 25 °C; (b) T = 50 °C; (c) T = 75 °C; (d) T = 100 °C; (e) T = 125 °C; (f) T = 150 °C

In order to investigate the influence of thermal damage on strain burst behaviours in greater depth, the frequency spectrum analysis was carried out. The AE signals were analysed using the Fast Fourier Transform (FFT) method (see Equation 5.3), as the frequency spectrum can be used to investigate the internal damage level during strain burst.

$$X_k = \sum_{k=0}^{N-1} x_n . e^{-i2\pi kn/N} \tag{5.3}$$

Figure 5.17 demonstrates the main frequency behaviour when the temperature was increased from room temperature (25 °C) to 150 °C. The average results show that the main frequency was approximately 261 kHz for room temperature samples and continually decreased to around 113 kHz as the temperature was increased. It is believed that the micro-cracking processes occurred over a long time period at low temperatures. However, when temperature increased, this micro-cracking period gradually diminished due to the thermal damage inside the specimens.

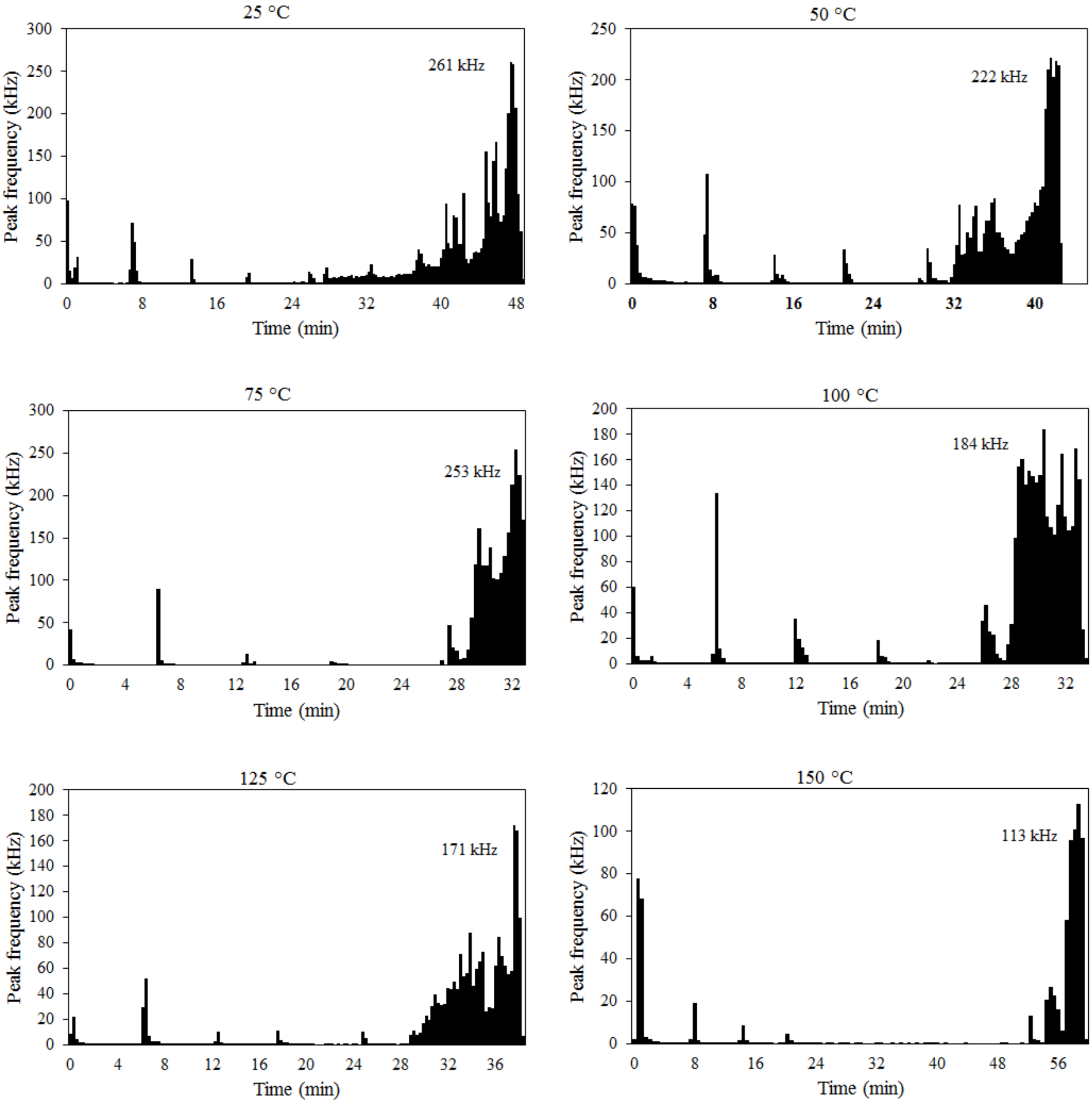

Figure 5.17 Influence of temperature on main frequency

5.3.4 - Kinetic energy analysis for strain burst due to thermal damage

The kinetic energy of the rock fragments ejected from the free face of the tested rock specimens can be used as an indicator for quantitatively evaluating the intensity of strain burst. Therefore, calculating the fragment ejection velocities can help us to better understand the energy mechanism of strain burst. A high-speed camera was employed to observe the fragment ejections. The fragment ejection speed was measured by analysing the high-speed videos. The captured images were used to track the movements of the ejected fragments. Note that since the ejected rock fragments are not of uniform size, only fragments with diameters larger than 10 mm and weighing more than 0.5 g were assessed. The granite sample treated with a temperature of 75 °C (B1#4) was taken as an example and the calculation procedure for the velocity of the ejected fragments are illustrated in Figure 5.18. Figure 5.18 provides a sketch of the ejected fragment trace, the coordinate system for estimating the location of fragments before and after ejection, a demonstration of a rock fragment, and location analysis.

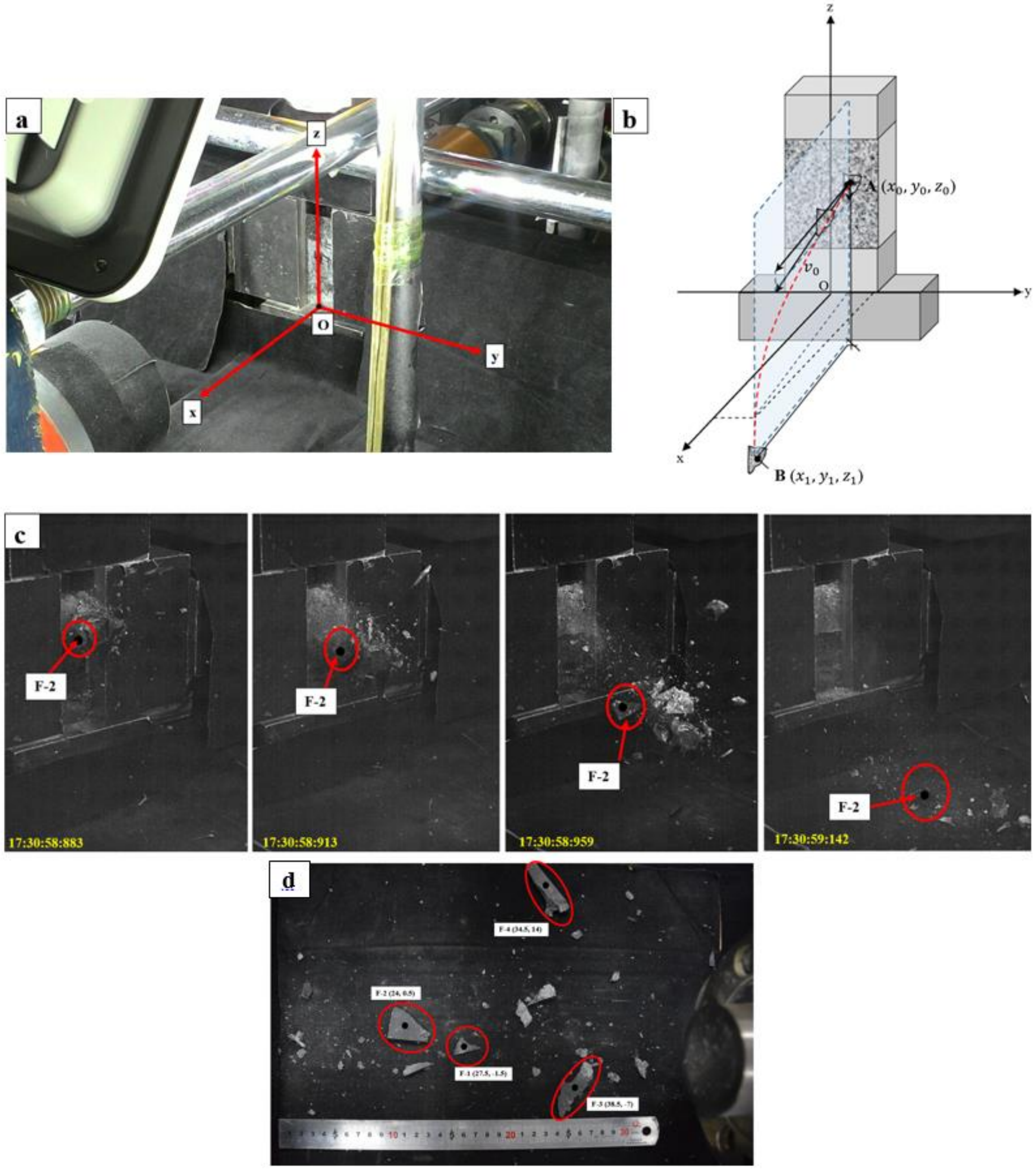

Figure 5.18 (a) Fragment coordinate information system, (b) sketch of the ejected fragment trace, (c) high-speed camera images of the ejected fragment (the numbers at the bottom-left corner of the images denote the time in h:m:s:ms and (d) location analysis of the ejected fragments

The kinetic energy calculation analysis of the ejected fragments can be described as follows. First, a three-dimensional spatial coordinate system was set up in which the centre bottom of the steel rig was selected as the origin point, denoted by a red circle (see Figure 5.18a). Then, the motion trail of relatively large fragments was traced after bursting, as illustrated in Figure 5.18b. The specific spatial locations of the fragments were determined from the side and top view of the high-speed photos (see Figure 5.18d). Figure 5.18c presents, the movement tracking of the fragment, F-2, from the free face of the granite sample at the onset of bursting to the bottom platform. After calculating the movement time, Δt, locations of the fragments before and after ejection were identified with respect to the spatial coordinate system. As can be seen in Figure 5.18b, the initial ejection location of the fragment is point A (x_0, y_0, z_0), which has an initial speed of V_0 and the final dropping down point is point B (x_1, y_1, z_1).

After measuring the velocity, the total kinetic energy of the ejected fragments was calculated by using Equation 5.4.

$$E_k = \sum_{i=1}^{n} \frac{1}{2} m_i \overline{v}_i^2 \tag{5.4}$$

where n is the number of fragments having D > 10 mm and m > 0.5 g, m_i is the mass of the ith rock fragment and $\bar{v}_i$ is the initial ejection velocity of the ith rock fragment. By using the equation above, the total kinetic energies for all granite specimens treated with different temperatures were calculated. Note that average velocity values of the ejected fragments were taken as the ejection velocity of a granite specimen. The ejection velocities and strain bursting of the granite specimens exposed to different temperature conditions from room temperature (25 °C) to 150 °C are displayed in Figure 5.19. Due to the thermal damage occurred inside the granite samples leading to the degradation of the mechanical characteristics, the ejection velocity of the fragments dramatically decreased when the temperature level was below 100 °C. With improved compactness between 100 °C and 150 °C, the velocity of the ejected fragments increased slightly, which is associated with relatively intense strain bursting (see Figure 5.20a).

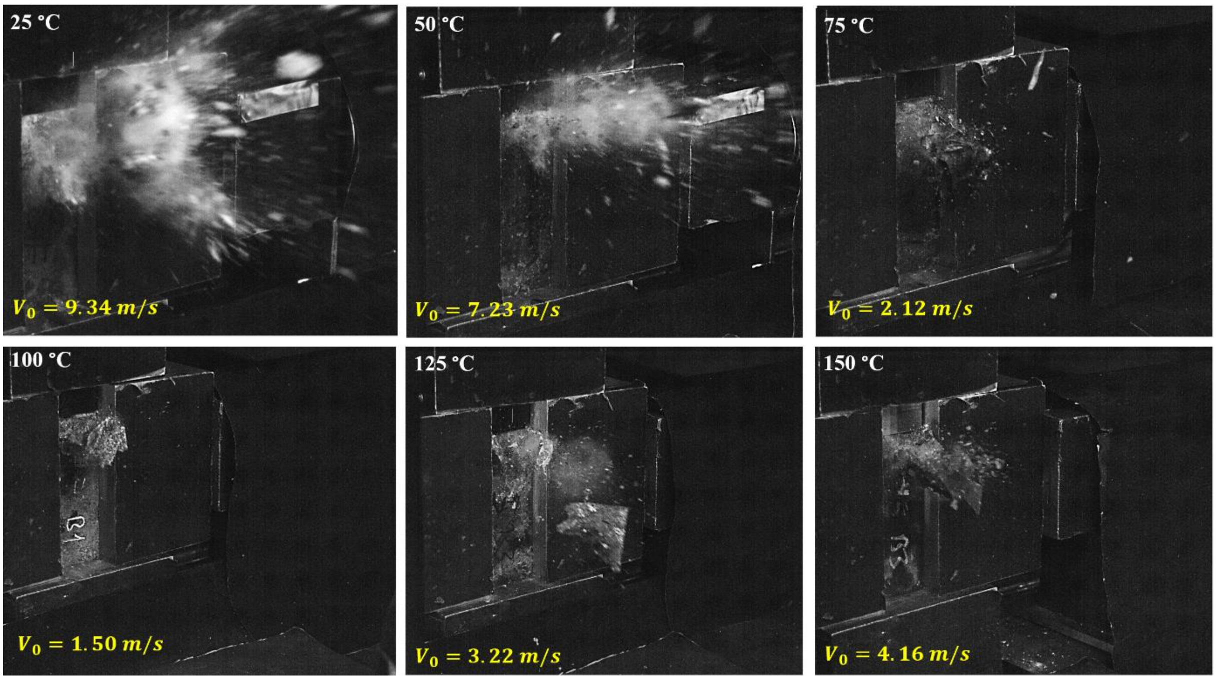

Figure 5.19 Ejection velocities of rock fragments from the granite specimens treated with different temperature conditions

The kinetic energy of the ejected fragments showed a trend similar to the ejection velocities. Kinetic energy continually decreased with the temperature, until the critical temperature level of 100 °C was reached. This is because the granite specimens manifested thermal damage (see Figure 5.20b). The strain burst stress and total elastic strain energy showed a decline in temperatures below 100 °C due to thermally induced damage and is shown in Figure 5.20a. It can also be seen that the amount of total elastic strain energy released from the granite specimens decreased because the thermally induced microcracks reduced the amount of strain energy accumulation (see Figure 5.21b). When the temperature increased from 100 °C to 150 °C, the accumulated strain energy within the granite specimens increased (see Figure 5.21a). Therefore, this led to the higher amount of the strain energy release associated with an increase in kinetic energy, as shown in Figure 5.20a.

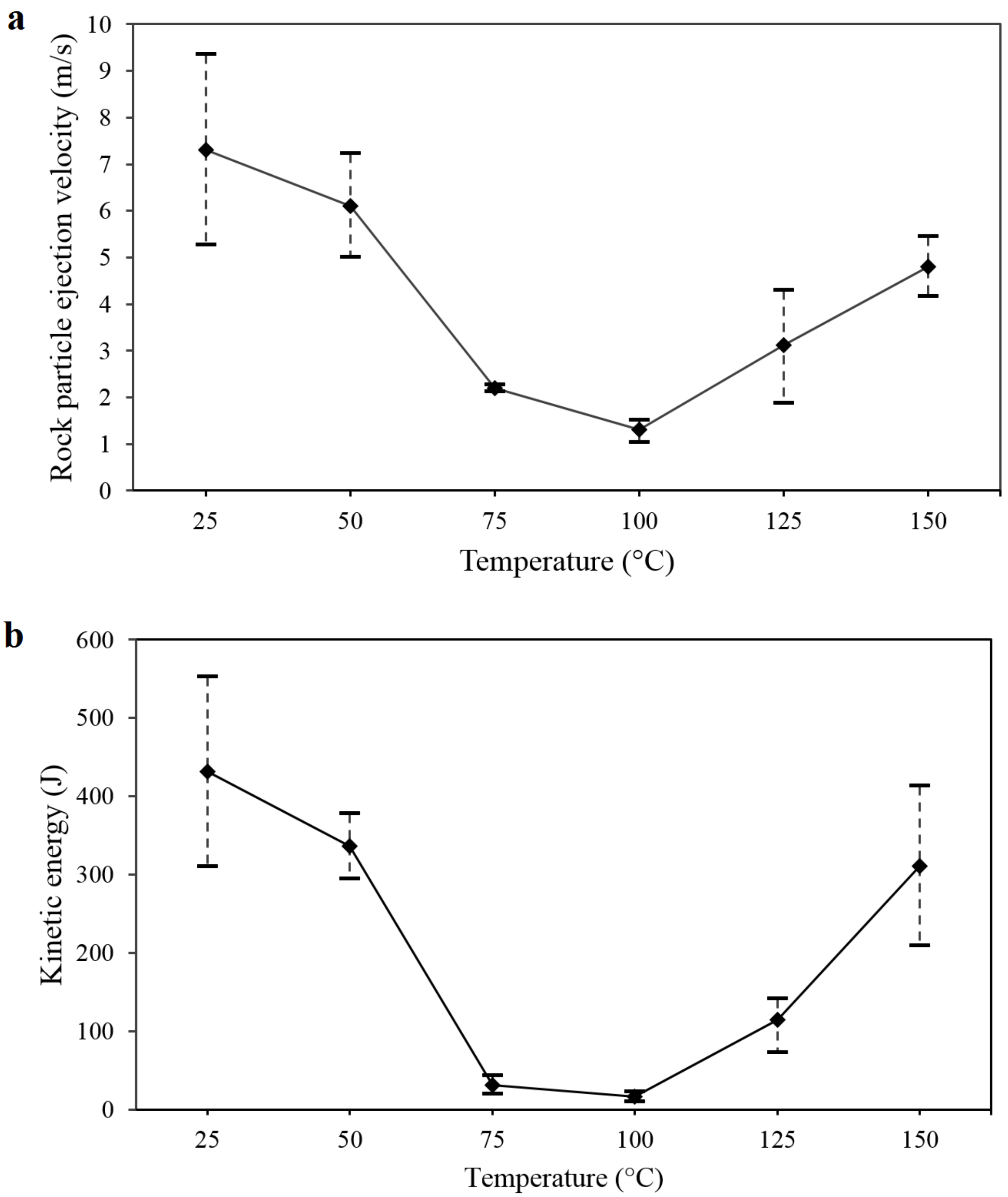

Figure 5.20 Ejection velocity and kinetic energy of the granite specimens treated with different temperature conditions

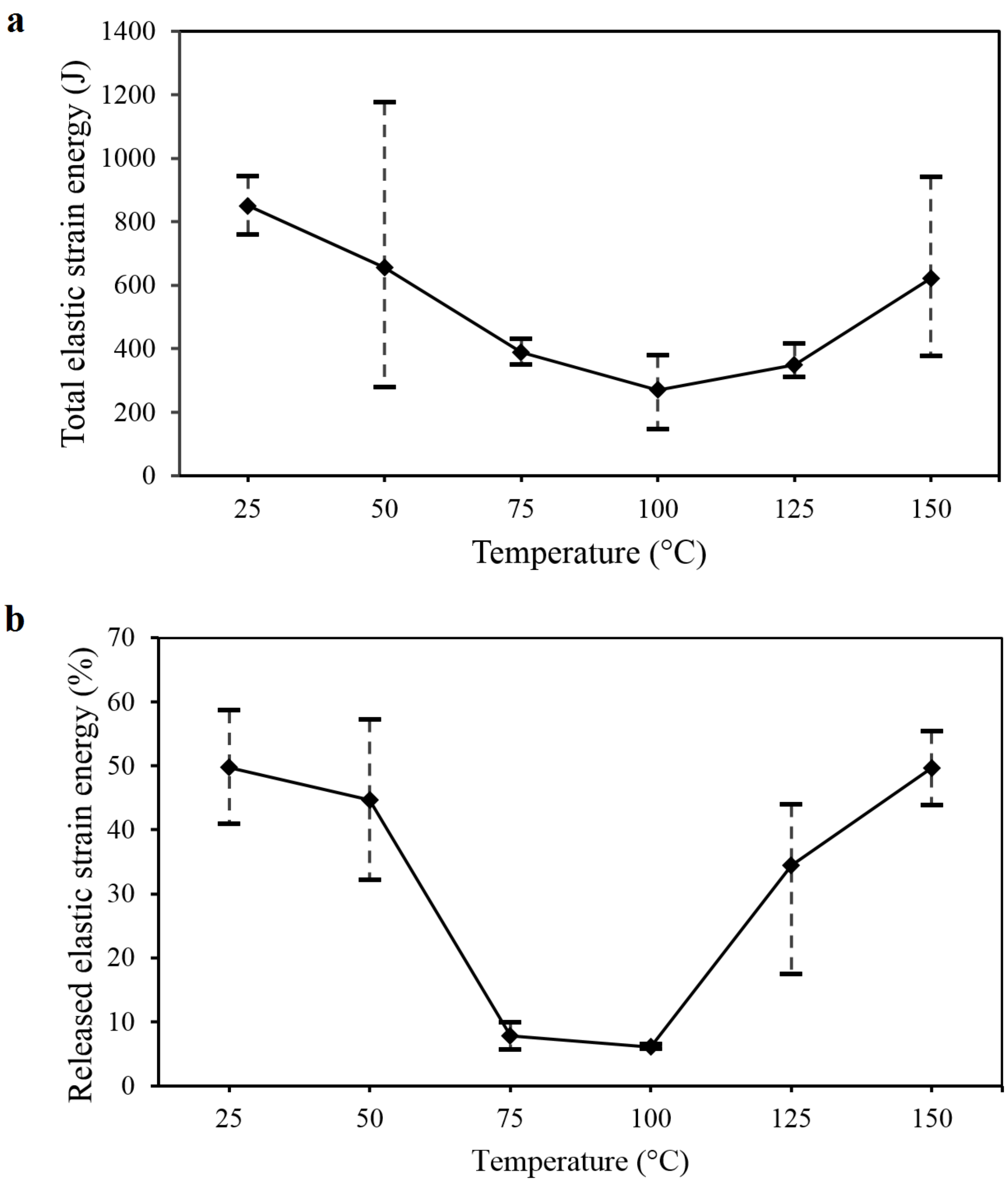

Figure 5.21 Total elastic strain energy and amount of released elastic strain energy with respect to different temperature levels

Table 5.4 presents the changes in strain burst stress, accumulated total elastic strain energy, released kinetic energy and the velocity of the ejected fragments. In general, the higher the strain burst stress, the higher the total elastic strain energy, with greater energy release and thus higher kinetic energy levels. When the temperature increased from room temperature (25 °C) to the critical temperature level (100 °C), strain burst stress, total elastic strain energy, kinetic energy and the ejection velocity of the fragments decreased by 45%, 68%, 96%, and 82% respectively. It is believed that thermally induced microcracking caused mechanical degradation and this resulted in less strain energy accumulation which led to small kinetic energy. When the temperature level was above 100 °C, bursting stress, accumulated strain energy, kinetic energy release and fragment ejection velocity increased when compared to the results captured at the temperature of 100 °C. This led to more intense strain burst characteristics. The results demonstrate that thermal damage has some influence on strain burst behaviour of brittle rock.

Table 5.4 Temperature influence on strain burst stress, total elastic strain energy, kinetic energy and ejection velocity of the fragments

Temperature (°C)	**25**	**50**	**75**	**100**	**125**	**150**
Strain burst stress (%)	0	-15.7	-32.2	-44.6	-35.9	-15.8
Total elastic strain energy (%)	0	-22.9	-54.1	-68.2	-58.9	-26.9
Kinetic energy (%)	0	-22.1	-92.8	-96.3	-73.4	-27.9
Ejection velocity of the fragments (%)	0	-16.3	-70.0	-82.0	-57.2	-34.3

5.4 - Discussions

Strain burst stresses for the samples exposed to temperatures up to 100 °C declined by 44.6%, compared to the stresses of the specimens at the room temperature (25 °C) (see Figure 5.8). It is believed that creation of new micro-cracks due to temperature exposure led to a weakening of the bonding among mineral grains of the samples, which can be attributed to the anisotropy in the thermodynamic properties of different rock minerals, and this caused a degradation of the overall rock strength. The failure mechanism for the granite specimens exposed to temperatures up to 100 °C might have been due to intergranular fracture mechanism in which micro-cracks first develop at the mineral grain boundaries that was consistent with the existing literature (Yin, et al., 2012; Zuo et al. 2014; Li et al. 2016; Feng et al. 2017). As the temperature increased from 100 up to 150 °C, the strain burst stress showed a gradual rise. It is believed that the closure of pre-existing micro-cracks due to the thermal expansion of mineral grains by high temperature may render the rocks denser and more compact (Funatsu et al. 2014; Gautam et al. 2016). In order to understand this phenomenon, SEM analysis needs to be conducted, which is a subject of our future work. However, experimental evidence in the literature suggests that the above-mentioned mechanisms of intergranular and transgranular thermal cracking could be behind the observed behaviour in this study. In fact Zuo et al. (2014) and Feng et al.

(2017) reported that when the temperature was more than 100 °C, the coupled fracture mechanism of intergranular and transgranular thermal cracking (in which the micro-cracks develop within the mineral grains) was the main mechanism for improved compactness of the specimens after the gradual closure of the pre-existing defects in the crystal.

Since the effects of the microcracking process are related to the magnitude of the AE events, damage evaluation will be better understood with cumulative AE energy. It was observed that the rate of thermal damage accumulation increased as the temperature increased from room temperature (25° C) up to 100 °C. It is believed that the weakening of the minerals' bonding caused a mechanical degradation on the strength of the rocks and this triggered the rapid thermal damage accumulation and bursting. On the other hand, when the temperature increased from 100 °C to 150 °C, the granite specimens exhibited slower damage accumulation and revealed intense strain burst. This can be attributed to the improved densification of the samples due to the thermal dilation of mineral grains which decreased the distance between the interfaces of the minerals and their mutual attraction was enhanced.

From an energy point of view, kinetic energies of the granite specimens were calculated to assess the influence of thermal damage on the intensity of strain burst. The samples treated with temperatures from room temperature (25 °C) to 100 °C manifested dramatically less intense strain burst associated with slower particle ejection velocities due to the thermal damage. At temperatures from 100 °C to 150 °C, more intense strain burst was displayed with faster rock fragment ejection. It is believed that this increase in kinetic energy was caused by the enhanced compactness of the samples due to the fact that thermally-induced volumetric expansion of minerals led to the closure of the pre-existing micro-cracks and original defects in the samples.

The aforementioned experimental results give useful enlightenments about the impact of thermal damage on strain burst characteristics. However, more experiments considering higher temperature levels should be performed to better understand the mechanism of strain burst under high geo-stress and high-temperature conditions.

5.5 - Conclusion

In this chapter, temperature influence on the strain burst behaviour of granite samples was investigated using a unique true-triaxial strain burst testing system. Based on acoustic emission, stress and kinetic energy analyses conducted on granite samples exposed to various temperatures the following conclusions can be drawn:

1. The strain burst stress of granite changes with temperature from room temperature 25 °C to 150 °C. A temperature level of 100 °C was identified as the critical transition temperature, which induces the change in the strain burst behaviours of granite. As the temperature increased from 25 °C to 100 °C, the strain burst stress diminished by approximately 45%. It is believed that this declining trend is caused by the development of microcracks that are induced by temperatures. At 100-150 °C, the strain burst stress showed a slightly rising trend, but it is still less than that at room temperature. This can be attributed to the improved compaction of the grains in brittle rock by the closure of pre-existing micro-cracks due to the thermal expansion of minerals at higher temperatures.

2. The evolution of AE characteristics can be divided into three deformation stages. Those stages are the AE quiet linear elastic deformation stage, AE growth stage and AE active strain burst stage. The cumulative AE energy showed a sharp increase at the initial stage, then accumulated slowly during the stress maintenance phase before increasing dramatically until strain burst occurred. Corresponding with the failure characteristics of the granite specimens exposed to different temperature conditions, the total cumulative AE energy and cumulative AE counts decreased as the temperature increased from 100 °C to 150 °C. It was found that cumulative AE energy characteristics reflect the damage evolution better as the size of micro-cracks are related to the magnitude of the AE events. Moreover, when the temperature increased, a low-frequency band was observed due to the thermal damage inside the specimens, which can also be an indicator for strain burst.

3. The thermal damage for strain burst (D_{SB}) increased the rate of bursting at ~95% of normalised axial stress levels. This can be due to the fact that as temperature caused thermally induced micro-cracks that helped to reduce the accumulated energy at the initial loading stage. A good relationship was observed between the trend of the b-values and the micro- and macro- cracking during the strain burst test. The estimated b-values showed a continuously declining trend during the test indicating that a large amount of macro-cracks were generated prior to strain burst. Therefore, b-value analysis can be used as a precursor to assess the degradation of the rock and strain burst process.

4. The kinetic energy of the ejected fragments dramatically decreased until they reached the critical temperature of 100 °C. This is because of manifested thermally induced damage which caused less elastic strain energy accumulation. When the temperature increased from 100 °C to 150 °C, kinetic energy had also a slight rise which is associated with the higher initial velocity of ejected fragments which may occur due to the expansion of mineral grains by increased temperature. This helped to improve the compactness of the rock which implies that a more intense or severe strain burst may be encountered in situations where temperatures rise above the critical temperature of 100 °C.

The results of this study demonstrate that thermally induced damage can change strain burst characteristics of brittle rocks.

Chapter 6: Conclusions and recommendations

6.1 - Introduction

The final chapter of this thesis presents the strain burst proneness indexes and criteria proposed to evaluate the propensity of strain burst and the summary of the work done in this research, providing conclusions and recommendations for future work. Firstly, the methodology presented for prediction of strain burst in deep underground mines is discussed. Secondly, the main contributions of this research are summarised. Finally, a list of recommended future work is given followed by some additional research questions inspired by this study.

6.2 - Quantifying the influence of intrinsic rock parameters on strain burst and application to real engineering problems

As mining progresses to greater depths, the rate and severity of strain burst hazards encountered tend to inevitably increase, resulting in significant operational and safety challenges. Strain burst is a sudden and violent rock fracturing and spontaneous instability phenomenon accompanied by the abrupt release of strain energy of an excavation whereby the rock mass rupture is initiated by mining-induced, or dynamic stress changes until the rock mass strength (critical strain burst stress level) is reached. Such a failure characteristic poses a serious threat to the safety and efficiency of deep underground engineering operations. Therefore, the research on strain burst mechanism and prediction have become one of the key scientific and technical problems in rock mechanics field.

Determination of strain burst proneness of rock is one of the challenging issues in the field of strain burst research. Timely identification of potential precursor information enables effective and specifically targeted measures to mitigate strain burst hazards. Is it possible to forecast strain burst before it occurs? How can the magnitude of potential strain burst be predicted? What magnitude of measures should be taken into account for eliminating, or minimising the risk of strain burst and its destructive consequences to an acceptable level? These real engineering application related questions will be explained in this chapter under strain burst proneness assessment section. This chapter critically assesses the underlying mechanism and consequences of strain burst evaluation methods and proposes a new energy based indexes for practical use in real engineering applications in geomechanics.

There have been many research conducted to assess the potential risk, vulnerability and proneness of strain burst and some discriminant indices of criterion were proposed including the elastic strain energy storage index (Kidybinski 1981), the rock brittleness index (Wang and Park 2001), the decrease modulus index (Singh 1989), the burst potential index (Mitri et al. 1999). Cook (1966) pointed out the significance of energy release for inducing rock burst and proposed the energy release rate index as rockburst prediction. The burst potential index was proposed by Mitri et al. (1999) to evaluate the potential rockburst risk after excavation and it was stated that rockburst tends to occur when the rock energy storage rate reaches the limit of energy storage. Kidybinski (1981) proposed the elastic strain energy index to assess the intensity of rockburst. Wiles (2002) studied the correlation between pillar burst and the local energy release rate and provided an indicator that can be used for predicting the potential for rockburst. Recently, Weng et al. (2017) investigated the energy accumulation and dissipation characteristics of rockburst failure process and they introduced a strain energy density index for examining the energy distribution in the surrounding rock mass when rock fails due to strain burst or spalling. Table 6.1 presents some examples of empirical criteria of strain burst proneness in the literature which were derived from the mechanical parameters obtained by laboratory tests.

Table 6.1 Example indices for strain burst prediction

Index or equation	Explanation	Reference
σ_θ/σ_c	Ratio of the maximum tangential stress to the uniaxial compressive strength of rock	Russenes 1974; Hoek and Brown 1980
Elastic strain energy index	Ratio of the elastic energy stored to the dissipated energy in one cycle of cycling compression test	Kidybinski 1981
Burst potential index (BPI=ESR/E)100%	Ratio of the energy storage rate to the maximum strain energy that the rock mass can sustain before failure	Mitri et al. 1999
Rock mass index	Ratio of the compressive strength to the tangential stress	Palmstrom 1995

Rock brittleness index ($PES = \sigma_c^2/2E_u$)	The ratio of square of the uniaxial compressive strength of to double amount of the unloading tangential elastic modulus	Wang and Park 2001
Local energy release rate index	The difference in energy stored in the rock mass before and after brittle failure	Jiang et al. 2010
Strain energy density index	Demonstrating the strain energy accumulation and dissipation	Weng et al. 2017
Rockburst energy release rate index	The ratio of the energy release of an element generating brittle failure to the limit energy storage of that element	Xu et al. 2017

Damage accumulation leading to strain burst is a static process followed by the dynamic release of stored strain energy in which stored strain energy is converted to kinetic energy as in the form of ejections of rock fragments. Therefore, strain burst from beginning to the ending is combined quasi-static and dynamic behaviour. In this respect, to fully understand the strain burst mechanism it is essential to consider quasi-static and dynamic parameters for forecasting the potential and intensity of strain burst. Although the strength and deformability of rocks can be approximately predicted, the intrinsic structure and the internal failure mechanism still remain for further investigation. Due to the complex physical and mechanical properties of rock mass, the main causes related geomechanical properties and the strain burst mechanism present a challenging concern to researchers in rock mechanics.

6.3 - New strain burst proneness indexes based on excess stored strain energy

In this section, strain burst characteristics based on the energy theory was analysed and energy indexes were proposed to quantitatively evaluate the intensity of strain burst of brittle rock. Based on the energy evolution characteristics of brittle granite under uniaxial and triaxial compression, true-triaxial loading-unloading and three-point bending, new strain burst proneness indexes were proposed and new strain burst criterion based on these indexes were presented. Note that these indexes were proposed for brittle hard granite.

6.3.1 - The excess strain energy index $\boldsymbol{\Omega_{SB}}$

According to the circumferential-strain controlled uniaxial and triaxial compression tests, the elastic stored strain energy, fracture energy and excess strain energy that is the potential energy for strain burst, of the granite specimens during the entire loading were accurately calculated and the rule of energy accumulation and release in granite was systematically analysed. It was found that the maximum strain energy stored and excess strain energy in the rock are affected by the confining pressure and temperature.

Based on the above-mentioned theory, here a new energy index for strain burst proneness Ω_{SB} was proposed, can be calculated as in Equation 6.1:

$$\Omega_{\mathrm{SB}} = \frac{\mathrm{d}\Phi_{\mathrm{EX}}}{\mathrm{dU_E}} \tag{6.1}$$

where $\mathrm{d}\Phi_{\mathrm{EX}}$ and $\mathrm{dU_E}$ are the excess strain energy released during brittle failure (strain burst) and the elastic stored strain energy after Class II behaviour starts, respectively. The energy calculations are shown as follows (see Chapter 3):

$$dU_E = \frac{\sigma_A^2}{2E} \tag{6.2}$$

$$\mathrm{d}\Phi_{CW} = \sum_{i=\sigma_A}^{\sigma_B} \frac{\sigma_i^2 - \sigma_{i+1}^2(M-E)}{2EM} \tag{6.3}$$

$$\mathrm{d}\Phi_{FM} = \sum_{i=\sigma_B}^{\sigma_C} \frac{\sigma_i^2 - \sigma_{i+1}^2(M-E)}{2EM} \tag{6.4}$$

$$dU_{RE} = \frac{\sigma_C^2}{2E} \tag{6.5}$$

$$\mathrm{d}\Phi_{EX} = dU_E - \mathrm{d}\Phi_{CW} - \mathrm{d}\Phi_{FM} - dU_{RE} \tag{6.6}$$

where Φ_{CW} is the energy consumption dominated by cohesion degradation during stable fracturing, Φ_{FM} is the energy dissipated during the mobilisation of frictional failure, U_{RE} is the residual stored elastic strain energy, σ_A is the point of axial strain reversal, σ_B is the point of brittle failure intersection (see Figure 3.4 in Chapter 3), E is the elastic stiffness of the specimen and M ($M = \delta\sigma/\delta\varepsilon$) is the post-peak modulus between two incremental stress points, σ_i and σ_{i+1} which can vary significantly with the fracture development.

From the above analyses, the strain burst proneness of the thermally-treated granite specimens at different confining pressure can be classified into three grades: low, medium and strong strain burst proneness. The grading standards of strain burst proneness based on Ω_{SB} are listed in Table 6.1. According to the calculated Ω_{SB} and the failure pattern of the granite specimens (see Figure 3.8 in Chapter 3), a new criterion for strain burst proneness with Ω_{SB} was proposed as follows:

Confinement

$$\left.\begin{array}{c} \Omega_{\mathrm{SB}} > 0.08 \text{ low strain burst proneness} \\ 0.04 < \Omega_{\mathrm{SB}} < 0.08 \text{ medium strain burst proneness} \\ \Omega_{\mathrm{SB}} < 0.04 \text{ strong strain burst proneness} \end{array}\right\} \tag{6.7}$$

Temperature

$$\left.\begin{array}{c} \Omega_{\mathrm{SB}} < 0.2 \text{ low strain burst proneness} \\ 0.2 < \Omega_{\mathrm{SB}} < 0.4 \text{ medium strain burst proneness} \\ \Omega_{\mathrm{SB}} > 0.4 \text{ strong strain burst proneness} \end{array}\right\} \tag{6.8}$$

Table 6.2 Classification of strain burst proneness using the excess strain energy index Ω_{SB}

Confining pressure (MPa)	$\boldsymbol{\Omega_{\mathrm{SB}}}$	**Strain burst proneness**
0	0.187	Low
0	0.272	Low
0	0.205	Low
10	0.071	Medium
20	0.079	Medium
20	0.087	Medium
30	0.021	Strong
30	0.040	Strong
40	0.037	Strong
40	0.038	Strong
50	0.024	Strong
60	0.007	Strong

Figure 6.1 presents the influence of confining pressure and temperature on strain burst proneness. It can be seen that the strain burst proneness of brittle granite is strongly dependent on the pre-heating temperature and confinement. The results demonstrated that the higher the confining pressure and temperature, the stronger the strain burst proneness will be. It is believed that due to the anisotropy in the thermodynamic properties of different rock minerals, the amount and width of the microcracks inside the specimen increased, and this triggered the rapid thermal damage accumulation and bursting. In other words, the fundamental reason for the increase of strain burst proneness is the thermally induced damage by microcracking. Thermally induced damage caused less elastic strain energy accumulation and hence the excess strain energy which is a measure for the intensity of the intrinsic strain burst in the rock decreased with increasing temperature, resulting in stronger strain burst proneness.

Confining pressure importantly influenced the strain burst proneness. The energy storage capacity of granite was enhanced with increasing confinement in which higher dissipated energy consumption is required for promoting crack propagation. Hence, the damage degree of granite under highly-stressed conditions becomes more violent, leading to stronger strain burst propensity, as depicted in Figure 6.1.

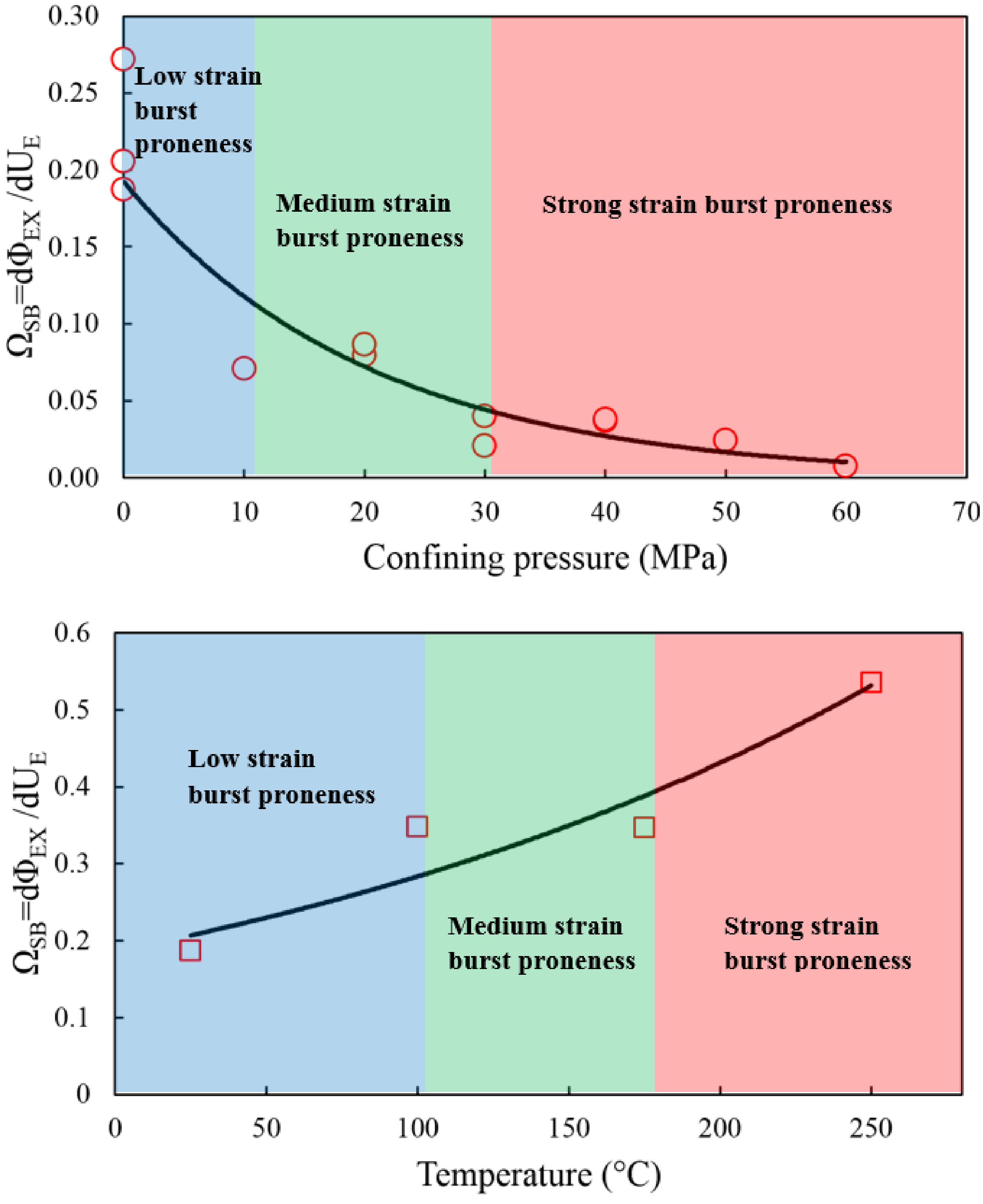

Figure 6.1 Influence of confining pressure and temperature on strain burst proneness

6.3.2 - Released energy index $\boldsymbol{\lambda_{SB}}$

The kinetic energy of the ejected fragments during strain burst can serve as a significant precursor for evaluating the strain burst intensity quantitatively. Using a high-speed camera, the ejection failure process of rock fragments were observed in true-triaxial loading-unloading strain burst tests. The ejection velocities and kinetic energies from the tested granite specimens were quantitatively estimated by analysing the recorded videos. After measuring the velocity, the total kinetic energy of the ejected fragments was calculated by using Equation 6.9.

$$E_k = \sum_{i=1}^{n} \frac{1}{2} m_i \bar{v}_i^2 \tag{6.9}$$

where n is the number of fragments having D > 10 mm and m > 0.5 g, m_i is the mass of the ith rock fragment and $\bar{v}_i$ is the initial ejection velocity of the ith rock fragment. By using the equation above, the total kinetic energies for all granite specimens treated with different temperatures were calculated. In addition, the strain burst stress (σ_{SB}) and total elastic strain energy ($\mathrm{U_E}$) of the granite samples exposed to different temperatures were calculated.

Based on the kinetic energy and stress analyses, a released energy index λ_{SB} for strain burst proneness, was proposed, which can be described by:

$$\lambda_{\mathrm{SB}} = \frac{E_k}{\mathrm{U_E}} \tag{6.10}$$

According to the calculated λ_{SB} of the thermally-treated granite specimens, a new criterion for strain burst proneness with index λ_{SB} was proposed as follows:

$$\left.\begin{array}{c} \lambda_{\mathrm{SB}} < 0.5 \text{ low to moderate strain burst} \\ \lambda_{\mathrm{SB}} > 0.5 \text{ medium to intense strain burst} \\ \frac{\sigma_{SB}}{\sigma_{UCS}} > 1.2 \text{ low strain burst proneness} \\ 1 < \frac{\sigma_{SB}}{\sigma_{UCS}} < 1.2 \text{ moderate strain burst proneness} \\ \frac{\sigma_{SB}}{\sigma_{UCS}} < 1\text{intense strain burst proneness} \end{array}\right\} \begin{array}{c} (6.11) \\ \\ (6.12) \end{array}$$

where σ_{USC} is the uniaxial compressive strength.

The strain burst proneness of thermally-induced granite specimens is given in Table 6.2. It can be seen that strain burst proneness increased with an increased temperature which can be attributed to the mechanical strength degradation induced by thermal microstructures, rendering the rock relatively weaker.

Table 6.3 Classification of strain burst proneness using the released energy index λ_{SB} and $\frac{\sigma_{SB}}{\sigma_{cm}}$

Temperature (°C)	$\boldsymbol{\lambda_{SB}}$	$\boldsymbol{\frac{\sigma_{SB}}{\sigma_{cm}}}$	**Strain burst proneness**
25	0.586	1.67	Low
	0.409	1.50	Low
50	0.572	1.24	Low
	0.322	1.87	Low
75	0.056	1.02	Moderate
	0.099	1.13	Moderate
100	0.058	1.06	Moderate
	0.059	0.92	Intense
	0.065	0.65	Intense
125	0.174	1.11	Moderate
	0.439	0.98	Intense
	0.419	0.96	Intense
150	0.554	1.06	Moderate
	0.439	1.67	Low

6.3.3 -Energy release rate index Ψ_{SB}

Energy release rate which is a measure of the energy that is dissipated per unit increase in an area during crack growth is important for the successful assessment of fracturing characteristics during strain burst. In this study, the effects of various loading rates on the strain burst proneness for thermally-treated granite was analysed and discussed. The applied energy is equal to the work done on the crack surface for its propagation which can be determined by the applied load and the displacement in the system.

Based on the above-mentioned theory, an energy release rate index Ψ_{SB} for strain burst proneness was presented, as follows:

$$\Psi_{\mathrm{SB}} = \frac{G_I}{W} \tag{6.13}$$

Where G_I and W are the energy-release rate and applied energy on granite under mode I fracture, respectively.

A strain burst proneness criterion based on Ψ_{SB} index was proposed (see Equation 6.14) and the coupled influence of loading rate and temperature on strain burst proneness was investigated in this study.

$$\left.\begin{array}{c} \Psi_{\mathrm{SB}} > 1 \text{ (Low strain burst proneness)} \\ 0.75 < \Psi_{\mathrm{SB}} < 1 \text{ (Moderate strain burst proneness)} \\ \Psi_{\mathrm{SB}} < 1 \text{ (Intense strain burst proneness)} \end{array}\right\} \tag{6.14}$$

The detailed strain burst proneness of granite under various levels of temperature at different loading rates are given in Table 6.3. The results showed that the strain burst proneness decreases with increasing loading rate as the strength and fracture toughness of granite, resulting in slight strain burst proneness. Increased temperature, on the other hand, caused stronger strain burst proneness of granite due to the thermal damage resulting in deterioration of the tensile stress resistance.

Table 6.4 Classification of strain burst proneness using the energy release rate index Ψ_{SB}

Temperature (°C)	**Loading rate (mm/min)**	Ψ_{SB}	**Strain burst proneness**
RT	0.02	0.641	Intense
	0.05	1.242	Low
	0.08	1.265	Low
	0.1	1.484	Low
100	0.02	0.737	Intense
	0.05	1.045	Low
	0.08	0.837	Moderate
	0.1	1.144	Low
175	0.02	0.631	Intense
	0.05	0.847	Moderate
	0.08	0.479	Intense
	0.1	0.731	Intense
250	0.02	1.016	Low

	0.05	0.752	Intense
	0.08	0.947	Moderate
	0.1	0.840	Moderate

Based on the above-mentioned strain burst proneness indexes and criteria, a methodology for forecasting the propensity of strain burst is proposed, as depicted in Figure 6.2. Using these indexes can provide guidelines for the development of an effective and reliable method to forecast the propensity of strain burst. According to the energy calculations in this new testing methodology, calculating the excess strain energy, stored elastic strain energy and energy release rate evolution characteristics can be used for improved understanding of the performance and design of rock support systems in strain burst-prone mines. Appropriate rock support design can be provided by considering the energy absorption capacity of rock support and the energy characteristics obtained from the laboratory tests conducted for investigating the underlying mechanism of strain burst damage. Therefore, this research will lead to better and more efficient prediction methods for brittle rock failure and strain burst, towards planning guidelines and ultimately safer deep underground working environments.

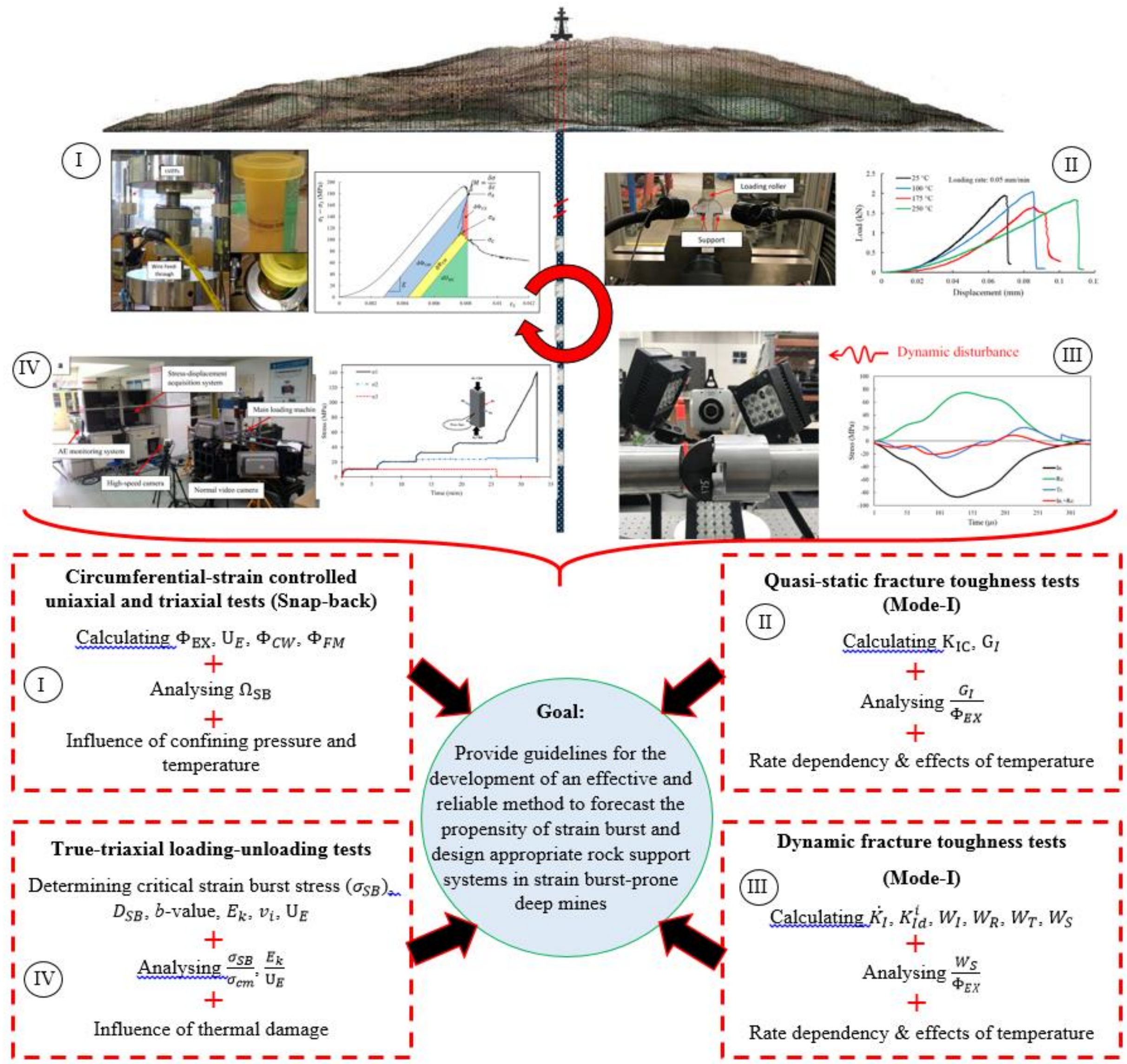

Figure 6.2 Methodology employed for forecasting the propensity of strain burst by quasi-static and dynamic combination mechanism

6.4 - Conclusions

The objective of this research is fourfold: first, to investigate the energy evolution characteristics during strain burst by conducting circumferential strain controlled tests under the combined influence of thermal damage and confining pressure, and second determining quasi-static and dynamic fracture toughness on thermally treated Australian CCNSCB granite specimens at various loading rates and examine the relation between the quasi-static and dynamic mode-I fracture toughness and energy release rates; third, investigate the influence of deviatoric stresses and temperature effects on strain burst behaviour using rectangular prism granite specimens exposed to different pre-heating temperatures under true-triaxial loading/unloading conditions; and finally proposing strain burst criteria or index for strain burst proneness by the results from the tests mentioned above and upscale these finding to apply for the real engineering applications.

Apart from this, three other motivating branches of interest can be directed to systematically and thoroughly assess the influence of external factors including confining pressure, thermal damage and loading rate on the mechanical properties and energy characteristics of brittle Australian granite during strain burst in deep mining operations.

Based on the acoustic emission, stress, kinetic energy analyses and fracture characterisation carried out on granite samples exposed to various temperature, confinement and loading rate the following key conclusions can be drawn:

Forecasting the propensity of strain burst

1. An energy calculation method was developed based on post-peak energy analysis. AE responses during compression tests were used to assess the energy and crack evolution characteristics of Australian granite specimens under different confinement. Using AE characteristics, fracture energy was split into two-class: 1) energy consumed dominantly by gradual weakening of cohesive behaviour and 2) energy dissipated during the mobilisation of frictional failure. A portion of elastic energy, released from the Class II rock, was defined as excess strain energy which is a measure for the propensity of the intrinsic strain burst in the rock. It directly determines the intrinsic ejection velocity of the rock fragments when a bursting event occurs. Therefore, this methodology can be used for quantitative predictions of bursting strain energy in the field which could facilitate

improving the early warning efficiency and provides a comprehensive guideline for the mitigation methods to reduce strain burst intensity.

2. Confinement has significantly affected the post-peak energy redistribution characteristics and fracture mechanism of granite. The elastic stored strain energy, energy consumed by dominating cohesion weakening, and energy dissipated during mobilisation of frictional failure were 8.74, 2.53 and 12.1 times the values at unconfined condition, resulting in more severe strain burst indicating that rising up the confining pressure improved the efficiency of energy accumulation. This explains why the damage degree of granite is more prominent in the process of deep excavations.

3. The temperature has significantly affected the post-peak energy redistribution characteristics and fracture mechanism of granite. The elastic stored strain energy, total fracture energy, excess strain energy diminished by 80, 82 and 43%, respectively when the temperature increased from room temperature to 250 °C. This declining trend was attributed to the development of micro-cracks that were induced by elevated temperatures. Thermally induced damage caused less strain energy accumulation and hence the excess strain energy decreased with increasing temperature. Another parameter to express the intensity of a burst event, ejection velocity, dropped down as the gradual increase of temperature. The proposed approach can provide an early warning of brittle rock instability, which is significant for strain burst assessment in deep mining operations.

4. The fracturing mechanism of granite was influenced by both confining pressure (excavation depth) and temperature. The dominant failure pattern of granite changed from multiple splitting failure to splitting-shear composite failure as the level of confinement increased. When the temperature was less than 100 °C, granite samples experienced more induced intergranular thermal fracturing. Coupled fracture mechanism of intergranular and transgranular thermally induced cracking were the main fracture mechanism triggering strain burst when the temperature exceeded 100 °C.

Quasi-static and dynamic fracture characterisation

1. The CCNSCB specimen combines the merits of two ISRM-suggested methods (CCNBD and NSCB methods), and thus it allows accurate determination of the mode I fracture toughness of granite under quasi-static and dynamic loadings.

2. The experimental results indicated that the quasi-static fracture toughness and energy-release rate in mode I are a function of loading rate and they presented a rising trend with increasing loading rate. At high loading rates, transgranular fractures became dominant which consumed more energy than intergranular fractures; this in turn, resulted in more straight fracture path and posed a less rough fracture surface when compared to the low loading rate condition.

3. Under the same loading rate, the quasi-static mode I fracture toughness and energy-release rate of granite showed a gradual fall (17% and 30%, respectively) with ascending temperature from 25 °C to 250 °C due to the thermally-induced micro-cracks within the rocks. These findings of this investigation will be useful in achieving a better understanding of initiation of fracturing during strain burst under various temperature and loading rate conditions.

4. The stress-strain curves of granite under various impact velocities and temperatures showed the same deformation stages; elastic deformation, yielding and failure. When the impact velocity was high, the loading rate strengthening effect became more remarkable and the strength of granite increased under all temperatures. The failure modes of Australian granite also exhibited rate dependence at the same temperature level. Along with the high impact velocity, the failure mode of the pre-heated granite changed from tensile splitting (characterisation of Class I) to pulverisation or breaking into many small pieces in which the specimens were pulverised by the excess energy in Class II loading. Under the same dynamic impact, an increase in the treatment temperature weakened the interaction force between the particles and aggravated the fragmentation degree of granite.

5. The DIFT of Australian granite was obtained by the quasi-static analysis that was evidenced by the dynamic force balance until the time to fracture. The DIFT of the granite presented an ascending trend with the loading rate at a given heat-treatment temperature

and decreased with increasing temperature, revealing the deterioration of the ability to resist fracturing with the rise of temperature. Therefore, in order to effectively crush the deep rock, a favourable measure should be applied to reduce the intensity of strain burst by considering a combined application of a thermal treatment and impact with a proper loading rate.

Effects of thermal damage on strain burst mechanism for brittle rocks under true-triaxial loading-unloading conditions

1. The strain burst stress of granite changes with temperature from room temperature 25 °C to 150 °C. A temperature level of 100 °C was identified as the critical transition temperature, which induces the change in the strain burst behaviours of granite. As the temperature increased from 25 °C to 100 °C, the strain burst stress diminished by approximately 45%. It is believed that this declining trend is caused by the development of microcracks that are induced by temperatures. At 100-150 °C, the strain burst stress showed a slightly rising trend, but it is still less than that at room temperature. This can be attributed to the improved compaction of the grains in brittle rock by the closure of pre-existing micro-cracks due to the thermal expansion of minerals at higher temperatures.

2. The evolution of AE characteristics can be divided into three deformation stages. Those stages are the AE quiet linear elastic deformation stage, AE growth stage and AE active strain burst stage. The cumulative AE energy showed a sharp increase at the initial stage, then accumulated slowly during the stress maintenance phase before increasing dramatically until strain burst occurred. Corresponding with the failure characteristics of the granite specimens exposed to different temperature conditions, the total cumulative AE energy and cumulative AE counts decreased as the temperature increased from 100 °C to 150 °C. It was found that cumulative AE energy characteristics reflect the damage evolution better as the size of micro-cracks are related to the magnitude of the AE events. Moreover, when the temperature increased, a low-frequency band was observed due to the thermal damage inside the specimens, which can also be an indicator for strain burst.

3. The thermal damage for strain burst (D_{SB}) increased the rate of bursting at ~95% of normalised axial stress levels. This can be due to the fact that as temperature caused

thermally induced micro-cracks that helped to reduce the accumulated energy at the initial loading stage. A good relationship was observed between the trend of the b-values and the micro- and macro- cracking during the strain burst test. The estimated b-values showed a continuously declining trend during the test indicating that a large amount of macro-cracks were generated prior to strain burst. Therefore, b-value analysis can be used as a precursor to assess the degradation of the rock and strain burst process.

4. The kinetic energy of the ejected fragments dramatically decreased until they reached the critical temperature of 100 °C. This is because of manifested thermally induced damage which caused less elastic strain energy accumulation. When the temperature increased from 100 °C to 150 °C, kinetic energy had also a slight rise which is associated with the higher initial velocity of ejected fragments which may occur due to the expansion of mineral grains by increased temperature. This helped to improve the compactness of the rock which implies that a more intense or severe strain burst may be encountered in situations where temperatures rise above the critical temperature of 100 °C.

Quantifying the influence of intrinsic rock parameters on strain burst and application to real engineering problems

1. To estimate and classify the strain burst proneness of brittle rock, energy evolution characteristics of granite were used to assess the tendency of strain burst. Excess strain energy (Ω_{SB}), released energy (λ_{SB}), and energy-release rate (Ψ_{SB}) indexes were proposed on the basis of energy characteristics for brittle rock.
2. Based on the strain burst proneness of granite specimens obtained through circumferential-strain controlled uniaxial and triaxial compression tests, true triaxial loading-unloading strain burst tests, and three-point bending mode I fracture toughness tests, and the indexes proposed, new criterions for strain burst proneness were put forward. The influence of confining pressure, temperature and loading rate on the strain burst proneness was also analysed and discussed.

6.5 - Recommendations for future work

In addition to the results reported in this thesis, the following interests can be recommended for future work:

1. Conducting circumferential-strain controlled tests with simultaneously increasing the temperature and confining pressure.
2. The growth of the microcracks in rocks is accompanied by significant inelastic deformation near the crack tip. This highly damaged region adjacent to the crack tip is called a fracture process zone (FPZ) within the material undergoes micro-damaging. In the FPZ, micro-cracks close or open depending on their orientation with respect to the direction of the applied load, and crack growth, in fact, occurs by connecting the micro-cracks at a critical load. Therefore, PFZ during strain burst should be analysed and discussed more in-depth to estimate the PFZ in underground excavation and thus more appropriate supporting system can be applied with some economic benefits.
3. In the view of the study on dynamic fracture properties of rock under coupling of temperature and static pressure will to be carried out for a better understanding of dynamic fracture characteristics during strain burst.
4. 3D X-ray micro-CT technique deserves examination for accurately quantification of the thermally-induced damage under different loading conditions.
5. The effects of confining pressure on the dynamic fracture parameters of brittle rock should be studied to understand the fracture propagation characteristics under confined environment. This will help to identify the initiation of unstable crack growth.
6. The effect of intermediate principal stress on rock failure is commonly acknowledged, and it was first verified that, under constant σ_3 condition, the rock strength in the conventional triaxial extension was higher than that in the conventional triaxial compression test. Therefore, the influence of intermediate stress on strain burst mechanism under true-triaxial unloading conditions should be subjected to detailed investigation.
7. The influence of loading and unloading rate on strain burst behaviour under true-triaxial loading-unloading conditions should be studied.
8. The energy dissipation due to the formation of rock fragments triggered by tension and shear failures during strain burst process should be systematically investigated.

References

Ai, C., Zhang, J., Li, Y., Zeng, J., & Yang, X. (2016). Estimation criteria for rock brittleness based on energy analysis during the rupturing process. *Rock Mech Rock Eng, 49*(12), 4681-4698.

Akbardoost, J., Ayatollahi, M., Aliha, M., Pavier, M., & Smith, D. (2014). Size-dependent fracture behavior of Guiting limestone under mixed mode loading. *Int J Rock Mech Min Sci, 71*, 369-380.

Akdag, S., Karakus, M., Nguyen, G., & Taheri, A. (2017). Influence of specimen dimensions on bursting behaviour of rocks under true-triaxial loading conditions. In J. Wesseloo (Ed.), *8th International Conference on Deep and High Stress Mining* (pp. 447-457). Perth: Australian Centre for Geomechanics.

Akdag, S., Karakus, M., Nguyen, G., Taheri , A., & Bruning, T. (2019). Evaluation of the propensity of strain burst in granite based on post-peak energy analysis. *Underground Space,* (Accepted).

Akdag, S., Karakus, M., Taheri, A., Nguyen, G., & Manchao, H. (2018). Effects of thermal damage on strain burst mechanism for brittle rocks under true-triaxial loading conditions. *Rock Mech Rock Eng, 51*, 1657-1682.

Aliha, M., & Ayatollahi, M. (2014). Rock fracture toughness study using cracked chevron notched Brazilian disc specimen under pure modes I and II loading-a statistical approach. *Theor Appl Fract Mech, 69*, 17-25.

Aliha, M., & Bahmani, A. (2017). Rock fracture toughness study under mixed mode I/III loading. *Rock Mech Rock Eng, 50*(7), 1739-1751.

Aliha, M., Ayatollahi, M., Smith, D., & Pavier, M. (2010). Geometry and size effects on fracture trajectory in a limestone rock under mixed mode loading. *Eng Fract Mech, 77*(11), 2200-2212.

Aliha, M., Hosseinpour, G., & Ayatollahi, M. (2013). Application of cracked triangular specimen subjected to three-point bending for investigating fracture behavior of rock materials. *Rock Mech Rock Eng, 46*(5), 1023-1034.

Aliha, M., Sistaninia, M., Smith, D., Pavier, M., & Ayatollahi, M. (2012). Geometry effects and statistical analysis of mode I fracture in guiting limestone. *Int J Rock Mech Min Sci, 51*, 128-135.

Aoki, H., & Matsukara, Y. (2008). Estimating the unconfined compressive strength of intact rocks from Equotip hardness. *Bull Eng Geol Environ, 67*(1), 23-29.

Atkinson, R., & Ko, H. (1973). A fluid cushion, multiaxial cell for testing cubical rock specimens. *Int J Rock Mech Min Sci Geomech Abstr, 10*, 351-361.

Ayatollahi, M., & Akbardoost, J. (2014). Size and geometry effects on rock fracture toughness: mode I fracture. *Rock Mech Rock Eng, 47*, 677-687.

Ayatollahi, M., & Aliha, M. (2008). On the use of Brazilian disc specimen for calculating mixed mode I-II fracture toughness of rock materials. *Eng Fract Mech, 75*(16), 4631-4641.

Ayatollahi, M., & Aliha, M. (2009). Mixed mode fracture in soda lime glass analyzed by using the generalized MTS criterion. *Int J Solids Struct, 46*(2), 311-321.

Ayatollahi, M., & Sedighiani, K. (2012). Mode I fracture initiation in limestone by strain energy density criterion. *Theor Appl Fract Mech, 57*, 14-18.

Ayatollahi, M., Mahdavi, E., Alborzi, M., & Obara, Y. (2016). Stress intensity factors of semi-circular bend specimens with stright-through and chevron notches. *Rock Mech Rock Eng, 49*, 1161-1172.

Bazant, Z. (1996). Analysis of work-of-fracture method for measuring fracture energy of concrete. *J Eng Mech, 122*, 138-144.

Berto, F., Pook, L., & Campagnolo, A. (2017). Corner point singularities under in-plane and out-of-plane loading: a review of recent results. *Eng Solid Mech, 5*(3), 167-176.

Bieniawski, Z., & Bernede, M. (1979). Suggested methods for determining the uniaxial compressive strength and deformability of rock materials: part 1. Suggested method for determination of the uniaxial compressive strength of rock materials. *Int J Rock Mech Min Sci Geomech Abstr, 16*, 137-138.

Bluhm, J. (1975). Slice synthesis of a three dimensional work of fracture specimen. *Eng Frac Mech, 7*, 593-604.

Bruning, T., Karakus, M., Akdag, S., Nguyen, G., & Goodchild, D. (2018a). Influence of deviatoric stress on rockburst occurrence: An experimental study. *Int J Min Sci Technol, 28*(5), 763-766.

Bruning, T., Karakus, M., Nguyen, G., & Goodchild, D. (2018b). Experimental study on the damage evolution of brittle rock under triaxial confinement with full circumferential strain control. *Rock Mech Rock Eng, 51*, 3321-3341.

Cai, M. (2008). Influence of stress path on tunnel excavation response - Numerical tool selection and modeling strategy. *Tunn Undergr Sp Technol, 23*, 618-628.

Carpinteri, A., & Accornero, F. (2018). Multiple snap-back instabilities in progressive microcracking coalescence. *Eng Fract Mech, 187*, 272-281.

Carpinteri, A., Lacidogna, G., & Puzzi, S. (2009). From criticality to final collapse: Evolution of the "b-value" from 1.5 to 1.0. *Chaos Soliton Frac, 41*, 843-853.

Carpinteri, A., Lacidogna, G., Accornero, F., Mpalaskas, A., Matikas, T., & Aggelis, D. (2013). Influence of damage in the acoustic emission parameters. *Cem Concr Compos, 44*, 9-16.

Chang, S., Lee, C., & Jeon, S. (2002). Measurement of rock fracture toughness under modes I and II and mixed-mode conditions by using disc-type specimens. *Eng Geol, 66*, 79–97.

Chen, B., Feng, X., Li, Q., Luo, R., & Li, S. (2015). Rock burst intensity classification based on the radiated energy with damage intensity at Jinping II hydropower station, China. *Rock Mech Rock Eng, 48*(1), 289-303.

Chen, R., Xia, K., Dai, F., Lu, F., & Luo, S. (2009). Determination of dynamic fracture parameters using a semi-circular bend technique in split Hopkinson pressure bar testing. *Eng Fract Mech, 76*, 1268-1276.

Chen, Y., Ni, J., Shao, W., & Azzam, R. (2012). Experimental study on the influence of temperature on the mechanical properties of granite under uni-axial compression and fatigue loading. *Int J Rock Mech Min Sci, 56*, 62-66.

Coli, M., Livi, E., Berry, P., Bandini, A., & Jia, X. N. (2010). Studies for rockburst prediction in the Carrara marble (Italy). In F. Xie (Ed.), *Proceeding of the 5th International Symposium on In-situ Rock Stress* (pp. 367-373). Beijing, China: CRC Press.

Cook, N. (1966). The design of underground excavations. *Proceedings of Eighth Rock Mechanics Symposium* (pp. 45-52). Minnesota: American Rock Mechanics Association.

Dai, F., & Xia, K. (2013a). Laboratory measurements of the rate dependence of the fracture toughness anisotropy of Barre granite. *Int J Rock Mech Min Sci, 60*, 57-65.

Dai, F., Chen, R., Iqbal, M., & Xia, K. (2010). Dynamic cracked chevron notched Brazilian disc method for measuring rock fracture parameters. *Int J Rock Mech Min Sci, 47*, 606-613.

Dai, F., Wei, M., Xu, N., Ma, Y., & Yang, D. (2015a). Numerical assessment of the progressive rock fracture mechanism of cracked chevron notched Brazilian disc specimens. *Rock Mech Rock Eng, 48*(2), 463-479.

Dai, F., Wei, M., Xu, N., Zhao, T., & Xu, Y. (2015b). Numerical investigation of the progressive fracture mechanism of four ISRM-suggested specimens for determining the mode I fracture toughness of rocks. *Comput Geotech, 69*, 424-441.

Dai, F., Xia, K., & Nasseri, M. (2013b). Micromechanical model for the rate dependence of the fracture toughness anisotropy of Barre granite. *Int J Rock Mech Min Sci, 63*, 113-121.

Dai, F., Xia, K., Zheng, H., & Wang, Y. (2011). Determination of dynamic rock mode I fracture parameters using cracked chevron notched semi-circular bend specimen. *Eng Fract Mech, 78*, 2633-2644.

Diederichs, M., Kaiser, P., & Eberhardt, E. (2004). Damage initiation and propagation in hard rock tunnelling and the influence of near-face stress rotation. *Int J Rock Mech Min Sci, 41*, 785-812.

Ding, Q., Ju, F., Mao, X., Ma, D., Yu, B., & Song, S. (2016). Experimental investigation of the mechanical behavior in unloading conditions of sandstone after high temperature treatment. *Rock Mech Rock Eng, 49*, 2641-2653.

Du, K., Tao, M., Li, X., & Zhou, J. (2016). Experimental study of slabbing and rockburst induced by true-triaxial unloading and local dynamic disturbance. *Rock Mech Rock Eng, 49*, 3437-53.

Dwivedi, R., Goel, R., Prasad, V., & Sinha, A. (2008). Thermo-mechanical properties of Indian and other granites. *Int J Rock Mech Min Sci*, 303-315.

Eberhardt, E., Stead, D., Stimpson, B., & Read, R. (1998). Identifying crack initiation and propagation thresholds in brittle rock. *Can Geotech J, 35*(2), 222-233.

Erarslan, N. (2013). A study on the evaluation of the fracture process zone in CCNBD rock samples. *Exp Mech*, *53*, 1475-1489.

Fairhurst, C., & Hudson, J. (1999). Draft ISRM suggested method for the complete stress-strain curve for intact rock in uniaxial compression. *Int J Rock Mech Min Sci, 36*, 279-289.

Feng, G., Feng, X., Chen, B., Xiao, Y., & Yu, Y. (2015). A microseismic method for dynamic warning of rockburst development processes in tunnels. *Rock Mech Rock Eng, 48*, 2061-2076.

Feng, G., Kang, Y., Chen, F., Liu, Y., & Wang, X. (2018). The influence of temperatures on mixed-mode (I + II) and mode-II fracture toughness of sandstone. *Eng Fract Mech, 189*, 51-63.

Feng, G., Kang, Y., Meng, T., Hu, Y., & Li, X. (2017). The influence of temperature on mode I fracture toughness and fracture characteristics of sandstone. *Rock Mech Rock Eng, 50*(8), 2007-2019.

Feng, X., Zhang, X., Kong, R., & Wang, G. (2016). A novel mogi type true triaxial testing apparatus and its use to obtain complete stress-strain curves of hard rocks. *Rock Mech Rock Eng, 49*, 1649-1662.

Fowell, R. (1995). ISRM commission on testing methods. Suggested method for determining mode I fracture toughness using cracked chevron notched Brazilian disc (CCNBD) specimens. *Int J Rock Mech Min Sci Geomech Abstr, 32*(1), 57-64.

Fowell, R., & Xu, C. (1994). The use of cracked Brazilian disc geometry for rock fracture investigations. *Int J Rock Mech Min Sci Geomch Abstr, 31*(6), 571-579.

Funatsu, T., Kuruppu, M., & Matsui, K. (2014). Effects of temperature and confining pressure on mixed-mode (I-II) and mode II fracture toughness of Kimachi sandstone. *Int J Rock Mech Min Sci, 67*, 1-8.

Funatsu, T., Seto, M., Shimada, H., Matsui, K., & Kuruppu, M. (2004). Combined effects of increasing temperature and confining pressure on the fracture toughness of clay bearing rocks. *Int J Rock Mech Min Sci, 41*, 927-938.

Funatsu, T., Shimizu, N., Kuruppu, M., & Matsui, K. (2015). Evaluation of mode I fracture toughness assisted by the numerical determination of K-resistance. *Rock Mech Rock Eng, 48*, 143-157.

Gao, G., Yao, W., Xia, K., & Li, Z. (2015). Investigation of the rate dependence of fracture propagation in rocks using digital image correlation (DIC) method. *Eng Fract Mech, 138*, 146-155.

Gao, Y., Feng, X., Zhang, X., Feng, G., Jiang, Q., & Qiu, S. (2018). Characteristic stress levels and brittle fracturing of hard rocks subjected to true triaxial compression with low minimum principal stress. *Rock Mech Rock Eng, 51*(12), 3681-3697.

Gautam, P., Verma, A., Maheshwar, S., & Singh, T. (2016). Thermomechanical analysis of different types of sandstone at elevated temperature. *Rock Mech Rock Eng, 49*, 1985-1993.

Ghouli, S., Ayatollahi, M., & Bushroa, A. (2018). Fracture characterization of ceria partially stabilized zirconia using the GMTSN criterion. *Eng Fract Mech, 199,* 647-657.

Gong, F., Si, X., Li, L., & Wang, S. (2018). Experimental investigationof strain rockburst in circular caverns under deep three-dimensional high-stress conditions. *Rock Mech Rock Eng*. doi:https://doi.org/10.1007/s00603-018-1660-5

Gong, Q., Yin, L., Wu, S., Zhao, J., & Ting, Y. (2012). Rock burst and slabbing failure and its influence on TBM excavation at headrace tunnels in Jinping II hydropower station. *Eng Geol, 124,* 98-108.

Gong, W., Peng, Y., Wang, H., He, M., Sousa, L., & Wang, J. (2015). Fracture angle analysis of rock burst faulting planes based on true-triaxial experiment. *Rock Mech Rock Eng, 48,* 1017-1039.

Gowd, T., & Rummel, F. (1980). Effect of confining pressure on the fracture behaviour of a porous rock. *Int J Rock Mech Min Sci Geomech Abstr, 17,* 225-229.

Griffith, A. (1921). The phenomena of rupture and flow in solids. *J Appl Mech, 221,* 163-198.

Grosse, C., & Ohtsu, M. (2008). *Acoustic emission testing.* Berlin: Springer.

Gutenberg, B., & Richter, C. (1956). Magnitude and energy of earthquakes. *Annals of Geophysics, 9*(1), 1-15.

Haimson, B., & Chang, C. (2000). A new true triaxial cell for testing mechanical properties of rock, and its use to determine rock strength and deformability of Westerly granite. *Int J Rock Mech Min Sci, 37,* 285-296.

He , M., Sousa, L., Miranda, T., & Zhu, G. (2015). Rockburst laboratory tests database — Application of data mining techniques. *Eng Geol, 185,* 116-130.

He, B., Zelig, R., Hatzor, Y., & Feng, X. (2016). Rockburst generation in discontinuous rock masses. *Rock Mech Rock Eng,* 1-22.

He, M., Jia, X., Coli, M., Livi, E., & Sousa, L. (2012c). Experimental study of rockbursts in underground quarrying of Carrara marble. *Int J Rock Mech Min Sci, 52,* 1-8.

He, M., Miao, J., & Feng, J. (2010). Rock burst process of limestone and its acoustic emission characteristics under true-triaxial unloading conditions. *Int J Rock Mech Min Sci, 47*, 286-298.

He, M., Nie, W., Zhao, Y., & Guo, W. (2012b). Experimental investigation of bedding plane orientation on the rockburst behavior of sandstone. *Rock Mech Rock Eng, 45,* 311-26.

He, M., Xia, H., Jia, X., Gong, W., Zhao, F., & Liang, K. (2012a). Studies on classification, criteria and control of rockbursts. *J Rock Mech Geotech Eng, 4*(2), 97-114.

Hedley, D. (1992). *Rockburst handbook for Ontorio hardrock mines.* CANMET Special Report.

Heuze, F. (1983). High-temperature mechanical, physical and thermal properties of granitic rocks - A review. *Int J Rock Mech Min Sci, 20*(1), 3-10.

Hoek, E., & Brown, E. (1980). *Underground excavations in rock.* London: The Institution of Mining and Metallurgy.

Hua, A., & You, M. (2001). Rock failure due to energy release during unloading and application to underground rock burst control. *Tunn Undergr Sp Technol, 16*, 241-246.

Huang, D., & Li, Y. (2014). Conversion of strain energy in triaxial unloading tests on marble. *Int J Rock Mech Min Sci, 66*, 160-168.

Huang, R., Wang, X., & Chan, L. (2001). Triaxial unloading test of rocks and its implication for rock burst. *Bull Eng Geol Env, 60*, 37-41.

Iqbal, M., & Mohanty, B. (2006). Experimental calibration of stress intensity factors of the ISRM suggested cracked chevron-notched Brazilian disc specimen used for determination of mode-I fracture toughness. *Int J Rock Mech Min Sci, 43*, 1270–1276.

Iqbal, M., & Mohanty, B. (2007). Experimental calibration of ISRM suggested fracture toughness measurement techniques in selected brittle rocks. *Rock Mech Rock Eng, 40*(5), 453–475.

Irwin, G. (1957). Analysis of stresses and strains near the end of a crack. *J Appl Mech, 24*, 361-364.

Jiang, Q., Feng, X., Xiang, T., & Su, G. (2010). Rockburst characteristics and numerical simulation based on a new energy index: a case study of a tunnel at 2500 m depth. *Bull Eng Geol Environ, 69*, 381-388.

Karakus, M., Akdag, S., & Bruning, T. (2016). Rock fatigue damage assessment by acoustic emission. In P. Ranjith, & J. Zhao (Ed.), *International Conference on Geo-mechanics, Geo-energy and Geo-resources, IC3G*, (pp. 9-82-88). Melbourne, Australia.

Keles, C., & Tutluoglu, L. (2011). Investigation of proper specimen geometry of mode I fracture toughness testing with flattened Brazilian disc method. *Int J Fract, 169*, 61-75.

Keshavarz, M., Pellet, F., & Loret, B. (2010). Damage and changes in mechanical properties of gabbro thermally loaded up to 1000 °C. *Pure Appl Geophys, 167*, 1511-1523.

Kidybinski, A. (1981). Bursting liability indices of coal. *Int J Rock Mech Min Sci Geomech Abstr, 18*, 295-304.

Kim, J., Lee, K., Cho, W., Choi, H., & Cho, G. (2015). A comparative evaluation of stress-strain and acoustic emission methods for quantitative damage assessments of brittle rock. *Rock Mech Rock Eng, 48*, 495-508.

Klepaczko, J., Bassim, M., & Hsu, T. (1984). Fracture toughness of coal under quasi-static and impact loading. *Eng Fract Mech, 19*(2), 305-316.

Kolsky, H. (1949). An investigation of the mechanical properties of materials at very high rates of loading. *Proc Phys Soc Sect B, 62*(11), 676-700.

Kolsky, H. (1953). *Stress waves in solids.* Oxford: Clarendon Press.

Kong, B., Wang, E., Li, Z., Wang, X., Liu, J., & Li, N. (2016). Fracture mechanical behavior of sandstone subjected to high-temperature treatment and its acoustic emission characteristics under uniaxial compression conditions. *Rock Mech Rock Eng, 49*, 4911-4918.

Kong, R., Feng, X., Zhang, X., & Yang, C. (2018). Study on crack initiation and damage stress in sandstone under true triaxial compression. *Int J Rock Mech Min Sci, 106*, 117-123.

Kumari, W., Ranjith, P., Perera, M., Chen, B., & Abdulagatov, I. (2017b). Temperature-dependent mechanical bahviour of Australian Strathbogie granite with different cooling treatments. *Eng Geol, 229*, 31-44.

Kumari, W., Ranjith, P., Perera, M., Shao, S., Chen, B., Lashin, A., Rathnaweera, T. (2017a). Mechanical behaviour of Australian Strathbogie granite under in-situ stress and temperature conditions: An application to geothermal energy extraction. *Geothermics, 65*, 44-59.

Kuruppu, M. (1997). Fracture toughness measurement using chevron notched semi-circular bend specimen. *Int J Fract, 86*, 33-38.

Kuruppu, M., & Chong, K. (2012). Fracture toughness testing of brittle materials using semi-circular bend (SCB) specimen. *Eng Fract Mech, 91*, 133-150.

Kuruppu, M., Obara, Y., Ayatollahi, M., Chong, K., & Funatsu, T. (2014). ISRM-suggested method for determining the mode I static fracture toughness using semi-circular bend specimen. *Rock Mech Rock Eng, 47*(1), 267-274.

Lambert, D., & Ross, A. (2000). Strain rate effects on dynamic fracture and strength. *Int J Impact Eng, 24*(10), 985-998.

Landis, E., Nagy, E., & Keane, D. (2003). Microstructure and fracture in three dimensions. *Eng Fract Mech, 70*, 911-925.

Li, D., Sun, Z., Xie, T., Li, X., & Ranjith, P. (2017). Energy evolution chracteristics of hard rock during triaxial failure with different loading and unloading paths. *Eng Geol, 228*, 270-281.

Li, M., Mao, X., Cao, L., Pu, H., & Mao, R. (2016). Effects of thermal treatment on the dynamic mechanical properties of coal measures sandstone. *Rock Mech Rock Eng, 49*, 3525-3539.

Li, Q. (2001). Strain energy density failure criterion. *Int J Solids Struct, 38*(38-39), 6997-7013.

Li, S., Feng, X., Li, Z., Chen, B., Zhang, C., & Zhou, H. (2012). In situ monitoring of rockburst nucleation and evolution in the deeply buried tunnels of Jinping II hydropower station. *Eng Geol, 137-138*, 85-96.

Li, X., Du, K., & Li, D. (2015). True triaxial strength and failure modes of cubic rock specimens with unloading the minor principal stress. *Rock Mech Rock Eng, 48*, 2185-2196.

Li, X., Feng, F., Li, D., Du, K., Ranjith, P., & Rostami, J. (2018). Failure characteristics of granite influenced by sample height-to-width ratios and intermediate principal stress under true-triaxial unloading conditions. *Rock Mech Rock Eng, 51*(5), 1321-1345.

Li, Y., Huang, D., & Li, X. (2014). Strain rate dependency of coarse crystal marble under uniaxial compression: strength, deformation and strain energy. *Rock Mech Rock Eng, 47*, 1153-1164.

Liang, C., Wu, S., Li, X., & Xin, P. (2015). Effects ofstrain rate on fracture characteristics and mesoscopic failure mechanism of granite. *Int J Rock Mech Min Sci, 76*, 146-154.

Lim, I., Johnston, I., & Choi, S. (1994). Assessment of mixed mode fracture toughness testing methods for rock. *Int J Rock Mech Min Scie Geomech Abstr, 31*(3), 265-272.

Liu, S., & Xu, J. (2013). Study on dynamic characteristics of marble under impact loading and high temperature. *Int J Rock Mech Min Sci, 62*, 51-58.

Liu, S., & Xu, J. (2015). Analysis on damage mechanical characteristics of marble exposed to high temperature. *Int J Damage Mech, 24*(8), 1180-1193.

Lockner, D. (1993). The role of acoustic emission in the study of rock fracture. *Int J Rock Mech Min Sci Geomech Abstr, 30*, 883-899.

Mahanta, B., Singh, T., & Ranjith, P. (2016). Influence of thermal treatment on mode I fracture toughness of certain Indian rocks. *Eng Geol, 210*, 103-114.

Mahanta, B., Tripathy, A., Vishal, V., Singh, T., & Ranjith, P. (2017). Effects of strain rate on fracture toughness and energy release rate of gas shales. *Eng Geol, 218*, 39-49.

Masri, M., Sibai, M., Shao, J., & Mainguy, M. (2014). Experimental investigation of the effect of temperature on the mechnical behavior of Tournemire shale. *Int J Rock Mech Min Sci, 70*, 185-191.

Meng, Q., Zhang, M., Han, L., Pu, H., & Nie, T. (2016). Effects of acoustic emission and energy evolution of rock specimens under the uniaxial cyclic loading and unloading compression. *Rock Mech Rock Eng, 49*, 3873-3886.

Michelis, P. (1985). A true triaxial cell for low and high pressure experiments. *Int J Rock Mech Min Sci & Geomech Abstr, 22*(3), 183-188.

Mindess, S., Banthia, N., & Yan, C. (1987). The fracture toughness of concrete under impact loading. *Cem Concr Res, 17*(2), 231-241.

Mitri, H., Tang, B., & Simon, R. (1999). FE modeling of mining-induced energy release and storage rates. *J S Afr Inst Min Metall*, 103-110.

Mogi, K. (1971). Fracture and flow of rocks under high triaxial compression. *J Geophys Res, 76*(5), 1255-1269.

Mohamadi, M., & Wan, R. (2016). Strength and post-peak response of Colorado shale at high pressure and temperature. *Int J Rock Mech Min Sci*, 34-46.

Munoz, H., & Taheri, A. (2017). Specimen aspect ratio and progressive field-strain pattern development of sandstone under uniaxial compression by 3D Image Correlation. *J Rock Mech Geotech Eng, 9*(4), 599-610.

Munoz, H., & Taheri, A. (2018). Postpeak deformability parameters of localized and nonlocalized damage zones of rocks under cyclic loading. *Geotechnical Testing Journal, 42*(6), 22p. doi:https://doi.org/10.1520/GTJ20170266

Munoz, H., Taheri, A., & Chanda, E. (2016a). Fracture energy-based brittleness index development and brittleness quantification by pre-peak strength parameters in rock uniaxial compression. *Rock Mech Rock Eng*, 1-20.

Munoz, H., Taheri, A., & Chanda, E. (2016b). Pre-peak and post-peak rock strain characteristics during uniaxial compression by 3D Digital Image Correlation. *Rock Mech Rock Eng, 49*(7), 2541-2554.

Nakano, M., Kishida, K., Yamauchi, Y., & Sogabe, Y. (1994). Dynamic fracture initiation in brittle materials under combined mode I/II loading. *J Phys IV France, 04*(C8), C8-698-C698-700.

Nasseri, M., Goodfellow, S., Lombo, L., & Young, R. (2014). 3-D transport and acoustic properties of Fontainebleau sandstone during true-triaxial deformation experiments. *Int J Rock Mech Min Sci, 69*, 1-18.

Nasseri, M., Graselli, G., & Mohanty, B. (2010). Fracture toughness and fracture roughness in anisotropic granitic rocks. *Rock Mech Rock Eng, 43*(4), 403-414.

Nasseri, M., Mohanty, B., & Young, R. (2006). Fracture toughness measurements and acoustic emission activity in brittle rock. *Pure Appl Geophys, 163*, 917-945.

Nasseri, M., Tatone, B., Graselli, G., & Young, R. (2009). Fracture toughness and fracture roughness interrelationship in thermally treated Westerly granite. *Pure Appl Geophys, 166*, 801-822.

Nemat-Nasser, S., & Horii, H. (1982). Compression-induced nonplanar crack extension with application to splitting, exfoliation and rockburst. *J Geophys Res, 87*, 6805-6821.

Nicksiar, M., & Martin, C. (2012). Evaluation of methods for determining crack initiation in compression tests on low-porosity rocks. *Rock Mech Rock Eng, 45*, 607-617.

Okubo, S., Nishimatsu, Y., & He, C. (1990). Loading rate dependence of Class II behaviour in uniaxial and triaxial compression tests - an application of a proposed new control method. *Int J Rock Mech Min Sci, 24*, 559-562.

Ouchterlony, F. (1982). Review of fracture toughness testing of rocks. *Solid Mech Arch, 7*, 131-211.

Ouchterlony, F. (1988). ISRM suggested methods for determining fracture toughness of rocks. *Int J Rock Mech Min Sci Geomech Abstr, 25*, 71-96.

Palmstrom, A. (1995). RMi-a rock mass characterization system for rock engineering purposes (PhD thesis). *Oslo University, Norway*.

Peng, J., Rong, G., Cai, M., Yao, M., & Zhou, C. (2016). Physical and mechanical behaviors of a thermal-damaged coarse marble under uniaxial compression. *Eng Geol, 200,* 88-93.

Peng, R., Ju, Y., Wang, J., Xie, H., Gao, F., & Mao, L. (2015). Energy dissipation and release during coal failure under conventional triaxial compression. *Rock Mech Rock Eng, 48,* 509-526.

Physical Acoustics Corporation. (2007). *PCI-2 based AE system user's manual.* Princeton Junction.

Renani, H., & Martin, C. (2018). Cohesion degradation and friction mobilization in brittle failure of rocks. *Int J Rock Mech Min Sci, 106,* 1-13.

Rummel, F., & Fairhurst, C. (1970). Determination of the post-failure behavior of brittle rock using a servo-controlled testing machine. *Rock Mech Rock Eng, 2*, 189-204.

Russenes, B. (1974). Analysis of rock spalling for tunnels in steep valley sides (MSc Thesis). *Norwegian Ins Tech Dep of Geology, Norway*.

Sagar, R., Prasad, B., & Kumar, S. (2012). An experimental study on cracking evolution in concrete and cement mortar by the b-value analysis of acoustic emission technique. *Cem Concr Research, 42*, 1094-1104.

Shi, X., Yao, W., Liu, D., Xia, K., Tang, T., & Shi, Y. (2019). Experimental study of the dynamic fracture toughness of anisotropic black shale using notched semi-circular bend specimens. *Eng Fract Mech, 205*, 136-151.

Singh, S. (1989). Classification of mine workings according to their rockburst proneness. *Min Sci Technol, 8*, 253-262.

Sirdesai, N., Singh, T., Ranjith, P., & Singh, R. (2017). Effect of varied durations of thermal treatment on the tensile strength of red sandstone. *Rock Mech Rock Eng, 50*, 205-213.

Su , G., Jiang, J., Zhai, S., & Zhang, G. (2017a). Influence of tunnel axis stress on strainburst: An experimental study. *Rock Mech Rock Eng, 50*, 1551-1567.

Su, G., Hu, L., Feng, X., Yan, L., Zhang, G., Yan, S., Yan, Z. (2018a). True Triaxial experimental study of rockbursts induced by ramp and cyclic dynamic disturbances. *Rock Mech Rock Eng, 51*(4), 1027-1045.

Su, G., Shi, Y., Feng, X., Jiang, J., Zhang, J., & Jiang, Q. (2018b). True-triaxial experimental study of the evolutionary features of the acoustic emissions and sounds of rockburst processes. *Rock Mech Rock Eng, 51*(2), 375-389.

Su, G., Zhai, S., Jiang, J., Zhang, G., & Yan, L. (2017b). Influence of radial stress gradient on strainburts: An experimental study. *Rock Mech Rock Eng, 50*(10), 2659-2676.

Sun, Q., Zhang, W., Xue, L., Zhang, Z., & Su, T. (2015). Thermal damage pattern and thresholds of granite. *Environ Earth Sci, 74*, 2341-2349.

Sun, X., Xu, H., He, M., & Zhang, F. (2017). Experimental investigation of the occurrence of rockburst in a rock specimen through infrared thermography and acoustic emission. *Int J Rock Mech Min Sci, 93*, 250-259.

Takahashi, M., & Koide, H. (1989). Effect of the intermediate principal stress on strength and deformation behavior of sedimentary rocks at the depth shallower than 2000 m. (pp. 19-26). Pau, France: ISRM International Symposium. International Society for Rock Mechanics.

Tang, C., & Xu, X. (1990). A new method for measuring dynamic fracture toughness of rock. *Eng Fract Mech, 35*(4-5), 783-791.

Tarasov, B., & Potvin, Y. (2013). Universal criteria for rock brittleness estimation under triaxial compression. *Int J Rock Mech Min Sci, 59*, 57-69.

Tutluoglu, L., & Keles, C. (2011). Mode I fracture toughness determination with straight notched disk bending method. *Int J Rock Mech Min Sci, 48*(8), 1248-1261.

Tutluoglu, L., & Keles, C. (2012). Effects of geometric factors in mode I fracture toughness for modified ring tests. *Int J Rock Mech Min Sci, 51*, 149-161.

Walton, G., Alejano, L., Arzua, J., & Markley, T. (2018). Crack damage parameters and dilatancy of artificially jointed granite samples under triaxial compression. *Rock Mech Rock Eng, 51*(6), 1637-1656.

Wang, J., & Park, H. (2001). Comprehensive prediction of rockburst based on analysis of strain energy in rocks. *Tunn Undergr Sp Technol, 16*(1), 49-57.

Wang, Q., Feng, F., Ni, M., & Gou, X. (2011). Measurement of mode I and mode II rock dynamic fracture toughness with cracked straight through flattened Brazilian disc impacted by split Hopkinson pressure bar. *Eng Fract Mech, 78*(12), 2455-2469.

Wang, Q., Jia, X., & Wu, L. (2004). Wide-range stress intensity factors for the ISRM suggested method using CCNBD specimens for rock fracture toughness tests. *Int J Rock Mech Min Sci, 41*, 709-716.

Wang, Q., Jia, X., Kou, S., Zhang, Z., & Lindqvist, P. (2003). More accurate stress intensity factor derived by finite element analysis for the ISRM suggested rock fracture toughness specimen CCNBD. *Int J Rock Mech Min Sci, 4*(2), 233–241.

Wang, Q., Yang, J., Zhang, C., Zhou, Y., Li, L., Zhu, Z., & Wu, L. (2015). Sequential determination of dynamic initiation and propagation toughness of rock using an experimental–numerical–analytical method. *Eng Fract Mech, 141*, 78-94.

Wang, Q., Zhang, S., & Xie, H. (2010). Rock dynamic fracture toughness tested with holed-cracked flattened Brazilian discs diametrically impacted by SHPB and its size effect. *Exp Mech, 50*(7), 877-885.

Wang, Z., Shi, H., & Wang, J. (2018). Mechanical behavior and damage constitutive model of granite under coupling of temperature and dynamic loading. *Rock Mech Rock Eng, 51*(10), 3045-3059.

Wawersik, W., & Fairhurst, C. (1970). A study of brittle rock fracture in laboratory compression experiments. *Int J Rock Mech Min Sci, 7*, 561-575.

Wawersik, W., Carlson, L., Holcomb, D., & Williams , R. (1997). New method for true-triaxial rock testing. *Int J Rock Mech Min Sci, 34*, 330-344.

Wei , M., Dai, F., Xu, N., & Zhao, T. (2017a). Experimental and numerical investigation of cracked chevron notched Brazilian disc specimen for fracture toughness testing of rock. *Fatigue Fract Eng Mater Struct, 41*, 197-211.

Wei, M., Dai, F., Liu, Y., Xu, N., & Zhao, T. (2017b). An experimental and theoretical comparison of CCNBD and CCNSCB specimens for determining mode I fracture toughness of rocks. *Fatigue Fract Eng Mater Struct, 41*, 1002-1018.

Wei, M., Dai, F., Xu, N., & Zhao, T. (2016b). Stress intensity factors and fracture process zones of ISRM-suggested chevron notched specimens for mode I fracture toughness testing of rocks. *Eng Fract Mech, 168*, 174-189.

Wei, M., Dai, F., Xu, N., & Zhao, T. (2018). Experimental and numerical investigation of cracked chevron notched Brazilian disc specimen for fracture toughness tesing of rock. *Fatigue Fract Eng Mater Struct, 41*, 197-211.

Wei, M., Dai, F., Xu, N., Liu, J., & Xu, Y. (2016c). Experimental and numerical study on the cracked chevron notched semi-circular bend method for characterizing the mode I fracture toughness of rocks. *Rock Mech Rock Eng, 49*, 1595-1609.

Wei, M., Dai, F., Xu, N., Liu, Y., & Zhao, T. (2017c). Fracture prediction of rocks under mode I and mode II loading using the generalized maximum tangential strain criterion. *Eng Fract Mech, 186*, 21-38.

Wei, M., Dai, F., Xu, N., Xu, Y., & Xia, K. (2015). Three-dimensional numerical evaluation of the progressive fracture mechanism of cracked chevron notched semicircular bend rock specimens. *Eng Fract Eng, 134*, 286-303.

Wei, M., Dai, F., Xu, N., Zhao, T., & Liu, Y. (2017d). An experimental and theoretical assessment of semi-circular bend specimens with chevron and straight-through notches for mode I fracture toughness testing of rocks. *Int J Rock Mech Min Sci, 99*, 28-38.

Wei, M., Dai, F., Xu, N., Zhao, T., & Xia, K. (2016a). Experimental and numerical study on the fracture process zone and fracture toughness determination for ISRM-suggested semi-circular bend rock specimen. *Eng Fract Mech, 154*, 43-56.

Weng, L., Huang, L., Taheri, A., & Li, X. (2017). Rockburst characteristics and numerical simulation based on strain energy density index: A case study of a roadway in Linglong gold mine, China. *Tunn Undergr Space Technol, 69*, 223-232.

Westergaard, H. (1939). Bearing pressures and crack. *J Appl Mech, 6*, A49-A53.

Wiles, T. (2002). Loading system stiffness-a parameter to evaluate rockburst potential. *First International Seminar on Deep and High Stress Mining.* Perth, Australia: Australian Centre for Geomechanics.

Xia, K., Dai, F., & Chen, R. (2011). Split Hopkinson pressure bar tests of rocks: Advances in experimental techniques and applications to rock strength and fracture. In Y. Zhou, & J. Zhao, *Advances in rock dynamics and applications* (pp. 35-78). CRC Press/Balkema.

Xie, H., Li, L., Peng, R., & Ju, Y. (2009). Energy analysis and criteria for structural failure of rocks. *J Rock Mech Geotech Eng, 1*(1), 11-20.

Xu, H., Feng, X., Yang, C., Zhang, X., Zhou, Y., & Wang, Z. (2019). Influence of initial stresses and unloading rates on the deformation and failure mechanism of Jinping marble under true triaxial compression. *Int J Rock Mech Min Sci, 117,* 90-104.

Xu, J., Jiang, J., Xu, N., Liu, Q., & Gao, Y. (2017). A new energy index for evaluating the tendency of rockburst and its engineering application. *Eng Geol, 230,* 46-54.

Xu, N., Dai, F., Wei, M., Xu, Y., & Zhao, T. (2016b). Numerical observation of three-dimensional wing cracking of cracked chevron notched Brazilian disc rock specimen subjected to mixed mode loading. *Rock Mech Rock Eng, 49*(1), 79-96.

Xu, X., & Karakus, M. (2018). A coupled thermo-mechanical damage model for granite. *Int J Rock Mech Min Sci, 103,* 195-204.

Xu, X., Karakus, M., Gao, F., & Zhang , Z. (2018). Thermal damage constitutive model for rock considering damage threshold and residual strength. *J Cent South Univ, 25*(10), 2523-2536.

Xu, Y., Dai, F., Zhao, T., Xu, N., & Liu, Y. (2016a). Fracture toughness determination of cracked chevron notched Brazilian disc rock specimen via Griffith energy criterion incorporating realistic fracture profiles. *Rock Mech Rock Eng, 49,* 3083-3093.

Yang, R., Yue, Z., Sun, Z., Xiao, T., & Guo, D. (2009). Dynamic fracture behavior of rock under impact load using the caustics method. *Min Sci Technol, 19*(1), 79-83.

Yang, S., Ju, Y., Gao, F., & Gui, Y. (2016). Strength, deformability and X-ray micro-CT observations of deeply buried marble under different confining pressures. *Rock Mech Rock Eng, 49,* 4227-4244.

Yang, S., Ranjith, P., Jing, H., Tian, W., & Ju, Y. (2017). An experimental invesitation on thermal damage and failure mechanical behavior of granite after exposure to different high temperature treatments. *Geothermics, 65,* 180-197.

Yao, M., Rong, G., Zhou, C., & Peng, J. (2016). Effects of thermal damage and confining pressure on the mechanical peroperties of coarse marble. *Rock Mech Rock Eng, 49,* 2043-2054.

Yin , T., Bai, L., Li, X., Li, X., & Zhang , S. (2018). Effect of thermal treatment on the mode I fracture toughness of granite under dynamic and static coupling load. *Eng Fract Mech, 199,* 143-158.

Yin, T., Li, X., Xia, K., & Huang, S. (2012). Effect of thermal treatment on the dynamic fracture toughness of Laurentian granite. *Rock Mech Rock Eng, 45,* 1087-1094.

Yu, J., & Shang, X. (2019). Analysis of the influence of boundary pressure and friction on determining fracture toughness of shale using cracked Brazilian disc test. *Eng Fract Mech, 212,* 57-69.

Zhang , C., Feng, X., Zhou, H., Qiu, S., & Wu, W. (2012). Case histories of four extremely intense rockbursts in deep tunnels. *Rock Mech Rock Eng, 45,* 275-288.

Zhang , Q., & Zhao, J. (2013b). Determination of mechanical properties and full-field strain measurements of rock material under dynamic loads. *Int J Rock Mech Min Sci, 60,* 423-439.

Zhang, P., Mishra, B., & Heasley, K. (2015). Experimental investigation on the influence of high pressure and high temperature on the mechanical properties of deep reservoir rocks. *Rock Mech Rock Eng, 48*, 2197-2211.

Zhang, Q., & Zhao, J. (2013a). Effect of loading rate on fracture toughness and failure micomechanisms in marble. *Eng Fract Mech, 102*, 288-309.

Zhang, Q., & Zhao, J. (2014). A review of dynamic experimental techniques and mechanical behaviour of rock materials. *Rock Mech Rock Eng, 47*, 1411-1478.

Zhang, Z., Kou, S., Liang, L., & Lindqvist, P.-A. (2000). Effects of loading rate on rock fracture: fracture characteristics and energy partitioning. *Int J Rock Mech Min Sci, 37*, 745-762.

Zhang, Z., Yu, J., Kou, S., & Lindqvist, P.-A. (2001). Effects of high temperatures on dynamic rock fracture. *Int J Rock Mech Min Sci, 38*, 211-225.

Zhao, J., Feng, X., Zhang, X., Zhang, Y., Zhou, Y., & Yang, C. (2018). Brittle-ductile transition and failure mechanism of Jinping marble under true triaxial compression. *Eng Geol, 232*, 160-170.

Zhao, J., Zhou, Y., Hefny, A., Cai, J., Chen, S., Li, H., Seah, C. (1999). Rock dynamics research related to cavern development for ammunition storage. *Tunn Undergr Space Technol, 14*(4), 513-526.

Zhao, X., & Cai, M. (2014). Influence of specimen height-to-width ratio on the strainburst characteristics of Tianhu granite under true-triaxial unloading conditions. *Can Geotech J, 52*, 890-902.

Zhao, X., Cai, M., Wang, J., & Li, P. (2015). Objective determination of crack initiation stress of brittle rocks under compression using AE measurement. *Rock Mech Rock Eng, 48*, 2473-2484.

Zhao, X., Wang, J., Cai, M., Cheng, C., Ma, L., Su, R., Li, D. (2014). Influence of unloading rate on the strainburst characteristics of Beishan granite under true-triaxial unloading conditions. *Rock Mech Rock Eng, 47*, 467-483.

Zhao, Y., Gong, S., Hao, X., Peng, Y., & Jiang, Y. (2017). Effects of loading rate and bedding on the dynamic fracture toughness of coal: Laboratory experiments. *Eng Fract Mech, 178*, 375-391.

Zhao, Y., Zhao, G.-F., & Jiang, Y. (2013). Experimental and numerical modelling investigation on fracturing in coal under impact loads. *Int J Fract, 183*(1), 63-80.

Zheng, Z., Feng, X., Zhang, X., Zhao, J., & Yang, C. (2019). Residual strength characteristics of CJPL marble under true triaxial compression. *Rock Mech Rock Eng, 52*(4), 1247-1256.

Zhou, L., Zhu, Z., Qiu, H., Zhang, X., & Lang, L. (2018). Study of the effect of loading rates on crack propagation velocity and rock fracture toughness using cracked tunnel specimens. *Int J Rock Mech Min Sci, 112*, 25-34.

Zhou, S., Xia, C., Hu, Y., Zhou, Y., & Zhang, P. (2015). Damage modeling of basaltic rock subjected to cyclic temperature and uniaxial stress. *Int J Rock Mech Min Sci, 77*, 163-173.

Zhou, X., & Yang, H. (2018). Dynamic damage localization in crack-weakened rock mass: Strain energy density factor approach. *Theor Appl Fract Mec, 97*, 289-302.

Zhou, Y., Xia, K., Li, X., Li, H., Ma, G., Zhao, J., Dai, F. (2012). Suggested methods for determining the dynamic strength parameters and mode-I fracture toughness of rock materials. *Int J Rock Mech Min Sci, 49*, 105-112.

Zhou, Z., Cai, X., Ma, D., Du, X., Chen, L., Wang, H., & Zang, H. (2019). Water saturation effects on dynamic fracture behavior of sandstone. *Int J Rock Mech Min Sci, 114*, 46-61.

Zuo, J., Xie, H., Dai, F., & Ju, Y. (2014). Three-point bending test investigation of the fracture behavior of siltstone after thermal treatment. *Int J Rock Mech Min Sci, 70*, 133-143.

APPENDIX A – Failed specimens and locations of the ejected rock fragments under true-triaxial unloading condition

Figure A.1 Specimen B1#1 after strain burst test (25 °C)

Figure A.2 Locations of the ejected fragments for B1#1 after strain burst test (25 °C)

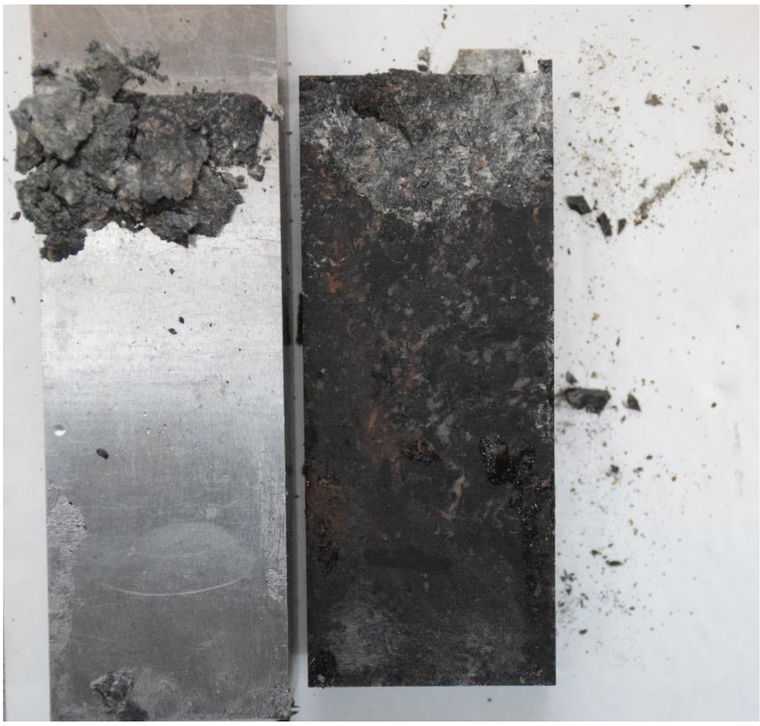

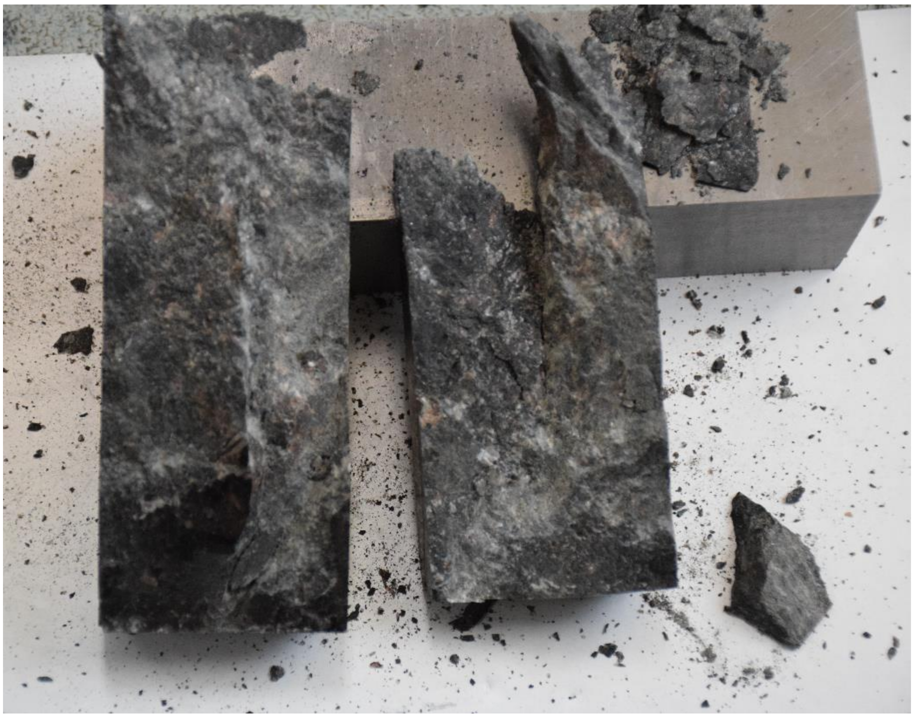

Figure A.3 Specimen B1#2 after strain burst test (25 °C)

Figure A.4 Specimen B2#1 after strain burst test (50 °C)

Figure A.5 Locations of the ejected fragments for B2#1 after strain burst test (50 °C)

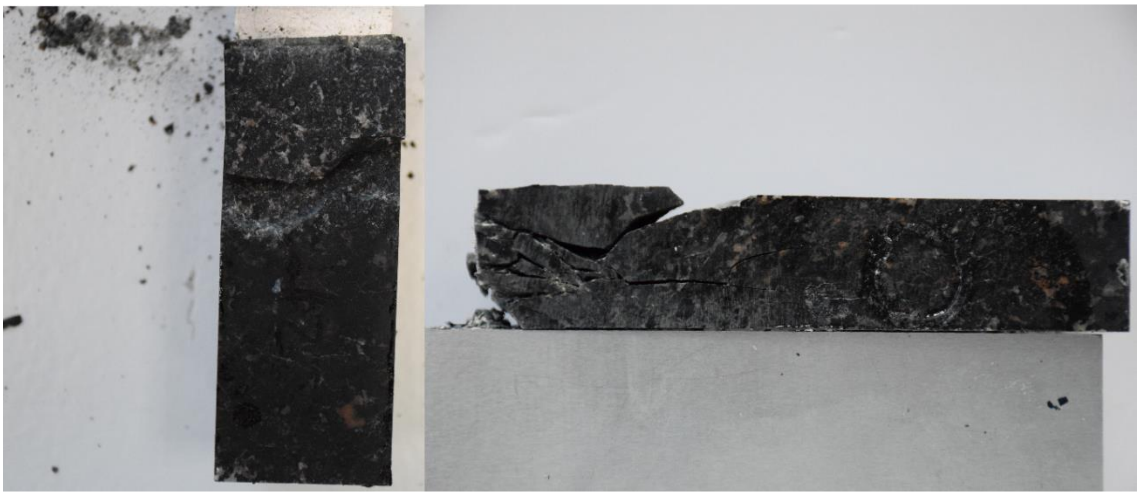

Figure A.6 Specimen B2#2 after strain burst test (50 °C)

Figure A.7 Locations of the ejected fragments for B2#2 after strain burst test (50 °C)

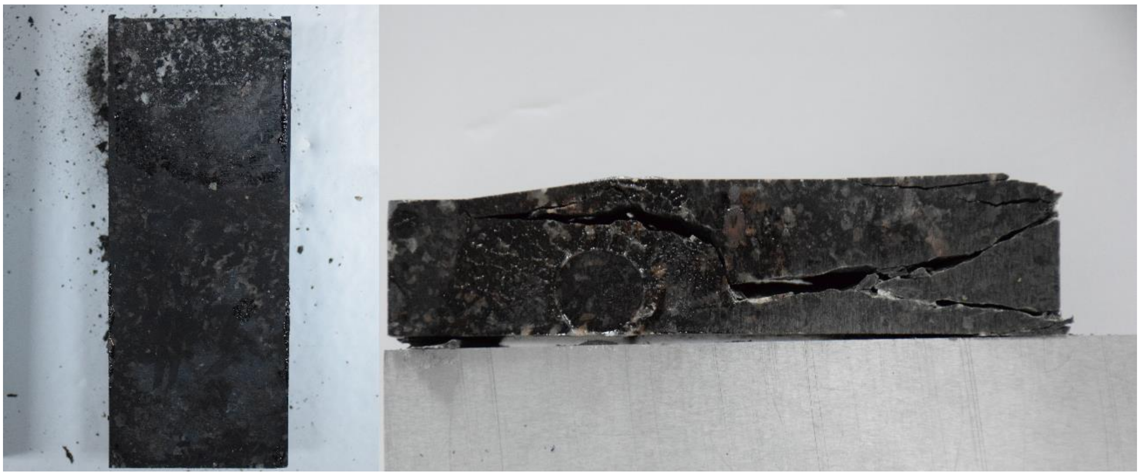

Figure A.8 Specimen B2#3 after strain burst test (50 °C)

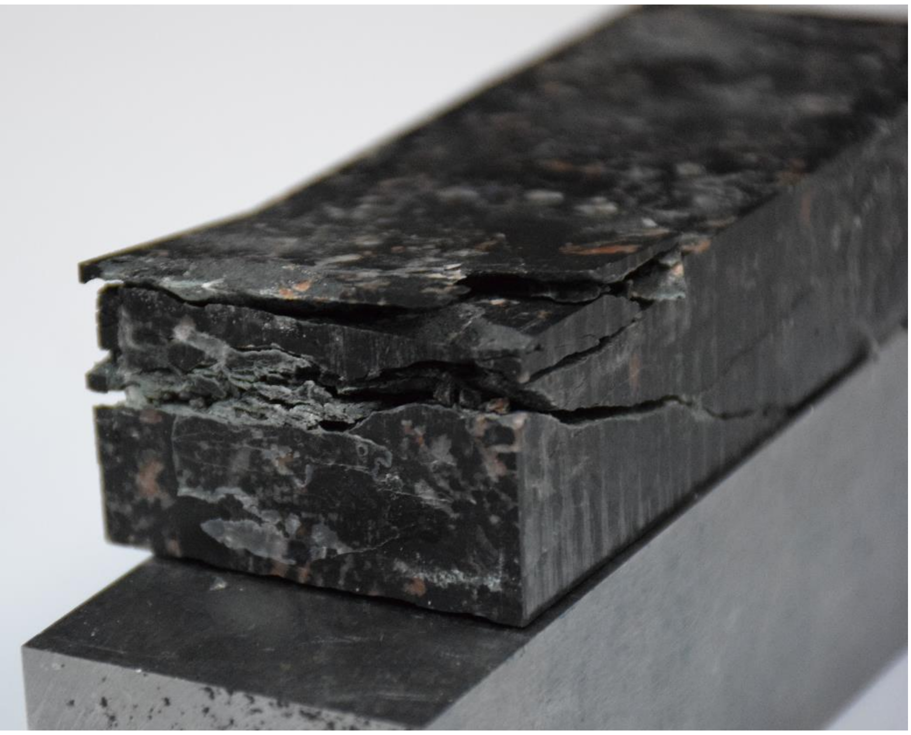

Figure A.9 Specimen B1#3 after strain burst test (75 °C)

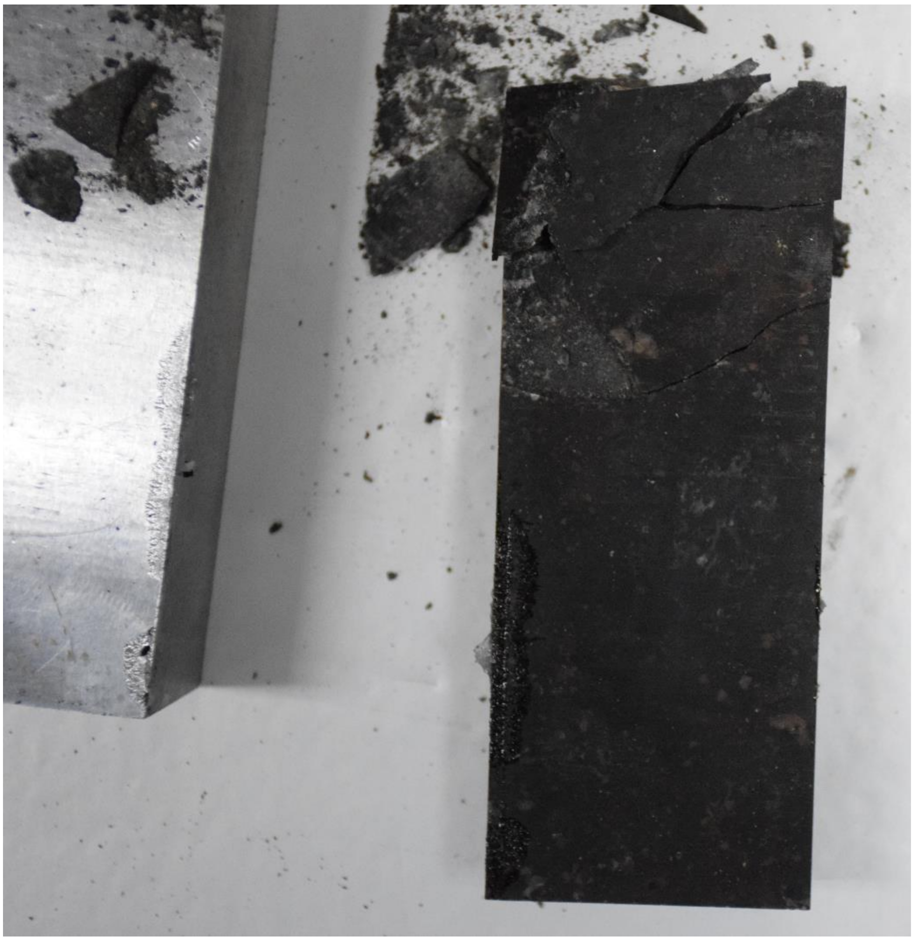

Figure A.10 Specimen B1#4 after strain burst test (75 °C)

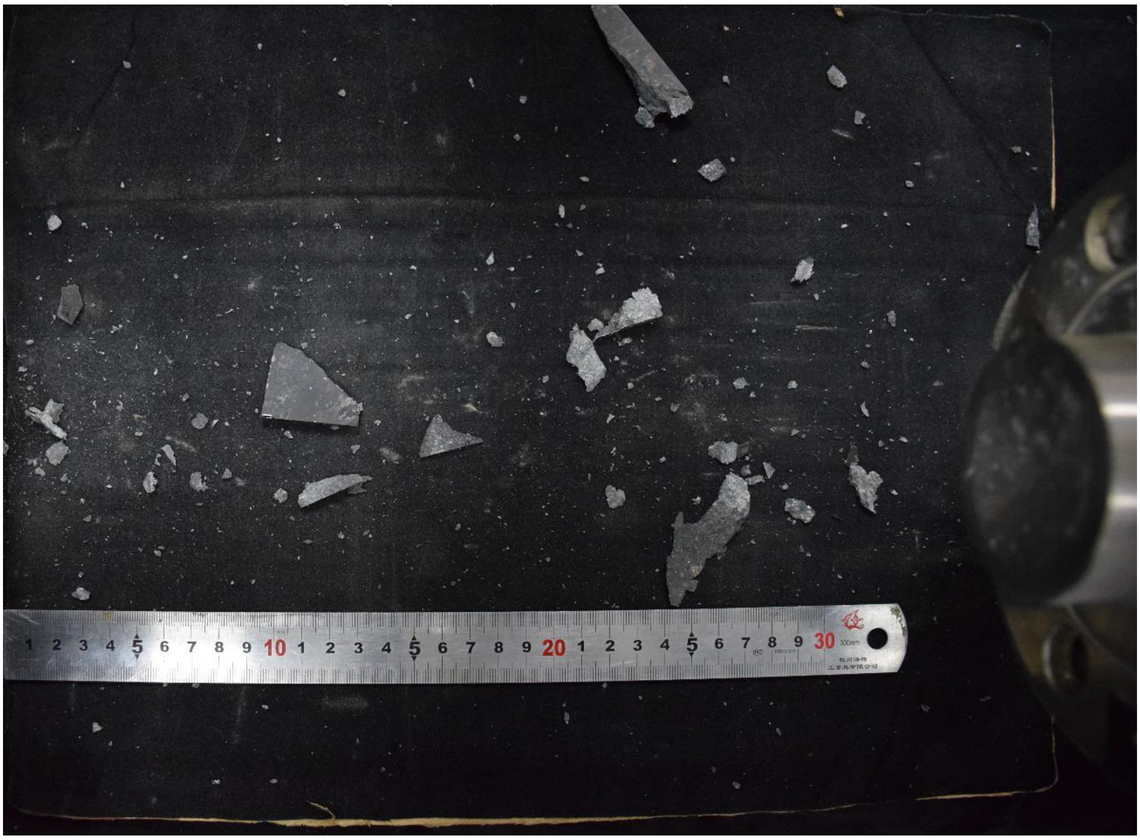

Figure A.11 Locations of the ejected fragments for B1#4 after strain burst test (75 °C)

Figure A.12 Specimen B1#6 after strain burst test (100 °C)

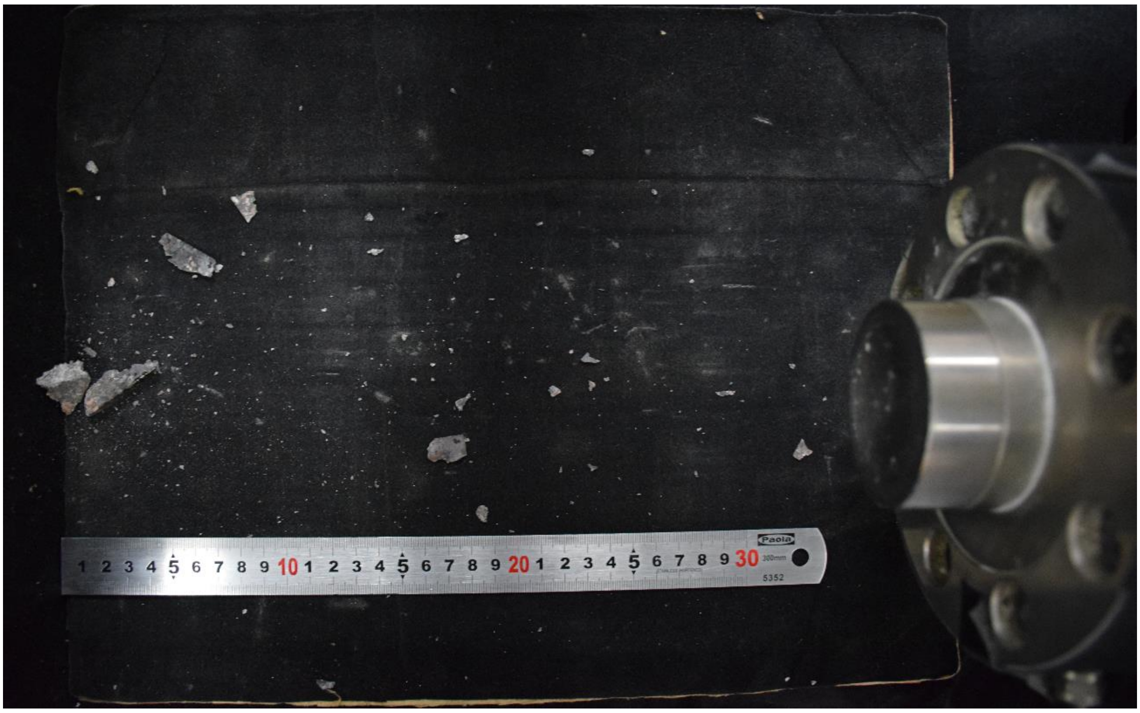

Figure A.13 Locations of the ejected fragments for B1#6 after strain burst test (100 °C)

Figure A.14 Specimen B1#7 after strain burst test (100 °C)

Figure A.15 Locations of the ejected fragments for B1#7 after strain burst test (100 °C)

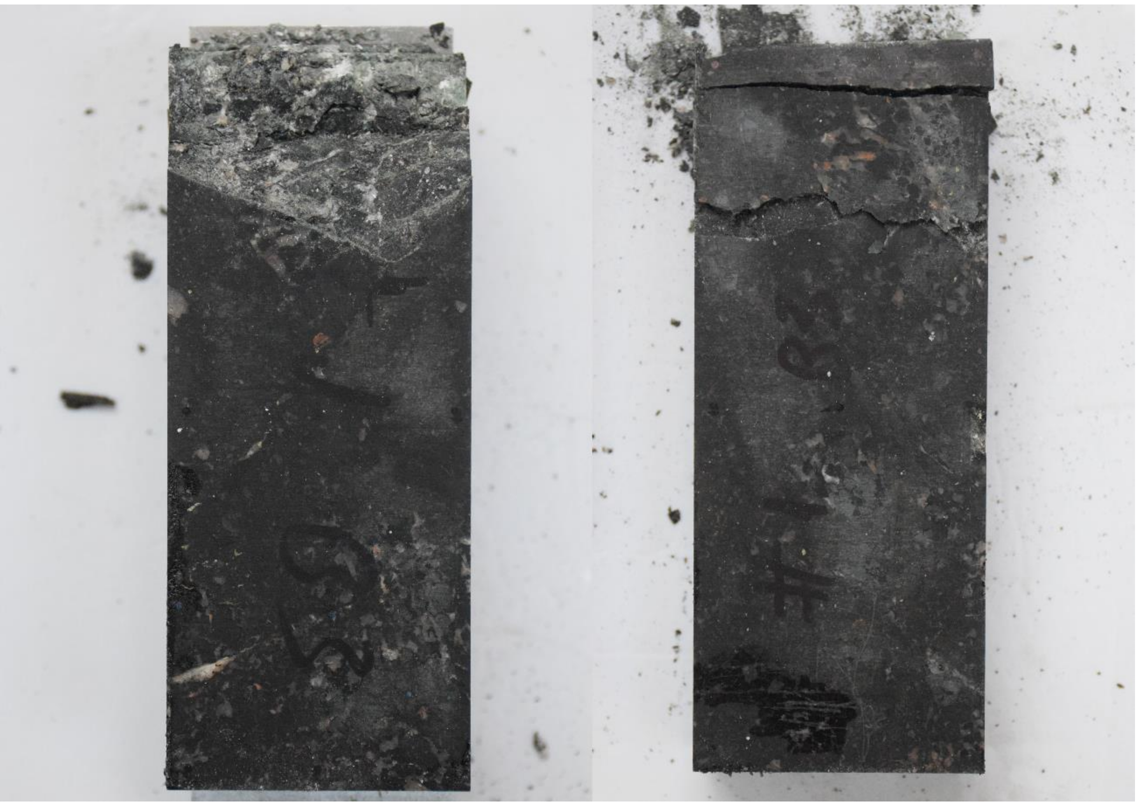

Figure A.16 Specimen B3#1 after strain burst test (100 °C)

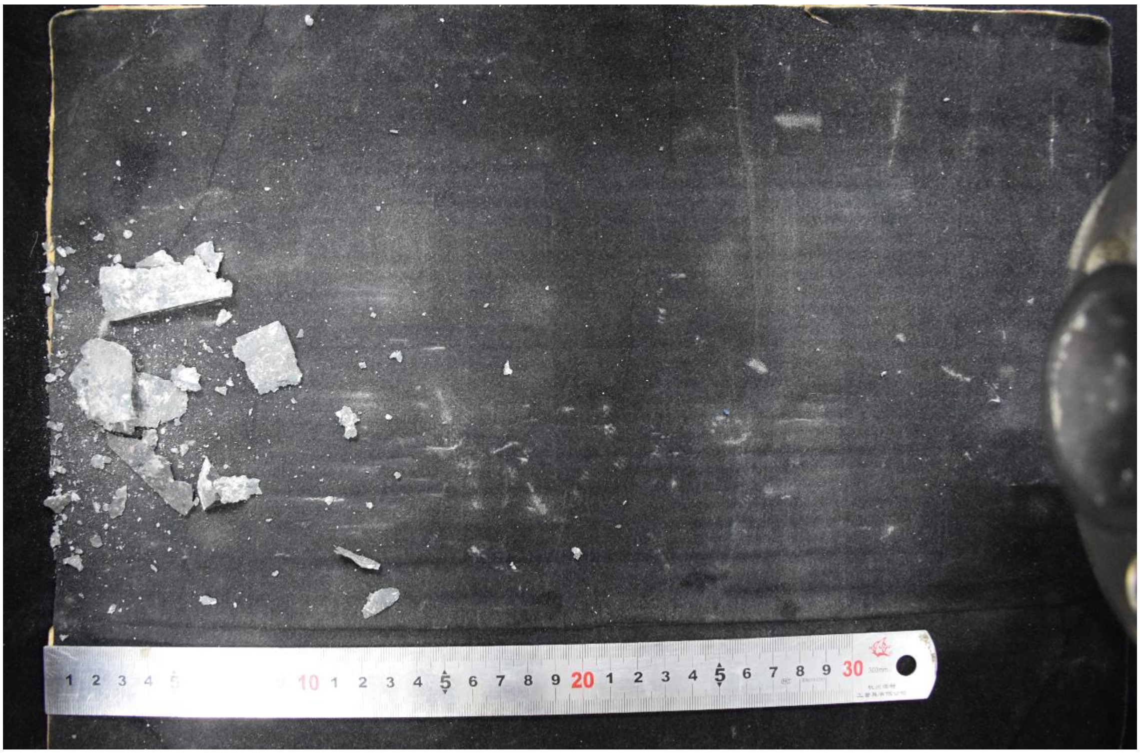

Figure A.17 Locations of the ejected fragments for B3#1 after strain burst test (100 °C)

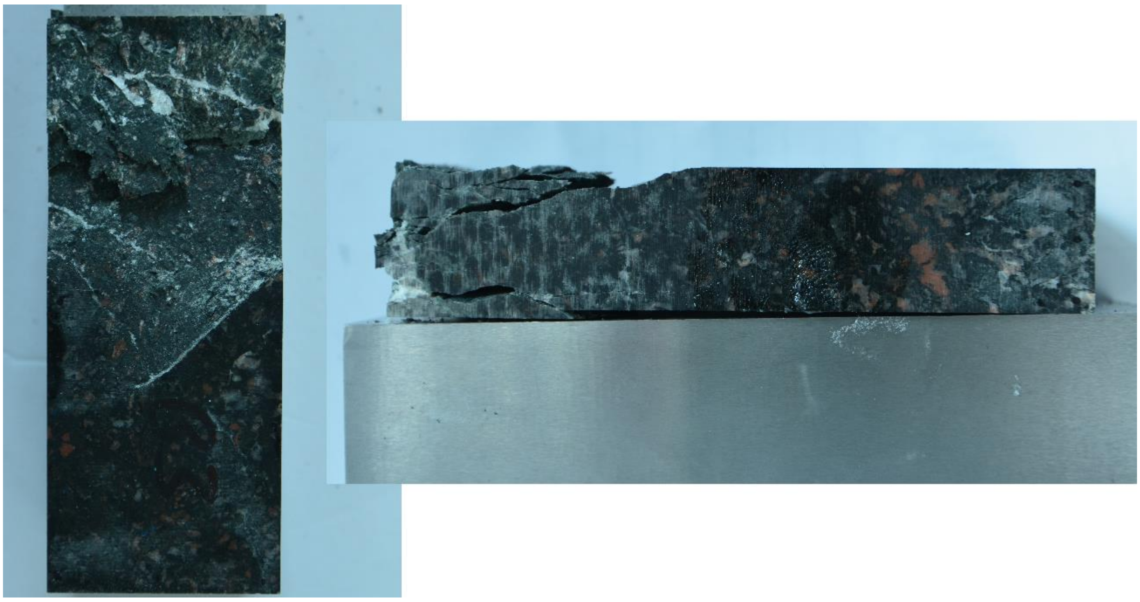

Figure A.18 Specimen B3#2 after strain burst test (125 °C)

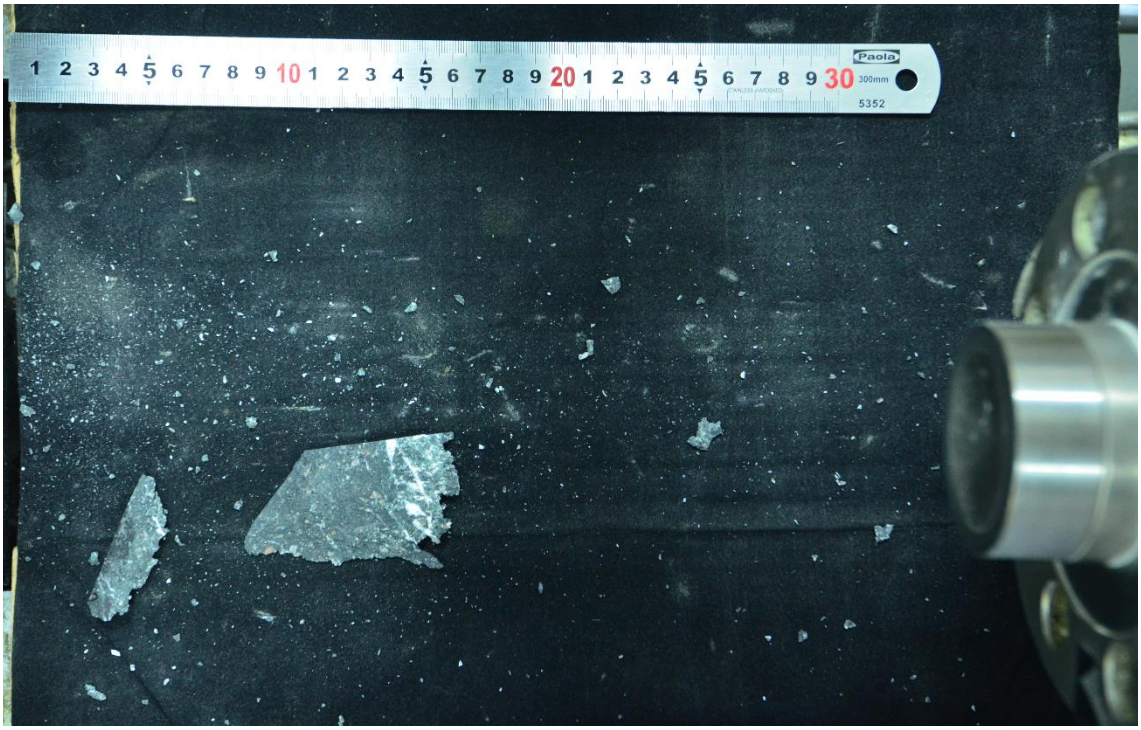

Figure A.19 Locations of the ejected fragments for B3#2 after strain burst test (125 °C)

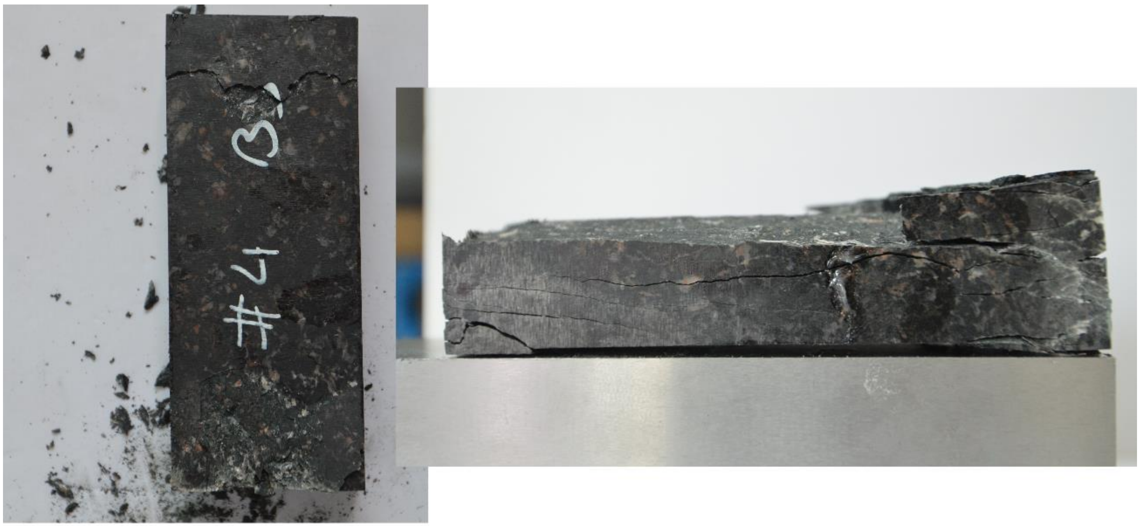

Figure A.20 Specimen B3#4 after strain burst test (125 °C)

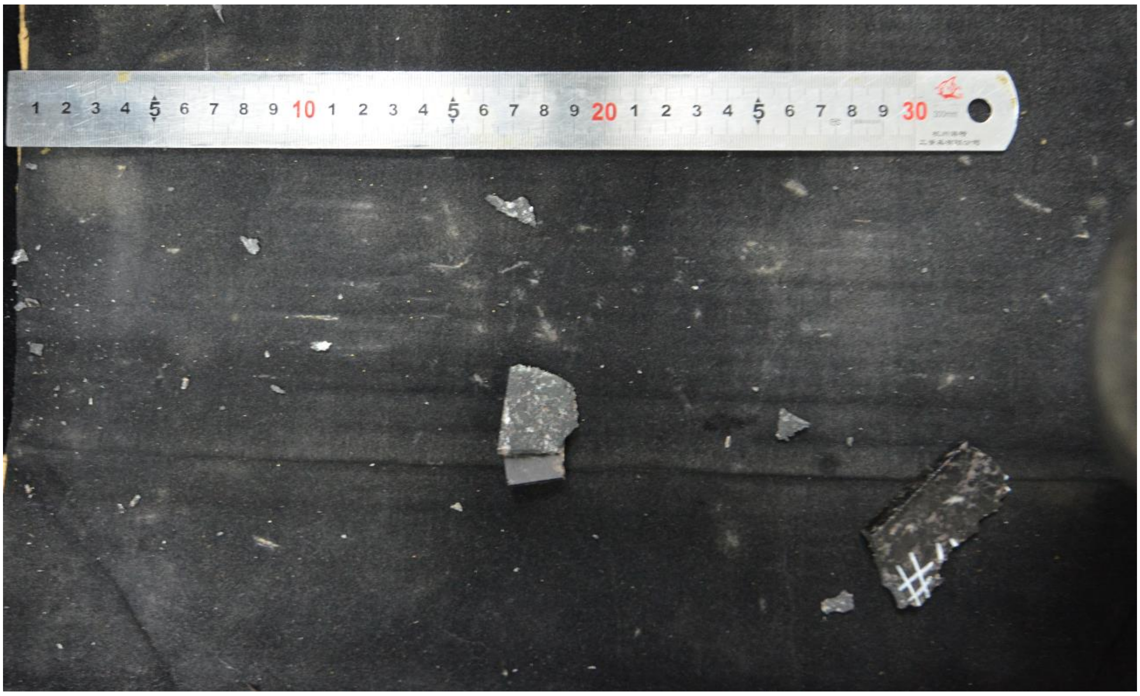

Figure A.21 Specimen B3#4 after strain burst test (125 °C)

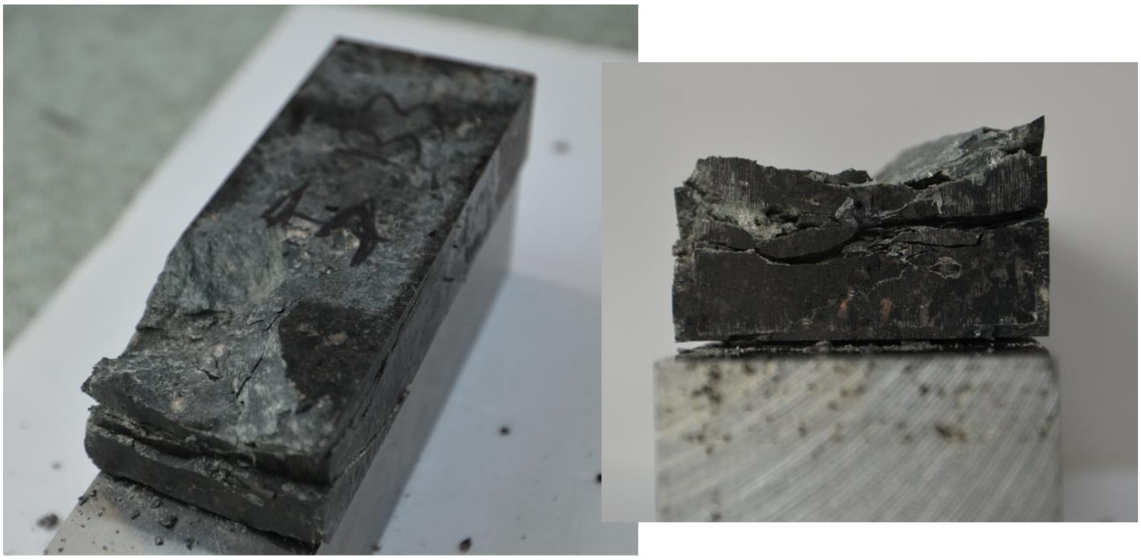

Figure A.22 Specimen B3#5 after strain burst test (125 °C)

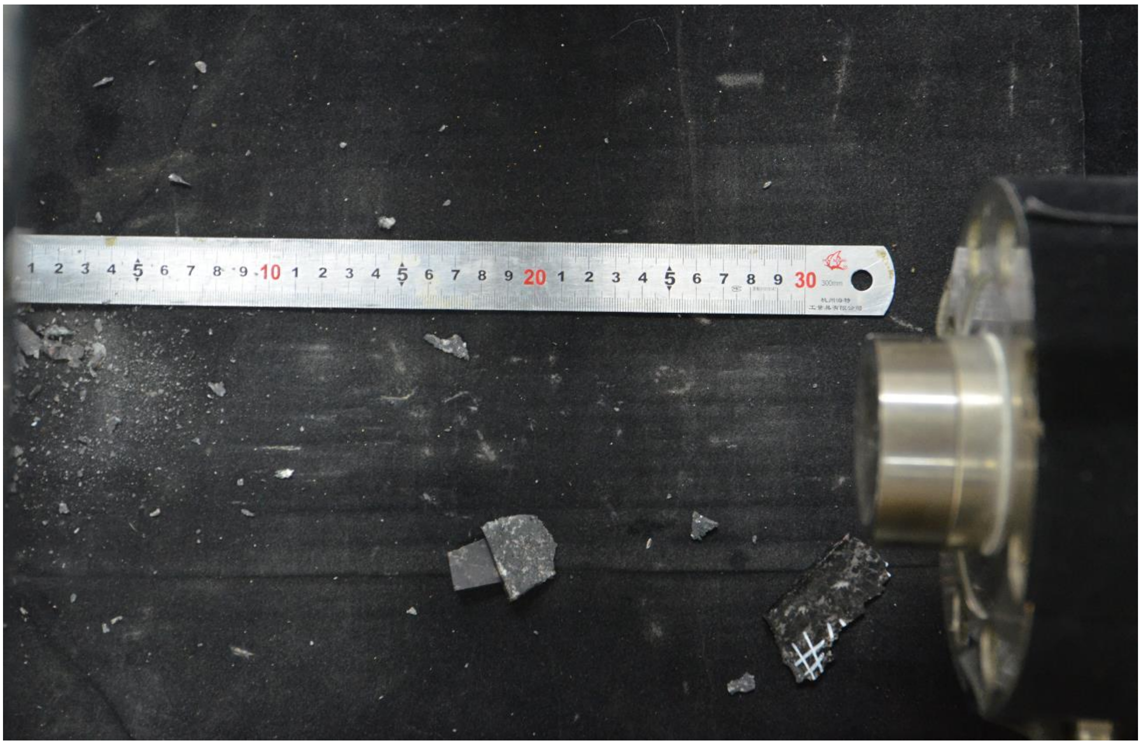

Figure A.23 Specimen B3#5 after strain burst test (125 °C)

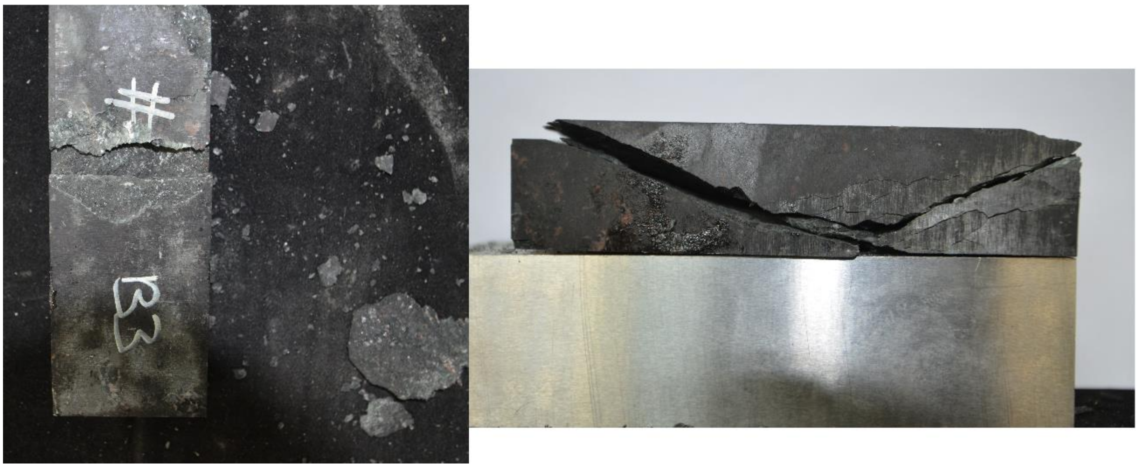

Figure A.24 Specimen B3#6 after strain burst test (150 °C)

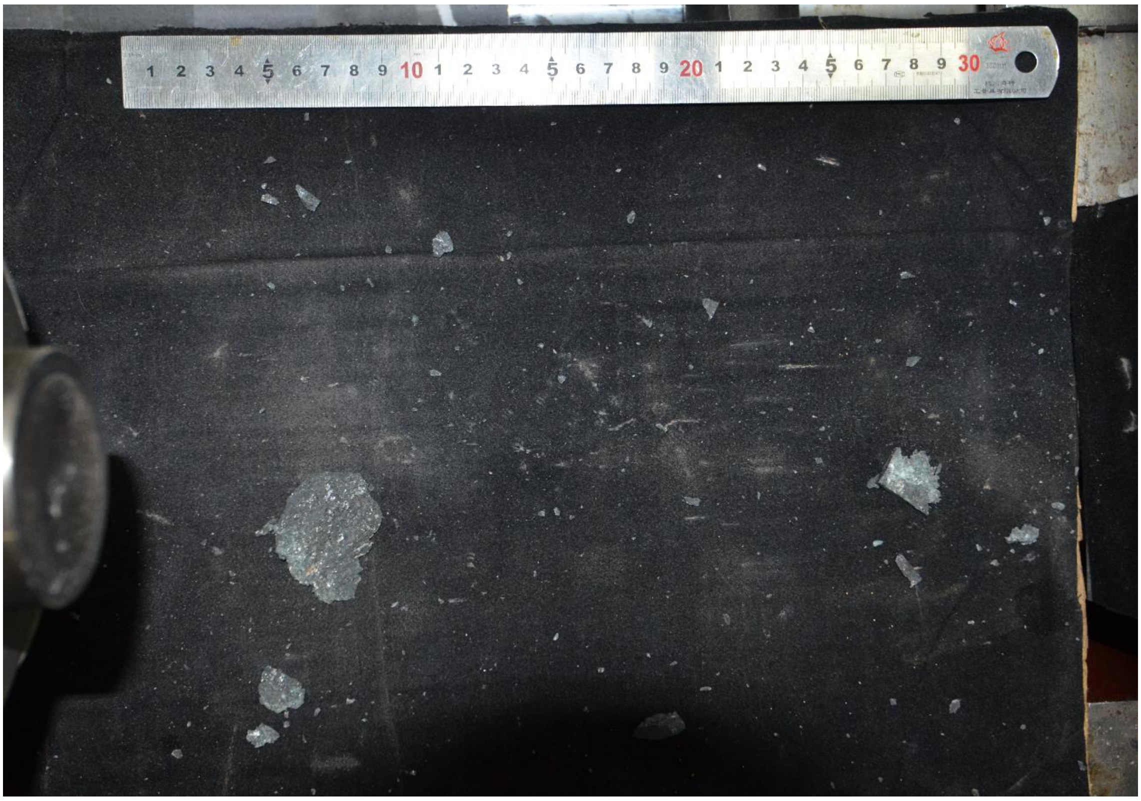

Figure A.25 Specimen B3#6 after strain burst test (150 °C)

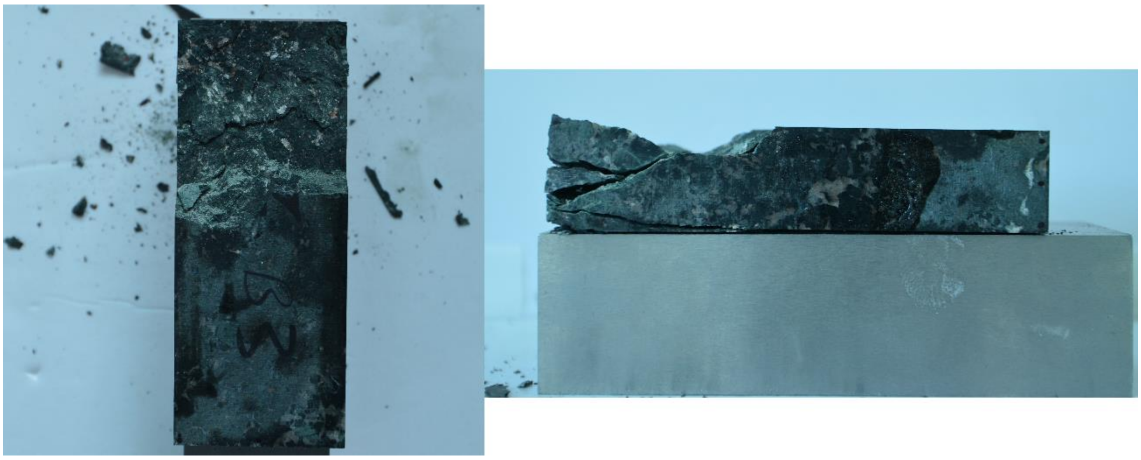

Figure A.26 Specimen B3#7 after strain burst test (150 °C)

Figure A.27 Specimen B3#8 after strain burst test (150 °C)